

Statistical Trends in Atmospheric Properties of Close-in Giant Exoplanets

ACADEMISCH PROEFSCHRIFT

ter verkrijging van de graad van doctor
aan de Universiteit van Amsterdam
op gezag van de Rector Magnificus
prof. dr. K. I. J. Maex

ten overstaan van een door het College voor Promoties ingestelde
comissie, in het openbaar te verdedigen in de Agnietenkapel
op woensdag 8 september 2021, te 10:00 uur

door

Claire Julie Baxter

geboren te Melrose

Promotiecommissie:

Promotor: Prof. dr. C. Dominik Universiteit van Amsterdam

Copromotor: dr. J.M.L.B. Désert Universiteit van Amsterdam

Overige leden: prof. dr. A.H.M.J. Triaud University of Birmingham
prof. dr. L. Kaper Universiteit van Amsterdam
prof. dr. R.A.D. Wijnands Universiteit van Amsterdam
dr. A. Oklopčić Universiteit van Amsterdam
dr. D.M. Stam TU Delft

Faculteit der Natuurwetenschappen, Wiskunde en Informatica



UNIVERSITY OF AMSTERDAM



ANTON PANNEKOEK
INSTITUTE

The research reported in this thesis was carried out at the Anton Pannekoek Institute for Astronomy (API), University of Amsterdam. This work is based on observations made with the Spitzer Space Telescope, which is operated by the Jet Propulsion Laboratory, California Institute of Technology under a contract with NASA. Support for this work was provided by NASA through an award issued by JPL/Caltech. The work was supported by fundings from NASA grant NNX16AC64G, the Amsterdam Academic Alliance (AAA) Program, and the European Research Council (ERC) European Union's Horizon 2020 research and innovation program (grant agreement no. 679633; Exo-Atmos) and with occasional funding from the Leids Kerkhoven-Bosscha Fonds (LKBF).

quote

S. omeone

CONTENTS

1	Introduction	1
1.1	Exoplanets	1
1.1.1	Exoplanets in general	1
1.1.2	Exoplanet discovery and diversity	1
1.1.3	The strength of the multiple system planets: masses from TTVs	3
1.2	Exoplanet atmospheres	4
1.2.1	Methods for probing exoplanet atmospheres	4
1.2.1.1	Transmission spectroscopy	4
1.2.1.2	Emission Spectroscopy	6
1.2.1.3	Phase curves	7
1.2.2	Instrumentation for probing exoplanet atmospheres used in this thesis	8
1.2.2.1	<i>Spitzer</i> /IRAC	8
1.2.2.2	HST/WFC3	8
1.2.3	Systematics and Noise Sources	8
1.2.3.1	<i>Spitzer</i> /IRAC intrapixel sensitivity	10
1.2.3.2	Pixel Level Decorrelation	10
1.2.4	Properties and Climates of exoplanets	11
1.2.4.1	Chemistry	11
1.2.4.2	Temperature structure	12
1.2.4.3	Clouds and hazes	14
1.2.4.4	Dynamics, climate and variability	17
1.2.4.5	Inflated hot Jupiters	19
1.2.5	Models of Exoplanet Atmospheres	19
1.2.5.1	Exo-Transmit	20
1.2.5.2	VULCAN and PLATON	20
1.2.5.3	ScCHIMERA	20
1.3	Exoplanet atmosphere diversity	21
1.3.1	Looking at planet ensembles	21
1.3.1.1	Transmission surveys	21
1.3.1.2	Emission surveys	22
1.3.2	The Ultra-hot Jupiters as a separate class	25

1.3.3	The cool planets	26
1.4	This Thesis	27
2	Evidence for disequilibrium chemistry from vertical mixing in hot Jupiter atmospheres: A comprehensive survey of transiting close-in gas giant exoplanets with warm-<i>Spitzer</i>/IRAC	31
2.1	Introduction	33
2.2	Observations	35
2.3	Analysis	38
2.3.1	Transit lightcurve analysis	38
2.3.1.1	Extracting <i>Spitzer</i> photometric lightcurves	38
2.3.1.2	Instrumental Systematic Modelling	40
2.3.1.3	Fitting lightcurves to obtain transit parameters	42
2.3.2	Interpreting Transmission Spectrophotometry with 1-D Atmospheric Modeling	44
2.3.2.1	Stellar Irradiation and T-P profiles	44
2.3.2.2	Grid of stellar spectra	47
2.3.2.3	Modeling the photo-chemical kinetics with VULCAN	48
2.3.2.4	Creating the transmission spectra with PLATON	48
2.3.2.5	Calculating the model <i>Spitzer</i> /IRAC transit depths	48
2.4	Results	51
2.4.1	Measured transit depths and their ratios	51
2.4.1.1	Results of measured transit depths	51
2.4.1.2	Comparison to literature	54
2.4.1.3	Transit depth ratio	54
2.4.1.4	Searching for trends in the difference of transit depths	55
2.4.1.5	Transit depth versus equilibrium temperature	56
2.4.2	Results from the 1-D grid of model transmission spectra	56
2.4.2.1	General trends observed in the grids of models	56
2.4.2.2	Statistical comparison of planet atmospheres with model grid	60
2.5	Discussion	62
2.5.1	Expected opacities at 3.6 and 4.5 μm	62
2.5.2	Discussion on Transit Survey	64
2.5.2.1	Comparing transit depths to fiducial model grid	64
2.5.2.2	Effect of metallicity in hot Jupiter atmospheric spectra	65
2.5.2.3	Vertical mixing and non-equilibrium effects	66
2.5.2.4	Effects of clouds on the cool and hot Jupiter atmospheric spectra	67
2.5.2.5	Outliers and the effect of nightsides	68
2.5.2.6	Radius Anomaly	69
2.5.2.7	Stellar Variability	69

2.5.3	Comparing Transmission and Emission with warm <i>Spitzer</i> /IRAC	70
2.5.3.1	Probing different pressures with emission and transmission	71
2.5.3.2	Comparing to brown dwarfs with a Color-Magnitude diagram	72
2.6	Conclusion	74
Appendix 2.A	Pipeline results Figures and Tables	75
Appendix 2.B	VULCAN validation on HD 209458b	94
Appendix 2.C	Radius Anomaly	94
3	A transition between the hot and the ultra-hot Jupiter atmospheres	103
3.1	Introduction	104
3.2	Observations	105
3.3	Data analysis	106
3.3.1	Calculating the planetary brightness temperatures	106
3.3.2	Extracting the planetary flux deviation from a blackbody	107
3.3.3	Irradiation, equilibrium, effective, and max dayside temperatures definitions	108
3.3.4	Grid of forward emission models to interpret observations	108
3.4	Results	110
3.4.1	Deviation between equilibrium and brightness temperatures	110
3.4.2	Increasing trend in brightness temperature ratio versus equilibrium temperature	112
3.4.3	Increasing trend in planetary deviation from a blackbody	112
3.5	Discussion	113
3.5.1	Summary of our main results	113
3.5.2	Expected opacities at $3.6\ \mu\text{m}$ and $4.5\ \mu\text{m}$	115
3.5.3	Grid of forward models	116
3.5.4	Interpretation of the transition from hot Jupiters to ultra-hot Jupiters	117
3.5.4.1	Assumptions on albedo, redistribution, clouds, and thermal structure	117
3.5.4.2	Transition in thermal inversions	118
3.6	Clues from HST/WFC3	120
3.7	Conclusions	122
Appendix 3.A	Details of the data analysis	123
3.A.1	Fitting correlations with x and y errors	123
Appendix 3.B	Importance of using stellar models	124
3.B.1	Effect of different stellar models on measured temperature	124
Appendix 3.C	Comparing effective temperatures with Schwartz & Cowan (2015)	126
Appendix 3.D	KELT-9b Eclipse: the hottest of the UHJs	127
4	Periodic variability in the brightness of an ultra-hot Jupiter atmosphere	135
4.1	Introduction	136

4.2	Observations	137
4.3	Data Analysis	137
4.3.1	<i>Spitzer</i> /IRAC photometric lightcurve reduction	137
4.3.2	<i>Spitzer</i> /IRAC secondary eclipse fitting	138
4.4	Results	139
4.4.1	<i>Spitzer</i> /IRAC secondary eclipse lightcurves	139
4.4.2	Brightness variability of WASP-18b in time	142
4.4.3	Testing the method to measure variability	142
4.4.4	Variability of WASP-18b at various wavelengths	145
4.5	Discussion & Conclusion	145
	Appendix 4.A Supplementary plots	147
5	Transit timing variations of cool Kepler planets from Spitzer/IRAC analysis	151
5.1	Introduction	152
5.2	Observations	153
5.3	Data Analysis	155
5.3.1	<i>Spitzer</i> /IRAC lightcurve reduction	155
5.3.2	<i>Spitzer</i> /IRAC lightcurve fitting	156
5.3.2.1	Obtaining the best fits of the multi-planet systems	156
5.3.2.2	Obtaining the best fits of the Kepler-16 system	158
5.3.3	TTV predictions of the multi-planet systems	159
5.3.4	Kepler-16b photodynamical model	159
5.4	Results	161
5.4.1	Transit times for the multi-planet systems	161
5.4.2	Comparing multi-planet system transit times to predictions	163
5.4.3	Kepler-16b lightcurves and transit parameters	163
5.4.4	Comparing Kepler-16b to photodynamical model	165
5.5	Discussion and Conclusion	169
	Appendix 5.A Supplementary plots	170
	Bibliography	179
	Contribution from co-authors	191
	Nederlandse Samenvatting	193
	Summary	197
	Acknowledgements	201

1

INTRODUCTION

1.1 Exoplanets

1.1.1 Exoplanets in general

“How did we come to be here?” and “Are we alone in the universe?” are two of the most thought-provoking questions that philosophers have been asking for thousands of years. These questions lie at the heart of exoplanet research. We, exoplanet scientists, are answering these questions by studying the formation, chemistry, and climates of planets around other stars.

In 1992, the first exoplanet was identified around a pulsar, PSR B1257+12 (Wolszczan & Frail 1992). And then in 1995, the first exoplanet orbiting a sun-like star, 51-Pegasi b, was found (Mayor & Queloz 1995). This Nobel Prize-winning discovery raised more questions than it answered as this planet was unlike any in our solar system, even though it revolved around a star much like our own sun. It had half the mass of Jupiter, yet its distance from its parent star was 20 times shorter than that between Earth and the Sun.

Since 1995, the list of exoplanet discoveries has grown exponentially. Many of these discoveries were gas giant planets on close-in orbits, or “hot Jupiters”, due to their favorable discovery signatures. What we now know as 51-Pegasi b was but the first of around 700 hot Jupiters discovered to date, with the total confirmed exoplanet tally exceeding 4000¹. In addition to this, there are more than 4500 planet candidates discovered with Kepler, K2 and TESS pending confirmation. With this large and continuously growing sample of exoplanets, answering the key questions and solving the puzzle of how we came to be here is well underway.

1.1.2 Exoplanet discovery and diversity

On average, 50% of the stars in our galaxy host at least one planet (Howard et al. 2012; Dressing & Charbonneau 2013; Batalha et al. 2013; Silburt et al. 2015). The 4,340 exoplanets confirmed to date range from small rocky planets to large gas giants. Figure 1.1 shows a plot

¹Calculated using the hot Jupiter definition from Winn (2010) and the NASA Exoplanet Archive: <https://exoplanetarchive.ipac.caltech.edu/>

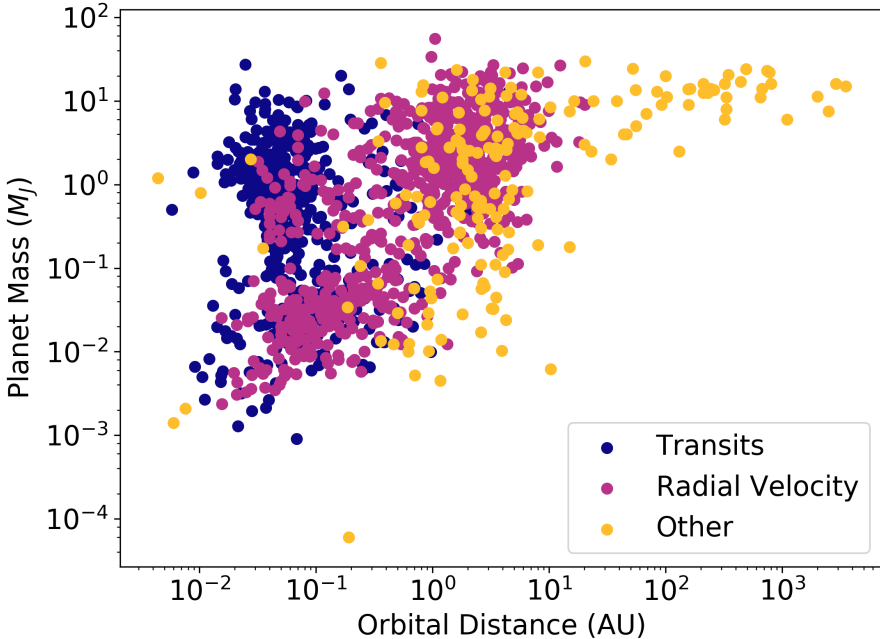


Fig. 1.1: Mass of the planet (or minimum mass for radial velocity planets) in Jupiter masses against the orbital distance in astronomical units for all of the confirmed exoplanets (4340 planets as of 5th February 2021, NASA Exoplanet Archive). Colors show the discovery methods: blue is transiting planets, purple is radial velocity detections and orange is all other detection methods.

of mass vs orbital distance of all these planets colour-coded by discovery technique. Out of the many methods employed, two account for the vast majority of discoveries: transiting planets (3306 planets, shown in blue) and radial velocity planets (823 planets, coded purple).

Transiting planets pass in front of their star and create a periodic shadow in the flux measured from their star. The dimming of the stellar light when the planet passes in front of the star has a characteristic depth. This depth is a measure of the radius of the planet relative to the radius of the star (R_p^2/R_s^2). On the other hand, radial velocity planets are detected by observing a signature of the movement of the host star due to the gravitational pull throughout the planetary orbit. Other techniques - represented by the colour orange in Figure 1.1 - include microlensing, imaging, transit/eclipse timing variations, and pulsar timing.

The exoplanet population can be broadly classified into four families according to mass. At the lower end of the mass spectrum are the terrestrial planets, similar to the four smallest planets of our solar system: Mercury, Venus, Earth and Mars. Within this group fall exoplanets with masses similar to the mass of Earth (around $0.5\text{--}2 M_\oplus$ and sometimes even smaller). The second family are the Super-Earths. These planets are more massive than Earth

($1 M_{\oplus} = 3.1 \times 10^{-3} M_J$) but less massive than Uranus or Neptune and orbit their host stars at distances shorter than that between Earth and the Sun. Terrestrial planets and Super-Earths occupy the bottom left cluster of Figure 1.1. Super-Earths are considered the most abundant in our galaxy (Borucki et al. 2011; Howard et al. 2012; Morton & Swift 2014; Batalha 2014; Petigura et al. 2013b, 2018; Fulton et al. 2017; Bryson et al. 2020). Rocky planets on short period orbits close to their host stars are known as hot-rocks or lava planets. They are so hot that their surface is mostly or entirely covered by lava oceans (e.g., Léger et al. 2011; Elkins-Tanton 2012; Winn et al. 2018).

The third family is the Neptunian exoplanets, with masses similar to those of Neptune and Uranus. These are planets with rocky cores and hydrogen/helium-dominated atmospheres. Warm-Neptunes ($2-6 M_{\oplus}$ on short orbital periods) are a ubiquitous outcome of planet formation, occurring around more than 25% of all stars (e.g., Buchhave et al. 2014; Fulton et al. 2017).

Finally, the largest exoplanets have masses similar to that of Jupiter. Due to their size, these planets are the easiest to find with current detection techniques. However, in absolute numbers, they are less common as other types of planets (e.g., Gould et al. 2006; Howard et al. 2012; Fressin et al. 2013; Santerne et al. 2012; Wright et al. 2012). Cooler Jupiter-like planets (top right cluster of Figure 1.1) are predominantly discovered by radial velocity and are ideal targets for direct imaging. In contrast, hot Jupiters (top left cluster of Figure 1.1) are mostly discovered by the transit method. Hot Jupiters are, as the name suggests, a similar mass to Jupiter but are on orbits that lie within the orbit of Mercury and so receive much more insolation from their host stars. As a result, their temperature is typically more than 1500K (1200°C). It is these gas giant planets that are the focus of this thesis.

1.1.3 The strength of the multiple system planets: masses from TTVs

Out of the 4,000+ exoplanets discovered to date, 1864 belong to 745 multi-planet systems. Gravitational interactions between planets in the same system cause the planets to deviate from Keplerian orbits. This means that the orbital period is no longer a constant value and thus the time between each transit (planet crossing the star) will vary. This phenomenon is called transit timing variation (TTV). TTVs are useful in many areas of exoplanet science (e.g., Schneider 2003; Agol et al. 2005; Holman & Murray 2005). For example, they have been used to infer the presence of a non-transiting planet in a system where at least one planet is transiting or to confirm that a transit signal is indeed due to a planet and not a false positive. Additionally, TTVs can be used for planet characterization by constraining the masses and other orbital elements (e.g., Ballard et al. 2011; Holman et al. 2010; Carter et al. 2012).

The Kepler mission provided four years of almost continuous optical photometric observations of several hundred multi-planet systems. Several studies have used this data to constrain the parameters of the orbital dynamics and planetary masses. In Chapter 5 of this thesis, we follow up on four of these systems using multiple transit observations per planet. We aim to confirm the TTV signal at another wavelength (near infrared with *Spitzer*/IRAC compared

to optical with Kepler) to lengthen the baseline of the previous Kepler observations and to look for signatures of more planets.

1.2 Exoplanet atmospheres

1.2.1 Methods for probing exoplanet atmospheres

There are two main methods for characterizing the atmospheres of exoplanets: direct imaging and transmission/emission spectroscopy. These can both be performed at either high or low resolution.

The probability of a planet transiting is R_s/a , where R_s is the stellar radius and a is the planetary orbital distance (Borucki & Summers 1984). This means that there is a very small fraction of the population of exoplanets that are viable for transmission spectroscopy. In theory, direct imaging can be used to observe the atmospheres of these non-transiting planets. However, directly imaging exoplanets is difficult since telescopes and observatories have to overcome the very high contrast ratios between the star and the planet. With the detectors quickly becoming saturated by the stellar flux, there is often not enough time to gather enough photons from the planet. Nevertheless, with state-of-the-art coronagraphic and adaptive optics systems, several exoplanets have been directly imaged (e.g., Marois et al. 2008, 2010; Lagrange et al. 2010; Rameau et al. 2013; Kuzuhara et al. 2013).

This thesis focuses on characterizing the atmospheres of transiting planets. The transit method is a common technique for discovering planets. The measured transit depth and eclipse depth are wavelength and atmospheric composition-dependent quantities so can also be used to observe and study the atmospheres of planets (e.g., Seager & Sasselov 2000; Brown 2001; Charbonneau et al. 2005; Deming et al. 2005). In Figure 1.2 we show a schematic of a planet orbiting a star, which includes the transit (the planet in front of the star), the eclipse (the planet behind the star), and this full observation is called a phase curve. These techniques can each be used to study the properties of planetary atmospheres, giving us different parts of the story each time.

1.2.1.1 Transmission spectroscopy

The fractional change in the brightness of a star as a planet transits is equal to the radius of the planet divided by the radius of the star (R_p^2/R_s^2). However, during the transit, a small fraction of the starlight passes through and is partially absorbed by the upper atmosphere of the planet. The strength of this atmospheric absorption is wavelength dependent due to the opacities of different molecular and atomic species. At wavelengths where the atmosphere is more opaque, the transit depth will be larger due to absorption of the stellar light, and where it is more transparent the transit depth will be smaller. Observing the planet transit across different wavelengths results in a transmission spectrum of the atmosphere. Transmission spectra can be compared with models of the chemistry and molecular opacities to gain insights into the

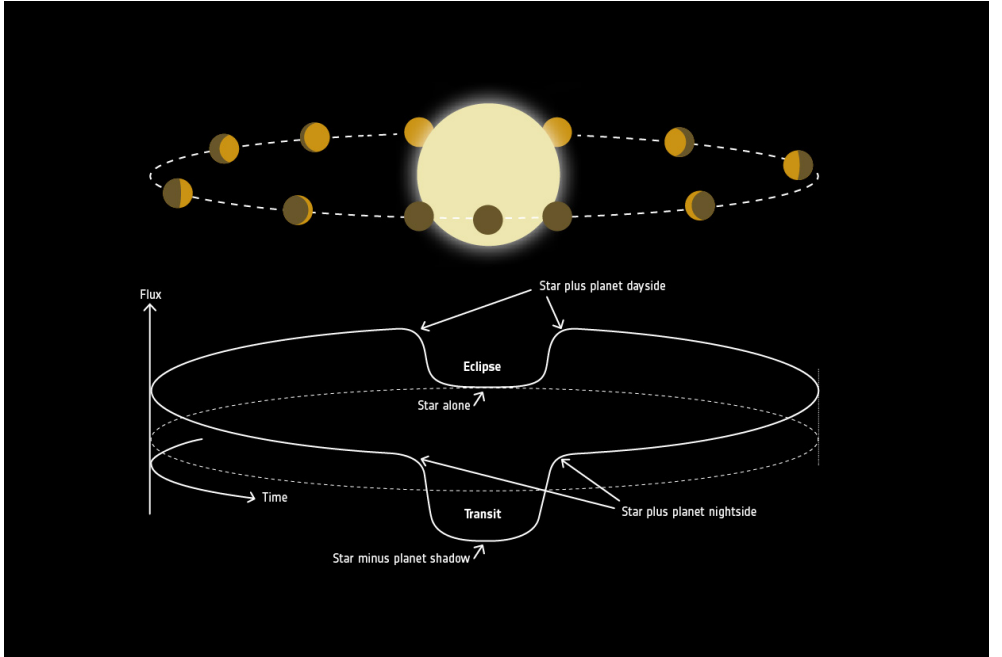


Fig. 1.2: Illustrative graphic detailing the full orbit of a planet around its host star, showing the transit and the eclipse. The full orbit observation is known as the phase curve, it captures all phases of the planet's tidally locked dayside. Image Credit: ESA

atmospheric composition (Charbonneau et al. 2002; Vidal-Madjar et al. 2003; Tinetti et al. 2007; Swain et al. 2008).

Typically, differences in the transit depth are larger for hot, puffy atmospheres with large scale heights (H):

$$H = \frac{k_B T}{\mu_m g}, \quad (1.1)$$

where T is the temperature, μ_m is the mean molecular mass, g is the gravitational acceleration and k_B is Boltzmann's constant. The scale height is a measure of the increase in altitude when the atmospheric pressure decreases by a factor of e , and for hot Jupiter atmospheres is on the order of a few hundred kilometers. In many cases, we use the equilibrium temperature (T_{eq}) for T and the planetary surface gravity for g .

The measured difference in the transit depth (R_p^2/R_s^2) resulting from an absorption feature can be written in terms of the number of scale heights crossed (N_H),

$$\Delta\delta = \frac{\pi(R_p + N_H H)^2}{\pi R_s^2} - \frac{\pi R_p^2}{\pi R_s^2} \approx 2N_H \delta \left(\frac{H}{R_p} \right). \quad (1.2)$$

where δ is the transit depth (R_p^2/R_s^2) and $\Delta\delta$ is the difference in the transit depth inside and

outside a molecular feature. Hotter planets are expected to have larger atmospheric absorption signals ($\Delta\delta$), due to the dependence on H which scales with the temperature. However, the technique of transmission spectroscopy has successfully been applied to cooler targets as well (e.g., Désert et al. 2011a; Berta et al. 2012; Crossfield & Kreidberg 2017). In Chapter 2 we use equation 1.2 to determine how many scale heights the *Spitzer* Space Telescope probes on average between 3.6 and 4.5 μm for a survey of 49 transiting planets ranging from 600 to 2600 Kelvin. We show that, for our sample of planets, we probe an average of 0.5 scale heights between the two *Spitzer*/IRAC bandpasses at the 7σ level.

1.2.1.2 Emission Spectroscopy

The dayside emission of a planet can be measured by observing the planet before, during, and after it passes behind the star. Similar to the transit, this creates a dip in the light measured throughout time. The depth of that dip, or the eclipse depth, is a measure of the fractional flux of the planet relative to the star (F_p/F_s). Here, F_p and F_s are used to represent the disk-averaged spectral density multiplied by the disk area for the planet and the star respectively. The eclipse depth, in absence of any spectral features, can be represented by the ratio of two Planck functions multiplied by the transit depth,

$$\frac{F_p(\lambda)}{F_s(\lambda)} = \frac{B_\lambda(T_p)}{B_\lambda(T_s)} \frac{R_p^2}{R_s^2}, \quad (1.3)$$

where $B_\lambda(T)$ is the Planck function,

$$B_\lambda(T) \equiv \frac{2hc^2}{\lambda^5} \frac{1}{e^{hc/(\lambda k_B T)} - 1} \quad (1.4)$$

in which T is the temperature of the planet or the star, λ is the wavelength, h is Planck's constant, and c is the speed of light. Assuming the temperature of the star is known, this formulation can also be used to solve for the planetary temperature at a specific wavelength, this is known as the brightness temperature, T_B . In Chapter 3, we calculate the brightness temperature of our planets by using stellar models instead of a blackbody for the star. Additionally, we incorporate the *Spitzer* spectral response functions and rigorously integrate the formulation over the bandpasses to accurately determine the brightness temperatures of a survey of planets with emission at 3.6 and 4.5 μm .

Unlike transmission spectroscopy, where the starlight is passing through the stellar atmosphere, emission spectroscopy measures the emission of the planet relative to the star. The emission spectrum of the planet will deviate from a blackbody depending on the atmospheric composition and temperature structure probed by the photons traveling through the atmosphere (see Section 1.2.4.2 for more on the temperature structure). The crucial difference between the information gathered from transmission spectroscopy and emission spectroscopy is the depth probed in the atmosphere. Due to the slant geometry, an optical depth of 1 is reached at much lower pressures in transmission compared to the normal geometry

in emission (Fortney 2005). Therefore in general, transmission spectroscopy probes the upper more tenuous layers of the atmosphere at pressures around 1 millibar, whereas emission spectroscopy probes deeper layers at pressures of around 0.1-10 bar (depending on the wavelength).

1.2.1.3 Phase curves

A phase curve observation consists of observing the planet throughout its entire orbit, including the transit and the eclipse. Planets on close-in orbits of $\lesssim 10$ days typically become tidally locked, with permanent day and night sides (e.g., Guillot et al. 1996). Therefore, a phase curve allows us to observe the planet as a function of its rotational phase, as demonstrated in Figure 1.2. At each orbital phase, different longitudes of the planet’s dayside are rotating into the view of the observer. The difference in brightness between any two points in phase can be used to reconstruct a brightness map of the planet’s surface (Knutson et al. 2007, 2012; Crossfield et al. 2012; Borucki et al. 2009; Snellen et al. 2009). At optical wavelengths, the planetary brightness is dominated by reflected light from the star, and so a phase curve observation provides constraints on the planet’s albedo. On the other hand, at infrared wavelengths, the planetary brightness is dominated by thermal emission, resulting in longitudinal information about the planet temperature (Parmentier et al. 2018).

As well as the eclipse depth (F_p/F_s) and the transit depth (R_p^2/R_s^2), a phase curve observation can provide us with the measurement of the maximum flux, the phase of the maximum flux relative to eclipse (known as the phase curve offset), and the relative amplitude of the phase curve (day-to-night temperature contrast). Since these planets are tidally locked, the substellar point is brighter than the limbs of the planet. This brightest point can lag (negative offset, westward shift) or lead the substellar point (positive offset, eastward shift). These shifts are measured with the phase curve offset as well as the day-to-night temperature contrast (Showman & Guillot 2002). Parameterizing the phase curve like this is useful for studying the energy balance and the dynamics of the atmosphere (Cowan et al. 2012b; Schwartz & Cowan 2015). In Chapter 3, we use the phase curve offset measured in each of the two *Spitzer*/IRAC bandpasses to determine if a measurement of the efficiency of redistribution from eclipses will change over the two wavelengths.

Similar to transits and eclipses, these phase curves can be measured spectro-photometrically or spectroscopically. At the wavelengths with a strong opacity source and strong atmospheric absorption, a phase curve probes higher in the atmosphere (at low pressures), whereas outside an absorption band the phase curve observation probes deeper (high pressures) (Showman et al. 2009; Kataria et al. 2015). This technique allows for maps of the chemistry and temperature structure and a map of the flux and brightness temperature (Cowan & Agol 2008; Showman et al. 2008; Knutson et al. 2009b; Stevenson et al. 2017). Furthermore, Arcangeli et al. (2021) measured the first emission spectrum at quadrature without the need to observe a full phase curve observation of WASP-12b.

1.2.2 Instrumentation for probing exoplanet atmospheres used in this thesis

This thesis mainly focuses on using multi-epoch observations of exoplanet atmospheres in emission and transmission in the two photometric bandpasses of the *Spitzer* Space Telescopes Infrared Array Camera (*Spitzer*/IRAC) (Werner et al. 2004). However, in Chapter 3 we expand on our work with *Spitzer* by studying full emission spectra taken with the Hubble Space Telescope Wide Field Camera 3 (HST/WFC3) to compare the effects of atmospheric properties at different wavelengths and depths in the atmosphere. Both of these telescopes are space-based observatories, which are advantageous over ground-based observatories as they offer both stability and sensitivity while bypassing the Earth’s atmosphere. This is especially important for this work because the atmosphere of the Earth absorbs in the infrared where there are absorption signatures of the particular molecules that we study, such as water vapor and carbon dioxide.

1.2.2.1 *Spitzer*/IRAC

Launched in 2003, *Spitzer* Space Telescope was cryogenically cooled with liquid helium cryostat to 15K and could observe between 3 and 24 μm over four photometric bands with the Infrared Array Camera (IRAC, Fazio et al. 2004). In 2009, *Spitzer* exhausted its supply of liquid helium and entered the post-cryogenic mission, so called “Warm-*Spitzer*” at \sim 30K (McMurtry et al. 2006), with just the two shorter wavelength bands remaining active, 3.6 and 4.5 μm . After 16 years of observations, the *Spitzer* Space Telescope was decommissioned on the 30th of January 2020. Nevertheless, there remains a wealth of knowledge available from the archival data, which is a focus of this thesis. The two remaining wavelength bands of *Spitzer*/IRAC mainly capture the atmospheric signatures of methane (CH_4), carbon monoxide (CO), carbon dioxide (CO_2), and water (H_2O). In Chapters 2 and 3 we show the atmospheric opacities of the molecules probed with *Spitzer*/IRAC in emission and transmission respectively.

1.2.2.2 HST/WFC3

The Hubble Space Telescope contains some of the current best instruments for measuring the atmospheres of exoplanets. The Wide Field Camera 3 (WFC3) is capable of measuring spectra from 0.8 to 1.7 μm with two separate grisms. In Chapter 3 we use the emission spectra measured with the WFC3/G141 grism, which captures the 1.4 μm water feature. We combine these observations with our *Spitzer*/IRAC photometry.

1.2.3 Systematics and Noise Sources

When attempting to measure the precise signal of an exoplanet atmosphere, dealing with the various noise sources becomes very important. The first noise source is unavoidable:

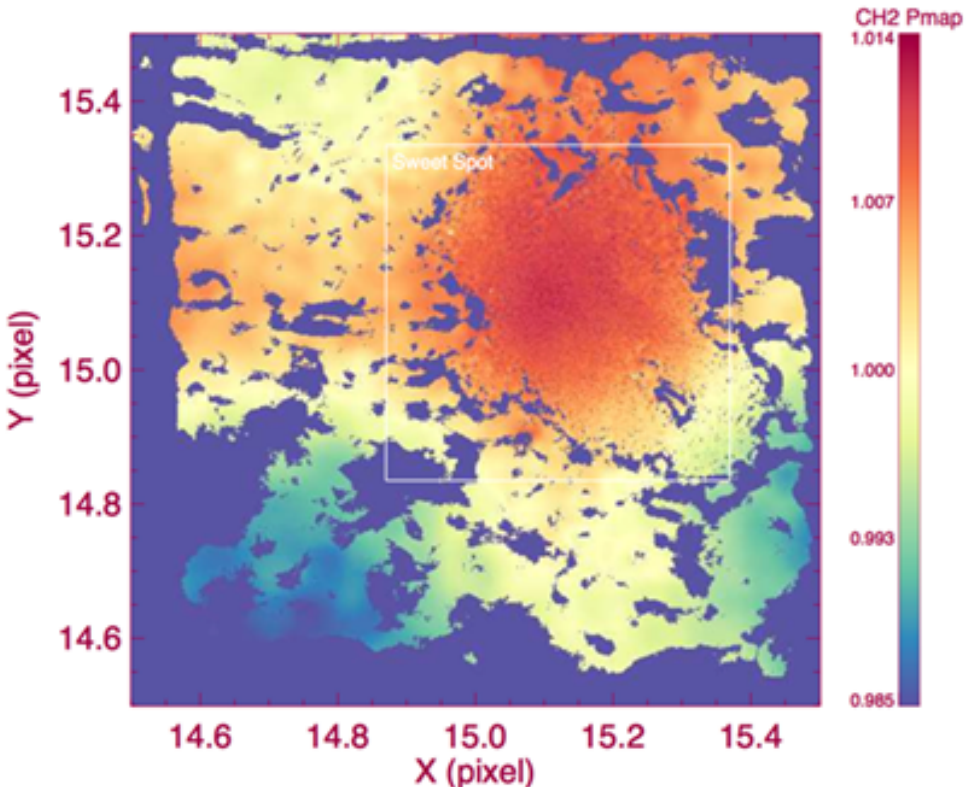


Fig. 1.3: Map of the intrapixel sensitivity of the central pixel on the detector at $4.5 \mu\text{m}$ for warm-*Spitzer*/IRAC data. The x and y axis show the fraction of the central pixel and the colour map shows the pixel sensitivity with red showing a higher sensitivity. Image Credit: *Spitzer*/IRAC Instrument Handbook².

photon noise or shot noise. Each atom inside the star emits a photon with some probability, this probability follows a Poisson distribution with a standard deviation of \sqrt{N} , where N is the number of events or counts detected. The other noise sources to correct for are the background noise, dark current, and readout noise. Background noise is the incoming light on the detector in the absence of any apparent sources (e.g. zodiacal light). Dark current arises from thermal fluctuations in the electrons of the detector. Readout noise is the amount of noise generated from the electronics itself, it is a similar contribution to the background noise for *Spitzer*. In our analysis of Spitzer lightcurves (first presented in Chapter 2) we measured and subtracted the background from our observations using several different techniques and determined which was the best for each planet.

1.2.3.1 *Spitzer*/IRAC intrapixel sensitivity

Each instrument that exoplanets scientists currently use has a set of challenges regarding detecting the signals of exoplanet atmospheres since none of these facilities were designed with exoplanet characterization in mind. The most important and strongest instrumental effect that we need to account for with *Spitzer* data is the gain variations within a single pixel, known as the intrapixel sensitivity effect. Figure 1.3 demonstrates the photometric gain at $4.5\text{ }\mu\text{m}$ of the central pixel of the *Spitzer*/IRAC detector. The target moves across the detector due to the following effects: a settling drift after slewing, a long-term drift due to an inconsistency in velocity corrections, jitter, and a thermally induced oscillating pointing drift due to periodic on-off cycling of the battery heater within the spacecraft. This movement in combination with the changes in gain causes temporal variations in the amount of flux measured from a constant source. The typical signature of a few scale heights in the atmosphere of a hot Jupiter is about 100 parts per million (0.1%). The amplitude of the intrapixel variations seen in *Spitzer* lightcurves is on the order of 1%. Thus, we need to accurately correct these systematics to obtain the precision required to detect atmospheric signatures.

We typically overcome the settling drift by having a peak-up throw-away observation of about half an hour and by discarding \sim 15 minutes from the beginning of the observation. Next, we model the long-term settling drift with a linear function of time. There have been many efforts over the years to model and correct the periodic systematics induced from the pointing variations (e.g., Charbonneau et al. 2008; Ballard et al. 2010; Knutson et al. 2012; Stevenson et al. 2012; Evans et al. 2015; Morello et al. 2015; Morello 2015; Buzasi et al. 2015; Deming et al. 2015; Krick et al. 2016).

All of these different methods culminated with a repeatability and reliability data challenge, the results of which were presented in Ingalls et al. (2016). Each of the methods were tested on ten real and ten simulated eclipses of XO-3b. The data challenge found that most of the methods were able to estimate accurate uncertainties on individual eclipses. However, they found that BiLinearly Interpolated Subpixel Sensitivity (BLISS; Stevenson et al. 2012), Pixel Level Decorrelation (PLD; Deming et al. 2015), and Independent Component Analysis (ICA; Morello et al. 2015; Morello 2015) were the most accurate and repeatable for correcting systematics on observations of large pointing fluctuations. Furthermore, they found that PLD was also able to obtain the highest accuracy on a the simulated dataset. In this thesis, we focus on using PLD (Deming et al. 2015), while also testing the original polynomial fitting (Charbonneau et al. 2008) as well as Gaussian Process models (GP; Evans et al. 2015).

1.2.3.2 Pixel Level Decorrelation

Unlike several of the other techniques, Pixel Level Decorrelation (Deming et al. 2015) does not require knowledge of the sub-pixel position or a map of the variations in the sub-pixel sensitivity. Instead, it assumes that the flux from the star will be a smooth function of position, such that when the target moves on the detector, the neighboring pixels will receive more or less flux depending on if the target is moving towards or away from the pixel in question. The

sub-pixel position is therefore encoded implicitly in a generalized function of pixel intensity. Such a smooth function can be differentiated and can also be Taylor expanded. Doing this allows us to model the flux in time as a weighted sum of individual pixel fluxes. To model the full photometric lightcurve in time (t) we combine the weighted pixel flux sum with a transit or eclipse model ($TD(t)/ED(t)$) and a linear slope in time (ft) to model the long-term drift:

$$\Delta S^t = \sum_{i=1}^N c_i \hat{P}_i^t + TD(t) + ft, \quad (1.5)$$

where S^t is the flux measured over time and Δ represents the total fluctuations from all sources. $\hat{P}_i^t = \frac{P_i^t}{\sum_{i=1}^N P_i^t}$ represents the normalized flux from pixel i at time t , where a grid of i pixels are chosen around the centroiding position.

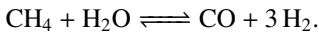
1.2.4 Properties and Climates of exoplanets

1.2.4.1 Chemistry

Since hot Jupiters are gas giants, their atmospheres are primarily composed of gaseous Hydrogen and Helium (Seager 1999), with most of their other constituents also being in gas phase, such as water, methane, carbon monoxide and carbon dioxide (Brown 2001).

A typical assumption when modeling atmospheres is that the chemical composition of the atmosphere is the same as our Sun (solar composition): 74.9% Hydrogen and 23.8% Helium, with all the heavier elements (which are known as *metals* in astrophysics) encompassing the other 1.3%. Starting from this assumption, a series of chemical networks are used to calculate the abundances of molecular species in the atmosphere. A common assumption for these chemical networks is that the atmosphere is in chemical equilibrium, meaning that the molecular abundances can be determined, in the first order, from the temperature and pressure alone. Under these assumptions, predictions can be made about which molecules would be expected to be abundant for different temperatures of planets.

Spitzer is an invaluable tool to test these assumptions because it is sensitive to the abundance of methane, water, carbon monoxide and carbon dioxide (CH_4 and H_2O at $3.6\ \mu m$ and CO , CO_2 , H_2O at $4.5\ \mu m$). The strength of the H_2O opacity is approximately equal in both *Spitzer*/IRAC bandpasses (see Figure 1 of Chapter 3). Therefore, *Spitzer* can be used to probe the relative abundance of CO and CH_4 (Madhusudhan 2019). Since these are both carbon-bearing species, and since carbon (C) is less abundant than hydrogen (H) and oxygen (O), there is a trade-off between CO and CH_4 with temperature. The following summary chemical reaction arising from the CH_4 - CO conversion reaction scheme plays an important role in determining the dominating carbon-bearing species in an atmosphere (e.g., Visscher et al. 2010; Moses et al. 2011; Visscher & Moses 2011):



For a nominal pressure of 1 bar, temperatures higher than \sim 1100 K favor CO creation, and lower temperatures favor CH₄ creation (e.g. Madhusudhan 2012; Mollière et al. 2015; Molaverdikhani et al. 2019). Therefore, hotter planet atmospheres are predicted to have carbon monoxide and cooler planets are predicted to have methane as the dominant carbon-bearing species, with the transition occurring at around 1100K, depending on the pressure being probed (emission probes deeper than transmission).

In reality, there are several phenomena that can cause an atmosphere to deviate from equilibrium: photochemistry, vertical mixing, higher metallicity, cloud/haze formation, tidal heating, winds, and other dynamical interactions (e.g., Madhusudhan 2019). In Chapter 2 we study the effects of some of these processes by modeling them and comparing several different grids of models to a survey of 49 planets in transmission.

1.2.4.2 Temperature structure

Just like on Earth, the temperature of a hot Jupiter atmosphere does not remain constant with altitude, i.e., it is not isothermal. Typically, the atmosphere gets hotter towards higher pressures. The gray dashed line in Figure 1.4 shows a typical temperature-pressure profile (TP) of a model atmosphere. In the deep atmosphere, at high pressures, the atmosphere is opaque and the energy is therefore transported convectively via bulk movement of gas. This results in inefficient transport and a large temperature gradient. Whereas in the upper more tenuous atmosphere, energy is transported radiatively which is a more efficient process, resulting in less steep temperature gradients.

The cyan line in Figure 1.4 shows an irradiated atmosphere with a nominal (non-inverted) temperature-pressure profile. The red line shows that of a highly irradiated atmosphere with a temperature inversion. A temperature inversion is where the temperature starts to increase with decreasing pressure. This is caused by the UV/visible absorption of the strong incident stellar irradiation, leading to the heating of the upper layers of the atmosphere. Earth's stratosphere contains a thermal inversion due to the absorption of Ozone (O₃). In hot Jupiters, molecules such as titanium oxide (TiO) and vanadium oxide (VO) are thought to be the cause of their thermal inversions (Hubeny et al. 2003; Fortney et al. 2008; Désert et al. 2008). Additionally, recent work has also suggested that temperature inversions in ultra-hot Jupiters may be caused by the absorption of metals and metal hydrides (Fe, Mg, SiO Lothringer et al. 2018) or other metal-rich species (AlO, CaO, NaH and MgH; Gandhi & Madhusudhan 2019).

The detection of molecular features in exoplanet atmospheres via emission spectroscopy not only tells us about the atmospheric chemistry on the dayside but it is also a probe of these vertical temperature profiles. For a nominal temperature-pressure profile (temperature decreasing with altitude), if a molecule is present and has an opacity at the wavelength of observation, then it will absorb the radiation and the measured eclipse depth will be smaller than the continuum. For example, Figure 1.5 shows an HST/WFC3 spectroscopic observation from Stevenson et al. (2014c) where the 1.4 μ m water absorption feature can be seen clearly in the emission spectrum. The temperature-pressure profile retrieved for the dayside of WASP-

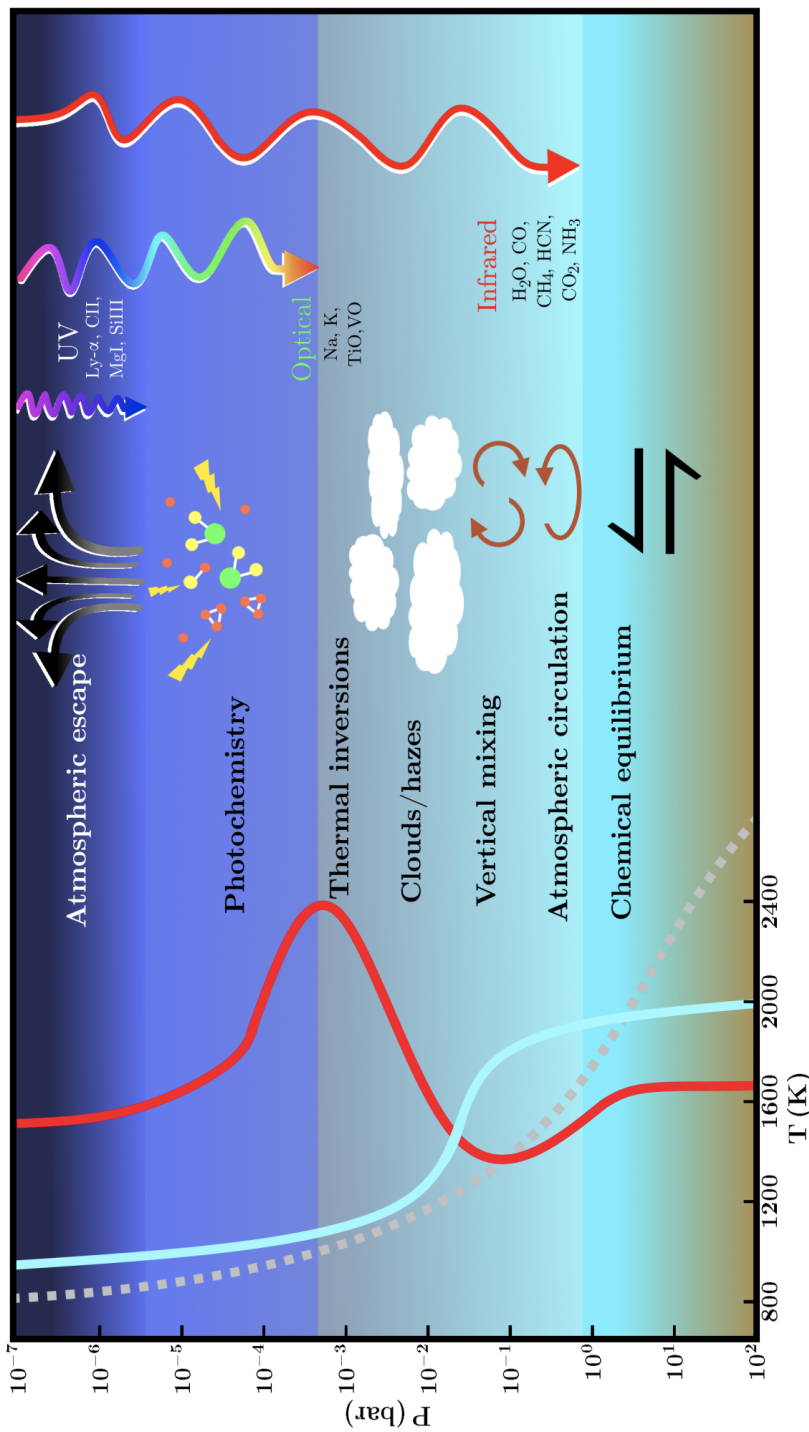


Fig. 1.4: Properties and processes active in the atmospheres of exoplanets. On the left and 3 model temperature-pressure profiles: grey-dashed is that of a non-irradiated atmospheres, cyan is an irradiated atmospheres with a nominal temperature-pressure profile and red is a highly irradiated atmosphere with a temperature inversion. Image Credit: (Madhusudhan 2019)

43b is very similar in shape to the diagram of an irradiated atmosphere in Figure 1.4.

For an inverted TP profile, a molecule will emit radiation at a temperature higher than the continuum and so the eclipse depth will appear larger at the wavelength of the opacity. Figure 1.6 shows an emission spectrum of WASP-18b, where you can see the $4.5\text{ }\mu\text{m}$ CO feature appearing in emission due to the temperature inversion. There have been a few studies finding evidence for temperature inversions in hot and ultra-hot Jupiters (e.g., Knutson et al. 2008, 2009a; Madhusudhan & Seager 2010; Haynes et al. 2015; Evans et al. 2017; Arcangeli et al. 2018). However, some of the early observations were revised (e.g., Diamond-Lowe et al. 2014). Temperature inversions were notoriously difficult to establish in the available observations of hot Jupiters. In Chapter 3 we use our sample of planets in emission with *Spitzer*/IRAC observations to statistically measure a transition from the hot Jupiters to the ultra-hot Jupiters which is likely due to temperature inversions, among other effects.

Figure 1.4 also shows the pressure levels where several physical processes occur in planetary atmospheres. Each of these processes is also inexorably intertwined with the temperature-pressure structure, but we will discuss some of them individually in the following sections.

1.2.4.3 Clouds and hazes

This thesis focusses on the study gas giant exoplanets ranging from those cooler than the Earth (Kepler-16b, 200K; Doyle et al. 2011) all the way to the hottest ultra-hot Jupiter (KELT-9b, 4000K; Gaudi et al. 2017). It is expected that somewhere in this range of temperatures, aerosols will form. Aerosol is the all-encompassing term for clouds, hazes, and dust. Clouds are particles forming in the atmospheres as a result of first order phase changes. Due to the temperature-pressure profile crossing a condensation curve of some molecule, e.g., gas to liquid water. Cloud formation can also occur as a result of thermochemical reactions. On the other hand, haze formation can be defined as the formation of particles via the breakdown of molecules due to energy input e.g., photochemistry of energetic particle bombardment. Both clouds and hazes have the effect of dampening the atomic and molecular signatures seen in the atmospheres of exoplanets, sometimes making the transmission spectra appear mostly flat in the visible and near-infrared wavelengths (e.g., Charbonneau et al. 2002; Fortney et al. 2003; Pont et al. 2008).

Even in our own solar system, aerosol composition is extremely diverse: from water on Earth, sulfuric acid on Venus (Hansen & Hovenier 1974), ammonia on Jupiter and Saturn (Brooke et al. 1998; Baines et al. 2009) and many different complex organics and hydrocarbons on the outer solar system planets and moons (e.g., Sromovsky et al. 2011; Romani & Atreya 1988; Sagan et al. 1992; Brown et al. 2002; Rages & Pollack 1992). Aerosols were therefore predicted to be found in the atmospheres of exoplanets. In fact, the very first transmission spectrum of an exoplanet showed dampening of the predicted absorption feature by atomic sodium in the atmosphere of HD 209458b. One of the possibilities that could account for the reduced sodium abundance was the presence of high altitude aerosols (Charbonneau et al. 2002). Given equilibrium chemistry, different molecules/elements will condense to form

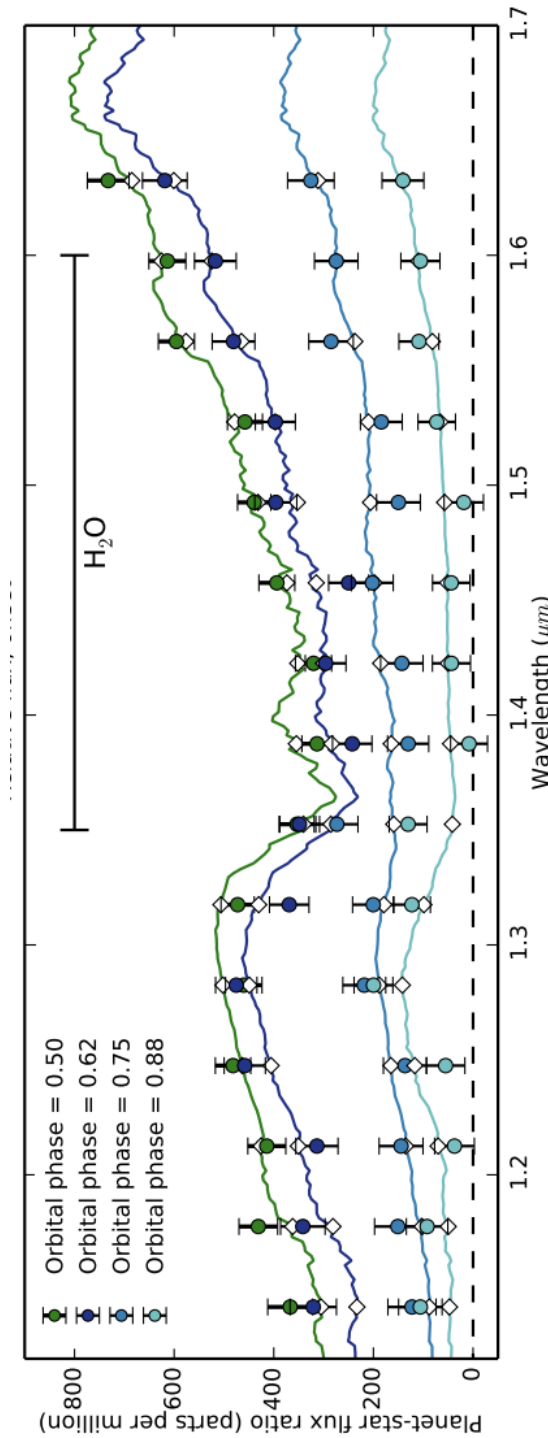


Fig. 1.5: Emission spectrum of WASP-43b taken from a spectroscopic phase curve observation. Green data and model shows the emission spectrum during phase 0.5, which is what would be observed with an eclipse only observation. This clearly shows the water absorption feature appearing due to a nominal temperature-pressure profile. Other lines show the planet as it approaches quadrature (phase 0.75). At quadrature, you are observing half of the dayside and half of the nightside. Image credit: Stevenson et al. (2014c).

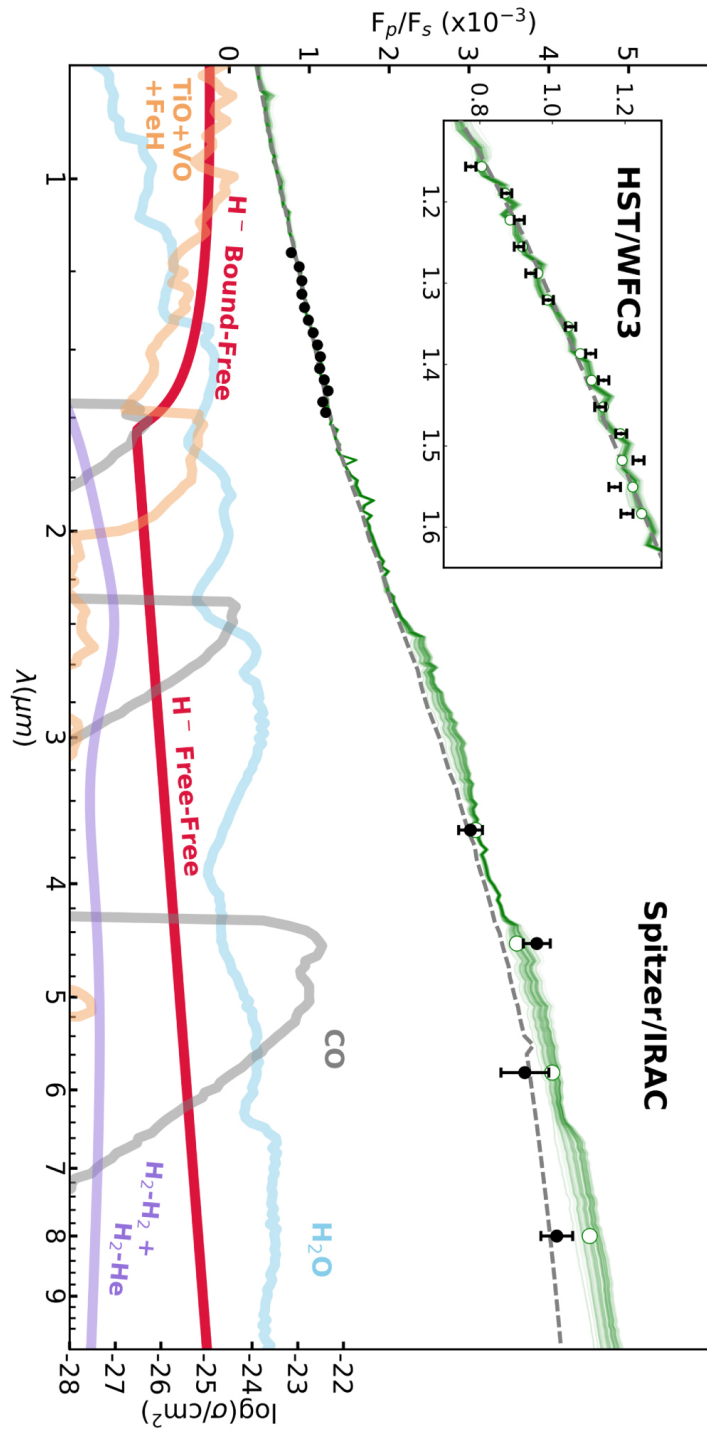


Fig. 1.6: Emission spectrum of WASP-18b from HST and Spitzer/IRAC (black data points). Green lines show the retrieved models, and the cross-sections of the important opacity sources are shown on the bottom of the Figure. The 4.5 μm *Spitzer* eclipse depth shows the CO feature appearing in emission due to the temperature-pressure profile. At the HST/WFC3 wavelengths, we see that the combination of H₂O and H- bound free opacity makes the emission appear like a blackbody. Image credit: Arcangeli et al. (2018).

clouds at different pressures (Lodders 2004; Marley et al. 2013). This depends on when the temperature-pressure profile of the atmosphere crosses the condensation curves of the cloud forming species.

As well as dampening molecular features in transmission spectra, clouds can leave their own spectral fingerprint. In particular, high altitude H₂ particles create a Rayleigh scattering slope in the transmission spectra (e.g., Lecavelier Des Etangs et al. 2008; Sing et al. 2015, 2016; Gibson et al. 2017). Similarly, clouds can plague our observations and leave spectral signatures via Mie scattering (e.g., Benneke et al. 2019) or their own absorption features (e.g., Wakeford & Sing 2015). It is hoped that in the future, the James Webb Space Telescope will be used to pin down the composition of aerosols using computations of possible cloud species in combination with the observations (e.g., Gao et al. 2020).

1.2.4.4 Dynamics, climate and variability

In this thesis, atmospheric dynamics and climate are important factors that we consider when studying the spectral features or temporal appearance of our exoplanet atmospheres. In Chapter 2, we study the transmission spectra in the infrared at pressures where H₂O, CH₄, CO, and CO₂ are dominant. We find that dynamical mixing in the atmosphere can affect the local abundances of these observed species. Furthermore, in Chapter 3, we study the dayside brightness temperatures which can also be affected by large-scale atmospheric weather patterns. Finally, in Chapter 4 we measure atmospheric variability in the dayside of an ultra-hot exoplanet atmosphere.

Based on timescale and gravitational arguments, hot Jupiters are expected to be tidally locked (e.g., Rasio et al. 1996; Guillot et al. 1996). This means that the planet always have one hemisphere facing the star, i.e. a permanent dayside, and one hemisphere facing away from the star, i.e. a permanent nightside. The dayside and nightside rotate into and out of view of an observer throughout a full phase curve observation. Phase curves provide a unique opportunity to study the structure of a planet at different longitudes and thus to understand more about their atmospheric dynamics. However, certain aspects of atmospheric dynamics can also be probed with eclipse-only and transit-only observations.

The permanent dayside of a planet receives all of the insolation from the host star, producing a strong horizontal temperature gradient that drives zonal and meridional winds. These winds redistribute heat from the dayside to the nightside of the planet. If the redistribution is very efficient then the temperature difference between the dayside and the nightside will be small, like on Venus. The efficiency of redistribution is determined by how fast the atmospheric winds can advect gas across the planet compared with the rate at which the planet can radiatively cool. On hot Jupiters, the radiative and advective timescales are a similar order of magnitude, resulting in low redistribution efficiencies and allowing for strong day-night temperature contrasts to remain (e.g., Showman & Guillot 2002; Perna et al. 2012). The rate at which planets redistribute heat is characterized by a so-called heat redistribution factor, f , which lies between 2/3 for a planet with no atmosphere and no heat redistribution

and 1/4 for a planet that is extremely efficient at redistributing heat (e.g., Koll et al. 2019). The exact mechanisms involved in determining the value of this redistribution factor are unknown, and it is not parameterized by the physical properties of the atmosphere. However, there has been observational and theoretical evidence that hotter planets should be less efficient at redistributing heat to their nightsides (Perez-Becker & Showman 2013; Schwartz & Cowan 2015). In Chapter 3 we will revisit these pieces of evidence and propose that ultra-hot Jupiters display a broad range of redistribution efficiencies.

The strong longitudinal winds resulting from this temperature contrast can distort the temperature pattern, shifting the hottest point of the atmosphere eastward (e.g., Showman & Guillot 2002). These eastward hot-spot offsets have been observed and have been attributed to equatorial jets (e.g., Knutson et al. 2012; Cowan et al. 2012a). However, there has also been a detection of a westward hot-spot offset in CoRoT-2b (Dang et al. 2018) and a variable hot-spot offset in HAT-P-7b (Armstrong et al. 2016). Westward and variable offsets could be explained by non-synchronous rotation, as suggested for CoRoT-2b, or magnetic effects, as suggested for both CoRoT-2b and HAT-P-7b.

In addition to the longitudinal winds from the day-night temperature contrast, it is possible that condensates can be transported from equatorial to polar regions through means of meridional circulation. This is suggested to be common in sub-Neptunes, hot Jupiters and ultra-hot Jupiters (Parmentier et al. 2013; Ehrenreich et al. 2020).

As well as meridional winds and longitudinal winds, there is also a vertical component to the dynamics in an atmosphere. The process of vertical (radial) transport prevents the gravitational settling of condensates. It also mixes chemical species from deeper in the atmosphere to observable pressures. Vertical mixing has the effect of causing the observed abundances to deviate from those expected from equilibrium chemistry calculations. In the 1D chemical diffusion framework, vertical mixing is often modeled with an eddy diffusion co-efficient, K_{zz} (e.g. Zhang & Showman 2018a; Miles et al. 2020). To capture all of the above dynamical effects in one model, 3D global circulation models are needed.

In Chapter 4 of this thesis, we measure variability in the brightness of an ultra-hot Jupiter, WASP-18b. Brightness variability is directly related to the dynamics and climate of atmospheres. Variability seems to be a common occurrence in brown dwarfs, with more than 50% of L and T brown dwarfs displaying temporal variability of a few percent (Metchev et al. 2015). Variability has also been detected in directly imaged free-floating planets (Biller et al. 2015) and even in Jupiter, which has been shown to be temporally variable in the equatorial banded structures observed at 5 μm (Antuñano et al. 2019). The question is whether exoplanets would display some kind of temporal variability as well. Observing variability in an exoplanet requires long observations with high sensitivity and stability. Fortunately, we have 10 observed almost consecutive eclipses of WASP-18b with *Spitzer*/IRAC at 4.5 μm , which allows us to study how the emission of the planet changes with time.

Ultra-hot atmospheres like WASP-18b can be significantly ionized, which can couple with the magnetic field of the planet and settle into an oscillatory pattern, creating variability in the brightness and the hot-spot offset (Rogers 2017). Variable wind speeds, causing the

advance and retreat of thermal structures, could lead to variable cloud coverage causing the emission from the dayside to vary (Armstrong et al. 2016). Furthermore, clouds can blow onto the dayside where they can then be photochemically destroyed and generate brightness variability (Jackson et al. 2019).

1.2.4.5 Inflated hot Jupiters

Due to the intense stellar insolation that a hot Jupiter receives compared to Jupiter, it is not unexpected that their atmospheres and interior structures behave differently. Guillot et al. (1996) predicted that hot Jupiters would not cool as efficiently as Jupiter which would lead to hotter interiors and larger planetary radii. This prediction was confirmed by observations, but, the magnitude of the radius anomaly was even larger than expected. Several mechanisms have been proposed to explain the distribution of hot Jupiter radius anomalies including a reduction of internal cooling (Burrows et al. 2007a), tidal dissipation (Bodenheimer et al. 2001), ohmic dissipation (Batygin & Stevenson 2010), and compositional gradients (Chabrier et al. 2007; Burrows et al. 2007a; Thorngren et al. 2016).

Thorngren & Fortney (2018) investigated the inflation of hot Jupiter atmospheres by looking at their radius anomalies as a function of stellar flux. They confirm that the vast majority of transiting gas giants have radii larger than expected. They also find that the magnitude of the radius anomalies of hot Jupiters correlates with incident flux and that the cooler gas giants ($<1000\text{K}$) are not observed to be inflated (Miller & Fortney 2011; Demory & Seager 2011; Laughlin et al. 2011). This implies that the mechanism for inflation is linked to the stellar flux. In Chapter 2 we use the radius anomalies for our sample of planets to test if they correlate with the *Spitzer* observations. We looked for a correlation between hot Jupiter inflation and the strength of the *Spitzer* transit difference. We predicted that an inflated atmosphere will have a lower surface gravity (g) and thus a larger scale height (H) and larger atmospheric signature. However, we do not observe such a correlation, suggesting more complex processes are happening in the atmosphere.

1.2.5 Models of Exoplanet Atmospheres

Predictions and conclusions about the composition of exoplanet atmospheres can be made by comparing observations to detailed models. Vast efforts have been made in the field of modeling exoplanets, from 1D radiative transfer codes to 3D global circulation models. In this thesis, we focus on the application of 1D forward models, whereby a grid of models is pre-computed and compared with the data (Zhang et al. 2019; Tsai et al. 2017; Piskorz et al. 2018; Line et al. 2013b). This is different to a retrieval method where the model parameters are tuned statistically in comparison with the data, which is more computationally expensive and so more simplifications are required. Our forward models contain physics and complexity which would not be possible to retrieve statistically, such as complex chemical networks, dynamical effects and self-consistent temperature-pressure calculations.

1D forward models of exoplanet atmospheres are calculated by solving the radiative transfer equation through different layers of an atmosphere. The optical thickness of a layer in an atmosphere is the opacity over all wavelengths, of all spectral lines, of all atomic and molecular species, integrated through the path of the atmosphere. Opacity functions used in radiative transfer codes are often taken from databases where they have been measured in laboratory experiments and/or theoretically calculated (e.g., HITRAN, ExoMol; Rothman et al. 2010; Freedman et al. 2008, 2014). Creating and completing such databases is an ongoing effort and scientists can dedicate years to just one molecule.

1.2.5.1 Exo-Transmit

The first code that we use in this thesis is a 1D radiative transfer code that produces transmission spectra of planet atmospheres: Exo-Transmit³ (Kempton et al. 2017b). Exo-Transmit contains the most common assumption when modelling exoplanet atmospheres, equilibrium chemistry. It solves the equation of radiative transfer for absorption of stellar light through an isothermal atmosphere using opacity sources from Freedman et al. (2008) and Lupu et al. (2014). Exo-Transmit has the functionality to include a Rayleigh slope or a gray cloud deck at a specific pressure. It is a great tool for first-order predictions of transmission spectra. However, it does not include any other sources of disequilibrium chemistry or realistic temperature-pressure profiles, which is the reason we use more complex modeling in Chapter 2.

1.2.5.2 VULCAN and PLATON

In Chapter 2, we use a photochemical kinetics code (VULCAN⁴; Tsai et al. 2017) to compute the atmospheric composition including disequilibrium effects such as photo-dissociation and vertical mixing via eddy diffusion.

Being able to include the vertical turbulence in the form of a vertical mixing coefficient is a considerable advantage to previous modeling efforts. We do not compute self-consistent temperature-pressure profiles, however, we use a realistic parameterisation from Heng et al. (2014). This allows us to create a grid specific to the planets in our survey and to see the effects of mixing from deeper layers in the atmosphere. In order to calculate the transmission spectra, we use a 1D radiative transfer code that can easily handle the temperature-pressure profiles and custom chemistry (PLATON⁵; Zhang et al. 2019).

1.2.5.3 ScCHIMERA

Finally, in Chapter 3 we use a grid of 1D forward models of emission spectra (Piskorz et al. 2018; Line et al. 2013b). These models are produced self-consistently, in that their

³https://github.com/elizakempton/Exo_Transmit

⁴<https://github.com/exoclime/VULCAN>

⁵<https://github.com/ideasrule/platon>

temperature-pressure profiles are calculated solving the two-stream source function for the planetary emission combined with a Newton-Raphson iteration scheme (McKay et al. 1989). These models do not include the effects of vertical mixing and non-equilibrium chemistry. However, the self-consistent calculation of the temperature-pressure profiles allows for a demonstration of the formation of temperature inversions due to the absorption of stellar irradiation. In an ideal world, all of these model attributes would be combined, but this is currently too computationally expensive.

1.3 Exoplanet atmosphere diversity

The last 30 years of exoplanet research has seen the field progress from the first exoplanet detection (Mayor & Queloz 1995), through to the detection of the first exoplanetary atmosphere (Charbonneau et al. 2002) and to the cataloging of thousands of exoplanets (e.g., Borucki et al. 2010; Batalha et al. 2013)). Having categorized these planets (e.g. hot Jupiters, warm-Neptunes, and terrestrial planets), the field currently focuses on assessing their characteristics using space and ground-based spectroscopy and photometry. We are now in a realm of comparative exoplanetology. This thesis comprises the largest survey of the emission of exoplanets as well as the largest survey in transmission with *Spitzer*/IRAC. The following section will discuss some of the notable survey results from the literature.

1.3.1 Looking at planet ensembles

1.3.1.1 Transmission surveys

In recent years, there have been several studies exploring the trends in HST/WFC3 transmission spectra of warm-Neptunes (Crossfield & Kreidberg 2017) and hot Jupiters (Stevenson et al. 2016; Sing et al. 2016; Heng 2016; Barstow et al. 2017; Fu et al. 2017; Tsiaras et al. 2018). Notably, Sing et al. (2016) performed a survey of 10 transiting planets by combining three instruments: HST/STIS (which probes the alkali lines and the Rayleigh slope), HST/WFC3 (which probes the $1.4\ \mu\text{m}$ water feature), and *Spitzer*/IRAC (which probes CH₄ and CO). They find that their sample of hot Jupiters is extremely diverse, exhibiting a continuum from the clear to cloudy atmospheres, see Figure 1.7. They define a metric based on the difference in the transit depth measured in the infrared vs the optical wavelengths. They note that it correlates with the spectral strength of the water feature, indicating that this metric can be used to classify similar objects.

Similarly, Stevenson (2016) creates a metric for measuring the strength of the water feature using HST/WFC3 spectra and finds that it strongly correlates with planet temperature. This implies that cooler atmospheres below 700K are likely to have damped features due to clouds. Around the same time, Heng (2016) creates a dimensionless cloudiness index for a sub-sample of 7 planets from Sing et al. (2016). Their index is based on the sodium and potassium lines of these planets and thus probing smaller particles than the metric of

Stevenson (2016), yet they still find a tentative decreasing cloudiness trend with increasing equilibrium temperature. Additionally, Crossfield & Kreidberg (2017) studied a sample of 6 warm-Neptunes with HST/WFC3 observations and found a correlation with the spectral features and the equilibrium temperature suggesting more optically thick clouds at lower temperatures.

Barstow et al. (2017) performed a consistent retrieval of the 10 hot Jupiters presented in Sing et al. (2016). They found that the planets between 1300-1700K are represented with deeper grayer clouds or clear atmospheres and the rest, cooler or hotter, are better with high altitude hazes causing Rayleigh scattering. And finally, Fu et al. (2017) collected all HST/WFC3 observations of 34 gas giants and compared them with a forward model for each planet calculated using Exo-Transmit. They found a negative slope in the absorption in scale heights vs equilibrium temperature which they attributed to decreasing cloudiness with increasing temperature.

Building on these works, in Chapter 2 we use the normalized difference between the two *Spitzer* infrared bandpasses to classify the chemical composition of the atmospheres of our sample. We tested how our metric correlates with all system parameters of the data and used it to compare our novel grids of forward models to the data. Finally, we incorporated important effects such as varying composition and disequilibrium chemistry into our modelling and compared the model grids with the data over a large range of system parameters.

1.3.1.2 Emission surveys

There has also been a lot of work done studying the atmospheres of surveys of exoplanets by measuring the emission from their daysides. Despite the extreme differences in the amount of insolation they receive, hot Jupiters have similar equilibrium temperatures to late-type brown dwarfs. There have been several studies looking at the color-color and color-magnitude diagrams of exoplanets (Triaud 2014b; Triaud et al. 2014; Dransfield & Triaud 2020; Melville et al. 2020). Triaud et al. (2014) calculate color-magnitude diagrams of a survey of 44 exoplanets using photometric distances and WISE magnitudes in combination with *Spitzer* emission in the four bandpasses (3.6, 4.5, 5.8, and 8.0 μm). Figure 1.8 displays the color-magnitude diagrams for the warm-*Spitzer* bandpasses. These figures show increasing scatter with increasing magnitude, which Triaud et al. (2014) attributes to increased atmospheric diversity at colder temperatures. Furthermore, they found that hot Jupiters have colors similar to brown dwarf (MLT) colors i.e., these planets do not have simply featureless spectra in the infrared. However, it is likely that these similar colors are due to different processes in the atmospheres of hot Jupiters and brown dwarfs.

Additional studies have focused on using the infrared *Spitzer* emission observations to constrain the energy budgets of hot Jupiters. Schwartz & Cowan (2015) calculated the day-side effective temperature of a survey of 50 planets with thermal emission measurements in at least two infrared wavelengths ($>0.8 \mu\text{m}$). They compared the dayside effective temperature (T_{eff}) with the irradiation temperature (T_0). If there is full redistribution of stellar

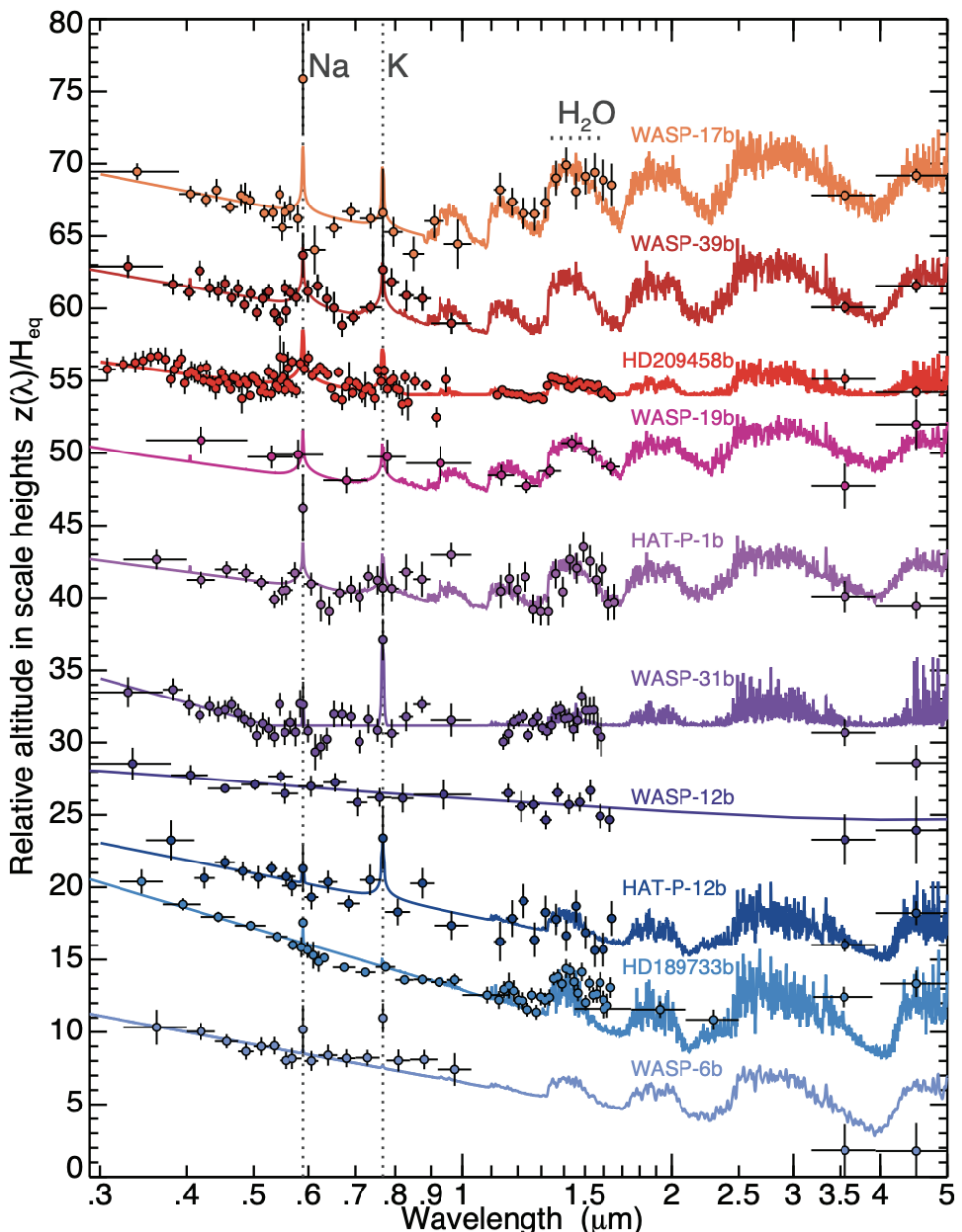


Fig. 1.7: HST and *Spitzer* transmission spectra of 10 hot Jupiters. Solid colored lines show fitted atmospheric transmission spectra models where the alkali lines and the water feature are noted. The spectra are ordered in terms of their cloudiness, with the clear atmospheres appearing at the top of the image. The 3.6 and 4.5 μm *Spitzer*/IRAC transit depths probe the CH_4 and CO molecular features respectively. Image credit: Sing et al. (2016)

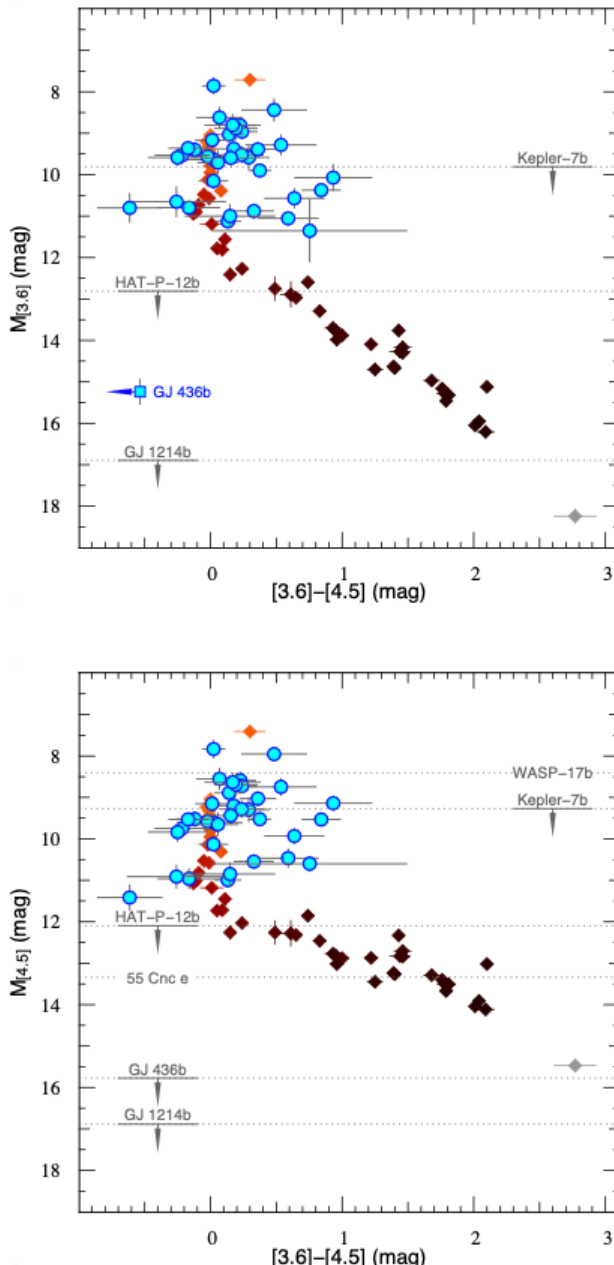


Fig. 1.8: Color-magnitude diagrams using the warm-*Spitzer* bandpasses. Blue dots show the planetary magnitudes and colors calculated from the secondary eclipse measurements. The colored diamonds show the magnitudes of ultra-cool brown dwarfs whose values were taken from Dupuy & Liu (2012). Image Credit: Triaud et al. (2014).

irradiation then the effective dayside temperature will be the equilibrium temperature, where $T_{eq,0} = (1/4)^{1/4} T_0 \approx 0.71 T_0$. They found that the daysides of hotter planets deviate further from equilibrium temperature estimations, implying that the hotter planets do not redistribute heat as efficiently from their day to nightsides. This supports the previous claim by Cowan & Agol (2011b) that the hottest planets have lower Bond albedo and/or less efficient heat transport, and is in agreement with theoretical predictions about redistribution efficiency in Perez-Becker & Showman (2013). However, Schwartz et al. (2017) incorporated phase offsets into their energy budget calculations of six planets. This pushed the results for these planets toward the lower Bond albedos scenario with slightly higher heat transport than previous measurements.

Furthermore, Garhart et al. (2020) performed a uniform analysis of 36 planets with *Spitzer*/IRAC secondary eclipses measured at 3.6 and 4.5 μm . They calculated the brightness temperatures and found an increasing trend in the brightness temperature ratio with equilibrium temperature. In Chapter 3, we use these results in combination with 42 other planets with both 3.6 and 4.5 μm emission measurements to study how the dayside emission changes between the hot and the ultra-hot Jupiters. We revisit the trends seen in Schwartz & Cowan (2015) and Garhart et al. (2020) with our expanded survey of 78 planets in emission. When we carefully analyzed and calculated the brightness temperatures, we found that the trend with dayside temperature and irradiation temperature is less significant than before. This was partially due to previous studies not incorporating a stellar model in place of a blackbody for the star. Additionally, in Chapter 2 we revisit the color-magnitude diagrams of Triaud (2014a) with our expanded survey in combination with GAIA data release 2 distances and find that the larger sample is in agreement with previous works.

1.3.2 The Ultra-hot Jupiters as a separate class

Ultra-hot Jupiters are the newest class of exoplanets, it was only in the last few years that their atmospheres started to be understood (e.g., Arcangeli et al. 2018; Parmentier et al. 2018; Lothringer et al. 2018; Kitzmann et al. 2018). Previously, emission spectra of these ultra-hot planets appeared to be blackbodies and the abundances retrieved from model fitting were very different from the general population of hot Jupiters (Stevenson et al. 2014a; Haynes et al. 2015; Evans et al. 2017; Sheppard et al. 2017). Retrieved abundances were driven in part by the strong CO feature seen with *Spitzer*/IRAC and the lack of H₂O feature at the HST/WFC3 wavelengths. This combination resulted in high retrieved C/O ratios, which would have required most of the oxygen to be locked up in CO leaving very little to form H₂O. These high C/O ratios lead to questions regarding formation, why should the ultra-hot planets differ in metallicity from their cooler counterparts?

In Arcangeli et al. (2018) they explored the effect of molecular dissociation of molecules such as H₂O and TiO, as well as the recombination of H atoms with electrons to form H-. They found that when including these effects they were able to explain the emission spectra without the need to invoke very high metallicity (see Figure 1.6). The H- continuum opacity

dominates the spectrum at the HST/WFC3 wavelengths and fills in the gap at $1.3\text{ }\mu\text{m}$ while we see the bump of H_2O in emission at $1.5\text{ }\mu\text{m}$, making the spectrum appear like a blackbody.

Furthermore, with TiO and VO dissociated on the dayside, there still remained temperature inversions in model atmospheres of ultra-hot Jupiters, which were due to the strong absorption of atomic metals (Fe , Mg , SiO) and metal hydrides such as FeH (Lothringer et al. 2018). Observations of temperature inversions in hot Jupiters were notoriously hard to find, with only hints of emission in the *Spitzer* bandpasses in a few planets (e.g., Nymeyer et al. 2011; Deming et al. 2012). However, there have now been a few observations of inversions in the ultra-hot Jupiters: WASP-33b, WASP-121b, and WASP-18b (Figure 1.6) (Haynes et al. 2015; von Essen et al. 2015; Evans et al. 2017; Arcangeli et al. 2018; Kreidberg et al. 2018b). It is in this context that in Chapter 3 we look at how the dayside emission in the two *Spitzer* bandpasses changes as the temperature of the planets increases. We find a transition at around 1700K, which is likely caused by temperature inversions resulting in a strong CO feature appearing in emission.

As is mentioned in Section 1.2.4.4, the extreme atmospheres of ultra-hot Jupiters, in particular the high degree of ionization due to the intense stellar irradiation, could result in the dayside emission being variable in time. Additionally, the effects of dissociation and recombination of H_2 were studied in Komacek & Tan (2018) and Bell & Cowan (2018). It was discovered that recombination of atomic hydrogen occurs when it is transported from the hot dayside to the cooler nightside of these planets. This recombination releases a significant amount of heat that can warm up the nightside of the planet, increasing the global efficiency of heat redistribution (Mansfield et al. 2020). This result is in contrast with previous suggestions of lower efficiency of heat redistribution in the hottest planets and might be why we do not see this trend in the brightness temperatures measured in Chapter 3. Additionally, dissociation, recombination and transport between the day and nightsides could also be a cause of the variability that we see in the dayside of WASP-18b in Chapter 4.

1.3.3 The cool planets

In this thesis (Chapters 2 and 5), we also study some of the coolest gas giants that we know of, with temperatures around 500K. Cooler exoplanets have lower signal-to-noise ratio both in transmission and emission, making their atmospheres extremely difficult to characterize. There have been several studies focusing on the characterization of individual cool gas-giant exoplanets. Notably, the atmosphere of the Neptune mass planet, GJ436b, has been studied on many occasions in both emission and transmission with HST and *Spitzer*/IRAC (Deming et al. 2007; Demory et al. 2007; Gillon et al. 2007b,a; Stevenson et al. 2010b; Beaulieu et al. 2011; Knutson et al. 2011; Lanotte et al. 2014; Knutson et al. 2014; Morley et al. 2017). With an equilibrium temperature of 670K, chemical equilibrium models would predict that the atmosphere would have a high methane abundance, however, the atmosphere of GJ436b was shown to be substantially methane deficient (Stevenson et al. 2010b; Knutson et al. 2011; Lanotte et al. 2014). Furthermore, methane depletion compared to equilibrium chemistry

expectations has been observed in many other warm giant planets with HST observations, e.g., WASP-107b and WASP-117 b (Kreidberg et al. 2018a; Spake et al. 2018) or combined HST and *Spitzer* e.g., GJ3470 b (Benneke et al. 2019), HAT-P-11 b (Chachan et al. 2019), HAT-P-26 b (Wakeford et al. 2017), and WASP-39 b (Wakeford et al. 2018).

Kammer et al. (2015) performed a small uniform survey of 5 cool gas giant planets (HAT-P-19b, WASP-6b, WASP-10b, WASP-39b, WASP-67b) with *Spitzer*/IRAC 3.6 and 4.5 μm . They found a tentative correlation in the brightness temperature ratio and planet mass. They did not discover a trend with the equilibrium temperature. However, in Chapter 3 we look for trends with the brightness temperature ratio against equilibrium temperature for the whole sample of planets in emission, including those from Kammer et al. (2015), and compare to models. We do find a trend with equilibrium temperature and brightness temperature ratio throughout the entire range of temperatures. However, notably, the models also suggest that there is a trend with brightness temperature ratio and equilibrium temperature of the coolest planets. This trend is also highly dependent on the metallicity of the host star and can switch between being correlated when $[\text{M}/\text{H}] = 1$ to anti-correlated when $[\text{M}/\text{H}] = -1$, see Figure 1.9. Furthermore, Wallack et al. (2019) present an analysis of 5 more cool gas giants (HAT-P-15b, HAT-P-17b, HAT-P-18b, HAT-P-26b, and WASP-69b) and find a tentative trend with $\text{CH}_4/(\text{CO} + \text{CO}_2)$ ratio and stellar metallicity, which is in agreement with our models.

Several theories have been discussed to explain the lack of methane in the coolest hot Jupiters: including using non-equilibrium photochemical models (Line et al. 2011), models with hydrogen depletion (Hu et al. 2015), invoking tidal heating due to high eccentricity (Agúndez et al. 2014) and finally, high metallicity models (230-1000x solar) (Moses et al. 2013b). Additionally, the trend of brightness temperature against mass from Kammer et al. (2015) and against stellar metallicity from Wallack et al. (2019) all suggest a link between the atmospheric composition and planetary formation scenarios.

Predictions based on the chemical composition of the protoplanetary disks suggest that planets formed close-in have low C/O ratios (e.g., Öberg et al. 2011; Eistrup et al. 2018). However, there has been evidence for planets having super-solar C/O ratios ($\text{C}/\text{O} > 0.54$) (e.g., Lodders 2004; Madhusudhan et al. 2011). This has interesting implications for their formation scenarios. In Chapter 3, we compare the sample of 78 planets in emission with a grid of models spanning different regions of parameter space. One of these parameters is the C/O ratio of the planetary atmosphere. We find that our sample of 78 planets statistically disfavors the models with high C/O ratios ($\text{C}/\text{O} = 0.85$).

1.4 This Thesis

This thesis focuses on the statistical characterization of exoplanet atmospheres in the infrared using the *Spitzer* Space Telescope.

Chapter 2 presents the data analysis pipeline used and augmented throughout the different chapters of this thesis. We reduce the data and simultaneously fit the transit parameters (using

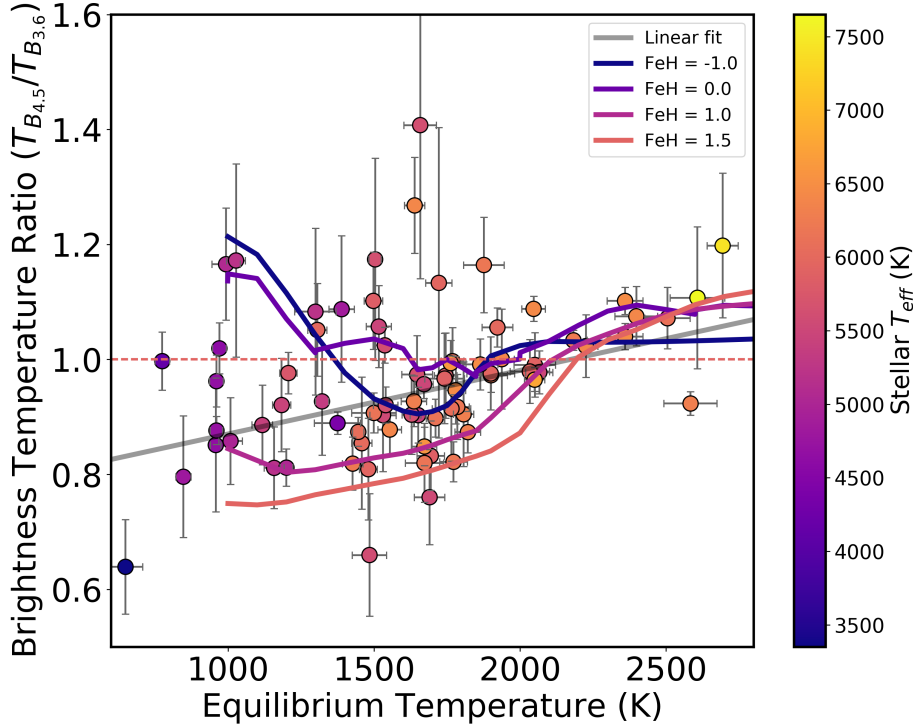


Fig. 1.9: Brightness temperature ratio from *Spitzer*/IRAC observations of our survey of 78 planets plotted against the equilibrium temperature. Remake of Figure 4 of Chapter 3 except the grids of models are not interpolated over all parameters, instead we show the tracks for the different metallicities of the host star, which is the largest contributing factor to the spread of the models. The different metallicities indicate both a positive and a negative correlation with ratio of brightness temperatures of the the coolest planets against their equilibrium temperature depending on host star metallicity.

Batman; Kreidberg 2015) with a pixel level decorrelation model and temporal ramp. We create an automated search through all of the parameter space to determine the optimum background correction, centroiding, and photometric methods for the reduction. We use the pipeline to uniformly analyse a survey of 49 planets in transmission at 3.6 and 4.5 μm . Using these two wavelengths, we then define a model-independent metric for characterizing the atmospheric composition (probing the relative abundance of CH₄ and CO). We search for statistical trends using this *Spitzer* metric as a function of other planetary and stellar parameters. We hone in on how the equilibrium temperature plays a role in determining the chemistry of the atmosphere and the strength of the *Spitzer* metric. Finally, we compare the entire survey to custom grids of forward models containing important disequilibrium chemistry and varying metallicities.

Chapter 3 presents a survey of 78 gas giant exoplanets in emission. Using the eclipse depths at 3.6 and $4.5\text{ }\mu\text{m}$, we carefully calculate the brightness temperatures by integrating properly over the *Spitzer* spectral response functions and by including a PHOENIX model for the stellar flux. We search for trends in the brightness temperatures and define a new metric for characterizing the dayside emission of the planets, called the deviation from a blackbody. Using this metric, we compare the sample to a comprehensive grid of self-consistent forward models, which contain temperature inversions and important phenomena for the ultra-hot Jupiters. Additionally, we alter our custom pipeline to analyse secondary eclipses and we analyse the hottest ultra-hot Jupiter known, KELT-9b, and comment on how this planet fits into the population.

Chapter 4 presents a focused look at one ultra-hot exoplanet in particular, WASP-18b. Using our custom data analysis pipeline, we analyse 10 almost consecutive eclipses at $4.5\text{ }\mu\text{m}$. We find a periodic signal in the brightness variability in time. We confirm the signal by performing different analyses of the data and then explore possible physical phenomena that could be responsible for a time variable brightness in the atmosphere.

Finally, Chapter 5 presents an analysis of seven of the coolest planets from our science exploration program. These planets are part of three multi-planet systems (Kepler-9, Kepler-18 and Kepler-32) and one circumbinary system (Kepler-16). Due to the low signal-to-noise of the multi-planet system planets, we alter the pipeline to extract only the transit times. We then compare the measured transit times to predictions made with timing variation models based on the original Kepler observations, which can help pin down the planetary masses. On the other hand, the signal-to-noise ratio of the Kepler-16b data is high, allowing us to extract exquisite transit lightcurves and to fit for the full range of transit parameters. We make predictions using a photo-dynamical model of the Kepler-16 system and compare this to the 3.6 and $4.5\text{ }\mu\text{m}$ transit lightcurves.

EVIDENCE FOR DISEQUILIBRIUM CHEMISTRY FROM VERTICAL MIXING IN HOT JUPITER ATMOSPHERES: A COMPREHENSIVE SURVEY OF TRANSITING CLOSE-IN GAS GIANT EXOPLANETS WITH WARM-*Spitzer*/IRAC



Claire Baxter, Jean-Michel Désert, Shang-Min Tsai, Kamen O. Todorov, Jacob L. Bean, Drake Deming, Vivien Parmentier, Jonathan J. Fortney, Michael Line, Daniel Thorngren, Raymond T. Pierrehumbert, Adam Burrows, Adam P. Showman

Astronomy & Astrophysics, 648, A127 (2021)

Abstract

Aims We present a large atmospheric study of 49 gas giant exoplanets using infra-red transmission photometry with *Spitzer*/IRAC at 3.6 and 4.5 μm .

Methods We uniformly analyse 70 photometric lightcurves of 33 transiting planets using our custom pipeline, which implements pixel level decorrelation. Augmenting our sample with 16 previously published exoplanets leads to a total of 49. We use this survey to understand how infra-red photometry traces changes in atmospheric chemical properties as a function of planetary temperature. We compare our measurements to a grid of 1-D radiative-convective equilibrium forward atmospheric models which include disequilibrium chemistry. We explore various strengths of vertical mixing ($K_{zz} = 0 - 10^{12} \text{ cm}^2/\text{s}$) as well as two chemical compositions (1x and 30x solar).

Results We find that on average, *Spitzer* probes a difference of 0.5 atmospheric scale heights between 3.6 and 4.5 μm , which is measured at 7.5σ level of significance. Changes in the opacities in the two *Spitzer* bandpasses are expected with increasing temperature due to the transition from methane dominated to carbon monoxide dominated atmospheres at chemical equilibrium. Comparing the data with our model grids, we find that the coolest planets show a lack of methane compared to expectations, which has also been reported by previous studies of individual objects. We show that the sample of coolest planets rule out 1x solar composition with $>3\sigma$ confidence while supporting low vertical mixing ($K_{zz} = 10^8 \text{ cm}^2/\text{s}$). On the other hand, we find that the hot planets are best explained by 1x solar metallicity and high vertical mixing models ($K_{zz} = 10^{12} \text{ cm}^2/\text{s}$). We interpret this as the lofting of CH₄ to the upper atmospheric layers. Changing the interior temperature changes the expectation for equilibrium chemistry in deep layers, hence the expectation from disequilibrium chemistry higher up. We also find a significant scatter in the transmission signatures of the mid-temperate

and ultra-hot planets, likely due to increased atmospheric diversity, without the need to invoke higher metallicities. Additionally, we compare *Spitzer* transmission with emission in the same bandpasses for the same planets and find no evidence for any correlation. Although more advanced modelling would test our conclusions further, our simple generic model grid points towards different amounts of vertical mixing occurring across the temperature range of hot Jupiters. This finding also agrees with the observed scatter with increasing planetary magnitude seen in *Spitzer*/IRAC color-magnitude diagrams for planets and brown dwarfs.

2.1 Introduction

Studying exoplanets is critical for gaining insights into the dominant composition and physical atmospheric processes and for understanding the theory of planet formation and evolution (Seager & Deming 2010; Crossfield 2015; Deming & Seager 2017). Hot Jupiters with large scale heights are ideal targets for detecting molecular signatures in their atmospheres via transmission spectroscopy (Seager & Sasselov 2000; Brown 2001). The atmospheres of such planets have been studied across a large range of wavelengths with a myriad of different instruments. Given the number of exoplanet atmospheres already observed, we now enter the era of statistical study of exoplanet atmospheres (e.g., Triaud et al. 2014; Beatty et al. 2014; Gao et al. 2020; Keating et al. 2019; Garhart et al. 2020; Baxter et al. 2020; Fu et al. 2017; Tsiaras et al. 2018; Wallack et al. 2019).

Wavelength dependent transit depths are in principle primarily sensitive to the atmospheric composition (Seager & Sasselov 2000), in practice these observations have often been plagued by the presence of clouds/hazes dampening the expected molecular signals (e.g., Fortney 2005; Sing et al. 2016; Barstow et al. 2017). Nevertheless, cloud-free hot Jupiter atmospheres in chemical equilibrium are predicted to exhibit traces of water, carbon monoxide and methane (Seager et al. 2000; Fortney 2005; Fortney et al. 2010). Studies are conducted to demonstrate whether such elements are statistically and systematically observed in exoplanets (Tsai et al. 2018). However, non-equilibrium chemistry and clouds are predicted to be present in close-in giant exoplanet atmospheres, and will impact their observations (e.g., Agúndez et al. 2012; Drummond et al. 2016; Steinrueck et al. 2019). Sing et al. (2016) performed a mini-survey of the transmission spectra of ten hot Jupiters. They characterize them in terms of a cloud index and find a transition between cloudy and cloud-free atmospheres. They note that a temperature-pressure profile crossing a condensation curve is not solely responsible for the resulting damped spectra, rather it is likely that non-equilibrium effects such as atmospheric circulation and vertical mixing play a role.

There are several important atmospheric processes to consider that can drive atmospheres away from cloud-free chemical equilibrium. Zhang et al. (2018) showed that atmospheric transport can move atmospheric abundances away from chemical equilibrium and greatly alter the expected spectroscopic observations. They develop a 1D framework to capture these complex atmospheric processes and parameterize it with an eddy diffusion co-efficient (K_{zz}). For hot Jupiters, K_{zz} ranges from 10^8 to 10^{12} cm²/s, based on the estimation of the mean vertical wind in global circulation models (GCM) (Moses et al. 2011; Parmentier et al. 2013). Additionally, Komacek et al. (2019) estimated that the strength of vertical mixing will increase for hotter planets. Particularly relevant to this work is the recent advances made in the field of brown dwarf atmospheres: Miles et al. (2020) study the strength of vertical mixing in cool brown dwarf atmospheres with temperatures 250–750 K, and find that the cooler objects support mixing close to the theoretical maximum yet the warmer objects show weaker than predicted mixing.

Additionally, the atmospheres of warm giant close-in exoplanets seem to be deficient in

methane. According to equilibrium chemistry, methane is predicted to be abundant in the atmospheres of exoplanets with equilibrium temperatures cooler than 1100 K (Madhusudhan 2012). In this context, (Stevenson et al. 2010b) showed that the atmosphere of GJ436b is substantially methane deficient relative to chemical equilibrium models, suggesting the presence of non-equilibrium processes such as those induced by vertical mixing, which has been tested by follow-up studies (Knutson et al. 2011; Lanotte et al. 2014). Several other studies have attempted to model the methane depletion of GJ 436b: using non-equilibrium photochemical models (Line et al. 2011), high metallicity (230-1000x solar) models (Moses et al. 2013b), models with hydrogen depletion (Hu et al. 2015), and invoking tidal heating due to high eccentricity (Agúndez et al. 2014). Morley et al. (2017) provide new data along with a reanalysis and new modeling, they confirm the methane depletion and find the best fitting models have high metallicity, disequilibrium chemistry and tidal heating resulting in an intrinsic temperature (T_{int}) of 300-350 K. T_{int} characterizes the heat flux escaping from the planetary interior, which is written as σT_{int}^4 . Recently, Fortney et al. (2020) suggested that the ongoing eccentricity damping of three warm Neptunes, including GJ 436b, heats their atmospheres and drives strong convective mixing resulting in a decreased CH₄/CO ratio.

Furthermore, methane depletion has been observed in a slew of other warm giant planets. HST/WFC3 observations of the transmission spectra of both WASP-107 b and WASP-117 b reveal no detection of methane expected from chemical equilibrium, only upper limits, suggesting a methane depletion in these atmospheres (Kreidberg et al. 2018a; Spake et al. 2018; Carone et al. 2021). Additionally, combined HST/WFC3 and *Spitzer*/IRAC transmission spectra observations of GJ3470 b (Benneke et al. 2019), HAT-P-11 b (Chachan et al. 2019), HAT-P-26 b (Wakeford et al. 2017) and WASP-39 b (Wakeford et al. 2018) all have lower than expected abundances of methane given their temperatures. All in all, methane has only been sparsely detected in the atmospheres of a few exoplanets (Swain et al. 2008; Tinetti et al. 2010; Guilluy et al. 2019).

In this paper, we aim to statistically characterize a large sample of hot Jupiters using the two remaining active detectors on *Spitzer*/IRAC at 3.6 μm . and 4.5 μm . (Fazio et al. 2004; Werner et al. 2004). At these two wavelengths we expect to see the absorption of methane (CH₄) and carbon monoxide or carbon dioxide (CO or CO₂) respectively. We uniformly analyze *Spitzer*/IRAC photometric transit lightcurves of a survey of 34 gas giant planets. This survey represents the largest analysis of *Spitzer*/IRAC observations of gas giants in transmission to date, and it spans equilibrium temperatures from 500 K to 2700 K.

This paper is organized as follows: In Section 2.2 we describe the observations and the survey of planets. In Section 2.3 we describe the data reduction, photometric extraction, lightcurve fitting, and the creation of our grid of 1-D atmospheric models. Section 2.4 describes the results for the transit survey and the statistical survey comparison to the grid of models. In Section 2.5 we discuss the context and implications for the different trends and statistics that we observe. Additionally, in Section 2.5 we describe the collection and combination of the secondary eclipse data with GAIA distances and discuss and comparison between transits and eclipses.

2.2 Observations

As part of the survey programs 90092 (PI Desert) and 13044 (PI Deming) we present the transit depth analysis 70 transit lightcurves of 33 planets in the Post Cryogenic Warm *Spitzer*/IRAC bandpasses of $3.6\text{ }\mu\text{m}$ and $4.5\text{ }\mu\text{m}$. With the goal of gaining a stronger understanding of the origins and nature of the exoplanets already discovered, we designed the survey to probe a wide range of masses, radii and equilibrium temperatures: ranging from cooler long-period gas giants ($\sim 200\text{K}$) from the *Kepler* mission to close-in hot Jupiters (up to 2300 K). Table 2.1 presents the observational information for the 33 planets in the survey. These exoplanets were selected due to their high expected signal-to-noise ratio and, in the case of the Kepler planets, their multiplicity. Additionally, we augment this sample with two extra planets to probe the coolest and the hottest regions of parameter space, these are WASP-121b from program 13044 (PI Deming) and WASP-107b from program 13052 (PI Werner). A full list of the observations is displayed in Table 2.1.

All observations from our survey were taken in "peak-up" mode. Meaning the main observation was preceded by a 30 minute peak-up observation allowing for accurate pointing and thus obtaining precise positioning of the target to within 0.1 pixels throughout the observations. This significantly reduces the ramp effect caused by the intrapixel sensitivity (discussed in Section 2.3.1.2).

We expand our survey to other transiting planets for which the transit depths in the *Spitzer* bandpasses are taken from the literature. First, we perform a search on exoplanets.org (Wright et al. 2011) which yielded $3.6\text{ }\mu\text{m}$ and $4.5\text{ }\mu\text{m}$ transits for 16 additional planets. Combining these with our survey allows us to gain insights into the current state of infrared exoplanet transmission spectra in a statistical manner. These additional planets and their transit depths are listed in Table 2.2. Figure 2.1 presents a visualization of the parameter space covered by all planets in our survey (analyzed and literature).

WASP-6b and WASP-34b are part of the original survey program 90092, however, we exclude them from our analysis because the transits were missed. In the case of WASP-6b, the predicted mid-transit times had a large degree of uncertainty on the ephemeris, and the observed transits in both channels did not have sufficient baseline to gain accurate constraints on the atmosphere. In the case of WASP-34b, both transits were missed due to an error in the ephemeris.

Table 2.1: Details of the *Spitzer* Observations used in our survey analysis showing the UT date of observation, the duration of observation in hours, and the program ID of each transit.

Target	λ $\mu\text{ m}$	UT Start Date	Duration	Program ID
			Hours	
GJ3470 b	4.5	2013 Jan 01	4.4	90092
GJ3470 b	3.6	2012 Dec 22	4.4	90092
HAT-P-12 b	4.5	2013 Mar 11	4.5	90092
HAT-P-12 b	3.6	2013 Mar 08	4.5	90092

Table 2.1: continued.

Target	λ $\mu\text{ m}$	UT Start Date	Duration Hours	Program ID
HAT-P-18 b	3.6	2013 Jun 17	5.0	90092
HAT-P-18 b	4.5	2013 Jul 09	5.0	90092
HAT-P-1 b	4.5	2013 Sep 20	5.2	90092
HAT-P-1 b	3.6	2013 Sep 11	5.2	90092
HAT-P-26 b	3.6	2013 Sep 09	4.5	90092
HAT-P-26 b	4.5	2013 Apr 23	4.5	90092
HAT-P-32 b	3.6	2012 Nov 18	5.4	90092
HAT-P-32 b	4.5	2013 Mar 18	5.4	90092
HAT-P-41 b	3.6	2017 Jan 18	12.1	13044
HAT-P-41 b	4.5	2017 Feb 03	12.1	13044
HATS-7 b	4.5	2016 Nov 04	5.2	13044
HATS-7 b	3.6	2016 Nov 01	5.2	13044
KELT-7 b	4.5	2017 Jan 04	10.3	13044
KELT-7 b	3.6	2016 Dec 27	10.3	13044
Kepler-45 b	4.5	2013 Sep 29	4.5	90092
Kepler-45 b	3.6	2013 Sep 22	4.5	90092
Kepler-45 b	4.5	2013 Sep 12	4.5	90092
Kepler-45 b	3.6	2013 Sep 07	4.5	90092
Kepler-45 b	3.6	2013 Oct 16	4.5	90092
Kepler-45 b	4.5	2013 Nov 15	4.5	90092
Kepler-45 b	4.5	2013 Aug 21	4.5	90092
Kepler-45 b	3.6	2013 Aug 06	4.5	90092
TrES-2 b	4.5	2012 Nov 26	4.3	90092
TrES-2 b	3.6	2012 Nov 21	4.3	90092
WASP-101 b	4.5	2017 Jan 17	8.0	13044
WASP-101 b	3.6	2017 Jan 06	8.0	13044
WASP-107 b	3.6	2017 May 02	8.7	13052
WASP-107 b	4.5	2017 Apr 26	8.7	13052
WASP-121 b	4.5	2017 Jun 05	8.5	13044
WASP-121 b	3.6	2017 Jun 02	8.5	13044
WASP-131 b	4.5	2017 Jun 04	11.3	13044
WASP-131 b	3.6	2016 Nov 04	11.3	13044
WASP-13 b	3.6	2013 Jul 07	7.5	90092
WASP-13 b	4.5	2013 Jan 22	7.5	90092
WASP-17 b	4.5	2013 May 14	8.2	90092
WASP-17 b	3.6	2013 May 10	8.2	90092
WASP-1 b	4.5	2013 Mar 20	6.8	90092

Table 2.1: continued.

Target	λ $\mu\text{ m}$	UT Start Date	Duration Hours	Program ID
WASP-1 b	3.6	2013 Mar 10	6.8	90092
WASP-21 b	4.5	2013 Sep 01	6.1	90092
WASP-21 b	3.6	2013 Aug 27	6.1	90092
WASP-29 b	4.5	2017 Mar 14	7.8	13044
WASP-29 b	3.6	2017 Feb 22	7.8	13044
WASP-31 b	4.5	2013 Mar 19	4.6	90092
WASP-31 b	3.6	2013 Mar 09	4.6	90092
WASP-34 b	4.5	2013 Mar 25	4.5	90092
WASP-34 b	3.6	2013 Mar 17	4.5	90092
WASP-36 b	3.6	2017 Feb 20	7.3	13044
WASP-36 b	4.5	2017 Aug 10	7.3	13044
WASP-39 b	4.5	2013 Oct 10	5.0	90092
WASP-39 b	3.6	2013 Apr 18	5.0	90092
WASP-4 b	4.5	2012 Dec 31	4.3	90092
WASP-4 b	3.6	2012 Dec 27	4.3	90092
WASP-62 b	3.6	2016 Nov 24	11.3	13044
WASP-62 b	4.5	2016 Dec 07	11.3	13044
WASP-63 b	4.5	2017 Jun 17	15.8	13044
WASP-63 b	3.6	2017 Apr 21	15.8	13044
WASP-67 b	3.6	2017 Jan 22	5.6	13044
WASP-67 b	4.5	2017 Aug 13	5.6	13044
WASP-69 b	4.5	2017 Aug 30	6.5	13044
WASP-69 b	3.6	2017 Aug 26	6.5	13044
WASP-6 b	3.6	2013 Jan 21	4.6	90092
WASP-6 b	4.5	2013 Jan 14	4.6	90092
WASP-74 b	4.5	2017 Jan 16	6.7	13044
WASP-74 b	3.6	2017 Jan 14	6.7	13044
WASP-79 b	4.5	2016 Nov 27	11.1	13044
WASP-79 b	3.6	2016 Nov 20	11.1	13044
WASP-94 Ab	3.6	2017 Feb 10	13.3	13044
WASP-94 Ab	4.5	2017 Aug 06	13.3	13044
XO-1 b	4.5	2013 May 25	5.4	90092
XO-1 b	3.6	2013 May 13	5.4	90092
XO-2 b	3.6	2013 Jan 02	4.9	90092
XO-2 b	4.5	2012 Dec 31	4.9	90092

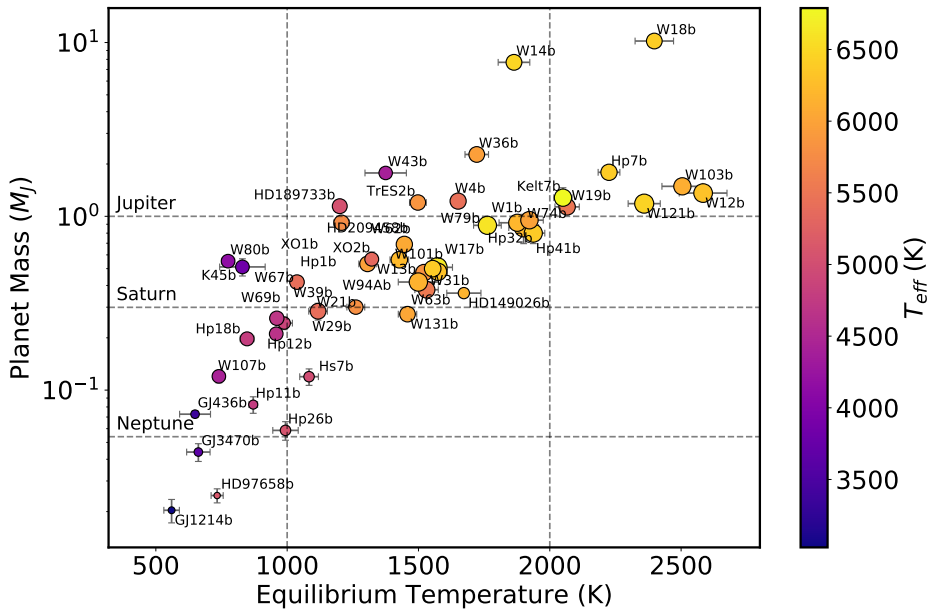


Fig. 2.1: Planet mass (M_{Jup}) versus equilibrium temperature in Kelvin (assuming zero albedo and full redistribution) for all the planets presented in the current survey. The color of the points shows the stellar temperature (T_{eff}) in Kelvin and the size of the points is scaled proportionately to the planetary radius. The gray dashed horizontal lines mark the masses of Jupiter, Saturn and Neptune. The gray dashed vertical lines mark the temperature regions discussed in Section 2.4.1.5.

2.3 Analysis

2.3.1 Transit lightcurve analysis

2.3.1.1 Extracting *Spitzer* photometric lightcurves

We designed a custom pipeline to produce a photometric lightcurve from the Basic Calibrated Data frames produced by the *Spitzer* level 1 pipeline. As is standard for these data, our pipeline corrects dark current, flat fields, corrects for pixel non-linearity, and converts to flux units.

We first calculate the mid-exposure timing of each data point in our transit lightcurves using the UTC-based MJD values from the headers of each fits file. Our custom pipeline then corrects transient bad pixels in the image timeseries by comparing each pixel intensity to a median of the 30 preceding and 30 following frames. We replace the pixel intensity with the median value if it is $\geq 4\sigma$ from this value. The fraction of transient bad pixels that are corrected is displayed in Table 2.10, this varies around 0.5% and 0.06% for channel 1 and channel 2, respectively. Our pipeline also consists of several different functions for three

Table 2.2: *Spitzer* measurements at $3.6\text{ }\mu\text{m}$ and $4.5\text{ }\mu\text{m}$ for planets that have already been published. We include these measurements to our survey.

Planet	T_{eq} (K)	$\delta_{3.6}$ (%)	$\delta_{4.5}$ (%)	Reference
GJ 1214 b	560 ± 30	1.354 ± 0.009	1.367 ± 0.004	1
GJ 436 b	649 ± 59	0.695 ± 0.011	0.705 ± 0.012	2, 16
HAT-P-11 b	871 ± 16	0.338 ± 0.002	0.336 ± 0.003	3
HAT-P-7 b	2225 ± 41	0.629 ± 0.024	0.604 ± 0.012	4
HD 149026 b	1673 ± 65	0.269 ± 0.004	0.253 ± 0.004	5
HD 189733 b	1200 ± 22	2.405 ± 0.008	2.416 ± 0.011	6
HD 209458 b	1446 ± 19	1.481 ± 0.012	1.466 ± 0.007	7
WASP-103 b	2505 ± 78	1.401 ± 0.033	1.433 ± 0.026	8
WASP-12 b	2584 ± 91	1.341 ± 0.02	1.306 ± 0.031	9
WASP-14 b	1864 ± 60	0.887 ± 0.013	0.888 ± 0.013	10
WASP-18 b	2398 ± 73	0.959 ± 0.057	0.972 ± 0.049	11
WASP-19 b	2066 ± 46	1.957 ± 0.05	2.036 ± 0.051	4
WASP-33 b	2694 ± 53	1.166 ± 0.022	1.061 ± 0.023	5
WASP-43 b	1375 ± 79	2.496 ± 0.009	2.525 ± 0.016	12
WASP-80 b	775 ± 25	2.937 ± 0.013	2.969 ± 0.014	13
K2-25b	482 ± 20	1.143 ± 0.16	1.158 ± 0.18	14
HD97658b	733 ± 23	074 ± 002	08 ± 002	15
HAT-P-2 b	1540 ± 30	0.465 ± 01	0.496 ± 008	17

(1) Fraine et al. (2013); (2) Knutson et al. (2011); (3) Chachan et al. (2019); (4) Wong et al. (2016); (5) Zhang et al. (2018); (6) Pont et al. (2013); (7) Sing et al. (2016); (8) Kreidberg et al. (2018b); (9) Stevenson et al. (2014b); (10) Wong et al. (2015); (11) Maxted et al. (2013); (12) Stevenson et al. (2016); (13) Triaud et al. (2015); (14) Thao et al. (2020); (15) Guo et al. (2020); (16) Morley et al. (2017); (17) Lewis et al. (2013);

important steps in the data reduction: background sky subtraction, finding the centroid of the object, and performing aperture photometry. Additionally, in between these steps, a sliding σ -clipping on any outliers is performed on the centroiding and on the resulting photometry.

Previous studies have demonstrated that the data reduction method chosen to produce the lightcurves can have significant effects on the resulting measured transit depths (Ingalls et al. 2016). We thus optimized the background subtraction, centroiding and aperture photometry methods by running the pipeline over a 3 dimensional grid of different methods for each step, we call these methods the pipeline parameters. We tested three methods of background subtraction:

1. The "Box" method: Median value from a 2×2 or 4×4 pixel box in all four corners of the frame.
2. The "Annulus" method: The mean of an annulus centred on the star of radii 6 or 8

pixels and size 2 or 4 pixels (using photutils).

3. The "Histogram" method: Fit a Gaussian to a histogram of all the pixels in the frame, excluding the star.

We also tested three methods of centroiding:

1. The "Barycenter" method: Center of light of a 3x3, 5x5 or 7x7 pixel box centered on the approximate position of the star.
2. The "Gaussian" method: Fit a two dimensional Gaussian function to the entire image using Astropy (Astropy Collaboration et al. 2018). All of the parameters of the 2D Gaussian were let free ($A, x_0, y_0, \sigma_x, \sigma_y, \theta$) for each frame. The centroid position was the x_0, y_0 from the Levenberg Marquardt Least Squares fit. (Agol et al. 2010)
3. The "Moffat" method: Same as above but instead a 2D Moffat function was fit to the entire image.

Finally, we varied the aperture radius from 2.5 to 5.0 pixels in increments of 0.25 pixels.

For each instance of the grid and thus each iteration of the data reduction pipeline, we performed a least-squares fit to our model (transit + systematic) and calculated the reduced χ^2 . The parameters yielding the lowest reduced χ^2 were used to create the lightcurve used for further analysis. There are a few exceptions to this, for example, some of the cooler planets have a lower signal-to-noise ratio (SNR) meaning the systematics dominate and there is thus a larger scatter in the measured parameters at each pipeline iteration. These planets were examined manually and pipeline parameters were chosen by hand looking for both repeatable measurements and close to the minimum reduced χ^2 . The optimum pipeline parameters including centroiding method, aperture size, background subtraction method and data reduction information for each planet are detailed in Table 2.9. Although the observations were made in "peak-up" mode, it is common that there is still some persistence at the beginning of the lightcurves. To correct for this, we devised a similar χ^2 test for cutting out the ramp at the beginning of the observations. We performed a series of cuts at the beginning of the lightcurve and refitted the model. Similarly, we chose the time to trim off the beginning of the lightcurve to be the one that gave the lowest reduced χ^2 and root mean square (RMS) of the residuals.

Prior to any further data analysis, the lightcurve intensities are converted to electron counts following the method described in the *Spitzer* handbook (multiply by EXPTIME*GAIN/FLUXCONV). This allows us to calculate the photometric errors using Poisson statistics.

2.3.1.2 Instrumental Systematic Modelling

Spitzer lightcurves exhibit significant amounts of correlated noise, which has been extensively studied and documented in the literature (Charbonneau et al. 2005; Agol et al. 2010;

Seager & Deming 2010; Stevenson et al. 2010a). The dominant source of this red noise at 3.6 and 4.5 μm is caused by an intrapixel sensitivity. Variations in the telescope pointing combined with undersampling of the stellar PSF results in variations in the centroiding with time $\sim 10\%$ of a pixel. When combined with the intrapixel sensitivity, this results in variations in the photometric lightcurve of order 1%, which is problematic since the atmospheric signal we are trying to extract is on the order of 0.01%. There have been many different methods developed for dealing with these systematics (e.g., Reach et al. 2005; Charbonneau et al. 2008; Ballard et al. 2010; Stevenson et al. 2012; Gibson et al. 2012; Morello et al. 2015; Morello 2015; Deming et al. 2015). Ingalls et al. (2016) presented the results of a data challenge on synthetic and real eclipse data of XO-3b, in which several systematic correction methods were tested against each other. They found that BLISS (Stevenson et al. 2012), Pixel Level Decorrelation (PLD) (Deming et al. 2015), and ICA techniques (Morello et al. 2015) were the most precise for correcting the systematics of data of similar quality to XO-3b. PLD achieved the highest accuracy to the synthetic input data (Deming et al. 2015). Thus, we present the results of the pixel level decorrelation function for correcting our systematics and, for comparison, we also test the polynomial function presented in Knutson et al. (2008).

Pixel Level Decorrelation Unlike most methods of systematic correction, PLD does not use the centroid position of the stellar PSF on the pixel as an input (Deming et al. 2015). PLD relates the intensities of the individual pixels directly to the photometry in one numerical step, whereas the other methods used two numerical steps: first finding the centroid position of the star and then relating that to the measured photometry with a different numerical process. To bypass this secondary measurement, PLD assumes that the measured brightness of the star is a smooth function of position. One can Taylor expand this continuous and differentiable function such that the flux of the star can be expressed as a linear sum of the individual pixel fluxes (described fully in Deming et al. (2015)).

$$\Delta S^t = \sum_{i=1}^N c_i \hat{P}_i^t + DT(t) + ft + h \quad (2.1)$$

Where S^t is the flux measured over time and Δ represents the total fluctuations from all sources. $\hat{P}_i^t = \frac{P_i^t}{\sum_{i=1}^N P_i^t}$ represents the normalized flux from pixel i at time t . Here, i is an integer pixel number, where a 2D grid of pixels centered on the PSF is chosen, each pixel being indexed with a single number. The number of pixels included can be selected depending on the size of the PSF and the brightness of the star. In our survey, we uniformly take a 2-dimensional grid of 3x3 pixels containing the PSF of the star on the middle pixel. $DT(t)$ is the transit shape, and $ft + h$ is a temporal ramp which is a typical behavior of warm *Spitzer* lightcurves due to the residual telescope pointing.

Polynomial We also corrected the intrapixel variations using the polynomial function of the position presented in Knutson et al. (2008). $F_{corr} = F(K_0 + K_1(x - x_0) + K_2(x - x_0)^2 +$

$K_3(y - y_0) + K_4(y - y_0)^2$, where x_0 and y_0 are the integer pixel numbers plus 0.5, such that the polynomial is a function of the distance from the center of the pixel, where it is understood to be the most sensitive (Stevenson et al. 2012). Similarly to the PLD, we opted to use a linear function of time to correct the ramp over the entire lightcurve.

2.3.1.3 Fitting lightcurves to obtain transit parameters

Transit Model The transit shape ($DT(t)$) was calculated using Batman (Kreidberg 2015). Batman produces a transit lightcurve with 9 tunable parameters: time of inferior conjunction (days), orbital period (days), planet radius (in units of R_s), semi-major axis (in units of R_s), orbital inclination (deg), eccentricity, angle of periastron (deg), limb darkening model and limb darkening coefficients.

We fixed the orbital period for all of our planets to the values from the literature (Table 2.7). Several planets in our sample have reported values of the eccentricity and angle of periastron passage, as a test for these planets we ran a fit of both a circular and an eccentric orbit and found that the eccentricity did not affect the measured transit depth. We thus fixed the eccentricity and angle of periastron to zero for the remainder of the analysis.

Limb Darkening Southworth (2008) demonstrated that the choice of limb darkening can affect the measured planetary radius. This is particularly important in the optical wavelengths where the limb darkening effects are stronger, however we investigated the effects for each of our planets as a standard output of our pipeline. We started by using linear coefficients for the limb-darkening law, which were calculated using the 1D Atlas code from Sing (2010) for the $3.6\ \mu\text{m}$ and $4.5\ \mu\text{m}$ *Spitzer* channels. We translated the interpolation routine from IDL to Python and interpolated the linear limb-darkening values and their 1σ errors using the effective temperature, surface gravity, and metallicity of every star in our sample (Table 2.7). We were then able to vary the limb darkening coefficients within the uncertainties and confirm that the limb-darkening does not have significant impact on the resulting measured transit depth at these wavelengths. For this reason, we fixed the limb-darkening to the linear coefficients for the remainder of the analysis.

This leaves 4 tunable parameters: the time of inferior conjunction (t_0), planet radius (R_p/R_s), semi-major axis (a/R_s) and the orbital inclination (i). The fixing and varying of these parameters is discussed in Section 2.3.1.3.

Estimating Uncertainties using MCMC After the optimum pipeline parameters and the cutting time at the beginning and end of the lightcurve were determined we performed a full statistical analysis on the photometric transit lightcurves to estimate the uncertainties and study the co-variances of the parameters.

Before performing any fitting, we normalized the lightcurves, which allowed us to directly compare the PLD values and the photon flux timeseries in each pixel with each other. An initial normalization was done by taking the median of the first 100 data points in the

lightcurve. We then performed an initial Levenberg-Marquardt least-squares fit to get the preliminary transit parameters, which were then used to cut out the transit and so that the normalisation scale was recalculated such that the median of the out-of-transit flux was 1.

A second least squares fit was performed before performing a 4σ clip of the residuals to remove any outlying photometric points not captured in the centroiding clipping. We performed a final least squares on the normalized σ clipped data to determine the initial guess for the parameters as an input for our Markov Chain Monte Carlo analysis. We first calculated the errors on the photometric points using Poisson statistics assuming photon noise (\sqrt{N}). Then, after the first initial least squares fit, we determine how close we are to photon noise for each fit and scale up the uncertainties. These results are shown in Table 2.10. As is commonly found for *Spitzer* timeseries transit observations our uncertainties are around 20-50% above the photon noise limit for the whole survey. Scaling up the uncertainties on the photometric points by this factor before running the final fit results in a reduced χ^2 of ~ 1 , which prevents us from underestimating the uncertainties on the physical transit parameters.

We estimated the uncertainties on the best-fit parameters using emcee, the open source Affine-Invariant Metropolis-Hastings algorithm for Markov Chain Monte Carlo analysis developed by Foreman-Mackey et al. (2013). We initialized the MCMC chains with 100 walkers, 1000 burn-in steps, and 2000 production steps. We also performed a prayer-bead analysis of the uncertainties as a sanity check, but here we adopt the results from the MCMC analysis, since the sampling can be much larger. For each MCMC run, we checked for convergence with the emcee recommended acceptance fraction (0.2-0.5) and the Gelman-Rubin statistic (≤ 1.1) (Gelman & Rubin 1992). If the signal to noise of the data was low, sometimes the MCMC had an extremely low acceptance fraction. When this happened, we doubled the number of walkers until proper convergence was achieved. We derived the 1σ error bars asymmetrically as 34% above and below the median.

Our combined astrophysical and instrumental (PLD) noise model has 14 free parameters in total for the first fit. We treated the two distinct groups of planets slightly differently in our data reduction. The planets were split into two groups, lower SNR planets (generally cooler with longer periods) and higher SNR planets (short-period hot Jupiters). For the higher SNR planets, we let t_0 , R_p/R_s , a/R_s and i free in the initial fit with uniform priors on all parameters, then we performed a second MCMC fit where we used a 1σ Gaussian prior on a/R_s and i based on the results from the first fit. For the lower SNR planets, where it is difficult to detect the transit in each individual lightcurve, we need to fix a/R_s and i to the literature values for the fitting. For both of these methods, the walkers are initialized in a tight cluster around the best fit Levenberg-Marquardt minimization. These lower SNR planets also had multiple transits in each band-pass, these were each analyzed, and the average transit depth was calculated using the weighted sum, where the weight is the inverse variance multiplied by an "over dispersion" factor as done in Ingalls et al. (2016). The over dispersion factor allows for underestimation of the individual uncertainties, see Lyons (1992) for further information.

Special Cases The systematics of WASP-13b were not properly captured by our pipeline, such that a bump at the end of the transit remained in the reduced light curve at $3.6\text{ }\mu\text{m}$. This had the consequence of making our fitted transit depth shallower than it would be. We thus removed this data from our fit and ran the pipeline again to get the optimal parameters and transit depths. In total we removed 36 minutes from the last quarter of the in-transit flux, however, the egress remained intact allowing us to still characterize the system.

Similarly, the $3.6\text{ }\mu\text{m}$ transit of WASP-131b showed a bump in the baseline before transit, likely a starspot occultation. Therefore, we also removed 50 minutes of flux in our MCMC fit.

Furthermore, our approach was slightly modified for HAT-P-26b due to its low signal-to-noise ratio, we set Gaussian priors on the semi-major axis and inclination in the initial fits based on the literature values.

2.3.2 Interpreting Transmission Spectrophotometry with 1-D Atmospheric Modeling

To interpret the results from our survey of transiting hot Jupiters, we compare the IRAC transit depths with a grid of simulated atmospheric spectra. First, double-gray analytical formulae are applied to construct the cloud-free temperature-pressure (T-P) profiles for a wide range of stellar irradiation Heng et al. (2014). Second, we use a photochemical kinetics model (VULCAN, Tsai et al. (2017) see Section 2.3.2.3) to compute the composition under the effects of photo-dissociation and vertical mixing. The T-P profiles and the chemical composition are not self-consistently computed, here, we focus on how the stellar flux impacts the disequilibrium chemistry. Last, a radiative transfer code (PLATON Zhang et al. (2019), see Section 2.3.2.4) is used to create transmission spectra to compare with the observational data. Our fiducial model grid spans a range of equilibrium temperatures (T_{eq}) from around 400 K to around 2400 K in ~ 100 K steps, planetary surface gravities (g_p) 500, 1500, 5000 cm/s^2 , planet radius (R_p) 0.5, 1, 1.5, $2 R_{\text{jup}}$ and stellar radius (R_s) 0.5, 1, 1.5, $2 R_{\odot}$ with 1x solar composition and equilibrium chemistry (no vertical mixing, no photo-chemistry, no boundary fluxes). We then expand our modeling in two dimensions. First, we incorporate non-equilibrium processes and capture vertical mixing in the form of an eddy diffusion coefficient (K_{zz}). Second, we test the effects of higher metallicity by creating the full set of grids with 30x solar metallicity. We describe the creation of these grids in full detail below.

2.3.2.1 Stellar Irradiation and T-P profiles

In our survey, most hot Jupiters populate a small range of close-in orbits, $a_{\text{mean}} = 0.037 \pm 0.013$ AU, while the parent stars span several spectral types, from early M stars to F stars. In fact, the stellar temperature varies from about 3000 K to 7000 K, while the radius also increases with earlier stellar types. Since for a planet at orbital distance (a) around a star with radius (R_s) and effective temperature (T_{eff}), the equilibrium temperature of the planet

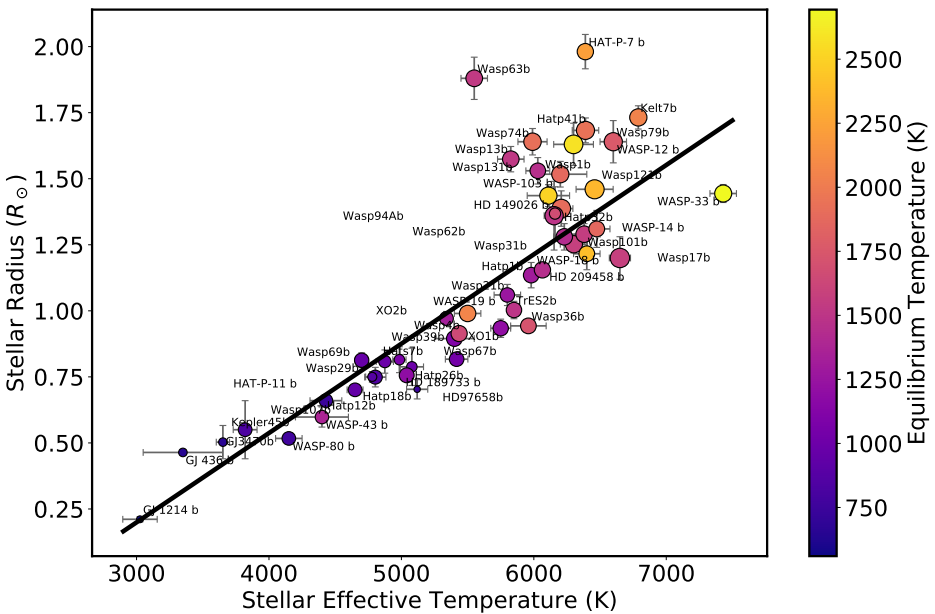


Fig. 2.2: Stellar Radius as a function of stellar effective temperature. Black line shows first order polynomial best fit used for creation of T-P grid (see Section 2.3.2.1). Color of points shows the equilibrium temperature of the planets, size of points is scaled to the planet radius.

(T_{eq}) is proportional to $T_{\text{eff}}(R_s/a)^{1/2}$. The stellar flux plays a bigger factor in determining the irradiation the planet received and its effective temperature. In this regard, we assume a fixed orbital distance for our model grid to isolate the effects of stellar irradiation. The mean value of the samples, 0.035 AU, is taken across the grid. In this setting, the effective temperature of the model planet is entirely determined by the stellar luminosity, and not by the orbital distance. We also note that the intrinsic temperature (T_{int}) is negligible and thus the effective temperature ($T_{\text{eff}}^4 = T_{\text{eq}}^4 + T_{\text{int}}^4$) is the same as the equilibrium temperature. Additionally, our assumed value of $T_{\text{int}}=150$ K has little effect on our model temperature pressure profiles of the hot Jupiters.

The next step is to determine the size, hence the energy flux of the stars. For main-sequence stars which follow the mass–luminosity and mass-radius relations, we fit a power law relation between the radius and effective temperature, see Figure 2.2. The power law fitting to our sample yields the following expression for the stellar radius: $R_S = m * T_{\text{eff}} + b$ where m and b are 0.0003381 and -0.81495, respectively. Once the effective temperature and the radius of the star are known, there is enough information to specify the incident irradiation of the model atmospheres.

We then compute the T-P profiles for the given stellar irradiation using the analytical double-gray radiative equilibrium solutions in Heng et al. (2014) (Equation 126.).

The parameters used in this calculation are chosen to match numerical radiative transfer results, listed in Table 2.3. Similar to the prescriptions in Guillot (2010) and Parmentier & Guillot (2014), the opacities do not have a pressure dependence. We reiterate that this relation allows us to uniquely express the equilibrium temperature of a planet at a given orbital distance as a function of stellar temperature. Our stellar grid, with effective temperatures from 3250 to 7000 K, produces irradiated atmospheres of temperature from 446 to 2248 K, at 0.035 AU. To reach the temperatures of the ultra-hot jupiters we also run additional models with an orbital distance at 0.02 AU. The resulting temperature pressure profiles are shown in Figure 2.4.

The simple prescription allows us to explore the parameter space in a basic way and to focus on the correlation with stellar irradiation. Although the intrinsic temperature is held constant in our T-P profiles, the realistic interior can be potentially hotter. Tremblin et al. (2017) and Sainsbury-Martinez et al. (2019) have shown that circulation can transport entropy downward and leads to a hotter deep interior over time. Thorngren et al. (2019) suggested much higher T_{int} for observed hot Jupiters (with $T_{\text{eq}} \gtrsim 1300$ K) than the 100K commonly assumed in GCMs. Fortney et al. (2020) also investigated the effects of heating from tidal dissipation for warm Jupiters (with $T_{\text{eq}} \gtrsim 1300$ K) with simplified chemical timescale analysis. The upshot of the hotter interior is lowering the quenched $[\text{CH}_4]/[\text{CO}]$ ratio. In short, a hot deep interior changes the expectation for equilibrium chemistry in deep layers, hence the expectation from disequilibrium chemistry higher up. Since the equilibrium abundance of CH_4 generally increases with depth (at least in our solar and 30x solar models), lowering vertical mixing also results in a lower $[\text{CH}_4]/[\text{CO}]$ ratio and can effectively be degenerate with a hotter interior. However, we find high vertical mixing matches the hot Jupiters better, even with the lower T_{int} of 150 K. Increasing the interior temperature will reduce CH_4 , so even higher vertical mixing would be required to recover the same CH_4 abundance for these planets. As for the cooler planets, the signature leading to our inference of low vertical mixing can also be explained by a hot interior if there is actually no CH_4 in the deep hot atmosphere. However, the sources of internal heating and their exact interior temperature for these cool planets are rather uncertain (see Fortney et al. (2020) for a detailed discussion).

In addition to this, our prescription for PT profiles is simplified compared to 1D radiative/convective models. Nevertheless, in this study, we are interested in the relative difference between two broad bandpasses (3.6 and 4.5 μm), and thus the prescription used for the TP profiles is less critical than for absolute measurements. The relative difference between 3.6 and 4.5 μm is globally similar for our prescription as compared to the 1D RC models. We aknowledge that the vertical mixing is likely to be affected by the choice of TPs, however testing this difference is beyond the scope of our current study.

Our simple model emphasizes the importance of the degeneracies between vertical mixing, interior temperature, and equilibrium chemistry, but is also a limit to the interpretation. A more detailed approach than the simple model we used is required to study the impact of the various processes on the observations with greater accuracy. However, such detailed study will also be limited by the unknown interior temperature. Therefore, we limit ourselves

Table 2.3: Fixed parameters used in the double-grey radiative equilibrium solution for creating temperature pressure profiles. For each TP profile we show the fixed irradiation temperature (T_{irr}), intrinsic temperature (T_{int}), longwave opacity (κ_L), shortwave opacity (κ_S), longwave scattering parameter (β_L) and the shortwave scattering parameter (β_S).

T_{irr}	T_{int}	κ_L	κ_S	β_L	β_S
631	150	0.02	0.00035	1	1
775	150	0.02	0.00068	1	1
919	150	0.02	0.001	1	1
1069	150	0.02	0.0014	1	1
1222	150	0.02	0.0017	1	1
1379	150	0.02	0.0019	1	1
1540	150	0.02	0.0022	1	1
1706	150	0.02	0.0035	1	1
1875	150	0.02	0.0038	1	1
2049	150	0.02	0.004	1	1
2227	150	0.02	0.0043	1	1
2410	150	0.02	0.006	1	1
2595	150	0.02	0.006	1	1
2786	150	0.02	0.006	1	1
2980	150	0.02	0.0061	1	1
3179	150	0.02	0.0062	1	1

to a simple approach as a sophisticated analysis with more advanced temperature pressure profiles is beyond the scope of this paper.

2.3.2.2 Grid of stellar spectra

As the effective temperature of the star rises, the spectral energy distribution shifts to shorter wavelengths. We therefore adopted the stellar spectral grid from (Rugheimer et al. 2013), which ranges from 4250 to 7000 K and covers F0 to K7 spectral types. The models start with the synthetic ATLAS spectra (Kurucz 1979) and then we co-add the observed spectra from International Ultraviolet Explorer for UV ($<= 300$ nm). See (Rugheimer et al. 2013) for the detailed stellar grid setup. Additionally, for late K and M stars ($T_{\text{eff}} < 4250$ K), we picked GJ 436 ($T_{\text{eff}} = 3350$ K) as our fiducial star. The high resolution spectrum of GJ436 is taken from the MUSCLES survey (France et al. 2016)¹ and scaled for the stellar fluxes with effective temperatures of 3250 K, 3500 K, 3750 K, and 4000 K.

¹<http://cos.colorado.edu/kevinf/muscles.html>

2.3.2.3 Modeling the photo-chemical kinetics with VULCAN

We explore the effects of photolysis, atmospheric mixing, and metallicity by using a photochemical kinetics model, VULCAN (Tsai et al. 2017)². The code solves the steady-state chemical compositions for a given temperature-pressure profile and has been benchmarked for hot Jupiters. In this work, we use the updated version that includes nitrogen chemistry and photochemistry (Tsai et al. in preparation). The chemical model with updated nitrogen chemistry and photochemistry has been tested on nitrogen dominated atmospheres for super-Earths (Zilinskas et al. 2020). The N-C-H-O network consists of about 600 thermal reactions (including forward and reverse) and 40 photodissociation reactions. We validate our updated model against the one-dimensional photochemical and thermochemical kinetics and diffusion model presented in Moses et al. (2011) for HD209458b, see Figure 2.16.

Vertical mixing is simulated through means of an eddy diffusion co-efficient (K_{zz}), which assumes that atmospheric motion resembles diffusion when convection and turbulence occur on much smaller scales than the magnitude of the pressure scale height. We vary the eddy diffusion coefficient to explore various strengths of vertical mixing, with constant values of 10^8 , 10^{10} , and 10^{12} cm²/s. The choice of the values is consistent with those extracted from GCM simulations (Moses et al. 2011; Parmentier et al. 2013; Zhang & Showman 2018b; Komacek et al. 2019). Furthermore, the elemental abundance of the atmosphere is assigned to two different metallicities: 1x solar and 30x solar (Lodders et al. 2009).

2.3.2.4 Creating the transmission spectra with PLATON

Finally, transmission spectra are then simulated using the open-source, transit-depth calculator and retrieval tool, PLATON (Zhang et al. 2019)³. The code has been modified to take non-equilibrium compositions from our calculation, including CH₄, CO, CO₂, C₂H₂, H₂O, O₂, OH, C₂H₄, C₂H₆, H₂CO, HCN, NH₃, NO. The main opacities relevant for the wavelengths of *Spitzer*/IRAC are displayed in Figure 2.3. We assume chemical equilibrium for the rest of the species in PLATON. The details of the forward model can be found in Zhang et al. (2019). We neglect stellar limb darkening in these models and the synthetic transit depth is expressed as $(R_p/R_s)^2$.

2.3.2.5 Calculating the model *Spitzer*/IRAC transit depths

We integrate the simulated transmission spectra with *Spitzer*/IRAC spectral response functions and weight with the stellar flux using the following equation:

$$\bar{\delta}_\lambda = \frac{\int_0^\infty \delta(\lambda) \lambda R(\lambda) F_s(\lambda) d\lambda}{\int_0^\infty \lambda R(\lambda) F_s(\lambda) d\lambda} \quad (2.2)$$

²<https://github.com/exoclime/VULCAN>

³<https://platon.readthedocs.io/en/latest/intro.html>

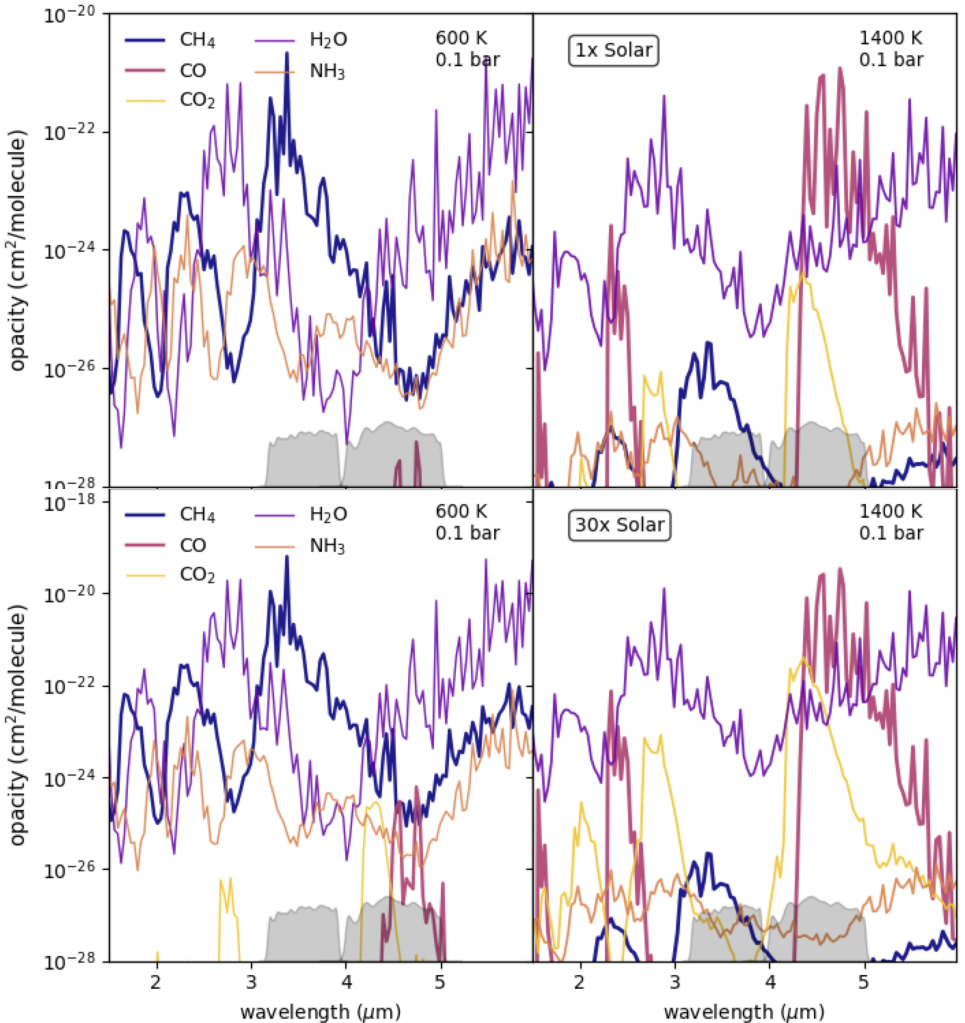


Fig. 2.3: Opacities for a chemical equilibrium atmosphere at 600 K (left) and 1400 K (right) at 0.1 bar. Top panels show the abundance weighted opacities for a solar composition atmosphere and the bottom panels show the abundance weighted opacities for a 30x solar composition atmosphere. Carbon monoxide, water, methane and carbon dioxide (for 30x solar) are the dominant absorbing species at the two IRAC channels (3.6 and 4.5 μm).

where $R(\lambda)$ is the spectral response function at either $3.6\ \mu\text{m}$ or $4.5\ \mu\text{m}$ [e-/photon] (Quijada et al. 2004) and $\delta(\lambda)$ is the transmission spectrum from PLATON and $F_s(\lambda)$ is the stellar flux. The output, $\bar{\delta}_\lambda$, is the weighted average transit depth that would be observed with *Spitzer*/IRAC in either of the two bandpasses.

Figure 2.6 shows the interpolated grid of fiducial models (solar composition, cloud-free with equilibrium chemistry), we plot the normalized IRAC transit depth difference against the equilibrium temperature, and overplot the results from our transit survey. Figure 2.7 shows the different tracks of the model grid that made up the shaded regions and Figure 2.8 shows the different vertical mixing and metallicity interpolated grids with the data. For the cloudy grid, we simply assume a gray cloud opacity such that the spectra are flat and thus the transit depth difference would be zero, which is shown as a vertical line on Figures 2.6 and 2.8.

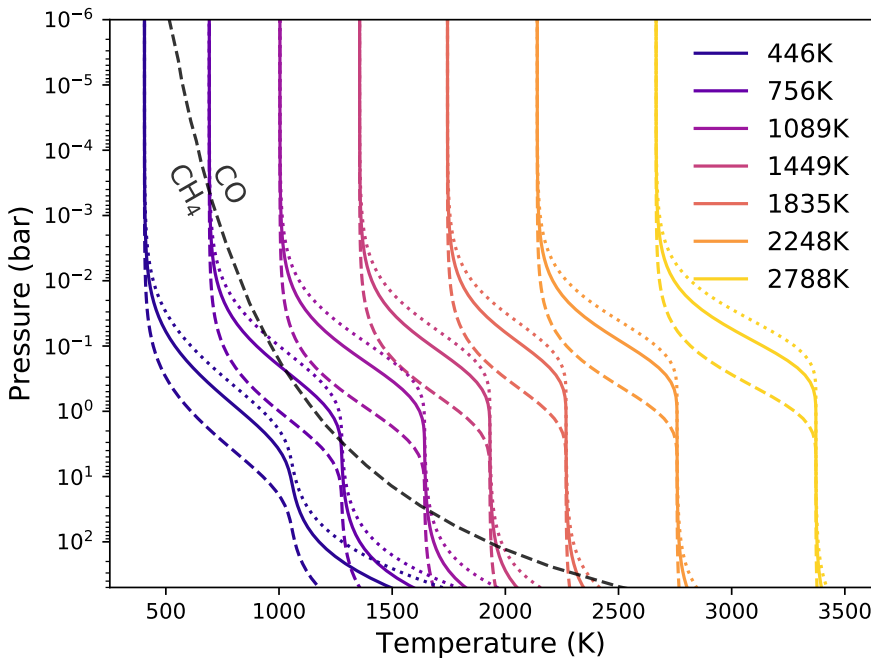


Fig. 2.4: Analytical Temperature-Pressure profiles for grid of models spanning equilibrium temperatures ~ 400 - 2800 K, showing every ~ 400 K. For each temperature we show three profiles where the surface gravity is varied: dotted, solid and dashed lines represent 500 , 1000 and $5000\ \text{cm/s}^2$ respectively. Grey dashed line represents the gas transition between CH_4 and CO dominated atmospheres when chemical equilibrium is assumed.

2.4 Results

2.4.1 Measured transit depths and their ratios

2.4.1.1 Results of measured transit depths

Table 2.4: Results from the MCMC analysis, we show the semi-major axis (a/R^*), the inclination (degrees), the percentage transit depth (R_p/R_s)², the corresponding impact parameter (b) and the mid-transit time in BJD_UTC. Values for the semi-major axis and the inclination are from the initial MCMC fits and then these are fixed with gaussian priors for a second MCMC run where the final values for the transit depths are determined.

Planet	λ (μm)	a/R^*	inc degrees	depth $(R_p/R_s)^2$	b	T0 BJD_UTC
HAT-P-32 b	3.6	$6.13^{+0.02}_{-0.02}$	$89.5^{+0.3}_{-0.5}$	$2.15^{+0.01}_{-0.01}$	$0.05^{+2.06}_{-2.90}$	$2456250.103520^{+0.000112}_{-0.000120}$
HAT-P-32 b	4.5	$6.13^{+0.02}_{-0.04}$	$89.4^{+0.4}_{-0.6}$	$2.21^{+0.02}_{-0.02}$	$0.06^{+2.62}_{-3.95}$	$2456370.504208^{+0.000154}_{-0.000152}$
XO-1 b	3.6	$11.46^{+0.05}_{-0.11}$	$89.5^{+0.3}_{-0.4}$	$1.67^{+0.01}_{-0.01}$	$0.09^{+3.56}_{-4.43}$	$2456426.076095^{+0.000115}_{-0.000120}$
XO-1 b	4.5	$11.24^{+0.20}_{-0.23}$	$88.8^{+0.5}_{-0.4}$	$1.72^{+0.01}_{-0.01}$	$0.24^{+5.40}_{-4.49}$	$2456437.900819^{+0.000158}_{-0.000157}$
HAT-P-1 b	3.6	$9.91^{+0.13}_{-0.13}$	$85.7^{+0.1}_{-0.1}$	$1.40^{+0.01}_{-0.01}$	$0.74^{+0.99}_{-0.99}$	$2456547.478364^{+0.000156}_{-0.000150}$
HAT-P-1 b	4.5	$10.07^{+0.16}_{-0.15}$	$85.8^{+0.1}_{-0.1}$	$1.39^{+0.01}_{-0.01}$	$0.73^{+1.25}_{-1.17}$	$2456556.409109^{+0.000187}_{-0.000190}$
WASP-17 b	3.6	$7.16^{+0.14}_{-0.16}$	$88.1^{+0.8}_{-0.7}$	$1.52^{+0.01}_{-0.01}$	$0.24^{+6.05}_{-4.97}$	$2456423.188874^{+0.000233}_{-0.000221}$
WASP-17 b	4.5	$7.24^{+0.09}_{-0.15}$	$88.6^{+0.8}_{-0.8}$	$1.57^{+0.02}_{-0.02}$	$0.17^{+6.13}_{-5.89}$	$2456426.923243^{+0.000288}_{-0.000285}$
WASP-39 b	3.6	$10.47^{+0.19}_{-0.17}$	$87.0^{+0.2}_{-0.2}$	$2.15^{+0.02}_{-0.02}$	$0.56^{+1.83}_{-1.68}$	$2456401.396438^{+0.000159}_{-0.000176}$
WASP-39 b	4.5	$11.38^{+0.28}_{-0.25}$	$87.7^{+0.3}_{-0.2}$	$2.16^{+0.02}_{-0.02}$	$0.45^{+3.14}_{-2.66}$	$2456575.774315^{+0.000200}_{-0.000194}$
HAT-P-12 b	3.6	$11.23^{+0.26}_{-0.26}$	$88.0^{+0.3}_{-0.3}$	$1.89^{+0.01}_{-0.01}$	$0.39^{+3.64}_{-3.30}$	$2456359.882148^{+0.000131}_{-0.000138}$
HAT-P-12 b	4.5	$10.90^{+0.35}_{-0.30}$	$87.8^{+0.4}_{-0.3}$	$1.93^{+0.03}_{-0.03}$	$0.41^{+4.47}_{-3.60}$	$2456363.095398^{+0.000197}_{-0.000187}$
HAT-P-18 b	3.6	$15.28^{+0.47}_{-0.41}$	$88.5^{+0.3}_{-0.3}$	$1.77^{+0.02}_{-0.02}$	$0.41^{+5.19}_{-4.07}$	$2456461.067141^{+0.000195}_{-0.000197}$
HAT-P-18 b	4.5	$15.48^{+0.45}_{-0.44}$	$88.5^{+0.3}_{-0.3}$	$1.93^{+0.02}_{-0.02}$	$0.41^{+5.07}_{-4.47}$	$2456483.099518^{+0.000215}_{-0.000215}$
TrES-2 b	3.6	$7.96^{+0.16}_{-0.15}$	$83.9^{+0.2}_{-0.2}$	$1.37^{+0.02}_{-0.02}$	$0.84^{+1.33}_{-1.34}$	$2456252.834601^{+0.000203}_{-0.000196}$
TrES-2 b	4.5	$8.20^{+0.25}_{-0.23}$	$84.2^{+0.3}_{-0.2}$	$1.40^{+0.02}_{-0.02}$	$0.83^{+2.09}_{-1.92}$	$2456257.775215^{+0.000268}_{-0.000267}$
WASP-4 b	3.6	$5.58^{+0.03}_{-0.04}$	$89.3^{+0.5}_{-0.7}$	$2.28^{+0.02}_{-0.02}$	$0.07^{+2.71}_{-4.14}$	$2456288.955465^{+0.000137}_{-0.000142}$
WASP-4 b	4.5	$5.46^{+0.05}_{-0.11}$	$88.7^{+0.9}_{-1.3}$	$2.34^{+0.03}_{-0.03}$	$0.12^{+4.80}_{-7.20}$	$2456292.969500^{+0.000208}_{-0.000212}$
XO-2 b	3.6	$8.17^{+0.09}_{-0.17}$	$88.9^{+0.7}_{-0.8}$	$1.07^{+0.01}_{-0.01}$	$0.15^{+5.81}_{-6.13}$	$2456295.370617^{+0.000139}_{-0.000140}$
XO-2 b	4.5	$7.77^{+0.22}_{-0.22}$	$87.6^{+0.7}_{-0.6}$	$1.07^{+0.01}_{-0.01}$	$0.33^{+5.43}_{-4.50}$	$2456292.754728^{+0.000198}_{-0.000191}$
GJ3470 b	3.6	$14.63^{+0.52}_{-0.50}$	$88.4^{+0.3}_{-0.3}$	$0.57^{+0.01}_{-0.01}$	$0.42^{+4.13}_{-3.73}$	$2456284.001794^{+0.000118}_{-0.000115}$
GJ3470 b	4.5	$14.41^{+0.65}_{-0.54}$	$88.4^{+0.4}_{-0.3}$	$0.61^{+0.01}_{-0.01}$	$0.41^{+5.23}_{-4.09}$	$2456294.011801^{+0.000151}_{-0.000150}$
WASP-21 b	3.6	$9.55^{+0.30}_{-0.28}$	$87.1^{+0.4}_{-0.4}$	$1.08^{+0.01}_{-0.01}$	$0.49^{+3.75}_{-3.34}$	$2456532.561048^{+0.000261}_{-0.000260}$
WASP-21 b	4.5	$9.61^{+0.40}_{-0.34}$	$87.1^{+0.5}_{-0.4}$	$1.14^{+0.02}_{-0.02}$	$0.48^{+5.28}_{-4.23}$	$2456536.882998^{+0.000308}_{-0.000322}$
WASP-31 b	3.6	$8.06^{+0.20}_{-0.18}$	$84.5^{+0.2}_{-0.2}$	$1.54^{+0.02}_{-0.02}$	$0.77^{+1.81}_{-1.66}$	$2456360.907660^{+0.000317}_{-0.000328}$
WASP-31 b	4.5	$8.86^{+0.34}_{-0.32}$	$85.2^{+0.3}_{-0.3}$	$1.50^{+0.03}_{-0.03}$	$0.74^{+2.86}_{-2.77}$	$2456371.125690^{+0.000407}_{-0.000412}$
WASP-1 b	3.6	$5.72^{+0.03}_{-0.05}$	$89.3^{+0.5}_{-0.8}$	$1.07^{+0.01}_{-0.01}$	$0.07^{+2.91}_{-4.60}$	$2456361.902274^{+0.000263}_{-0.000250}$
WASP-1 b	4.5	$5.41^{+0.17}_{-0.20}$	$86.5^{+1.2}_{-1.1}$	$1.09^{+0.02}_{-0.02}$	$0.33^{+6.58}_{-6.12}$	$2456371.982150^{+0.000354}_{-0.000364}$

Table 2.4: continued.

Planet	λ (μm)	a/R*	inc degrees	depth (R_p/R_s) ²	b (%)	T0 BJD_UTC
HAT-P-26 b	3.6	13.22 ^{+0.75} _{-0.94}	88.3 ^{+0.8} _{-0.7}	0.53 ^{+0.01} _{-0.01}	0.39 ^{+10.08} _{-9.85}	2456545.361384 ^{+0.000296} _{-0.000288}
HAT-P-26 b	4.5	13.92 ^{+0.16} _{-0.32}	89.5 ^{+0.3} _{-0.6}	0.55 ^{+0.01} _{-0.01}	0.11 ^{+4.33} _{-8.72}	2456405.622835 ^{+0.000356} _{-0.000364}
WASP-107 b	3.6	18.19 ^{+0.03} _{-0.04}	89.9 ^{+0.1} _{-0.1}	1.96 ^{+0.01} _{-0.01}	0.04 ^{+1.45} _{-2.26}	2457876.124941 ^{+0.000060} _{-0.000064}
WASP-107 b	4.5	18.09 ^{+0.05} _{-0.09}	89.8 ^{+0.1} _{-0.2}	2.06 ^{+0.01} _{-0.01}	0.06 ^{+2.54} _{-3.09}	2457870.403743 ^{+0.000081} _{-0.000077}
WASP-13 b	3.6	7.64 ^{+0.20} _{-0.19}	85.6 ^{+0.4} _{-0.3}	0.86 ^{+0.01} _{-0.01}	0.58 ^{+2.70} _{-2.50}	2456480.940869 ^{+0.000231} _{-0.000246}
WASP-13 b	4.5	7.78 ^{+0.27} _{-0.23}	85.7 ^{+0.4} _{-0.4}	0.87 ^{+0.01} _{-0.01}	0.59 ^{+3.43} _{-2.85}	2456315.526437 ^{+0.000293} _{-0.000303}
WASP-121 b	3.6	3.84 ^{+0.02} _{-0.03}	88.9 ^{+0.8} _{-1.1}	1.47 ^{+0.01} _{-0.01}	0.07 ^{+2.95} _{-4.10}	2457906.807311 ^{+0.000148} _{-0.000144}
WASP-121 b	4.5	3.82 ^{+0.02} _{-0.03}	89.0 ^{+0.8} _{-1.3}	1.49 ^{+0.01} _{-0.01}	0.07 ^{+3.02} _{-4.80}	2457910.632374 ^{+0.000183} _{-0.000171}
WASP-69 b	3.6	12.26 ^{+0.09} _{-0.08}	86.8 ^{+0.0} _{-0.0}	1.60 ^{+0.00} _{-0.00}	0.68 ^{+0.60} _{-0.58}	2457992.354188 ^{+0.000053} _{-0.000054}
WASP-69 b	4.5	12.30 ^{+0.11} _{-0.10}	86.8 ^{+0.1} _{-0.1}	1.67 ^{+0.01} _{-0.01}	0.68 ^{+0.77} _{-0.71}	2457996.222243 ^{+0.000066} _{-0.000069}
WASP-67 b	3.6	13.50 ^{+0.39} _{-0.33}	86.2 ^{+0.2} _{-0.2}	1.97 ^{+0.03} _{-0.03}	0.91 ^{+2.28} _{-2.72}	2457776.271136 ^{+0.000219} _{-0.000220}
WASP-67 b	4.5	13.90 ^{+0.31} _{-0.39}	86.3 ^{+0.1} _{-0.1}	1.92 ^{+0.03} _{-0.03}	0.89 ^{+1.84} _{-1.93}	2457979.305753 ^{+0.000282} _{-0.000276}
HATS-7 b	3.6	11.09 ^{+0.62} _{-1.07}	88.2 ^{+1.0} _{-1.3}	0.38 ^{+0.02} _{-0.02}	0.35 ^{+11.03} _{-14.14}	2457694.120917 ^{+0.000590} _{-0.000538}
HATS-7 b	4.5	10.80 ^{+0.48} _{-0.91}	88.4 ^{+1.1} _{-1.2}	0.40 ^{+0.03} _{-0.03}	0.30 ^{+12.05} _{-13.12}	2457697.305788 ^{+0.000797} _{-0.000795}
WASP-29 b	3.6	12.58 ^{+0.05} _{-0.11}	89.7 ^{+0.2} _{-0.4}	0.95 ^{+0.01} _{-0.01}	0.07 ^{+2.95} _{-4.91}	2457807.234478 ^{+0.000115} _{-0.000120}
WASP-29 b	4.5	12.53 ^{+0.05} _{-0.08}	89.7 ^{+0.2} _{-0.3}	0.93 ^{+0.01} _{-0.01}	0.06 ^{+2.59} _{-4.13}	2457826.848225 ^{+0.000150} _{-0.000149}
HAT-P-41 b	3.6	5.53 ^{+0.03} _{-0.06}	89.0 ^{+0.7} _{-0.9}	1.00 ^{+0.01} _{-0.01}	0.10 ^{+3.76} _{-4.92}	2457772.203860 ^{+0.000220} _{-0.000217}
HAT-P-41 b	4.5	5.55 ^{+0.03} _{-0.04}	89.3 ^{+0.5} _{-0.8}	1.09 ^{+0.01} _{-0.01}	0.07 ^{+2.78} _{-4.43}	2457788.367795 ^{+0.000274} _{-0.000263}
WASP-101 b	3.6	8.60 ^{+0.17} _{-0.16}	85.2 ^{+0.2} _{-0.2}	1.18 ^{+0.01} _{-0.01}	0.73 ^{+1.55} _{-1.54}	2457760.332526 ^{+0.000170} _{-0.000175}
WASP-101 b	4.5	8.51 ^{+0.19} _{-0.18}	85.0 ^{+0.2} _{-0.2}	1.14 ^{+0.01} _{-0.01}	0.74 ^{+1.72} _{-1.64}	2457771.089626 ^{+0.000225} _{-0.000227}
WASP-131 b	3.6	8.34 ^{+0.20} _{-0.19}	85.0 ^{+0.2} _{-0.2}	0.61 ^{+0.01} _{-0.01}	0.73 ^{+1.88} _{-1.80}	2457696.837080 ^{+0.000253} _{-0.000256}
WASP-131 b	4.5	8.41 ^{+0.28} _{-0.26}	85.0 ^{+0.3} _{-0.3}	0.61 ^{+0.01} _{-0.01}	0.73 ^{+2.63} _{-2.53}	2457909.718452 ^{+0.000336} _{-0.000332}
WASP-36 b	3.6	6.06 ^{+0.25} _{-0.22}	83.7 ^{+0.6} _{-0.5}	1.78 ^{+0.03} _{-0.03}	0.67 ^{+3.75} _{-3.19}	2457805.166629 ^{+0.000262} _{-0.000262}
WASP-36 b	4.5	6.19 ^{+0.44} _{-0.39}	84.4 ^{+1.1} _{-1.0}	1.82 ^{+0.03} _{-0.03}	0.60 ^{+6.70} _{-6.13}	2457975.813843 ^{+0.000346} _{-0.000353}
WASP-63 b	3.6	6.26 ^{+0.23} _{-0.21}	86.6 ^{+1.0} _{-0.8}	0.61 ^{+0.01} _{-0.01}	0.37 ^{+6.38} _{-5.07}	2457865.520635 ^{+0.000353} _{-0.000330}
WASP-63 b	4.5	6.52 ^{+0.16} _{-0.21}	87.7 ^{+1.1} _{-1.0}	0.55 ^{+0.01} _{-0.01}	0.26 ^{+7.01} _{-6.45}	2457922.436423 ^{+0.000470} _{-0.000461}
WASP-79 b	3.6	7.31 ^{+0.15} _{-0.14}	85.9 ^{+0.3} _{-0.3}	1.20 ^{+0.01} _{-0.01}	0.52 ^{+2.36} _{-2.05}	2457713.374126 ^{+0.000167} _{-0.000167}
WASP-79 b	4.5	7.12 ^{+0.15} _{-0.14}	85.6 ^{+0.3} _{-0.3}	1.17 ^{+0.01} _{-0.01}	0.55 ^{+2.29} _{-2.02}	2457720.699409 ^{+0.000215} _{-0.000213}
WASP-94 Ab	3.6	7.34 ^{+0.02} _{-0.04}	89.5 ^{+0.3} _{-0.5}	1.12 ^{+0.01} _{-0.01}	0.06 ^{+2.43} _{-3.56}	2457795.021530 ^{+0.000147} _{-0.000147}
WASP-94 Ab	4.5	7.34 ^{+0.02} _{-0.04}	89.5 ^{+0.4} _{-0.5}	1.13 ^{+0.01} _{-0.01}	0.07 ^{+2.62} _{-3.61}	2457972.780291 ^{+0.000187} _{-0.000180}
WASP-74 b	3.6	4.75 ^{+0.08} _{-0.07}	79.7 ^{+0.3} _{-0.2}	0.87 ^{+0.01} _{-0.01}	0.85 ^{+1.17} _{-1.01}	2457768.164558 ^{+0.000178} _{-0.000176}
WASP-74 b	4.5	5.13 ^{+0.11} _{-0.10}	80.8 ^{+0.3} _{-0.3}	0.86 ^{+0.01} _{-0.01}	0.82 ^{+1.44} _{-1.42}	2457770.304101 ^{+0.000228} _{-0.000230}
WASP-62 b	3.6	9.47 ^{+0.16} _{-0.16}	88.2 ^{+0.4} _{-0.3}	1.29 ^{+0.01} _{-0.01}	0.30 ^{+3.57} _{-3.02}	2457717.229937 ^{+0.000138} _{-0.000138}
WASP-62 b	4.5	9.32 ^{+0.20} _{-0.18}	87.9 ^{+0.4} _{-0.3}	1.20 ^{+0.01} _{-0.01}	0.35 ^{+3.88} _{-3.05}	2457730.466206 ^{+0.000165} _{-0.000167}
Kepler-45 b	3.6	-	-	3.37 ^{+0.13} _{-0.13}	-	-
Kepler-45 b	4.5	-	-	3.50 ^{+0.14} _{-0.14}	-	-

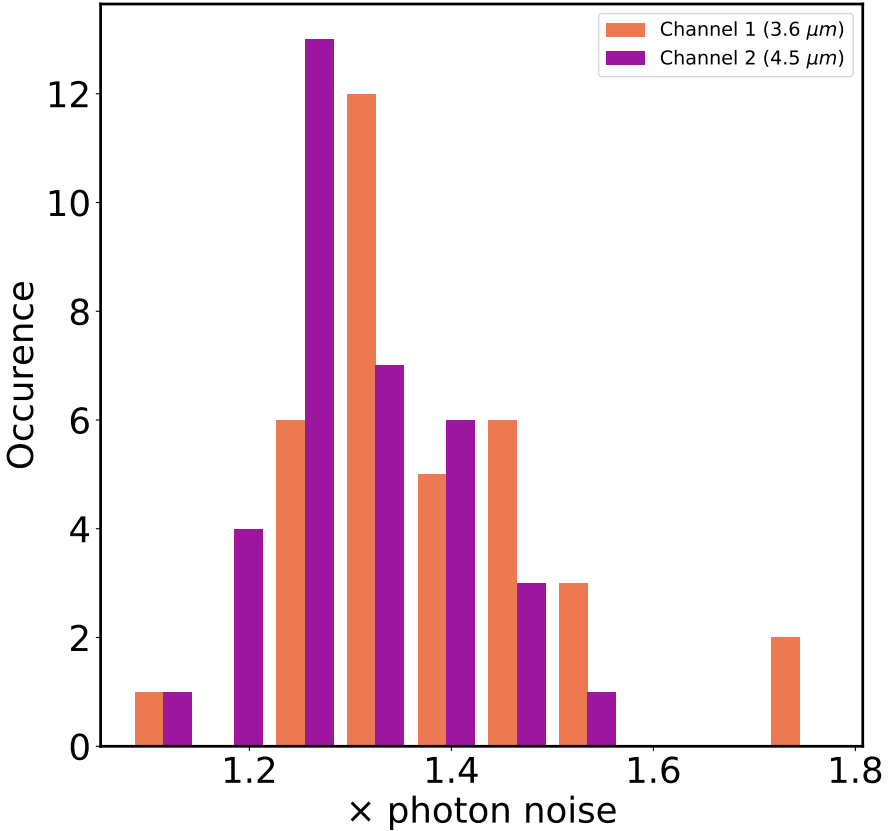


Fig. 2.5: Histogram showing the percentage above photon noise for each of the individual lightcurves. Channel 1 ($3.6 \mu\text{m}$) is displayed in orange and channel 2 ($4.5 \mu\text{m}$) in purple.

Table 2.4 summarizes the results of the MCMC analysis of the lightcurves, and it lists the final values and uncertainties for the transit depths, mid transit times and impact parameters from the final fits as well as the inclination and semi-major axis obtained from the first fits. We checked that the initial fits of the semi-major axis and the inclination are in agreement with the literature values before fixing them with Gaussian priors for the second fit. The survey as a whole was in statistical agreement with the literature values within $< 1\sigma$.

We also show the raw photometry with the best fit model for each visit in Appendix 2.A, and we show the corresponding RMS vs binsize plots in Appendix 2.A. Figure 2.13 shows the reduced, normalized and systematic corrected transit lightcurves for all planets in our

sample for both channel 1 and channel 2 with the best fit model resulting from the MCMC. We calculate the residuals, the χ^2 and the RMS of the residuals as sanity checks for each lightcurve (Table 2.10).

As mentioned in Section 2.3.1.3, before performing a complete MCMC analysis, we first check the fraction above photon noise and scale up the errors accordingly. Figure 2.5 displays a histogram of the fraction above photon noise for all analyzed lightcurves. The histograms have a median of 1.36 and 1.27 times photon noise for 3.6 μm and 4.5 μm respectively, which is typical for what has been achieved with *Spitzer* in the past (Ingalls et al. 2016).

2.4.1.2 Comparison to literature

Several of the planets from our survey have had their *Spitzer* lightcurves previously analyzed Sing et al. (e.g., 2016); Garhart et al. (e.g., 2020). We compare our results with those from Sing et al. (2016) and Garhart et al. (2020). Our measured transits are consistent within 3σ with those from the literature apart from a couple of outliers described below. Two of the largest outliers are the channel 2 transit depth of KELT-7b and the channel 1 transit depth of WASP-62b, both analyzed in Garhart et al. (2020) with PLD. We interpret the differences as due to the brightness of the host stars, and more specifically as due to the number of pixels selected for the pixel level decorrelation. These stars are bright and therefore 12 pixels are selected to model the systematics in Garhart et al. (2020) whereas we use 9 pixels uniformly for the entire survey (e.g., see Figure ??). We emphasize that these differences do not affect the general conclusion of the paper.

2.4.1.3 Transit depth ratio

We combine our results with transit measurements from the literature, which results in a survey of transit depths at 3.6 and 4.5 μm for 49 planets spanning a large range of equilibrium temperatures. We now compare all targets in our survey in a statistical manner. To do this, we opt to use a metric that is as free as possible from any assumptions - the normalized difference of the transit depths:

$$\bar{\Delta}_{tr} = \frac{(\delta_{ch2} - \delta_{ch1})}{\delta_{ch1}} \quad (2.3)$$

With this calculation, we tested for correlations with a number of other parameters: stellar parameters (Teff, logg, Fe/H, R_s), orbital parameters (semi-major axis (AU), eccentricity, inclination) and planetary parameters (T_{eq} , logg, R_p , M_p , scale height). We looked for correlations between using two statistical methods. First, we calculated the Pearson correlation coefficient (r) and its associated chance probability (p). Then, we fit a straight line using an orthogonal distance regression (ODR) to account for the errors on both the abscissa and ordinate values Boggs et al. (1989) and look at the resulting residual variance of the fits.

Table 2.5: Correlations between parameters and the transit depth ratio. We show the Pearson correlation coefficient (r), the associated chance probability (p) and the residual variance from an ODR linear fit to the data.

Parameter	r	p	Res Var
T_{eq} (a=0)	-0.35	0.01	7.23
T_{eff}	-0.34	0.02	7.14
Stellar log(g)	0.13	0.36	6.98
[Fe/H]	-0.21	0.15	4.48
R_p	-0.26	0.07	8.11
Inclination	0.20	0.18	7.03
a (AU)	0.07	0.63	8.46
Planetary log(g)	0.01	0.92	8.47
M_p (M_J)	0.09	0.56	8.78
H (km)	-0.17	0.25	8.50
R_s (R_\odot)	-0.40	0.00	7.06
Radius Anomaly	-0.25	0.14	6.86

2.4.1.4 Searching for trends in the difference of transit depths

We analyse our *Spitzer* survey by looking at the normalized difference in the transit depths. Our normalized transit depth difference metric has the benefit that it does not include any additional assumptions on the composition of the atmosphere. Several studies look at the number of scale heights crossed at different wavelengths, including the strength of the water feature in the HST/ WFC3 bandpass (e.g., Sing et al. 2016). Including the scale height requires assuming the mean molecular weight, which includes errors from the surface gravity and equilibrium temperature. Furthermore, our metric is also independent of the stellar radius - unlike the difference in transit depths ($\delta_{ch2} - \delta_{ch1}$). Ultimately, this metric is a proxy for the ratio of the optical depths at these two wavelengths. We expect that the strength and magnitude of this metric can be used to test how the dominant expected atmospheric opacities change with the equilibrium temperature of the planets, see Section 2.5.1.

We search for any correlations that could be present between the calculated normalized transit depth difference and the physical parameters of the planetary systems that we are exploring. Table 2.5 summarizes the correlations for each of the parameters. The three parameters with the strongest Pearson correlation coefficients and the lowest chance probabilities are T_{eq} , T_{eff} and R_s . Both T_{eff} and R_s are incidentally included in the calculation of the equilibrium temperature, T_{eq} (in our case with zero albedo and full redistribution). We also observe that the weakest correlations are with the planetary mass, planetary radius, and semi-major axis. This is not surprising since our sample is highly biased towards hot Jupiters with a relatively small range of radii and masses, and with similarly close-in orbits. This means that the span of these parameters is small and therefore the uncertainties will be large and the correlations will not be obvious.

2.4.1.5 Transit depth versus equilibrium temperature

In Figure 2.6 (left panel), we plot the normalized transit depth difference ($(\delta_{ch2} - \delta_{ch1})/\delta_{ch1}$) against the equilibrium temperature for all planets in our sample. This plot contains 49 planets with masses $0.02 - 10.2 M_{Jup}$, radii $0.24 - 1.9 R_{Jup}$ and equilibrium temperatures $550 - 2690$ K. The color scale on the data points shows the scale height (H) of each planet, ($H = kT_{eq}/\mu g$) calculated assuming a hydrogen dominated atmosphere with mean molecular weight (μ) of 2.3, equilibrium temperature (T_{eq}) calculated with zero albedo and zero redistribution and planetary surface gravity (g) from the literature.

In Table 2.6 we show the weighted mean of the normalized transit depth difference and the corresponding number of scale heights for each temperature bin in Figure 2.6. We also calculate the weighted mean of the absolute value of the normalized transit depth difference and the number of scale heights.

We find that the weighted mean of the absolute value normalized transit depth difference and the number of scale heights to be significant to 8.0σ and 7.5σ respectively. This means that we are statistically detecting the atmosphere with a very high significance.

All 9 of the cool (<1000 K) planets lie on the positive side of the transit depth metric with a weighted mean transit depth of 0.029 ± 0.007 , 4.0σ from zero (gray assumption). We also find that the weighted mean transit depth difference and the number of scale heights of the 1000-2000 K planets and the >2000 K planets are not significant ($<3\sigma$). We therefore treat all planets >1000 K as one sample. These 36 hot planets have an absolute value weighted mean 0.3σ from zero (cloudy) assumption. In total, 14 of these planets are consistent with the cloudy models (zero) within 1σ . However, since these hot planets span both positive and negative values of the transit depth difference, it is unsurprising that their weighted mean transit depth is only marginally deviating from zero. The weighted mean of the absolute value of the difference in the transit depths for the hot planets is 0.025 ± 0.004 (5.9σ) and is more scattered than the cooler planets.

2.4.2 Results from the 1-D grid of model transmission spectra

2.4.2.1 General trends observed in the grids of models

In Figure 2.7 we show a selection of tracks from the complete grid of models and in Figure 2.8 we show each interpolated grid as a shaded region in comparison with the survey data. The fiducial model grid (1x solar and equilibrium chemistry, no vertical mixing $K_{zz} = 0$), plotted in Figure 2.7 shows the effect of increasing equilibrium temperatures on the transit depths, at ~ 900 K the model grid switches from a negative transit depth difference to a positive transit depth difference.

The interpolated grid shows a spread in the expected difference in the two transit depths. An important aspect of the model grid, which largely influences the spread is the surface gravity. Lower surface gravities result in larger scale heights and lead to a larger signal in the difference of the two *Spitzer*/IRAC transit depths. The surface gravity also changes the

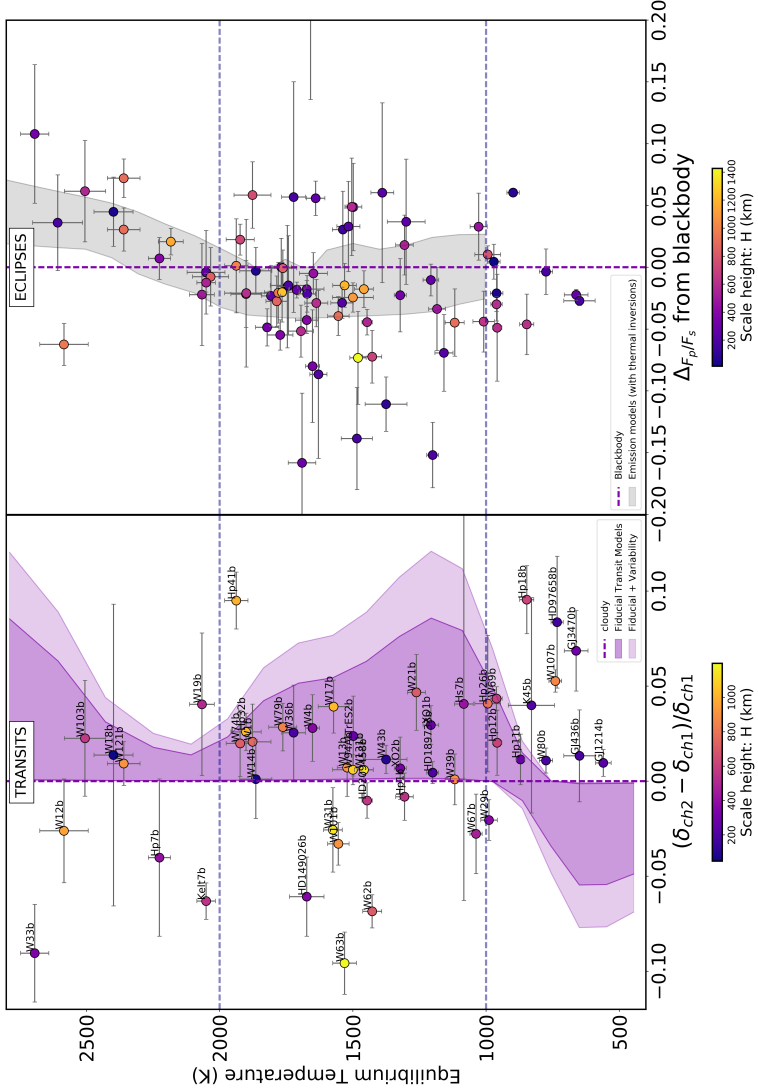


Fig. 2.6: Left panel: difference in transit depths between $4.5 \mu\text{m}$ and $3.6 \mu\text{m}$ normalized to the transit depth at $3.6 \mu\text{m}$ plotted against equilibrium temperature, $1-\sigma$ uncertainties are shown in gray, color bar depicts the scale height in km. The shaded area on the left panel shows our grid of solar composition cloud-free equilibrium chemistry models, the extended lighter region is corrected for stellar variability. The dashed purple vertical line at zero is where planets with low pressure gray clouds would lie. Right panel: the deviation from the blackbody in emission against the equilibrium temperature, presented in Baxter et al. (2020). Color scale shows the scale height in km and the shaded region shows grid of models containing temperature inversions.

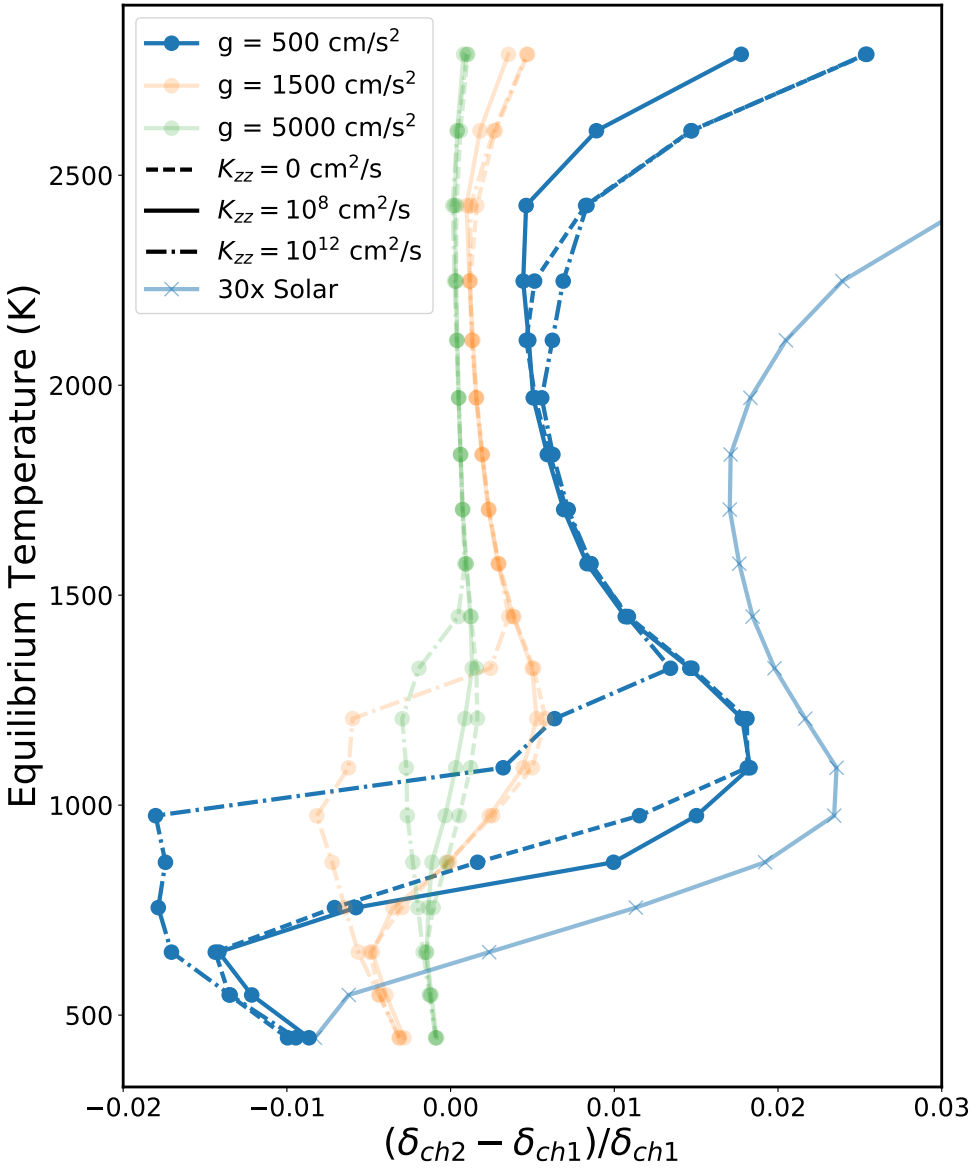


Fig. 2.7: Normalized *Spitzer* transit depth difference as a function of the equilibrium temperature for a selection of the grid tracks created with our atmospheric model framework described in Sections 2.3.2.3 and 2.3.2.4. We show a selection of grids with 1x solar composition and $R_p = 2R_J$. Different colors show different surface gravities: blue is $g = 500 \text{ cm/s}^2$, orange is $g = 1500 \text{ cm/s}^2$ and green is $g = 5000 \text{ cm/s}^2$. Different line styles show the effect of vertical mixing: solid line shows equilibrium chemistry, dashed is $K_{zz} = 10^8 \text{ cm}^2/\text{s}$ and dot-dashed is $K_{zz} = 10^{12} \text{ cm}^2/\text{s}$. Lighter blue line with 'x' markers shows a 30x solar track with $R_p = 2R_J$, $g = 500 \text{ cm/s}^2$ and $K_{zz} = 0 \text{ cm}^2/\text{s}$.

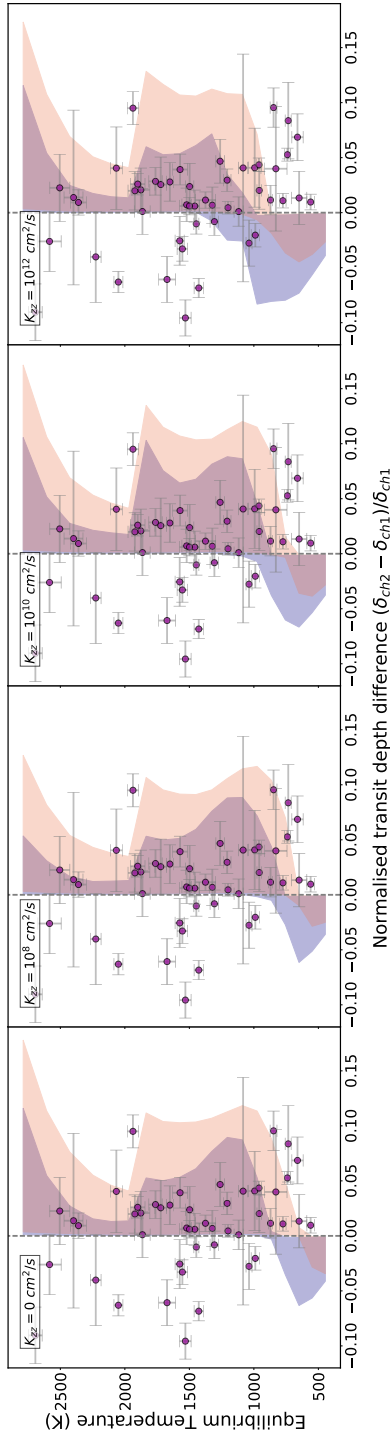


Fig. 2.8: Normalized *Spitzer* transit depth difference as a function of the equilibrium temperature for the complete grids of transmission models created with our atmospheric model framework described in Sections 2.3.2.3 and 2.3.2.4. At each temperature we show the models where the surface gravity is representative of our survey, i.e. at $T_{eq} > 1800 \text{ K}$ we only plot $g = 1500$ and 5000 cm/s^2 . Panels from left to right show equilibrium chemistry (no vertical mixing), $K_{zz} = 10^8$, $K_{zz} = 10^{10}$ and $K_{zz} = 10^{12} \text{ cm}^2/\text{s}$. Blue translucent shaded region shows the $1\times$ solar composition and orange translucent shaded region shows the $30\times$ solar composition overlap in purple. Gray dashed line represents a gray opacity source showing no spectral features. Planets from our sample are overplotted in purple circles with their 1σ errorbars.

Table 2.6: Weighted means of the normalized transit depth difference ($(\delta_{ch2} - \delta_{ch1})/\delta_{ch1}$), the absolute value of the normalized transit depth difference, the corresponding number of scale heights (NH), and its absolute value. This is shown for the different temperature ranges (<1000 K, 1000-2000 K, and >2000 K) presented in Figure 2.6. The intermediate columns labeled $N\sigma$ indicate the significance of the previous weighted mean and weighted error.

Planet Selection	$(\delta_{ch2} - \delta_{ch1})/\delta_{ch1}$	$N\sigma$	$ (\delta_{ch2} - \delta_{ch1})/\delta_{ch1} $	$N\sigma$
All planets	0.010 ± 0.005	1.9σ	0.028 ± 0.003	8.0σ
<1000 K	0.029 ± 0.007	4.0σ	0.032 ± 0.006	5.1σ
1000-2000 K	0.002 ± 0.006	0.3σ	0.023 ± 0.005	5.0σ
>2000 K	-0.032 ± 0.015	2.2σ	0.042 ± 0.010	4.1σ

Planet Selection	NH	$N\sigma$	$ NH $	$N\sigma$
All planets	0.2201 ± 0.0935	2.4σ	0.5032 ± 0.0669	7.5σ
<1000 K	0.4515 ± 0.1179	3.8σ	0.4900 ± 0.1043	4.7σ
1000-2000 K	0.0130 ± 0.1343	0.1σ	0.4840 ± 0.0968	5.0σ
>2000 K	-0.5907 ± 0.4271	1.4σ	0.9239 ± 0.3322	2.8σ

shape of the TP profile as seen in Figure 2.4. Figure 2.7 shows the effect of different surface gravities. We designed the model grid to span the parameters of the survey, notably with surface gravities of $g = 500, 1000, 1500$, and 5000 cm/s^2 . However, the for ultra-hot model planets with low surface gravity of $g = 500 \text{ cm/s}^2$ the upper atmosphere exceeds the Hill radius. These models do not represent any planets in our survey since the hottest planets in our survey tend to have larger surface gravity ($g \sim 1000 \text{ cm/s}^2$), we therefore discard these model planets from Figure 2.8.

The effect of vertical mixing can be seen in Figure 2.7. A large amount of mixing results in the transition between CH₄ to CO occurring at higher temperatures. Increasing the metallicity to 30x solar has the effect of lowering the temperature of the transition between negative and positive transit depth difference. Increased metallicity also results in a stronger positive signal for the hotter planets >1000 K.

2.4.2.2 Statistical comparison of planet atmospheres with model grid

We compare the data with the grids of models quantitatively by calculating the average number of standard deviations (based on the 1σ uncertainties) between each of the planets and their corresponding model grid point with the closest input parameters (T_{eq} , $\log(g_p)$, R_s and R_p). We then compute a weighted average for the whole grid, such that we can express the statistical significance of each grid with one number. We split this comparison into different temperature regimes based on the expected carbon chemistry. We compare the data to a transit depth difference of 0, representing a gray cloud opacity. Additionally, we also compare the data with the grids of models qualitatively by interpolating a shaded region between grid points, allowing us to visually compare the models with the *Spitzer*/IRAC transit depth difference e.g., see Figure 2.6.

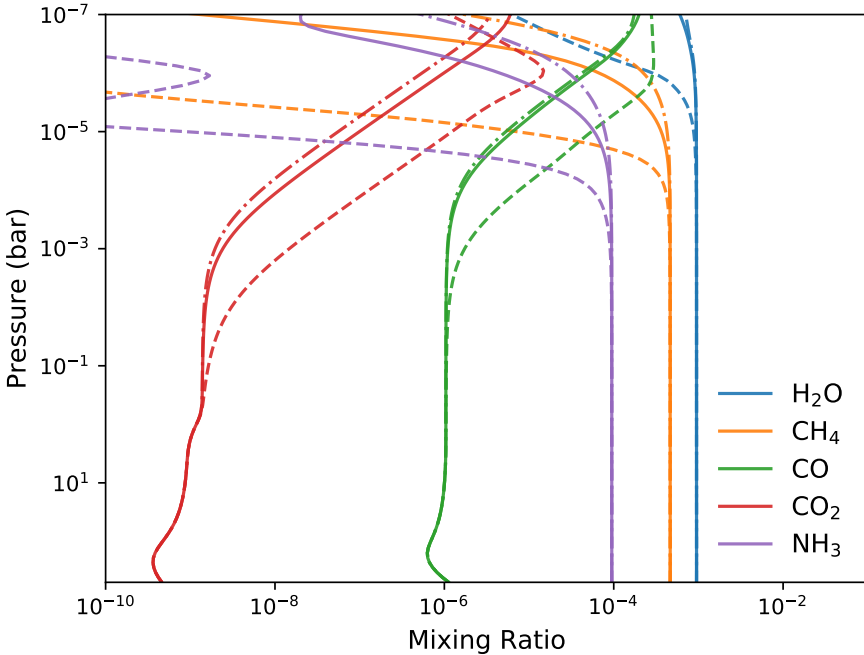


Fig. 2.9: Abundance mixing ratios at different pressures for the main species in the *Spitzer* bandpasses. The solid line shows the nominal situation ($a = 0.035$ AU, $T_{\text{eff}} = 3750$ K) dashed line shows $a = 0.06$ AU, $T_{\text{eff}} = 4250$ K, and the dashed-dotted line shows $a = 0.017$ AU, $T_{\text{eff}} = 4250$ K.

In Section 2.3.2.1 we fix the orbital distance to 0.035 AU in our model grid creation. We do this because in our sample of planets the equilibrium temperature has a much larger correlation with the stellar effective temperature than with the semi-major axis. The range of semi-major axes in our sample spans ~ 0.017 to ~ 0.06 AU. We explore how much our choice of model parameterization (fixing the orbital distance to 0.035 AU) affects our results with the following two tests. We start by creating models with the minimum and maximum orbital distance of our sample, 0.017 and 0.06 AU.

In the first test, we match the equilibrium temperature by changing the effective temperature of the star. For a 650 K planet, an orbital distance of 0.017 AU corresponds to a stellar effective temperature of 3250 K and 0.06 AU corresponds to 4250 K. Figure 2.9 shows the effects on chemistry, where the star with higher T_{eff} provides greater flux even at larger orbit and leads to more photolysis. Nevertheless, it mainly impacts the main species at the lower pressures ($P < 1$ mbar). We find that the resulting difference in our transit depth metric for a planet placed at the minimum and maximum orbital distance is 0.0025. This is a factor of 10 smaller than the mean errorbar in our sample, so we do not expect this to change our results.

In the second test, we match the equilibrium temperature by changing the stellar radius. This time the resulting difference in our transit depth metric is 3.2e-6, which is three orders of magnitude smaller than the mean errorbar of our sample. Since the changes in the models are so small compared to the size of the uncertainties, we do not expect that the different orbital distances are the reason behind the scatter seen in Figure 2.6.

Figure 2.10 displays the results of the statistical comparison of each model grid with the planets in our survey. Each planet transit depth measurement is compared to the corresponding transmission model with the closest parameters (T_{eq} , $\log(g_p)$, R_s and R_p). We calculate the statistical significance for a set of planets, which is quantified by the average number of sigmas, for all eight grids of models. In the two panels of Figure 2.10 we show the results of the cool planets ($T_{\text{eq}} < 1000$ K), followed by the hot planets ($T_{\text{eq}} > 1000$ K). We find that the hot planets are best fit by 1x solar and high vertical mixing, $K_{zz} = 10^{12}$ cm²/s. We rule out high metallicity models for these planets to $\sim 3\sigma$ confidence.

On the other hand, we find that the cool planets are best fit by 30x solar and a low amount of vertical mixing ($K_{zz} = 10^8$ or $K_{zz} = 0$ cm²/s). We find that the 1x solar composition and high amounts of vertical mixing ($K_{zz} = 10^{12}$ cm²/s) are ruled out with $> 3\sigma$ confidence for these cool planets.

We also find that the results of comparing the model grids to the full sample are that the full sample mimics the cool sample. This is because the different grids of models are divergent at the cool temperatures, so the results from the cool temperatures drive the statistical results for the full grid.

2.5 Discussion

2.5.1 Expected opacities at 3.6 and 4.5 μm

The features we see in the transmission spectra are a result of the underlying chemistry at the pressures probed by our observations. Figure 2.3 shows the abundance weighted opacities for the dominant opacity sources in the grid of models at the wavelengths of the *Spitzer* bandpasses. The dominating absorbing molecules in the *Spitzer* bandpasses are CH₄ and H₂O at 3.6 μm and CO, H₂O and CO₂ (for high metallicities) at 4.5 μm . Since H₂O opacity is about equally present in both IRAC bandpasses, the two *Spitzer* transit depths can be used to understand the relative abundance of CO and CH₄. The following summary chemical reaction plays an important role in determining the dominating carbon-bearing species in an atmosphere (e.g., Visscher et al. 2010; Moses et al. 2011; Visscher & Moses 2011; Ebbing & Gammon 2016):



At temperatures higher than ~ 1100 K the forward reaction is favored (CO creation), for nominal pressures of ~ 1 bar, whereas at temperatures lower than ~ 1100 K the reverse reaction is favored (CH₄ creation) (e.g. Madhusudhan 2012; Mollière et al. 2015; Molaverdikhani

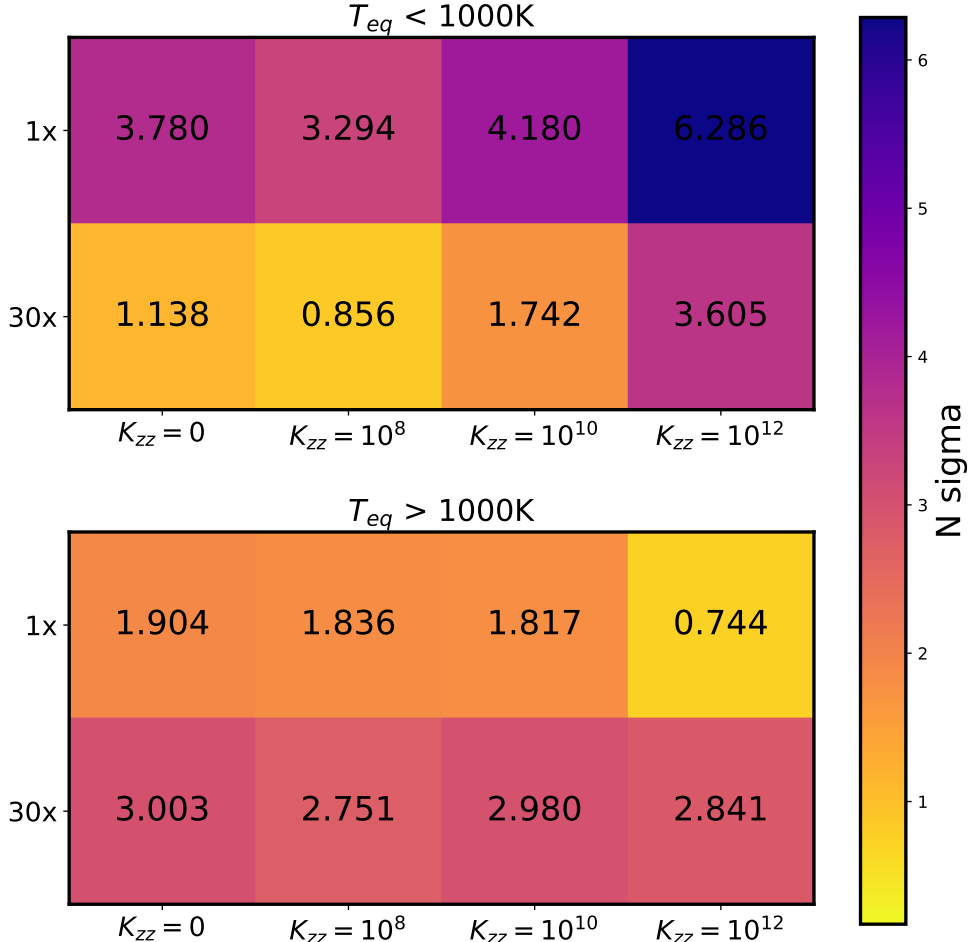


Fig. 2.10: Plot of the number of sigmas the data is from each model grid. We do this for eight grids and three sets/subsets of planets. The eight model grids are composed of two different metallicities (1x and 30x Solar) and four different vertical mixing scenarios ($K_{zz} = 0, 10^8, 10^{10}$ and 10^{12} cm²/s). The color bar represents the average number of sigmas each model grid is from the set of data, a lower $N \sigma$ (blue) means a better fit. The top panel shows the results for the cool planets ($T_{eq} < 1000$ K) and the bottom panel shows the hot planets ($T_{eq} > 1000$ K). The number of sigmas are written on each cell.

et al. 2019). The gas transition between CH₄ and CO is plotted as a function of temperature on Figure 2.4, it shows where the abundance of CH₄ and CO are the same Visscher (2012). A temperature pressure profile crossing this line results in CO or CH₄ becoming the dominant absorber.

We thus expect that the atmospheres of planets in thermochemical equilibrium with temperatures above ~ 1100 K have CO as the dominating carbon bearing species and the cooler atmospheres have CH₄. The result of this on the normalized difference of the transit depths

(Figure 2.6) is that the CH₄ planets would have a negative difference whereas CO planets have a positive difference. The transition from negative to positive transit depth differences seen in Figures 2.6, 2.7 and 2.8 shows the changing carbon chemistry (CH₄ to CO) with increasing equilibrium temperature. We find that the equilibrium temperature of the transition in the fiducial model grid (thermochemical equilibrium, 1x solar) is slightly lower than 1100 K presented in previous work (e.g., Madhusudhan 2012). We emphasize that the transition from CH₄ to CO depends on the temperature and pressure of the layer being probed with *Spitzer*/IRAC transmission photometry, and that this temperature is not necessarily at the planet's equilibrium temperature.

2.5.2 Discussion on Transit Survey

2.5.2.1 Comparing transit depths to fiducial model grid

Figure 2.6 shows the normalized difference of the two *Spitzer* transit depths with the fiducial grid of models. The fiducial models are calculated with opacities from thermochemical equilibrium and 1x solar composition. The sample of planets with temperatures hotter than 1000 K follow the fiducial models, however, we see that the cool planets appear to deviate from this model grid. Since we see that different chemical and physical processes are likely occurring at these different equilibrium temperatures we proceed by splitting Figure 2.6 into three temperature regimes based on the expected chemistry from our model grid: the cooler, methane planets (<1000 K), the hotter carbon monoxide hot planets (1000 K - 2000 K) and the few ultra-hot planets where molecular dissociation can occur ($T_{eq}>2000$ K).

There are 13 planets in our survey with $T_{eq} < 1000$ K. Our fiducial (1x solar and no vertical mixing) models demonstrate that the predicted carbon-bearing species for planets in this temperature regime is methane, which results in the models occupying the negative side of Figure 2.6. However, we find that the data show the opposite trend, all planets lie on the right side of Figure 2.6. We find that this equilibrium chemistry grid is ruled out at 3.8σ , which is statistically capturing the dearth of methane in the sample of coolest planets, see Section 2.4.2.2. This supports previous individual studies of cool gas giants with HST/WFC3 and it indicates that there are more complex physical processes happening not included in the fiducial models.

There are 28 planets in the mid-temperate/hot range (1000-2000 K) and 8 planets in the hot/ultra-hot range (>2000 K) of Figure 2.6. Of these 36 hot/ultra-hot planets, 14 of them are consistent to less than 1σ with the cloud-free solar composition model grid. In Section 2.4.2.2 we show that these planets are consistent with the fiducial model grid to 2σ . Additionally, we find that there is only 1 of these 36 hot/ultra-hot planets with a stronger positive signal than the fiducial model grid, meaning that a model grid with a higher CO abundance (e.g. 30x solar) is not required to explain our sample of observations. 30x solar is ruled out with 3σ confidence for the hotter planets.

There are several effects not included in the fiducial grid of models which contribute to

the statistical deviation. For example, we assume solar metallicity, no vertical mixing and cloud-free atmospheres. We compare the survey of planets to the model grids in a statistical manner and discuss the effects of each of these in detail below.

2.5.2.2 Effect of metallicity in hot Jupiter atmospheric spectra

The metallicity of a planet contributes to the atmospheric molecular abundances. Our fiducial model grid assumes 1x solar composition and solar metallicity. Increasing the metallicity would increase the amount of CO in the atmosphere (e.g., Venot et al. 2014). Figure 2.7 shows a 30x solar track and Figure 2.8 shows the whole interpolated grid (with no vertical mixing, see the first panel). Increasing the metallicity to 30x solar results in a lower temperature at which the model atmospheres transition between CH₄ and CO. This transition occurs at a temperature of around 600 K, much lower than the transition of 900 K for the fiducial grid.

In Section 2.4.2.2 we show that the cool planets lack the methane signature and are better fit with 30x solar composition models, with a significance of $>2.5\sigma$. This is the case for the lower values of vertical mixing ($K_{zz} = 0, 10^8$ and 10^{10} cm²/s), discussed in more detail in Section 2.5.2.3. These cool planets are also generally lower mass planets because of the detection biases for these systems, see Figure 2.1. Lower mass planets typically have higher metallicities Fortney et al. (2013); Welbanks et al. (2019). Therefore, a higher average metallicity in the 13 planets with temperatures <1000 K likely explains the lack of methane. Our findings support the predicted high metal enrichment in cool gas giants presented in Espinoza et al. (2017). They predict C/O ratios for a sample of 50 gas giants with $T_{eq} < 1000$ K, 6 of our 13 planets in this temperature range are also in their sample. Furthermore, our finding of high metallicity for these coolest warm giant planets supports the individual high metallicity measurements of several planets in the literature: HAT-P-12b (Line et al. 2013a), HAT-P-26b (Wakeford et al. 2017), GJ 436b (Morley et al. 2017) and HAT-P-11b (Mansfield et al. 2018b). All of these exoplanet atmospheres are found to have super-solar metallicities, except for GJ 3470b which is suggested to have a relatively low atmospheric metallicity for its planet mass (Benneke et al. 2019).

On the other hand, the planets with equilibrium temperatures >1000 K are consistent with the 1x solar composition models to less than 2σ for all values of K_{zz} . The higher metallicity grid is less favored for these planets (2.6σ deviation). Similar to the high abundance of CO at cooler temperatures, the high metallicity model grid shows stronger CO features throughout the entire temperature range, which is not favored by the planets in our survey. We do not find it necessary to statistically invoke high metallicity to explain the near-infrared spectral features of hot Jupiters.

Figure 2.3 shows the opacities for the 1x and 30x metallicity used in the creation of our model grids. In practice, differences in the opacities for the two cases would also affect the temperature pressure profile, however, in our analysis we do not compute the temperature pressure profiles self consistently. Nevertheless, we can predict what effect this might have. Higher metallicities would result in hotter temperatures in our TP profiles, which would in

turn result in a larger CO/CH₄ ratio. This means that we could explain the dearth of methane with less extreme enhancements in the metallicity of the models.

2.5.2.3 Vertical mixing and non-equilibrium effects

Another aspect not included in our fiducial model grid is the presence of non-equilibrium effects such as photochemistry, advection, convection, and turbulence in the atmosphere. To capture some of these non-equilibrium atmospheric processes, we introduce an eddy diffusion coefficient, K_{zz} , into our modeling (see Section 2.3.2.3). Theory suggests that for hot Jupiters K_{zz} can range from 10^8 to 10^{12} cm²/s based on the estimation from the mean vertical wind in GCMs (Moses et al. 2011). We create four different grids of models spanning the range of eddy diffusion coefficients: equilibrium chemistry, $K_{zz} = 10^8$, $K_{zz} = 10^{10}$ and $K_{zz} = 10^{12}$ cm²/s.

The model incorporating different K_{zz} show that the transition between CH₄ and CO being the dominating carbon bearer in these atmospheres occurs at higher temperatures for larger values of K_{zz} . This is because with larger values of K_{zz} , the mixing penetrates deeper into the atmosphere and can therefore dredge up methane to the observable pressures of hotter planets where methane is not expected. The models on Figure 2.8 (right panel) demonstrate that $K_{zz} = 10^{12}$ cm²/s can dredge up CH₄ for planets up to 1300 K.

For the cool planet data ($T < 1000$ K), we find that the models containing low amounts of vertical mixing are significantly favored over high vertical mixing for both metallicities. For 30x solar metallicity, the low mixing $K_{zz} = 10^8$ cm²/s fits marginally better than equilibrium chemistry ($K_{zz} = 0$) and is a 3σ better fit than the high vertical mixing ($K_{zz} = 10^{12}$ cm²/s). On the other hand, for the hot planets we find that $K_{zz} = 10^{12}$ cm²/s is favored over the lower mixing or no mixing for both the 1x and 30x solar metallicities.

Komacek et al. (2019) showed that for tidally locked hot Jupiters, vertical mixing increases with increasing equilibrium temperature and rotation rates: starting at $K_{zz} = 10^7 - 10^8$ cm²/s for the coolest (500 K) planets and going to $K_{zz} = 10^{11} - 10^{12}$ cm²/s for the hottest (1500-3000 K). We find that the cool planets support these results, with a vertical mixing of $K_{zz} = 10^8$ cm²/s favored by the data. However, the hotter planets seem to suggest a lower level of mixing than theory predicts, our models with $K_{zz} = 10^{10}$ cm²/s are marginally supported over the equilibrium and $K_{zz} = 10^8$ cm²/s grids, which is lower than the theoretical maximum of $K_{zz} = 10^{12}$ cm²/s. These findings are in line with the findings of Miles et al. (2020) for non-equilibrium processes in brown dwarfs. They found warmer brown dwarfs showed lower mixing than theory predicts, yet the cooler objects were close to the theoretical maximum.

Additionally, our non-equilibrium chemistry models include the effects of photochemical reactions. For hot planets ($T_{eq} > 1000$ K), CO is only dissociated in the upper atmosphere due to its strong bond, which has negligible influence on the *Spitzer* bandpasses. For cooler planets ($T_{eq} \leq 1000$ K), CH₄ is dissociated by atomic hydrogen produced by photolysis. This destruction of CH₄ can penetrate down to around 0.1 mbar with lower mixing ($K_{zz} = 10^8$ cm²/s).

Yet the competing effects of mixing can overtake and efficiently transport methane to the upper atmosphere. HCN is also produced by photochemistry and can reach abundances close to CH₄ in some cases. Nevertheless, HCN absorbs similarly at the two IRAC wavelengths, so we do not expect that it would have significant effects on the normalized transit depth difference.

Since vertical mixing is responsible for dredging CH₄ to the hotter planets, and not CO in the cooler planets, we conclude that the dearth of methane is not due to strong atmospheric mixing, it is likely due to the higher metallicity of these atmospheres. Another possible factor affecting the lack of methane signatures in the cool planets could be the amount of interior heating, see Fortney et al. (e.g., 2020). We find that several of the coolest planets are eccentric (see Table 2.7, which could cause some tidal heating. Our temperature pressure profile calculation assumes an interior heating of $T_{\text{int}} = 150$ K. However, substantial interior heating, $T_{\text{int}} > 300$ K, could result in pushing the deeper layers of these atmospheric TP profiles towards the CO regime (Morley et al. 2017; Benneke et al. 2019; Thorngren et al. 2019, 2020). If the interior is more CO dominated, then vertical mixing could dredge up CO in the cooler planets, resulting in a dearth of methane (e.g., Moses et al. 2013a). We did not test this as it is beyond the scope of our paper.

2.5.2.4 Effects of clouds on the cool and hot Jupiter atmospheric spectra

Clouds are ubiquitous in transiting exoplanet atmospheres (Sing et al. 2016). There are several mechanisms responsible for producing homogeneous and inhomogeneous clouds on tidally locked planets (Parmentier et al. 2013, 2021; Helling et al. 2016, 2019a,b). An example can be found in Line & Parmentier (2016) in which HD 189733b and HAT-P-11b can be explained by patchy clouds without the need to invoke global clouds or high mean molecular weight atmospheres.

Hazes are expected to be prominent in the cooler atmospheres. Morley et al. (2015) predicted that a transition between haze-free and hazy atmospheres will occur at 800–1100 K, implying that any planet below this temperature might show no molecular features. Gao et al. (2020) showed that the amplitude of the HST/WFC3 water feature on planets with temperatures <900 K is such that these atmospheres become dominated by haze formation. However, (Kawashima & Ikoma 2019) predict that molecular features such as CO and CH₄ are still detectable in the infrared for their sample of warm Jupiters (<1000 K) with hazy atmospheres.

Furthermore, if all planets with temperatures <1000 K in our survey were characterized by a gray cloud opacity, then we would expect the the transit depth difference to be evenly distributed around zero in Figure 2.6. However, these 13 planets have a mean transit depth of 0.026 ± 0.008 . This rules out a gray cloud (flat spectrum) at 4.0σ confidence for all planets. Suggesting that these planets cannot be characterized by a gray cloud opacity, and that there is a molecular feature.

Molaverdikhani et al. (2020) suggested that clouds could play a role in the heating of the

atmosphere, resulting in a lack of CH₄. However, such clouds would also dampen the CO feature significantly. This effect could be the reason for the few planets consistent with zero, but we do not expect that this effect explains the 4.0 σ detection for the sample of cool planets (<1000 K).

There are 14 planets with equilibrium temperature >1000 K that have transit depth differences consistent with zero (flat spectrum). The weighted mean transit depth difference of all these planets is -0.002 ± 0.006 , only 0.3 σ . However, the weighted mean of the absolute value of the transit depth difference is 0.025 ± 0.004 (5.9 σ).

Based on the prediction by Morley et al. (2015) we would not expect to have hazes at these temperatures. However, Gao et al. (2020) show that the HST water feature is dampened when compared to a cloud-free atmosphere, and they find the data is better fit by their models containing silicate clouds. Furthermore, (Line & Parmentier 2016) suggested that patchy cloud cover can mimic the spectral features of a high mean molecular weight atmosphere, resulting in a flatter transmission spectrum. Additionally, due to the varying temperature across the day and night sides of tidally locked highly irradiated hot Jupiters, clouds and hazes may behave differently at the east and west terminators of the planet (Kempton et al. 2017a). Such that photochemically generated hazes formed on the day side can be blown over to the nightside and dampen the transmission features. We therefore expect that clouds do play a role in dampening the spectral features in some of our planets, namely, those in the temperature region predicted to be cloudy by Gao et al. (2020) (>1000 K).

However, since there is still a strong signal in the absolute value of the transit depths of these planets (5.9 σ), there is indication that the population cannot be captured by a completely featureless model. Mie scattering theory results in a drop off in cloud opacity at 2-3 μm (e.g., Benneke et al. 2019), since we are detecting molecular features between 3-5 μm it may be that any possible cloud particles could exhibit Mie scattering in this regime. Including Mie scattering as a cloud prescription in our transmission spectrum forward modeling is beyond the scope of this paper. However, since the cloud opacity would be lower at 4.5 μm than it is at 3.6 μm , it would result in a negative transit depth metric, similar to the expected methane signature. However, we do not find planets with a negative transit depth metric, and hence find no evidence for Mie scattering clouds.

2.5.2.5 Outliers and the effect of nightsides

According to our grids of models, we do not expect any of the planets above 1400 K to have CH₄ as the dominating carbon bearing species in any of the metallicity or mixing scenarios. However, there are two hot planets which are significantly on the left: HD149026b and WASP-33b (2.9 σ and 3.5 σ from zero respectively). HD 149026b has previously been discrepant from models, for example, Zhang et al. (2018) found that they needed 30x solar metallicity to reproduce the *Spitzer* 3.6 and 4.5 μm phase curves. Furthermore, the biggest outlier, WASP-33 b, is a planet that is orbiting a δ Scuti star, with pulsating periods close to the transit duration (Herrero et al. 2011). Both of these planets indicate that there may be

additional factors that could significantly affect the transit light curves, however, statistically it is not unexpected to have a couple of outliers. In Section 2.5.2.7 we discuss how we treat stellar variability for the whole survey.

Additionally, three of the seven hottest planets above 2000 K (WASP-33b, WASP-121b, and WASP-18b) have evidence of a temperature inversion (von Essen et al. 2015; Haynes et al. 2015; Evans et al. 2017; Arcangeli et al. 2018). However, since transmission spectroscopy is not as sensitive to the temperature profile at low resolution (e.g., Brown 2001) so we do not expect to see the effect of temperature inversions in the transit depth difference of the two *Spitzer*/IRAC bandpasses. Additionally, the H⁻ opacity seen at the WFC3 bandpass (e.g. Arcangeli et al. 2018) does not become important at the *Spitzer*/IRAC bandpasses until equilibrium temperatures as high as 3500 K.

2.5.2.6 Radius Anomaly

Our sample subsequently spans a very large range of scale heights, ranging from HAT-P-2b with a scale height of 26 km to WASP-31b with a scale height of 1150 km. Figure 2.6 demonstrates that there is no trend with the atmospheric scale height and the strength of the spectral features indicated by the magnitude of the transit depth metric. Furthermore, the radius anomaly is thought to correlate with incident flux, with hotter planets having a more inflated radius (Thorngren & Fortney 2018). However, we do not find a trend with the radius anomaly and the strength of the spectral features seen with *Spitzer* (see Figure 2.17).

2.5.2.7 Stellar Variability

Contamination of the transmission spectrum from starspots, faculae and flares generate brightness temperature differences between the disk-integrated spectra of the star and the region occulted by a transiting planet (Désert et al. 2011c; Pont et al. 2008; Sing et al. 2011). If a planet occults a star spot at a different temperature to the photospheric one, it can change the shape of the lightcurve by appearing as a change in the flux during transit. On the other hand, if the star spot is not occulted, then the disk integrated spectrum of the star is fainter or brighter, depending on the spot properties, which can cause the measured transit depth to be different than the nominal one. Stellar variability can occur when star spots rotate in and out of view of the integrated stellar disk, which depends on the rotation period of the star.

To estimate the possible effect of stellar variability on our results, we aim to provide a quantitative estimate of how this would affect the sample as a whole, by expanding the interpolated model grid. We do this by looking at a worst case scenario variable star, HD 189733, which has a peak-to-peak variability of $\sim 3\%$ in the visible (Henry & Winn 2008). We follow the method in Désert et al. (2011c); Sing et al. (2011) and Berta et al. (2012) to calculate the effect of this variability on the transit depth metric. We first translate this 3% in V-band to 0.8% at 3.6 μm using the ratio of blackbodies, we set 2.8% spot coverage with spots at 1000 K less than the stellar photosphere. We can propagate this to a relative error on the transit depth and assuming it will affect 4.5 μm as much as 3.6 μm (in reality it

will be a smaller effect), we can then propagate this to an error on the transit depth metric ($\delta_{ch2} - \delta_{ch1}/\delta_{ch1}$). This leads to a 42% maximum error on the transit depth metric, we thus extend the models positive and negative by this percentage, which is plotted on Figure 2.6.

Despite choosing the worst case scenario to expand our model grid, the features arising from the changing chemistry with equilibrium temperature can still be clearly distinguished in the grid of models in Figure 2.6, i.e. the transition regions at ~ 1000 K and ~ 2200 K remain clear. The relative size of the variability region is on average one-third of the size of the average uncertainty on the data points. Nevertheless, this is a conservative upper estimate and will not apply as strongly to all planets in our sample, since not all stars are as variable as HD 189733. If the temperature difference between spot and photosphere is less or if the spot covering fraction is smaller, then this would result in a lower variability amplitude and smaller effect on the transmission spectrum. Additionally, 3% is the maximum peak-to-peak variability, this would only apply if the observations were taken at the peak and trough of the variability period. Since we designed the observations to have as few orbital periods as possible to be within one variability period of the star, it is unlikely that we reach the maximum variability between our two *Spitzer* observations.

2.5.3 Comparing Transmission and Emission with warm *Spitzer*/IRAC

Several of the planets from our survey have published secondary eclipse measurements. We utilize the secondary eclipse literature survey from Baxter et al. (2020) (and references therein) which contains $3.6\text{ }\mu\text{m}$ and $4.5\text{ }\mu\text{m}$ eclipses for 78 planets in total. Several of the eclipse depths presented in Table 1 of Baxter et al. (2020) were taken from Garhart et al. (2020), and some of these planets had dilution corrections due to companions in the field of view. The dilution corrections were applied before any analysis in Baxter et al. (2020), but this was not reported in their Table 1. We have thus reported the eclipse depths with dilution corrections in Table 2.8 of this work using the dilution correction factors presented in Table 4 of Garhart et al. (2020). We use the eclipse depth, equilibrium temperature, brightness temperatures at $3.6\text{ }\mu\text{m}$ and $4.5\text{ }\mu\text{m}$ and the deviation from the blackbody presented in Baxter et al. (2020). The deviation from the blackbody probes the temperature pressure profile. A positive deviation is either methane in absorption at $3.6\text{ }\mu\text{m}$ with a nominal TP profile or CO in emission at $4.5\text{ }\mu\text{m}$ if the TP profile is inverted. Twenty-four of the planets in (Baxter et al. 2020) are also in our transmission survey, which allows us to statistically compare the two samples. To better understand the dearth of methane planets presented in Section 2.4.2.2, we compare the difference in brightness temperature from emission with the normalized difference in transit depths for planets with both emission and transmission observations. Additionally, we create a color-magnitude plot and compare the emission to the brown dwarf spectral sequence with a focus on the coolest planets.

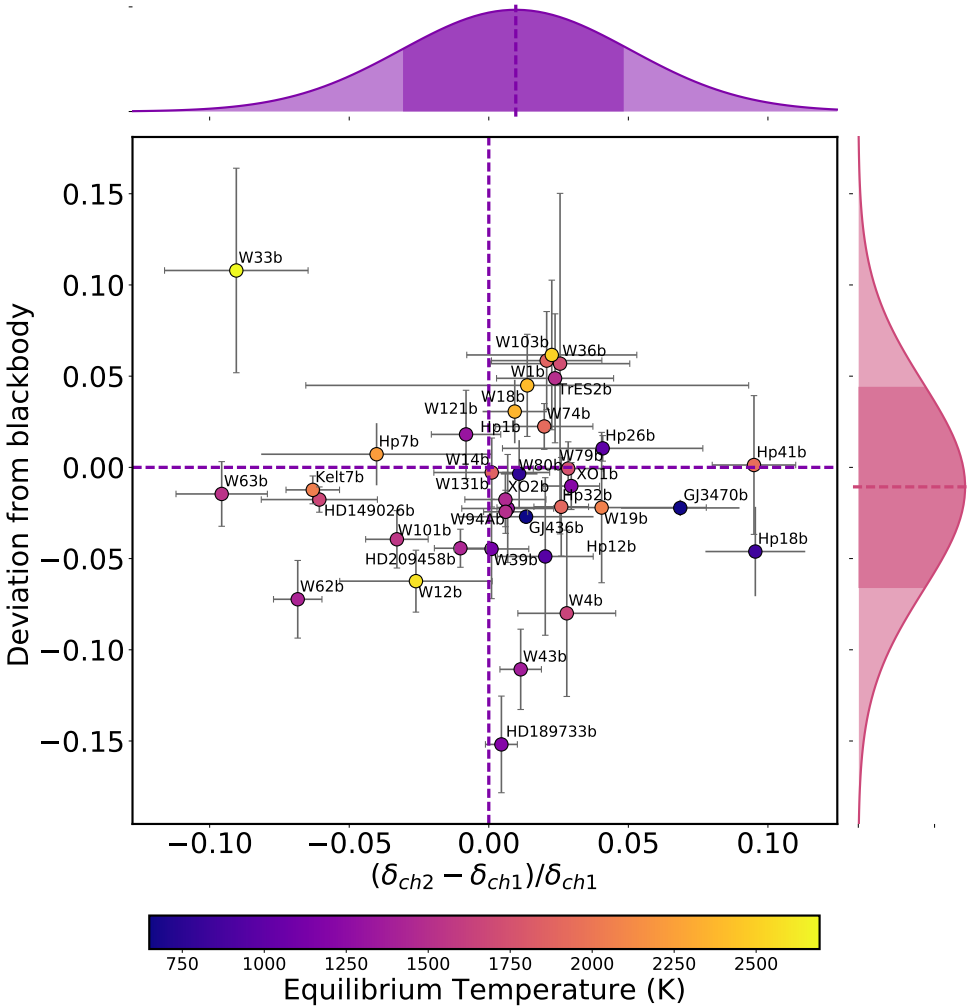


Fig. 2.11: Deviation from a blackbody calculated from emission against the normalized difference in the transit depth presented in Figure 2.6. Histograms on each axis show the mean and standard deviation of each axis. The equilibrium temperature of each planet is shown with the color scale.

2.5.3.1 Probing different pressures with emission and transmission

In Baxter et al. (2020), we demonstrate that the relative opacities in the two *Spitzer*/IRAC band-passes can act as a probe of the atmospheric temperature structure when observing the day-side emission. The deviation from blackbody metric described in Baxter et al. (2020) plotted against the equilibrium temperature shows that ultra-hot Jupiters have statistical evidence for thermal inversion. In a non-inverted atmosphere, a positive deviation indicates that the $3.6\text{ }\mu\text{m}$ brightness temperature is lower than that at $4.5\text{ }\mu\text{m}$ due to methane absorption at $3.6\text{ }\mu\text{m}$ and

a negative deviation indicates that the $4.5 \mu\text{m}$ T_b is lower due to CO absorption at $4.5 \mu\text{m}$. On the other hand, if the atmosphere is inverted, CO being the dominating carbon bearing species in the atmosphere would result in a positive deviation due to seeing CO in emission at $4.5 \mu\text{m}$. In this work we are focusing on the CH₄ to CO transition temperature and thus we do not account for temperature inversions.

In Figure 2.11 we compare the difference of the two IRAC brightness temperatures against the normalized difference in the transit depth. There appear to be no trends in the emission and transmission of the planets in our survey with both eclipses and transits, and we also find that the top left quadrant is almost empty, with the main outlier being WASP-33b. Given that the deviation from the blackbody can be positive or negative for a CO dominated atmosphere depending on the TP profile, we test for trends in the planets with equilibrium temperatures below 1800 K, which are not expected to have thermally inversions in their atmospheres. We find that the top left quadrant, which indicates CH₄ in transmission and CH₄ in emission, is empty. Meaning that any planets which show signs of methane in either emission or transmission do not show it in the other. For example, HD 149026b lies in the bottom left quadrant, it has a negative deviation from a blackbody, which indicates a CO absorption feature in emission (assuming a non-inverted TP profile). The expected corresponding transmission spectrum would predict a positive transit depth difference. However, this is not what we see. Possible reasons for these differences include: longitudinal abundance differences, more complex atmospheric processes such as atmospheric mixing, different cloud composition/abundances at different layers in the atmosphere, or changes in the thermal structure between emission and transmission (e.g., Fortney 2005). Additionally, similar to the results for the planets in transmission, we do not find a correlation between the deviation of the blackbody and the radius anomaly.

2.5.3.2 Comparing to brown dwarfs with a Color-Magnitude diagram

We create also a color-magnitude plot using these *Spitzer* secondary eclipses. Our work expands on that presented in Triaud et al. (2014) by extending their survey from 37 planets to the 78 planets presented in Baxter et al. (2020) and by using the newly released GAIA dr2 for more accurate distances (Gaia Collaboration et al. 2018). We calculate the planetary apparent magnitudes by using the apparent stellar magnitudes from the WISE spacecraft (Cutri & et al. 2012) in combination with the planet to star flux ratio from *Spitzer*. The two WISE channels W1 and W2 are known to overlap the two remaining *Spitzer* channels (Kirkpatrick et al. 2011). We then use the GAIA dr2 distances which were calculated using a Bayesian prior from Gaia Collaboration et al. (2018) and Bailer-Jones et al. (2018) to calculate the planetary absolute magnitudes. The equilibrium temperature, GAIA distances, and WISE magnitudes used are tabulated in Table 2.8. Errors are propagated fully throughout the calculation from the errors on all input properties.

Figure 2.12 shows the [3.6] - [4.5] color vs [3.6] magnitude diagram, we have overplotted the survey of brown dwarfs spanning M, L, and T spectral classes from Dupuy & Liu

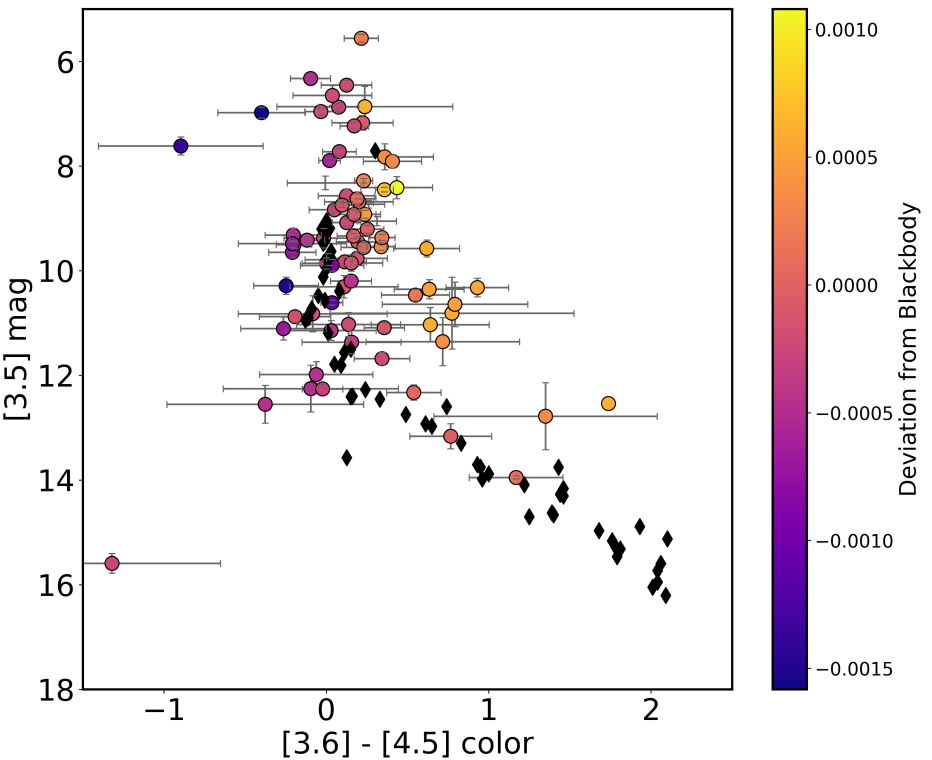


Fig. 2.12: $[3.6] - [4.5]$ color vs $[3.6]$ magnitude diagram of exoplanets and brown dwarfs planets with available eclipse depth measurements in the two warm *Spitzer* band-passes. Brown dwarf colors (estimated from the WISE catalog) are shown as black diamonds from Dupuy & Liu (2012). The color scale is the deviation from a blackbody metric described Baxter et al. (2020).

(2012) for comparison. The planets plotted on Figure 2.12 show an increasing scatter with increasing $3.6\mu\text{m}$ magnitude. This is unlike the brown dwarf spectral sequence which follows the a very tight L/T transition. This increase in scatter confirms the one seen in Triaud et al. (2014); Beatty et al. (2014); Melville et al. (2020) and Dransfield & Triaud (2020), which is suggested to be due to an increase in atmospheric diversity.

Figure 2.12 shows that the increase in scatter is driven by a small family of planets which lie redder than the brown dwarf spectral sequence. The color scale shows that this family of planets shows a positive deviation from a blackbody (Baxter et al. 2020). The positive deviation from a blackbody indicates methane absorption (nominal TP profile) or CO emission (inverted TP profile). Since these planets are around 1200–1500 K, we do not expect their atmospheres to be inverted, and we therefore think that these warmer planets could be displaying a signature of methane in their atmospheres. In Section 2.4.1.5 we show that the cooler

planets (<1000 K) deviate from equilibrium chemistry models by not showing signatures of methane in their atmospheres. Similarly, these warmer planets are not expected to have a high methane abundance given equilibrium chemistry, we again have to invoke non-equilibrium processes such as vertical mixing. Warmer planets are expected to have larger vertical mixing than their cooler counterparts (Komacek et al. 2019), creating an ideal scenario for dredging up methane. Furthermore, brown dwarfs are expected to have smaller mixing than gas giant planets, with K_{zz} ranging from $10^4 - 10^{8.5}$ for brown dwarfs and $10^7 - 10^{12}$ (Zahnle & Marley 2014; Leggett et al. 2017; Miles et al. 2020). Although this prediction is based on non-irradiated, higher gravity objects with mostly convective atmospheres, GCMs of highly irradiated, radiative atmospheres of hot Jupiters do display stronger mixing (Parmentier et al. 2013; Komacek et al. 2019). We therefore propose that the increased atmospheric diversity of planets compared to their brown dwarf counterparts seen in Figure 2.12 could be due, in part, to the diversity of processes involved, such as the presence of vertical mixing.

Furthermore, brown dwarfs are expected to have smaller mixing than gas-giant planets (Zahnle & Marley 2014). Although this prediction is based on non-irradiated, higher gravity objects with mostly convective atmospheres, GCMs of highly irradiated, essentially radiative atmospheres of hot Jupiters do display stronger mixing (Parmentier et al. 2013; Komacek et al. 2019). With K_{zz} ranging from $10^4 - 10^{8.5} \text{ cm}^2/\text{s}$ for brown dwarfs (Zahnle & Marley 2014; Leggett et al. 2017; Miles et al. 2020) and $10^7 - 10^{12} \text{ cm}^2/\text{s}$ for gas giants (Parmentier et al. 2013; Komacek et al. 2019). We therefore propose that the increased atmospheric diversity of planets compared to their brown dwarf counterparts seen in Figure 2.12 could be due, in part, to the diversity of processes involved, such as the presence of vertical mixing.

2.6 Conclusion

We have performed the data analysis of 70 lightcurves and presented in total 49 planets with transit depths at 3.6 and 4.5 μm with *Spitzer*/IRAC. This survey represents the largest analysis of *Spitzer*/IRAC observations of gas giant transits to date, and it spans equilibrium temperatures from 500 K to 2700 K. We have implemented our custom *Spitzer*/IRAC data analysis pipeline which thoroughly searches over a grid of data reduction parameters before employing pixel level decorrelation (Deming et al. 2015) to correct for the strong *Spitzer* systematics and extract the transit depths using an MCMC transit fitting algorithm.

We then statistically studied the sample of all planets with transmission in these two band-passes. We create a fiducial cloud-free 1-D atmospheric model grid with 1x solar composition and equilibrium chemistry spanning the parameters of the planets in our sample. We compare the survey of planets with this model grid and note a family of outliers with equilibrium temperature <1000 K, they do not show the expected methane abundance from these equilibrium chemistry models.

Next, we expand our grid in two dimensions by extending to 30x solar metallicity and incorporating non-equilibrium effects with different values of an eddy diffusion co-efficient

(K_{zz}). We find that the best fitting grid for the cool planets ($T < 1000$ K) has high metallicity (30x solar) and low or no vertical mixing ($K_{zz} = 0$ or $10^8 \text{ cm}^2/\text{s}$). On the other hand, we find that the hot planets ($T > 1000$ K) are best explained with 1x solar composition with a marginal better fit with the high vertical mixing model ($K_{zz} = 10^{12} \text{ cm}^2/\text{s}$). We conclude that the cool planets are better fit by models with higher metallicity as due to an observational bias resulting in lower masses. We find evidence supporting non-equilibrium chemistry in a survey of planets and find that our work agrees with the theory that hotter planets have higher vertical mixing.

Furthermore, we combine our transits with our previous literature eclipse survey. We do not find any trend between eclipses and transits, and propose that this is due to several effects: clouds at different pressures or more complex atmospheric processes. We then create a color magnitude diagram using the emission observations and compare to L/T transition brown dwarfs. With a larger sample size than previous studies, we also see the increase in scatter with increasing magnitude first seen in Triaud et al. (2014). We see that the increase in scatter is driven by a family of mid-temperate planets showing a methane signature, which is not expected from equilibrium chemistry. We propose that this increase in scatter is due to methane being dredged up due to high levels of vertical mixing in the atmosphere. Which supports the theory that brown dwarfs have ~ 100 x lower levels of vertical mixing than planets.

2.A Pipeline results Figures and Tables

Table 2.7: Jump Parameters used as starting points for the MCMC analysis. Eccentricity was fixed to 0 for all planets since it did not affect the resulting transit depths. Stellar parameters (T_{eff} , \log and $[\text{Fe}/\text{H}]$) are used to calculate linear limb-darkening parameters.

Planet	a/R_s	inc °	R_p/R_s	Period days	Eccentricity	T_{eff} Kelvin	$\log(g_*)$ $\log_{10}(\text{cm/s}^2)$	$[\text{Fe}/\text{H}]$ dex	Ref
HAT-P-32 b	6.05(4)	88.9(4)	0.1508(4)	2.150008(1)	0.16(6)	6207(88)	4.33(1)	-0.04(8)	13
XO-1 b	11.24(9)	88.8(2)	0.1320(5)	3.94150685(91)	0	5750(75)	4.50(1)	0.02(8)	6
HAT-P-1 b	9.85(7)	85.63(06)	0.1180(2)	4.46529976(55)	0	5980(49)	4.36(1)	0.13(1)	19
WASP-17 b	7.05(7)	86.83(68)	0.13	3.7354380(68)	0.03(2)	6650(80)	4.16(3)	-0.19(9)	1
WASP-39 b	11.37(24)	87.75(27)	0.1457(16)	4.0552765(35)	0	5400(150)	4.4(2)	-0.12(10)	18,10
HAT-P-12 b	11.77(21)	89.0(4)	0.1406(13)	3.2130598(21)	0.03(3)	4650(60)	4.61(1)	-0.29(5)	11
HAT-P-18 b	16.04(75)	88.8(3)	0.1365(15)	5.508023(6)	0.08(5)	4803(80)	4.57(4)	0.10(08)	14
TrES2 b	7.90(2)	83.87(02)	0.1254(5)	2.47061317(9)	0.02(2)	5850(50)	4.43(2)	-0.15(10)	9,22
WASP-4 b	5.46(2)	88.52(39)	0.1544(2)	1.33823204(16)	0.003(7)	5436(34)	4.46(5)	-0.05(4)	15,20
XO-2 b	8.18(3)	88.9(7)	0.1	2.615857(50)	0	5340(32)	4.48(5)	0.45(2)	5
GJ3470 b	13.94(49)	88.88(72)	0.0764(4)	3.3366487(43)	0.02(2)	3652(50)	4.78(12)	0.17(6)	3
WASP-21 b	9.62(17)	87.12(24)	0.1030(8)	4.3225126(22)	0	5800(100)	4.2(1)	-0.46(11)	21,4
WASP-31 b	8.00(19)	84.41(22)	0.127	3.4059096(50)	0	6302(102)	4.31(2)	-0.20(09)	2
WASP-1 b	5.69(6)	90.0(1.3)	0.1036(8)	2.5199454(5)	0.01(3)	6200(200)	4.3(3)	0.1(2)	17,7
HAT-P-26 b	13.44(83)	88.6(9)	0.0737(12)	4.234516(15)	0.12(6)	5079(88)	4.56(6)	-0.04(8)	12
WASP-107 b	18.2(1)	89.56(08)	0.1446(2)	5.72149242(46)	0	4330(120)	4.5(1)	0.02(10)	23
WASP-13 b	7.58(15)	85.64(24)	0.0922(8)	4.353011(13)	0	5826(100)	4.04(20)	0.0(2)	24,25
WASP-121 b	3.75(3)	87.6(6)	0.1245(5)	1.27492550(25)	0	6459(140)	4.24(1)	0.13(9)	26
WASP-69 b	11.96(17)	86.71(20)	0.1336(16)	3.8681382(17)	0	4700(50)	4.54(2)	0.15(8)	35
WASP-67 b	13.42(13)	85.8(3)	0.1345(48)	4.61442(1)	0	5417(85)	4.53(2)	0.18(6)	36
HATS7 b	10.59(51)	87.92(75)	0.0711(19)	3.185315(5)	0	4985(50)	4.54(5)	0.25(8)	37
WASP-29 b	12.15(44)	88.8(7)	0.101(2)	3.922719(7)	0.03(5)	4875(65)	4.54(4)	0.11(14)	38
HAT-P-41 b	5.45(18)	87.7(1.0)	0.1028(16)	2.694050(4)	0	6390(100)	4.14(2)	0.21(10)	32

Table 2.7: continued.

Planet	a/R_s	inc °	R_p/R_s	Period days	Eccentricity	T_{eff} Kelvin	$\log(g_*)$ $\log_{10}(cm/s^2)$	[Fe/H] dex	Ref
WASP-101 b	8.45(30)	85.0(2)	0.1140(9)	3.585720(4)	0	6380(120)	4.31(8)	0.20(12)	32
WASP-131 b	8.53(9)	85.0(3)	0.0815(7)	5.3222023(5)	0	6030(90)	4.09(3)	-0.18(8)	39
WASP-36 b	5.85(6)	83.15(13)	0.1368(6)	1.53736596(24)	0	5959(134)	4.49(1)	-0.26(10)	40
WASP-63 b	6.59(30)	87.8(1.3)	0.0781(11)	4.378080(6)	0	5550(100)	4.01(3)	0.08(7)	32
WASP-79 b	7.03(36)	85.4(6)	0.1049(24)	3.662380(5)	0	6600(100)	4.20(15)	0.03(1)	32
WASP-94 Ab	7.3(7)	88.7(7)	0.1094(8)	3.9501907(44)	0	6153(75)	4.18(1)	0.26(15)	41
WASP-74 b	4.86(20)	79.81(24)	0.0964(7)	2.137750(1)	0	5990(110)	4.39(7)	0.03(10)	33
WASP-62 b	9.55(41)	88.30(75)	0.1095(9)	4.411950(3)	0	6230(80)	4.45(10)	0.04(6)	34
Kepler-45 b	10.6(1.0)	87.0(7)	0.179(2)	2.455239(4)	0.11(10)	3820(90)	3.1(1)	0.13(13)	16

- (1) Anderson et al. (2011a); (2) Anderson et al. (2011b); (3) Biddle et al. (2014); (4) Bouchy et al. (2010); (5) Burke et al. (2007); (6) Burke et al. (2010); (7) Collier Cameron et al. (2007); (8) Doyle et al. (2011); (9) Esteves et al. (2015); (10) Faedi et al. (2011); (11) Hartman et al. (2009); (12) Hartman et al. (2011b); (13) Hartman et al. (2011c); (14) Hartman et al. (2011a); (15) Hoyer et al. (2013); (16) Johnson et al. (2012); (17) Maciejewski et al. (2014); (18) Maciejewski et al. (2016); (19) Nikolov et al. (2014); (20) Petrucci et al. (2013); (21) Seeliger et al. (2015); (22) Sorzetti et al. (2007); (23) Močnik et al. (2017); (24) Barros et al. (2012); (25) Skillen et al. (2009); (26) Delrez et al. (2016); (27) Holman et al. (2010); (28) Torres et al. (2011); (32) Stassun et al. (2017); (33) Stassun et al. (2018); (34) Stassun et al. (2019); (35) Anderson et al. (2014); (36) Hellier et al. (2012); (37) Bakos et al. (2015); (38) Hellier et al. (2010); (39) Hellier et al. (2017); (40) Mancini et al. (2016); (41) Neveu-VanMalle et al. (2014).

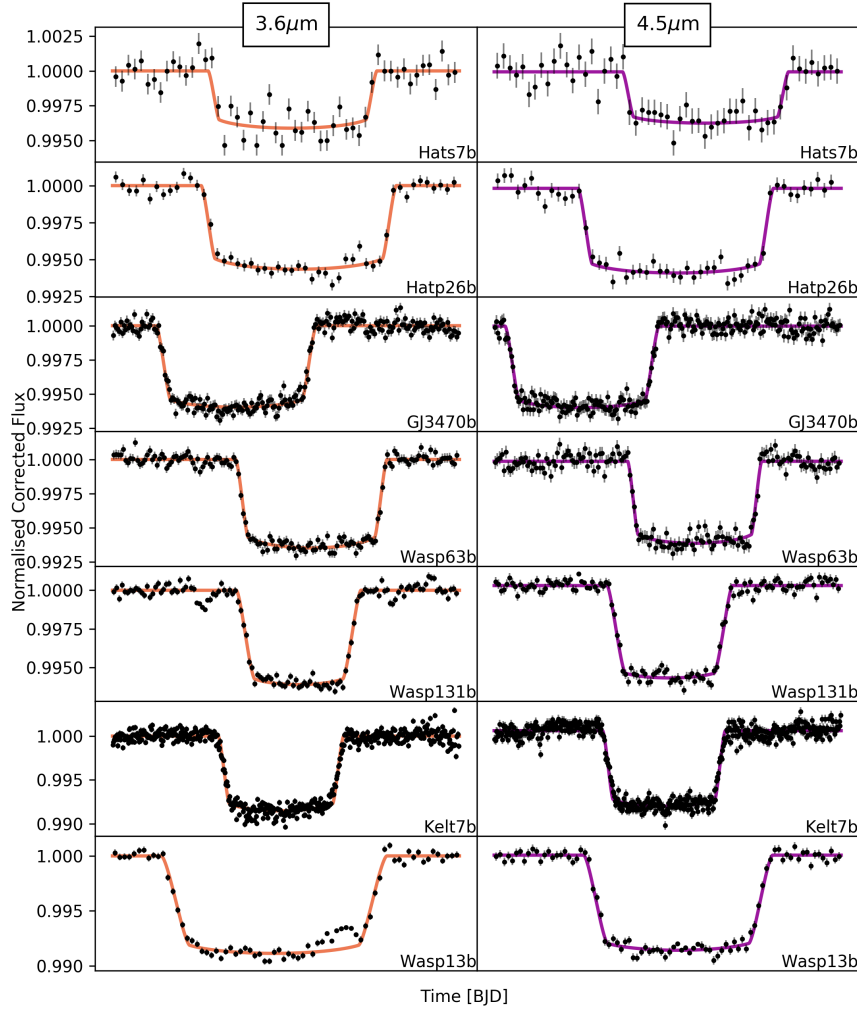


Fig. 2.13: Normalized and systematic corrected transit lightcurves for each planet at 3.6 (left column, orange) and $4.5\mu\text{m}$ (right column, purple). 1σ errorbars are those originally calculated from scaled photon noise. The data and the errorbars are binned in 5 minute intervals for display purposes. Continuous curves show the best fit transit models in each band-pass for comparison. Kepler-45b displays the result of 4 phase folded lightcurves in each channel.

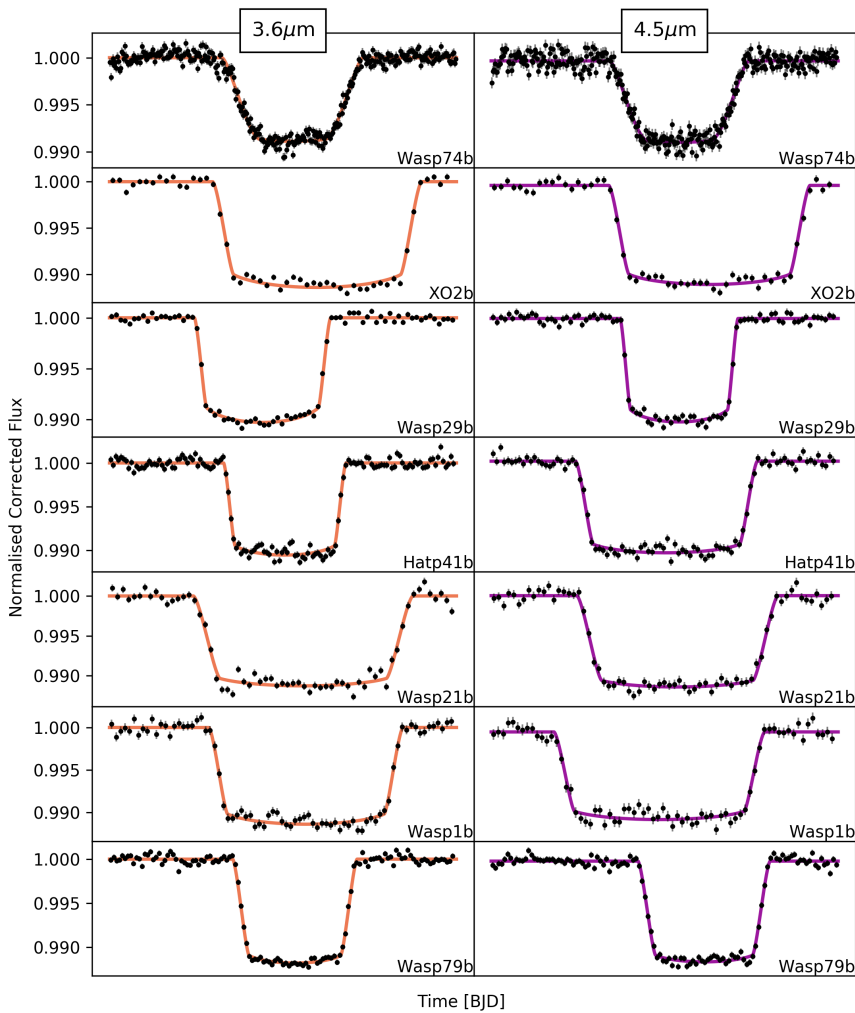


Fig. 2.13

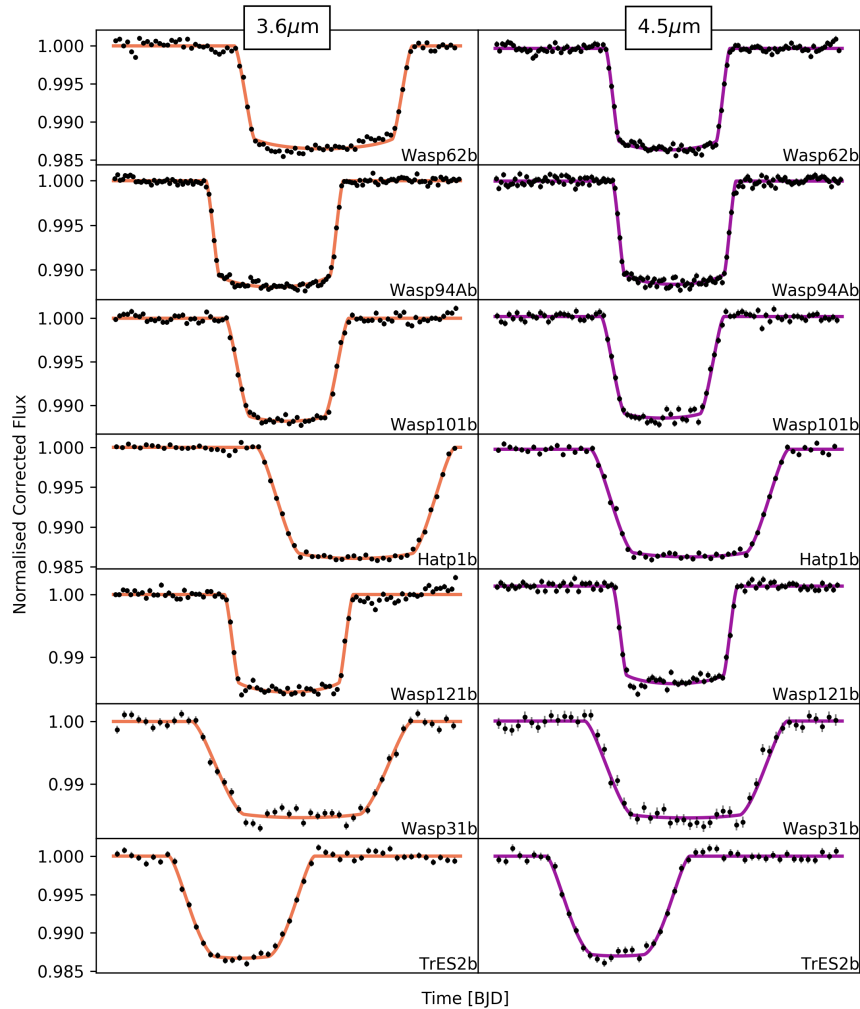
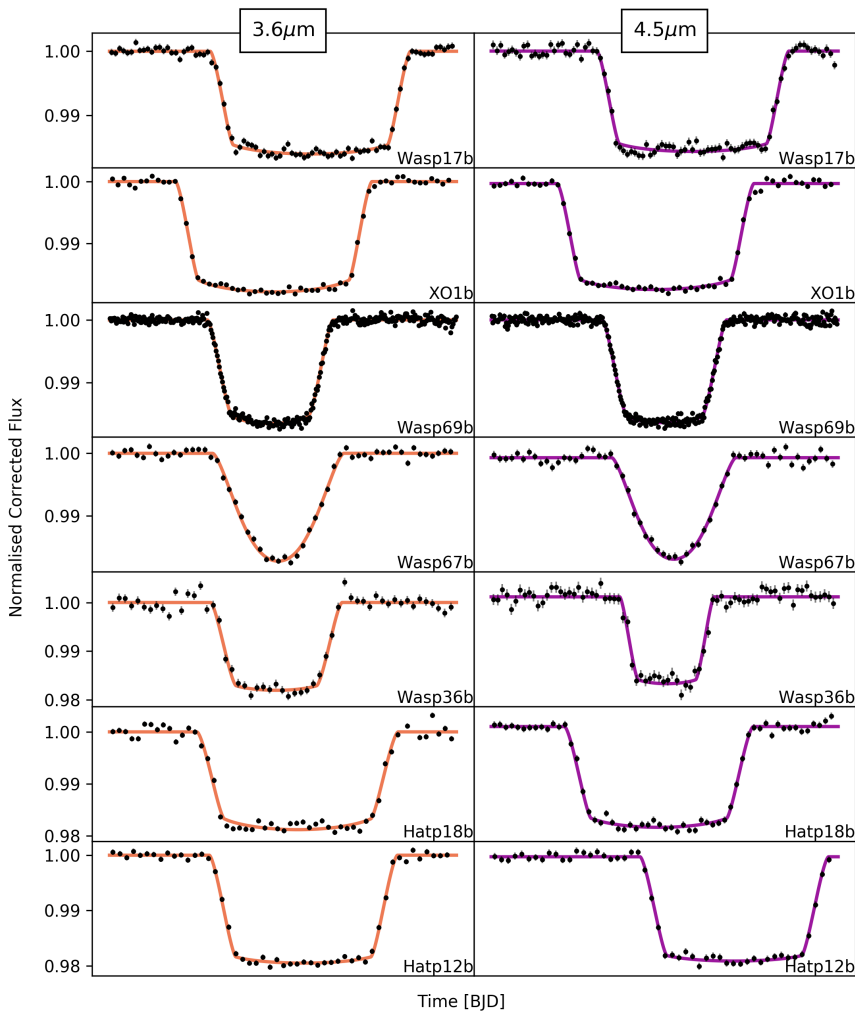


Fig. 2.13: *Continued.*

Fig. 2.13: *Continued.*

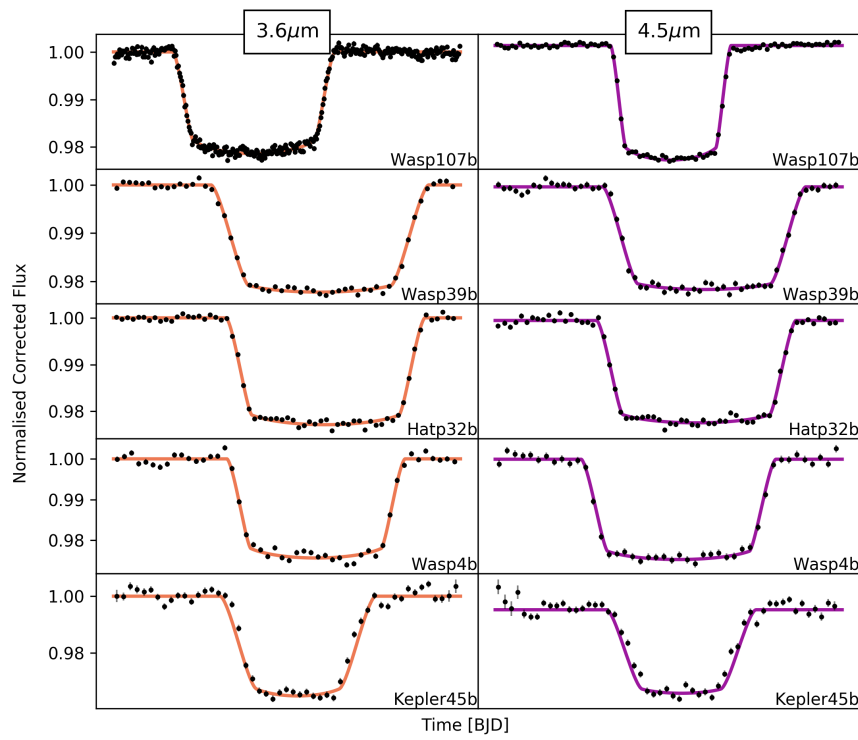


Fig. 2.13: *Continued.*

Table 2.8: Eclipse depths at 3.6 and 4.5 μm collected from the literature ($(F_p/F_s)_{3.6}$ and $(F_p/F_s)_{4.5}$ respectively). T_{eq} is the equilibrium temperature assuming no redistribution and 0 albedo. Distance is the estimated distance in parsec taken from Bailer-Jones et al. (2018). m_{W1}^s and m_{W2}^s are the stellar apparent magnitudes. $M_{3.6}^{pl}$ and $M_{4.5}^{pl}$ and the planetary absolute magnitudes in the wise 1 and wise 2 bandpasses (which are equivalent to the *Spitzer* channel 1 and channel 2 respectively), calculated using the planet to star flux ratio. Color is the 4.5 minus 3.6 micron magnitude color of the planets. The final column details the reference for each of the eclipse depths in the literature, the majority of which were collected from exoplanets.org (Wright et al. 2011) and have been individually verified.

Planet	$(F_p/F_s)_{3.6}$	$(F_p/F_s)_{4.5}$	T_{eq} (a=0)	Distance	$M_{3.6}^{pl}$	$M_{4.5}^{pl}$	m_{W1}^s	m_{W2}^s	color	Ref.
ppm	ppm	Kelvin	parsec	mag	mag	mag	mag	mag		
HAT-P-32 b	3640±160	4380±200	1901±57	289.2±5.3	8.7±0.1	8.5±0.07	9.9±0.02	9.91±0.02	0.2±0.09	1
XO-1 b	860±70	1220±90	1207±30	163.6±0.6	11.1±0.1	10.73±0.08	9.49±0.02	9.52±0.02	0.36±0.12	2
HAT-P-1 b	800±80	1350±220	1306±33	159.0±1.0	10.5±0.1	9.92±0.18	8.73±0.02	8.75±0.02	0.55±0.21	3
WASP-39 b	880±150	960±180	1118±35	214.0±1.7	11.1±0.2	11.12±0.21	10.16±0.02	10.22±0.02	0.03±0.28	4
HAT-P-12 b	660±270	640±180	958±18	142.8±0.5	12.3±0.4	12.35±0.31	10.08±0.02	10.14±0.02	-0.1±0.54	5
HAT-P-18 b	437±145	326±146	847±26	161.4±0.6	12.6±0.4	12.93±0.49	10.2±0.02	10.25±0.02	-0.38±0.61	6
TrES2 b	1270±210	2300±240	1498±32	215.3±1.0	10.4±0.2	9.72±0.12	9.78±0.02	9.79±0.02	0.63±0.21	7
WASP-4 b	3190±310	3430±270	1651±27	267.2±3.7	9.8±0.1	9.78±0.09	10.68±0.02	10.75±0.02	0.01±0.15	8
XO-2 b	810±170	980±200	1322±23	154.3±1.4	11.0±0.2	10.89±0.22	9.24±0.02	9.31±0.02	0.14±0.32	9
GJ3470 b	113±24	3±22	662±45	29.4±0.1	15.3±0.2	19.25±7.96	7.81±0.03	7.78±0.02	-3.92±7.97	10
WASP-1 b	1170±160	2120±210	1876±69	393.1±10.5	9.6±0.2	8.96±0.12	10.22±0.02	10.25±0.02	0.62±0.2	11
HAT-P-26 b	85±0	265±70	994±48	141.8±1.1	14.0±0.0	12.78±0.29	9.54±0.02	9.6±0.02	1.17±0.29	6
WASP-121 b	3685±114	4684±121	2359±61	269.9±1.6	8.3±0.0	8.05±0.04	9.36±0.02	9.39±0.02	0.23±0.06	12
WASP-87 b	2080±127	2708±137	2343±68	298.4±3.6	8.7±0.1	8.47±0.06	9.4±0.02	9.43±0.02	0.26±0.1	12
WASP-100 b	1267±98	1720±119	2200±171	364.4±2.7	9.1±0.1	8.74±0.08	9.62±0.02	9.64±0.02	0.31±0.12	12
WASP-78 b	2001±218	2013±351	1957±256	754.3±16.7	8.3±0.1	8.33±0.2	10.96±0.02	10.98±0.02	-0.01±0.24	12
HAT-P-41 b	1842±319	2303±177	1937±44	348.2±4.5	8.7±0.2	8.49±0.09	9.56±0.02	9.6±0.02	0.2±0.21	12
WASP-101 b	1161±111	1194±113	1554±40	201.2±1.1	9.9±0.1	9.86±0.11	9.04±0.02	9.07±0.02	0.0±0.15	12
WASP-131 b	304±96	289±80	1458±35	200.1±2.6	10.8±0.3	10.91±0.3	8.54±0.02	8.57±0.02	-0.08±0.46	12
WASP-36 b	914±578	1953±544	1722±45	386.3±5.2	10.8±0.7	10.04±0.3	11.15±0.02	11.2±0.02	0.77±0.75	12
WASP-63 b	486±96	560±130	1531±45	290.7±2.0	10.3±0.2	10.2±0.25	9.34±0.02	9.39±0.02	0.11±0.33	12

Table 2.8: continued.

Planet	$(F_p/F_s)_{3.6}$	$(F_p/F_s)_{4.5}$	T_{eq} (a=0)	Distance	$M_{3.6}^{pl}$	$M_{4.5}^{pl}$	m_{W1}^s	m_{W2}^s	color	Ref.
	ppm	ppm	Kelvin	parsc	mag	mag	mag	mag	mag	
WASP-94 A b	867±59	995±93	1500±76	211.2±2.5	9.8±0.1	9.72±0.11	8.8±0.02	8.84±0.02	0.11±0.13	12
WASP-62 b	1616±146	1359±130	1427±35	175.6±0.6	9.7±0.1	9.86±0.11	8.9±0.02	8.92±0.02	-0.21±0.15	12
CoRoT-1 b	4150±420	4820±420	1900±81	787.9±23.5	8.6±0.1	8.45±0.12	12.1±0.02	12.14±0.02	0.12±0.17	13
CoRoT-2 b	3550±200	5000±200	1537±40	213.3±2.5	9.5±0.1	9.21±0.05	10.06±0.02	10.1±0.02	0.34±0.09	13
GJ 436 b	155±22	34±20	649±59	9.8±0.0	15.6±0.2	16.92±0.64	6.02±0.11	5.69±0.05	-1.32±0.67	14
HAT-P-19 b	620±140	620±140	1009±40	202.1±1.5	12.0±0.2	12.05±0.25	10.5±0.02	10.56±0.02	-0.06±0.35	4
HAT-P-2 b	996±72	1031±61	1540±30	127.8±0.4	9.5±0.1	9.52±0.07	7.57±0.02	7.58±0.02	0.03±0.11	15
HAT-P-20 b	615±82	1096±77	971±24	71.0±0.2	12.3±0.1	11.79±0.08	8.56±0.03	8.65±0.02	0.54±0.17	16
HAT-P-23 b	2480±190	3090±260	2051±71	364.8±4.7	9.5±0.1	9.26±0.1	10.75±0.02	10.79±0.02	0.19±0.13	17
HAT-P-26 b	-27±50	223±81	994±48	141.8±1.1	-±2.0	12.97±0.4	9.54±0.02	9.6±0.02	-±2.05	6
HAT-P-3 b	1120±225	940±125	1158±34	134.6±0.5	11.1±0.2	11.37±0.15	9.38±0.02	9.45±0.02	-0.26±0.26	5
HAT-P-4 b	1420±160	1220±130	1694±47	320.5±2.8	9.3±0.1	9.52±0.12	9.73±0.02	9.77±0.02	-0.2±0.17	5
HAT-P-6 b	1170±80	1060±60	1673±42	275.4±3.6	9.4±0.1	9.54±0.07	9.29±0.02	9.3±0.02	-0.12±0.11	18
HAT-P-7 b	1560±130	1900±110	2225±41	341.1±2.4	8.6±0.1	8.44±0.07	9.28±0.02	9.3±0.02	0.19±0.12	19
HAT-P-8 b	1310±85	1110±75	1772±48	211.6±1.7	9.5±0.1	9.71±0.08	8.93±0.02	8.95±0.02	-0.2±0.11	18
HD 149026 b	400±30	340±60	1673±65	75.9±0.2	10.9±0.1	11.07±0.19	6.79±0.07	6.8±0.02	-0.19±0.22	20
HD 189733 b	2560±140	2140±200	1200±22	19.8±0.0	10.3±0.2	10.54±0.11	5.29±0.15	5.34±0.05	-0.25±0.2	21
HD 209458 b	1190±70	1230±60	1446±19	48.3±0.1	10.2±0.1	10.05±0.06	6.31±0.09	6.19±0.03	0.15±0.13	22
Kepler-12 b	1370±200	1160±310	1481±31	88.1±9.7	9.5±0.2	9.69±0.29	12.05±0.02	12.08±0.02	-0.21±0.33	23
Kepler-17 b	2500±300	3100±350	1745±39	720.8±10.3	9.8±0.1	9.58±0.13	12.55±0.02	12.59±0.02	0.19±0.19	24
Kepler-5 b	1030±170	1070±150	1807±35	899.8±16.5	9.4±0.2	9.4±0.16	11.68±0.02	11.74±0.02	-0.02±0.24	26
Kepler-6 b	690±270	1510±190	1504±21	587.0±5.0	10.6±0.4	9.85±0.14	11.58±0.02	11.64±0.02	0.79±0.45	26
KOI-13 b	1560±310	2220±230	2607±94	519.1±29.1	7.8±0.2	7.47±0.17	9.39±0.02	9.41±0.02	0.36±0.3	27
Qatar-1 b	1511±455	2907±415	1389±43	185.6±0.8	11.0±0.3	10.39±0.16	10.32±0.02	10.4±0.02	0.64±0.36	28

Table 2.8: continued.

Planet	$(F_p/F_s)_{3.6}$	$(F_p/F_s)_{4.5}$	T_{eq} (a=0)	Distance	$M_{3.6}^{pl}$	$M_{4.5}^{pl}$	m_{W1}^s	m_{W2}^s	color	Ref.
	ppm	ppm	Kelvin	parsec	mag	mag	mag	mag	mag	
TrES-3 b	3460±350	3720±540	1629±32	231.3±1.3	9.9±0.1	9.86±0.16	10.57±0.02	10.61±0.02	0.04±0.2	29
TrES-4 b	1370±110	1480±160	1785±41	516.0±6.9	8.8±0.1	8.79±0.12	10.24±0.02	10.28±0.02	0.05±0.15	30
WASP-10 b	1000±110	1460±160	960±24	141.0±0.7	11.7±0.1	11.34±0.12	9.93±0.02	10.0±0.02	0.34±0.17	4
WASP-103 b	4458±383	5686±138	2505±78	883.3±153.1	6.9±0.4	6.63±0.38	10.72±0.02	10.75±0.02	0.24±0.54	31
WASP-12 b	4210±110	4280±120	2584±91	427.2±6.0	7.9±0.0	7.88±0.05	10.11±0.02	10.11±0.02	0.02±0.07	32
WASP-121 b	3150±103	4510±107	2359±61	269.9±1.6	8.5±0.0	8.1±0.03	9.36±0.02	9.39±0.02	0.36±0.06	12
WASP-14 b	1870±70	2240±180	1864±60	162.0±0.8	9.3±0.0	9.17±0.09	8.57±0.02	8.6±0.02	0.17±0.1	33
WASP-18 b	3000±200	3900±200	2398±73	123.5±0.4	8.9±0.1	8.69±0.06	8.07±0.02	8.12±0.02	0.24±0.1	34
WASP-19 b	4830±250	5720±300	2066±46	268.3±1.7	9.1±0.1	8.96±0.06	10.44±0.02	10.49±0.02	0.13±0.09	35
WASP-2 b	830±350	1690±170	1300±71	153.2±1.6	11.4±0.5	10.64±0.11	9.58±0.02	9.64±0.02	0.72±0.47	11
WASP-24 b	1590±130	2020±180	1769±39	322.1±4.4	9.6±0.1	9.33±0.1	10.1±0.02	10.13±0.02	0.23±0.14	36
WASP-33 b	2600±500	4100±200	2694±53	121.9±1.0	8.4±0.2	7.98±0.06	7.38±0.04	7.44±0.02	0.43±0.22	37
WASP-43 b	3460±130	3820±150	1375±79	86.7±0.3	10.6±0.0	10.58±0.05	9.15±0.02	9.22±0.02	0.03±0.07	38
WASP-48 b	1760±130	2140±200	2033±68	454.1±4.4	8.9±0.1	8.76±0.11	10.33±0.02	10.37±0.02	0.17±0.14	17
WASP-5 b	1970±280	2370±240	1742±68	309.1±3.4	9.9±0.2	9.7±0.11	10.54±0.02	10.59±0.02	0.15±0.19	39
WASP-6 b	940±190	1150±220	1184±32	197.1±1.6	11.4±0.2	11.21±0.21	10.28±0.02	10.34±0.02	0.16±0.3	4
WASP-67 b	220±130	800±180	1028±32	189.5±1.5	12.8±0.6	11.43±0.25	10.03±0.02	10.08±0.02	1.35±0.69	4
WASP-69 b	421±29	463±39	961±21	50.0±0.1	12.3±0.1	12.28±0.09	7.32±0.04	7.44±0.02	-0.02±0.13	6
WASP-8 b	1130±180	690±70	927±27	90.0±0.4	10.5±0.2	11.05±0.11	7.91±0.02	7.92±0.02	-0.55±0.21	40
WASP-80 b	455±100	944±65	775±25	49.8±0.1	13.2±0.2	12.4±0.08	8.3±0.02	8.32±0.02	0.77±0.25	41
XO-3 b	1010±40	1580±36	2046±40	213.1±2.7	9.6±0.1	9.13±0.04	8.75±0.02	8.76±0.02	0.47±0.07	42
XO-4 b	560±90	1350±85	1639±35	272.7±2.9	10.3±0.2	9.39±0.08	9.37±0.02	9.4±0.02	0.93±0.19	18
HAT-P-13 b	851±107	1090±124	1648±53	246.8±2.2	7.2±0.1	6.95±0.13	8.96±0.02	9.01±0.02	0.22±0.19	12
HAT-P-30 b	1603±107	1783±147	1637±43	214.0±2.2	6.9±0.1	6.8±0.09	9.04±0.02	9.08±0.02	0.08±0.12	12

Table 2.8: continued.

Planet	$(F_p/F_s)_{3.6}$	$(F_p/F_s)_{4.5}$	T_{eq} (a=0)	Distance	$M_{3.6}^{pl}$	$M_{4.5}^{pl}$	m_{W1}^s	m_{W2}^s	color	Ref.
	ppm	ppm	Kelvin	parsec	mag	mag	mag	mag	mag	
HAT-P-33 b	1663±127	1896±199	1780±34	396.1±7.5	6.5±0.1	6.33±0.12	10.0±0.02	10.02±0.02	0.13±0.16	12
HAT-P-40 b	988±168	1057±145	1765±66	464.5±6.4	6.7±0.2	6.62±0.15	9.98±0.02	10.01±0.02	0.04±0.24	12
KELT-2 A b	739±38	761±47	1710±31	134.1±0.8	7.0±0.1	6.99±0.07	7.27±0.04	7.34±0.02	-0.03±0.1	12
KELT-3 b	1788±97	1677±104	1822±44	210.3±5.4	6.3±0.1	6.43±0.09	8.57±0.02	8.6±0.02	-0.1±0.12	12
WASP-104 b	1709±195	2643±303	1516±43	185.9±1.5	7.9±0.1	7.5±0.13	9.84±0.02	9.91±0.02	0.41±0.18	12
WASP-46 b	1360±701	4446±589	1658±55	375.3±4.4	8.1±0.6	6.88±0.15	11.35±0.02	11.37±0.02	1.27±0.58	12
WASP-64 b	2859±270	2071±471	1690±52	369.9±3.0	7.0±0.1	7.38±0.25	10.96±0.02	11.01±0.02	-0.4±0.27	12
WASP-65 b	1587±245	724±318	1485±59	273.7±2.7	7.6±0.2	8.52±0.48	10.31±0.02	10.35±0.02	-0.9±0.51	12
WASP-76 b	2979±63	3762±82	2183±47	194.5±6.0	5.6±0.1	5.35±0.07	8.19±0.02	8.23±0.02	0.22±0.1	12
WASP-77 A b	2016±94	2487±127	1671±31	105.2±1.2	7.2±0.1	7.06±0.06	8.11±0.02	8.16±0.02	0.17±0.09	12
WASP-97 b	1359±84	1534±101	1540±42	151.1±0.5	7.7±0.1	7.65±0.07	8.96±0.02	9.01±0.02	0.08±0.1	12
WASP-74 b	1446±66	2075±100	1923±53	149.2±1.1	9.4±0.1	9.03±0.06	8.14±0.02	8.19±0.02	0.34±0.08	12
KELT-7 b	1688±46	1896±57	2050±35	136.7±0.9	8.7±0.0	8.65±0.04	7.5±0.03	7.52±0.02	0.1±0.06	12
WASP-79 b	1394±88	1783±106	1762±53	246.7±1.8	9.2±0.1	8.96±0.07	9.03±0.02	9.04±0.02	0.25±0.1	12

- (1) Zhao et al. (2014); (2) Machalek et al. (2008); (3) Todorov et al. (2010); (4) Garhart et al. (2020); (5) Kammer et al. (2015); (6) Todorov et al. (2013); (7) Wallack et al. (2019); (8) O'Donovan et al. (2010); (9) Beeler et al. (2011); (10) Machalek et al. (2009); (11) Benneke et al. (2019); (12) Wheatley et al. (2010); (13) Deming et al. (2011); (14) Morley et al. (2017); (15) Lewis et al. (2013); (16) Deming et al. (2015); (17) O'Rourke et al. (2014); (18) Todorov et al. (2012); (19) Christiansen et al. (2010); (20) Stevenson et al. (2012); (21) Charbonneau et al. (2008); (22) Diamond-Lowe et al. (2014); (23) Fortney et al. (2011); (24) Désert et al. (2011c); (25) Désert et al. (2011a); (26) Désert et al. (2011b); (27) Shporer et al. (2014); (28) Garhart et al. (2020); (29) Fressin et al. (2010); (30) Knutson et al. (2009a); (31) Kreidberg et al. (2018b); (32) Stevenson et al. (2014a); (33) Bleicic et al. (2013); (34) Nyfeler et al. (2011); (35) Anderson et al. (2013); (36) Smith et al. (2012); (37) Deming et al. (2012); (38) Bleicic et al. (2014); (39) Baskin et al. (2013); (40) Cubillos et al. (2013); (41) Triaud et al. (2015); (42) Machalek et al. (2010).

Table 2.9: The optimum parameters used for our pipeline which minimise the χ^2 of a least-squares fit to the systematics and the transit. If background method is “Annulus”, then the two parameters are the radius and width of a circular annulus, if it is “box” then the parameter is the size of the box taken in all of the 4 corners of the image. If the centroiding method is “baycenter” then the parameter is the number of pixels over which to create a box over the star for the flux weighting.

Planet	Channel	Aperture Size	Background Method	Background Params	Centroiding Method	Centroiding Params
		Pixels		Pixels		Pixels
HAT-P-32 b	ch1	2.50	Annulus	, 6, 4	Barycenter	3.0
HAT-P-32 b	ch2	2.50	Annulus	, 6, 4	Barycenter	5.0
XO-1 b	ch1	2.50	Annulus	, 6, 4	Moffat	-
XO-1 b	ch2	2.50	Annulus	, 6, 4	Gaussian	-
HAT-P-1 b	ch1	3.00	Box	4, -, -	Barycenter	5.0
HAT-P-1 b	ch2	3.50	Box	4, -, -	Barycenter	5.0
WASP-17 b	ch1	2.50	Annulus	, 6, 4	Barycenter	5.0
WASP-17 b	ch2	2.50	Annulus	, 6, 4	Barycenter	3.0
WASP-39 b	ch1	2.50	Annulus	, 6, 4	Barycenter	3.0
WASP-39 b	ch2	2.50	Annulus	, 6, 4	Barycenter	7.0
HAT-P-12 b	ch1	2.50	Annulus	, 6, 4	Moffat	-
HAT-P-12 b	ch2	2.50	Annulus	, 6, 4	Moffat	-
HAT-P-18 b	ch1	2.50	Annulus	, 6, 4	Barycenter	5.0
HAT-P-18 b	ch2	2.50	Annulus	, 6, 4	Moffat	-
TrES-2 b	ch1	2.50	Annulus	, 6, 4	Barycenter	5.0
TrES-2 b	ch2	2.50	Histogram	, -, -	Barycenter	3.0
WASP-4 b	ch1	2.50	Annulus	, 6, 4	Moffat	-
WASP-4 b	ch2	2.50	Annulus	, 6, 4	Barycenter	5.0
XO-2 b	ch1	2.50	Annulus	, 6, 4	Moffat	-
XO-2 b	ch2	2.50	Annulus	, 6, 4	Barycenter	7.0
GJ3470 b	ch1	2.50	Annulus	, 6, 4	Barycenter	3.0
GJ3470 b	ch2	2.50	Annulus	, 6, 4	Barycenter	3.0

Table 2.9: continued.

Planet	Channel	Aperture Size	Background Method	Background Params	Centroding Method	Centroding Params
		Pixels		Pixels		Pixels
WASP-21 b	ch1	2.50	Annulus	-, 6, 4	Barycenter	5.0
WASP-21 b	ch2	2.50	Annulus	-, 6, 4	Barycenter	5.0
WASP-31 b	ch1	2.50	Annulus	-, 6, 4	Barycenter	7.0
WASP-31 b	ch2	2.50	Annulus	-, 6, 4	Barycenter	7.0
WASP-1 b	ch1	2.50	Annulus	-, 6, 4	Barycenter	7.0
WASP-1 b	ch2	2.50	Annulus	-, 6, 4	Barycenter	3.0
HAT-P-26 b	ch1	2.50	Annulus	-, 6, 4	Barycenter	7.0
HAT-P-26 b	ch2	2.50	Annulus	-, 6, 4	Barycenter	5.0
WASP-107 b	ch1	2.25	Histogram	-, -, -	Barycenter	5.0
WASP-107 b	ch2	2.25	Histogram	-, -, -	Barycenter	3.0
WASP-13 b	ch1	2.25	Histogram	-, -, -	Gaussian	-
WASP-13 b	ch2	2.50	Histogram	-, -, -	Barycenter	3.0
WASP-121 b	ch1	1.00	Histogram	-, -, -	Barycenter	3.0
WASP-121 b	ch2	1.00	Box	4, -, -	Barycenter	3.0
WASP-69 b	ch1	2.00	Histogram	-, -, -	Gaussian	-
WASP-69 b	ch2	2.25	Histogram	-, -, -	Barycenter	3.0
WASP-67 b	ch1	2.00	Histogram	-, -, -	Moffat	-
WASP-67 b	ch2	2.00	Histogram	-, -, -	Moffat	-
HATS-7 b	ch1	2.00	Histogram	-, -, -	Barycenter	3.0
HATS-7 b	ch2	2.00	Histogram	-, -, -	Gaussian	-
WASP-29 b	ch1	2.25	Histogram	-, -, -	Gaussian	-
WASP-29 b	ch2	2.25	Histogram	-, -, -	Barycenter	3.0
HAT-P-41 b	ch1	2.25	Histogram	-, -, -	Barycenter	3.0
HAT-P-41 b	ch2	2.25	Histogram	-, -, -	Gaussian	-

Table 2.9: continued.

Planet	Channel	Aperture Size	Background Method	Background Params	Centroding Method	Centroding Params
		Pixels		Pixels		Pixels
WASP-101 b	ch1	2.25	Histogram	-,-,-	Barycenter	5.0
WASP-101 b	ch2	2.25	Histogram	-,-,-	Barycenter	3.0
WASP-131 b	ch1	2.25	Histogram	-,-,-	Barycenter	5.0
WASP-131 b	ch2	2.25	Histogram	-,-,-	Barycenter	3.0
WASP-36 b	ch1	2.00	Histogram	-,-,-	Gaussian	-
WASP-36 b	ch2	2.00	Histogram	-,-,-	Barycenter	3.0
WASP-63 b	ch1	2.25	Histogram	-,-,-	Barycenter	5.0
WASP-63 b	ch2	2.25	Histogram	-,-,-	Gaussian	-
WASP-79 b	ch1	2.50	Histogram	-,-,-	Barycenter	5.0
WASP-79 b	ch2	2.25	Histogram	-,-,-	Barycenter	3.0
WASP-94 Ab	ch1	2.50	Histogram	-,-,-	Moffat	-
WASP-94 Ab	ch2	2.25	Histogram	-,-,-	Barycenter	3.0
WASP-74 b	ch1	2.25	Histogram	-,-,-	Barycenter	3.0
WASP-74 b	ch2	2.00	Histogram	-,-,-	Barycenter	3.0
WASP-62 b	ch1	2.25	Histogram	-,-,-	Barycenter	3.0
WASP-62 b	ch2	2.25	Box	4,-,-	Barycenter	3.0
KELT-7 b	ch1	2.25	Histogram	-,-,-	Moffat	-
KELT-7 b	ch2	2.00	Histogram	-,-,-	Barycenter	3.0
Kepler-45 b	ch1	1.00	Histogram	-,-,-	Barycenter	3.0
Kepler-45 b	ch1	1.00	Histogram	-,-,-	Gaussian	-
Kepler-45 b	ch1	1.00	Histogram	-,-,-	Gaussian	-
Kepler-45 b	ch2	1.00	Histogram	-,-,-	Gaussian	-
Kepler-45 b	ch2	1.00	Histogram	-,-,-	Barycenter	3.0

Table 2.9: continued.

Planet	Channel	Aperture Size Pixels	Background Method	Background Params Pixels	Centroiding Method	Centroiding Params Pixels
Kepler-45 b	ch2	1.00	Histogram	-,-	Moffat	-
Kepler-45 b	ch2	1.00	Box	2,-,-	Gaussian	-

Table 2.10: Statistical tests outputted by our custom built pipeline. We measure the strength of the dependence on the chosen limb darkening parameters by varying them within 3σ of their error for 500 iterations, for each iteration we perform a least-squares fit and measure the variation on the measured R_p/R_s as a function of the final calculated error on R_p/R_s . Bad pix - the number of bad pixels corrected at the beginning of the analysis. Cut time (min) - the number of minutes cut from the beginning of each observation, this value is chosen such that we keep as much baseline as possible while minimizing the chi2 of the different possible baselines. Photon noise - the percentage above pure statistical noise we have for each lightcurve, typical values for *Spitzer* are 30–60% above photon noise.

Planet	$\lambda(\mu m)$	Vary 1d 3σ	Bad pix %	Cut time (min)	Photon noise %	MCMC acceptance fraction
HAT-P-32 b	3.6	0.804	0.306	0.0	1.31	0.384
HAT-P-32 b	4.5	0.603	0.056	0.0	1.32	0.383
XO-1 b	3.6	0.442	0.113	10.0	1.31	0.384
XO-1 b	4.5	0.194	0.061	10.0	1.23	0.385
HAT-P-1 b	3.6	0.018	0.270	10.0	1.47	0.386
HAT-P-1 b	4.5	0.035	0.052	10.0	1.34	0.385
WASP-17 b	3.6	0.198	0.309	50.0	1.41	0.385
WASP-17 b	4.5	0.106	0.058	30.0	1.37	0.386
WASP-39 b	3.6	1.188	0.294	20.0	1.39	0.382
WASP-39 b	4.5	0.416	0.062	0.0	1.32	0.381
HAT-P-12 b	3.6	0.387	0.289	10.0	1.35	0.382
HAT-P-12 b	4.5	0.273	0.062	10.0	1.34	0.383
HAT-P-18 b	3.6	0.382	0.243	20.0	1.47	0.382
HAT-P-18 b	4.5	0.183	0.067	0.0	1.34	0.385
TfES2 b	3.6	0.332	0.275	10.0	1.33	0.383
TfES2 b	4.5	0.193	0.069	5.0	1.26	0.385
WASP-4 b	3.6	1.424	0.295	10.0	1.53	0.384
WASP-4 b	4.5	0.771	0.049	30.0	1.48	0.385
XO-2 b	3.6	0.156	0.250	30.0	1.27	0.385
XO-2 b	4.5	0.052	0.048	20.0	1.24	0.383
GJ3470 b	3.6	0.523	0.007	5.0	1.22	0.382
GJ3470 b	4.5	0.246	0.006	5.0	1.28	0.383

Table 2.10: continued.

Planet	$\lambda(\mu\text{m})$	Vary ld	3σ	Bad pix %	Cut time (min)	Photon noise %	MCMC acceptance fraction
WASP-21 b	3.6	0.029	0.242	40.0	1.39	0.383	
WASP-21 b	4.5	0.020	0.070	10.0	1.32	0.383	
WASP-31 b	3.6	0.034	0.317	30.0	1.46	0.383	
WASP-31 b	4.5	0.037	0.055	10.0	1.43	0.383	
WASP-1 b	3.6	0.742	0.331	10.0	1.43	0.384	
WASP-1 b	4.5	0.490	0.055	40.0	1.39	0.387	
HAT-P-26 b	3.6	1.501	0.265	10.0	1.35	0.384	
HAT-P-26 b	4.5	0.689	0.069	10.0	1.29	0.383	
WASP-107 b	3.6	9.628	0.010	95.0	1.30	0.384	
WASP-107 b	4.5	4.939	0.048	15.0	1.26	0.385	
WASP-13 b	3.6	0.319	0.263	55.0	1.25	0.383	
WASP-13 b	4.5	0.137	0.060	10.0	1.26	0.384	
WASP-121 b	3.6	0.585	0.248	45.0	1.13	0.384	
WASP-121 b	4.5	0.343	0.070	30.0	1.08	0.382	
WASP-69 b	3.6	0.078	0.008	30.0	1.25	0.383	
WASP-69 b	4.5	0.057	0.009	25.0	1.21	0.382	
WASP-67 b	3.6	0.548	0.193	45.0	1.33	0.385	
WASP-67 b	4.5	0.196	0.075	30.0	1.24	0.385	
HATS-7 b	3.6	0.039	0.240	35.0	1.38	0.386	
HATS-7 b	4.5	0.017	0.056	30.0	1.40	0.385	
WASP-29 b	3.6	1.719	0.274	70.0	1.35	0.384	
WASP-29 b	4.5	0.822	0.054	10.0	1.22	0.381	
HAT-P-41 b	3.6	0.403	0.221	30.0	1.31	0.382	
HAT-P-41 b	4.5	0.201	0.061	150.0	1.27	0.384	
WASP-101 b	3.6	0.231	0.261	30.0	1.33	0.385	

Table 2.10: continued.

Planet	$\lambda(\mu\text{m})$	Vary ld 3 σ	Bad pix %	Cut time (min)	photon noise %	MCMC acceptance fraction
WASP-101 b	4.5	0.140	0.064	30.0	1.21	0.384
WASP-131 b	3.6	0.027	0.304	30.0	1.26	0.383
WASP-131 b	4.5	0.033	0.068	35.0	1.25	0.383
WASP-36 b	3.6	0.001	0.320	110.0	1.49	0.384
WASP-36 b	4.5	0.003	0.075	40.0	1.42	0.383
WASP-63 b	3.6	0.298	0.307	60.0	1.30	0.385
WASP-63 b	4.5	0.107	0.058	10.0	1.23	0.384
WASP-79 b	3.6	0.169	0.291	35.0	1.45	0.385
WASP-79 b	4.5	0.158	0.062	10.0	1.22	0.385
WASP-94 Ab	3.6	0.591	0.268	105.0	1.35	0.384
WASP-94 Ab	4.5	0.348	0.065	30.0	1.21	0.385
WASP-74 b	3.6	0.894	0.008	90.0	1.26	0.384
WASP-74 b	4.5	0.560	0.007	70.0	1.24	0.384
WASP-62 b	3.6	0.373	0.255	85.0	1.47	0.384
WASP-62 b	4.5	0.239	0.064	40.0	1.21	0.384
KELT-7 b	3.6	0.248	0.009	60.0	1.29	0.384
KELT-7 b	4.5	0.182	0.007	50.0	1.21	0.382
Kepler-45 b	3.6	0.022	0.277	30.0	1.50	0.383
Kepler-45 b	3.6	0.021	0.280	10.0	1.55	0.384
Kepler-45 b	3.6	0.026	0.269	40.0	1.71	0.384
Kepler-45 b	3.6	0.024	0.265	20.0	1.78	0.384
Kepler-45 b	4.5	0.005	0.047	20.0	1.44	0.384
Kepler-45 b	4.5	0.006	0.065	20.0	1.51	0.383
Kepler-45 b	4.5	0.008	0.059	20.0	1.41	0.383
Kepler-45 b	4.5	0.005	0.052	20.0	1.46	0.385

2.B VULCAN validation on HD 209458b

2.C Radius Anomaly

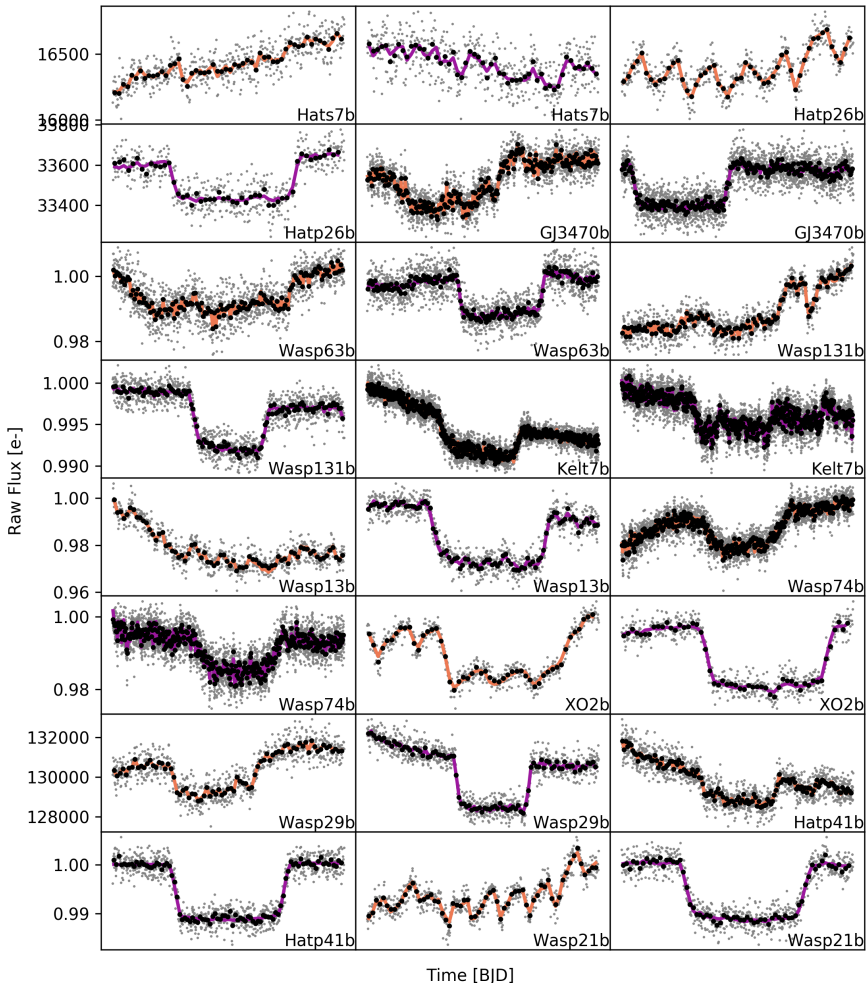


Fig. 2.14: Raw lightcurves for each planet. Flux binned in 5 minutes is shown in black and 30 seconds is shown in gray. Colored lines indicate the best-fit instrumental and transit model from our MCMC analysis.

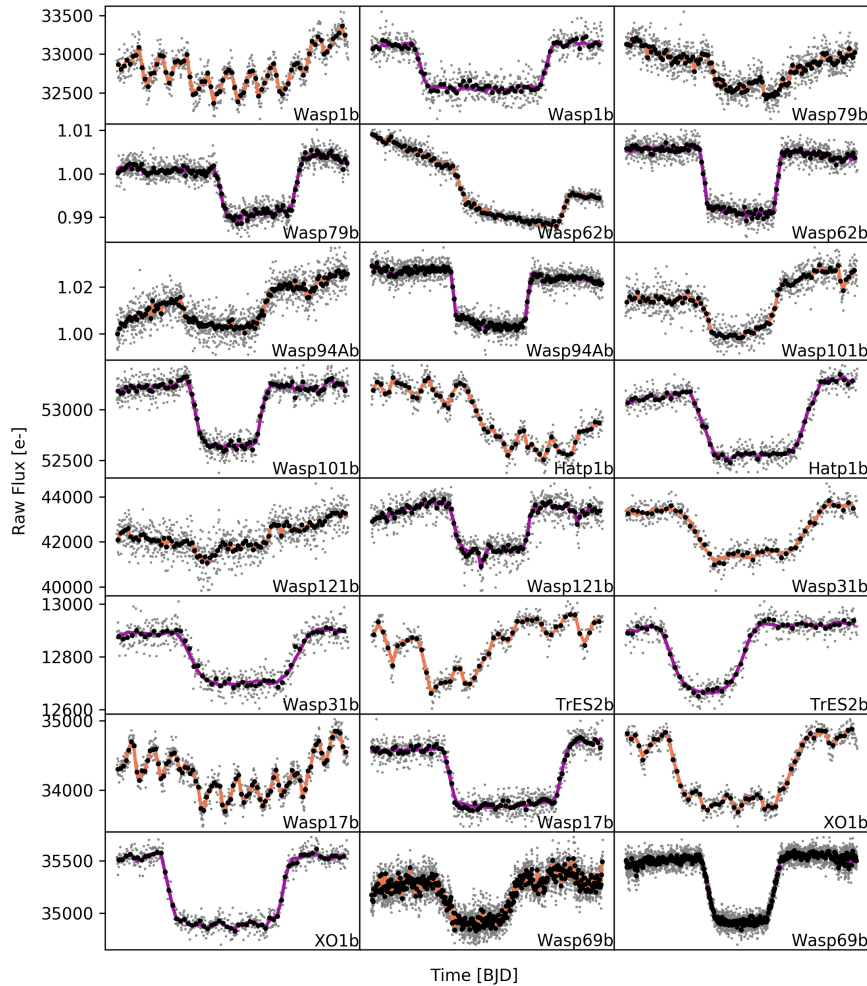


Fig. 2.14: Continued.

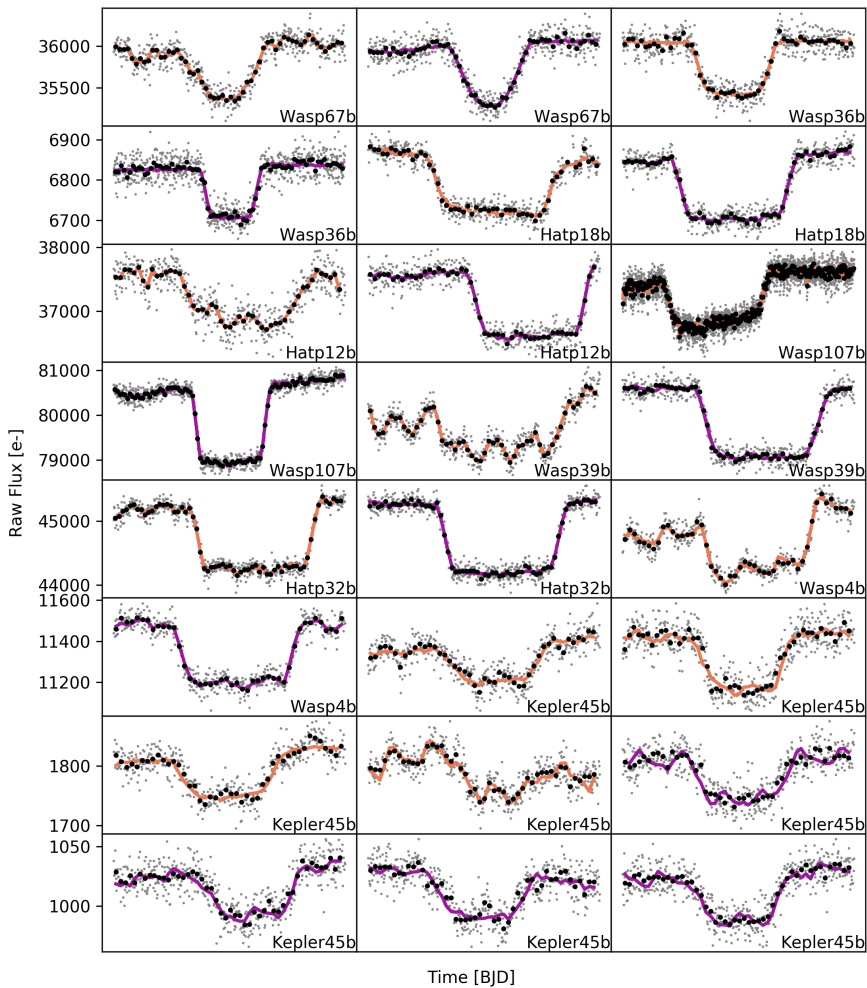


Fig. 2.14: *Continued.*

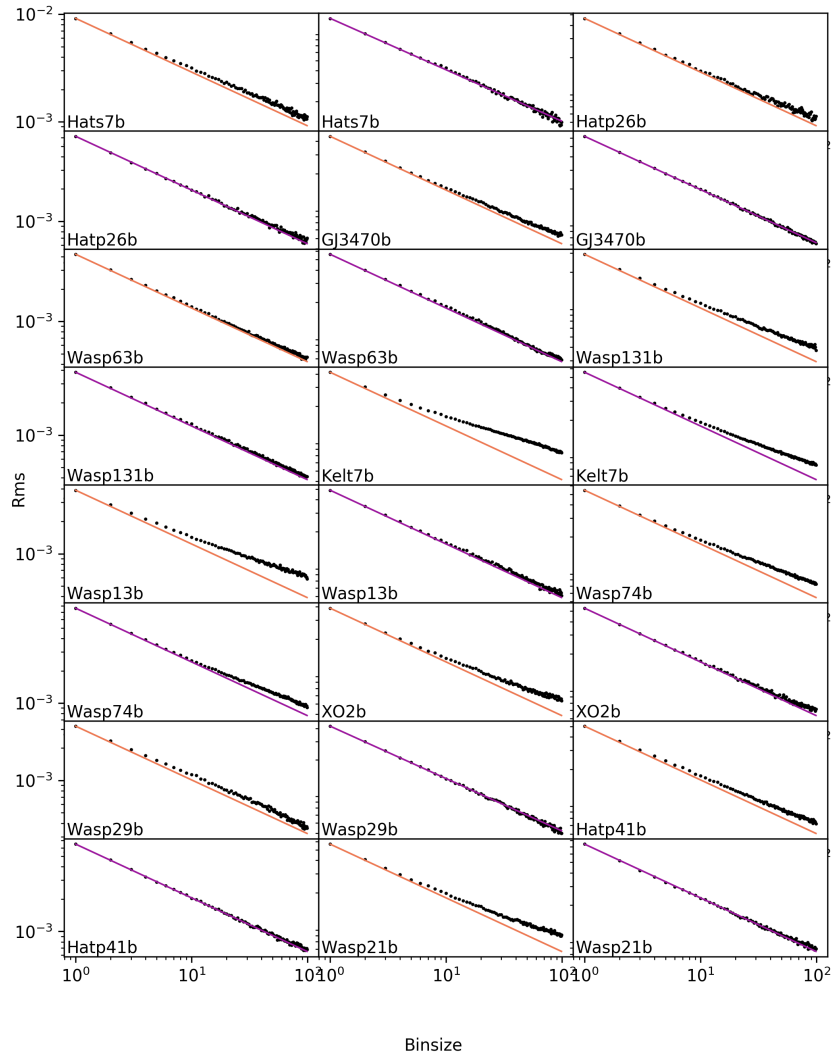


Fig. 2.15: RMS vs normalized binsize of each of the fitted lightcurves. Straight line is the \sqrt{N} theoretical value.

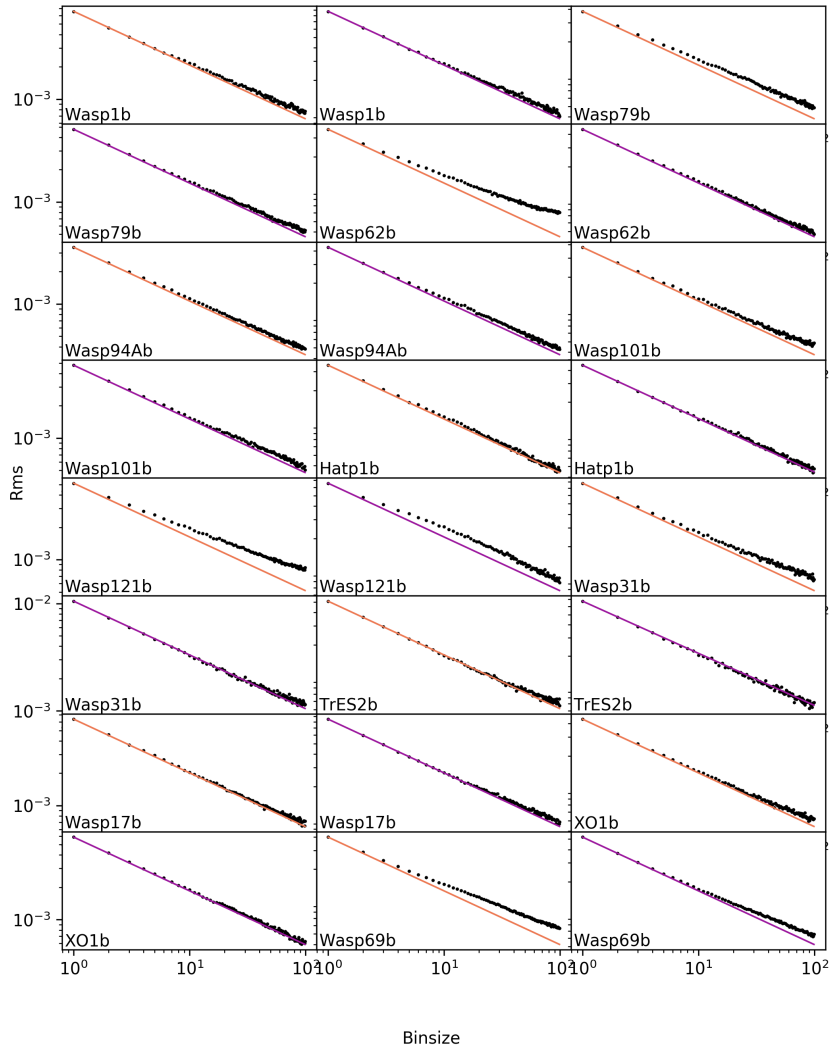


Fig. 2.15: *Continued.*

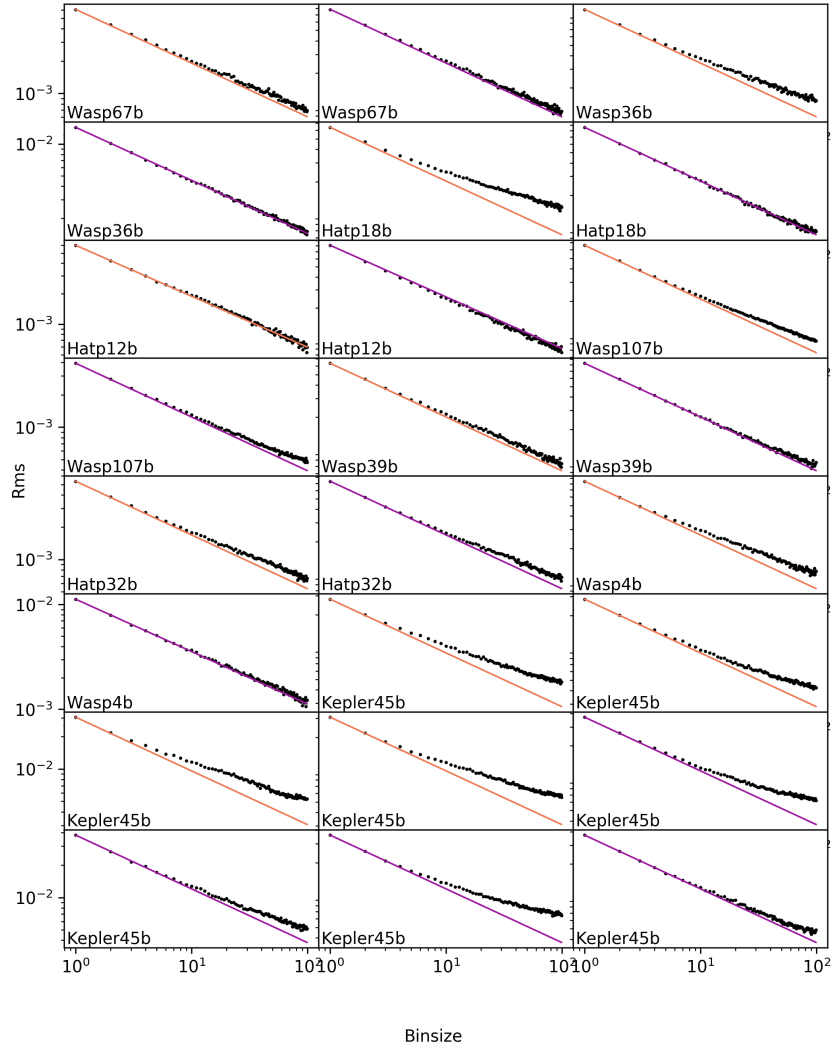


Fig. 2.15: *Continued.*

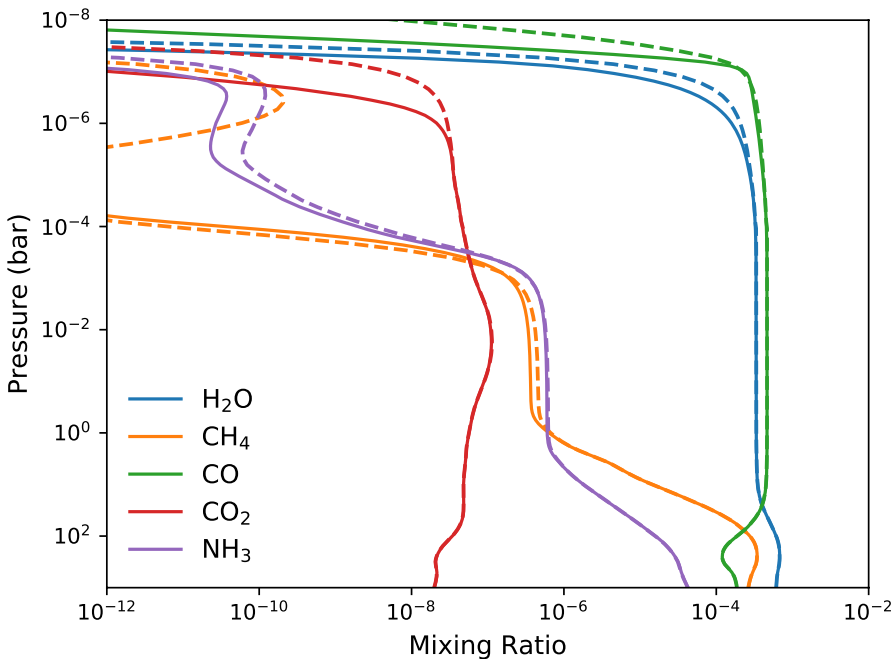


Fig. 2.16: Abundance mixing ratios at different pressures for the main species in the *Spitzer* bandpasses in HD 209458 b. The solid line shows the results from our VULCAN calculation and the dashed line the results from Moses et al. (2011). The temperature and eddy-diffusion structure are taken the same as the dayside-average P-T profile in Moses et al. (2011). The solar flux is also used as an analog for HD 290458 at a distance of 0.04747 AU.

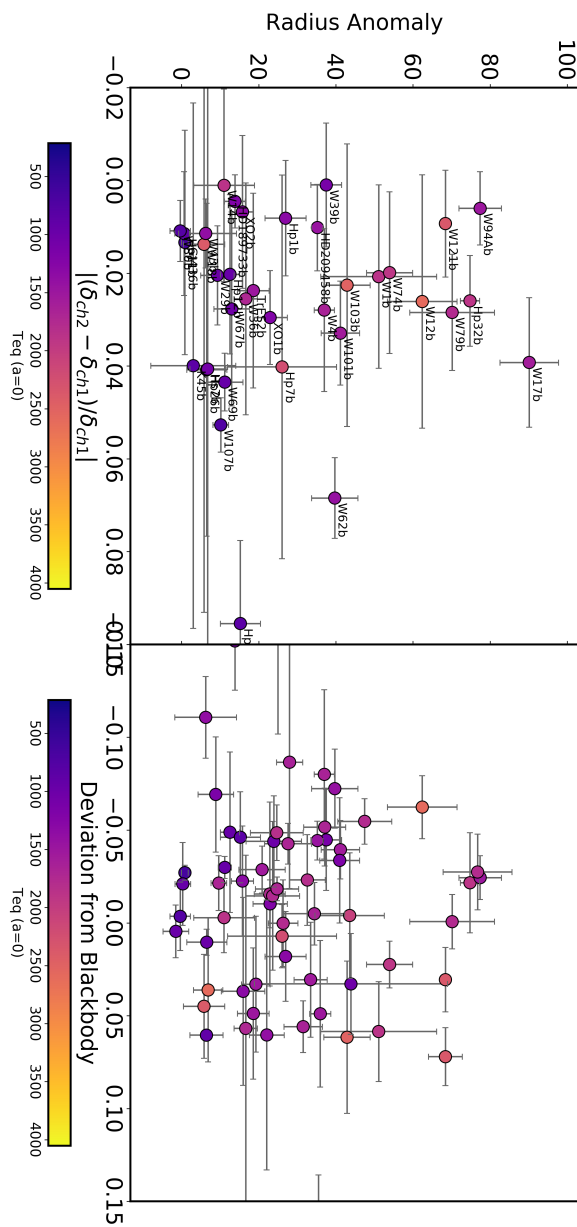


Fig. 2.17: Radius Anomaly (calculated using models from Thorngren et al. (2016); Thorngren & Fortney (2018) against the absolute value of the normalized difference in transit depths for the available planets. Color scale is the equilibrium temperature of the planet.

3

A TRANSITION BETWEEN THE HOT AND THE ULTRA-HOT JUPITER ATMOSPHERES

Claire Baxter, Jean-Michel Désert, Vivien Parmentier, Michael Line, Jonathan J. Fortney, Jacob Arcangeli, Jacob L. Bean, Kamen O. Todorov, Megan Mansfield

Astronomy & Astrophysics, 639, A36 (2020)

Abstract

A key hypothesis in the field of exoplanet atmospheres is the trend of atmospheric thermal structure with planetary equilibrium temperature. We explore this trend and report here the first statistical detection of a transition in the near-infrared (NIR) atmospheric emission between hot and ultra-hot Jupiters. We measure this transition using secondary eclipse observations and interpret this phenomenon as changes in atmospheric properties, and more specifically in terms of transition from non-inverted to inverted thermal profiles. We examine a sample of 78 hot Jupiters with secondary eclipse measurements at $3.6\text{ }\mu\text{m}$ and $4.5\text{ }\mu\text{m}$ measured with *Spitzer* Infrared Array Camera (IRAC). We calculate the planetary brightness temperatures using PHOENIX models to correct for the stellar flux. We measure the deviation of the data from the blackbody, which we define as the difference between the observed $4.5\text{ }\mu\text{m}$ eclipse depth and that expected at this wavelength based on the brightness temperature measured at $3.6\text{ }\mu\text{m}$. We study how the deviation between 3.6 and $4.5\text{ }\mu\text{m}$ changes with theoretical predictions with equilibrium temperature and incoming stellar irradiation. We reveal a clear transition in the observed emission spectra of the hot Jupiter population at $1660 \pm 100\text{ K}$ in the zero albedo, full redistribution equilibrium temperature. We find the hotter exoplanets have even hotter daysides at $4.5\text{ }\mu\text{m}$ compared to $3.6\text{ }\mu\text{m}$, which manifests as an exponential increase in the emitted power of the planets with stellar insolation. We propose that the measured transition is a result of seeing carbon monoxide in emission due to the formation of temperature inversions in the atmospheres of the hottest planets. These thermal inversions could be caused by the presence of atomic and molecular species with high opacities in the optical and/or the lack of cooling species.

Our findings are in remarkable agreement with a new grid of 1D radiative and convective models varying metallicity, carbon to oxygen ratio (C/O), surface gravity, and stellar effective temperature. We find that the population of hot Jupiters statistically disfavors high C/O planets ($\text{C}/\text{O} \geq 0.85$).

3.1 Introduction

Observing the infrared secondary eclipse of transiting tidally locked hot Jupiters allows us to measure their dayside thermal flux (e.g., Charbonneau et al. 2005; Deming et al. 2005; Cowan & Agol 2011a,b; Triaud et al. 2014; Schwartz & Cowan 2015; Schwartz et al. 2017; Zhang & Showman 2018b; Garhart et al. 2020). The dayside flux is determined by the temperature pressure (T-P) profile and the atmospheric opacities. In turn, the T-P profile is determined by the albedo, heat redistribution, and atmospheric opacities. Hot Jupiters have equilibrium temperatures around 1500K. But recently, a newer class of hot Jupiters has emerged, the ultra-hot Jupiters (UHJ). Ultra-hot Jupiters have equilibrium temperatures in excess of 2000K and receive irradiation 10-100 times the insolation of other hot Jupiters (e.g., Figure 9. Parmentier et al. 2018). There is evidence that they exhibit different atmospheric properties from their cooler counterparts (e.g., Bell et al. 2017; Arcangeli et al. 2018; Mansfield et al. 2018b; Parmentier et al. 2018; Kreidberg et al. 2018b). Investigations by Hubeny et al. (2003); Fortney et al. (2006) and Fortney et al. (2008) suggest that temperature inversions could appear in hot Jupiter atmospheres at temperatures as low as 1700K resulting from a fundamental change in atmospheric opacity due to TiO and VO (Gandhi & Madhusudhan 2019). Furthermore, Thorngren et al. (2019) suggest that the deep atmospheres of these planets are so hot that TiO and VO are able to stay in the gas phase at \sim 1700-2000K rather than being cold-trapped into clouds at depth.

Previous studies have looked for signatures of physical processes (chemistry, thermal inversions, redistribution, albedo, stellar activity) in a large sample of atmospheres, specifically by looking at the thermal eclipse measurements (Knutson et al. 2010; Cowan & Agol 2011b; Triaud et al. 2014; Schwartz & Cowan 2015; Schwartz et al. 2017; Zhang et al. 2018; Garhart et al. 2020; Keating et al. 2019; Melville et al. 2020). Triaud et al. (2014) created color-magnitude diagrams of planets with available *Spitzer*/IRAC eclipses in all four bandpasses (3.6, 4.5, 5.8, and 8.0 μm). They found that hot Jupiters lie closer to brown dwarf (MLT) colors than they do to blackbodies, (i.e., they do not have featureless spectra in the infrared).

Additional studies have focused on breaking the degeneracy between albedo and redistribution efficiency. Cowan & Agol (2011b) perform a statistical study on the energy budget of 24 hot Jupiters with secondary eclipses in at least one infrared waveband ($>0.8 \mu\text{m}$) and, when available, phase variation measurements. They found the sample as a whole could be represented with low Bond albedos. Additionally, in combination with Zhang et al. (2018), there is evidence of low redistribution efficiencies of the eight hottest planets (WASP-12b, WASP-18b, HAT-P-7b, OGLE-TR-56b, WASP-19b, CoRoT-1b, WASP-33b, HD149026b), suggesting that these atmospheres could exhibit different behaviors from the rest.

Following this, Schwartz & Cowan (2015) calculate the dayside temperature of 50 planets with thermal eclipse measurements in at least two infrared wavelengths ($>0.8 \mu\text{m}$). They note an unexpectedly steep correlation, such that the hotter planets had temperatures even hotter than irradiation temperature predictions. This supports the previous claim by Cowan & Agol (2011b) that the hottest planets have lower Bond albedo and/or less efficient heat

transport. Schwartz et al. (2017) incorporate phase offsets into their energy budget calculations of six planets, which pushes the results toward lower Bond albedos and slightly higher heat transport than before. Keating et al. (2019) and Beatty et al. (2019) estimate the nightside temperature of several hot Jupiters using *Spitzer* phase curves and find that despite the different levels of irradiation, they all demonstrate similar nightside temperatures. This suggests that they might all have some chemically similar high optically thick cloud layer that is emitting at the nightside temperature.

Additionally, Garhart et al. (2020) perform uniform analyses of 36 planets with *Spitzer*/IRAC secondary eclipses at 3.6 and 4.5 μm . They find an increasing trend in the brightness temperature ratio with equilibrium temperature. They find that this trend is present throughout the entire temperature range continuously between the coolest and the hottest planets (800K to 2500K).

Our study builds on the previous works by expanding to 78 planets, with almost double the number of ultra-hot Jupiters, and by employing a careful treatment of the stellar flux. We use the two warm *Spitzer*/IRAC bandpasses (3.6 μm and 4.5 μm) (Fazio et al. 2004; Werner et al. 2004) to study the near infrared trends in hot Jupiter emission. At these wavelengths, based on equilibrium chemistry, we expect to see spectral signatures of methane (CH₄) (in the cooler planets) and carbon monoxide (CO) (in the hotter planets). More specifically, we focus on the deviation of these points from a blackbody, particularly on its effect when including the ultra-hot Jupiters. Furthermore, we now compare our results to a grid of forward models that encompass the processes relevant for the coolest to the ultra-hot planet atmospheres (molecular dissociation, H⁻ opacity, latent heat, and the formation of temperature inversions). In Section 3.2 we describe the *Spitzer*/IRAC observations and data collection. In Section 3.3 we describe the data analysis and the various temperatures used. In Section 3.4 we present the results of the survey, we make a comparison to blackbodies, and demonstrate a transition to the ultra-hot Jupiters. In Section 3.5 we interpret our results in terms of albedo, redistribution, and temperature inversions.

3.2 Observations

Our comprehensive survey is composed of 78 planets with eclipse depths taken with the *Spitzer*/IRAC at 3.6 μm and 4.5 μm . The literature data for the planets in this survey were collected via exoplanets.org (Han et al. 2014), exoplanet.eu (Schneider et al. 2011), or directly from the studies. We analyzed two 4.5 μm eclipses of KELT-9b (Mansfield et al. 2020) using our custom pipeline (Baxter et al. in prep.) implementing Pixel Level Decorrelation to correct systematics (Deming et al. 2015) (Appendix 3.D). The planets, eclipse depths, stellar parameters, references, and key results and uncertainties are displayed in Table 3.2. Our work relies on the calculation of the equilibrium temperature, and since this parameter is sensitive to the eccentricity of the planetary orbit, especially on short period exoplanets, we opted to perform an eccentricity cut and only select planets with eccentricity less than 0.2.

3.3 Data analysis

3.3.1 Calculating the planetary brightness temperatures

The secondary eclipse depth measures the ratio of the planetary flux (F_p) to the stellar flux (F_s) at a given spectral bandpass. The planets selected for our survey have eclipse depths (F_p/F_s) measured in the two *Spitzer*/IRAC bandpasses (3.6 μm and 4.5 μm) (Werner et al. 2004). We remove the contribution of the stellar flux from the eclipse depths and convert the planetary flux to flux density ($\text{erg cm}^{-2} \text{s}^{-1} \text{\AA}^{-1}$), which we use to calculate the brightness temperature by inverting the Planck function for the planet

$$T_b(\lambda) = \frac{hc}{k_b\lambda} \left[\ln \left(\frac{2hc^2\pi\delta_{tra}}{\lambda^5 \bar{F}_s(\lambda)\delta_{occ}} \right) \right]^{-1}, \quad (3.1)$$

where δ_{tra} is the published transit depth (R_p/R_s)², and δ_{occ} is the eclipse depth measured at the *Spitzer* wavelengths (F_p/F_s), λ is the wavelength of the observed eclipse depth, either 3.6 μm or 4.5 μm , and $\bar{F}_s(\lambda)$ is the flux density of the stellar model weighted by the *Spitzer*/IRAC spectral response at this wavelength.

Since both the planetary and the stellar model need to be integrated over the *Spitzer* spectral response functions, the spectral response weighted brightness temperature needs to be calculated iteratively. We create a grid of brightness temperatures around an estimated value (obtained from solving equation 3.1 directly) and convert this to a grid of eclipse depths by convolving both the planetary blackbody function and the stellar models with the spectral responses. Our adopted brightness temperature is thus the one that produces the eclipse depth which best matches the data (lowest χ^2). For this minimization we chose grids encompassing 200K around the calculated brightness temperatures, with step sizes of 2K, which is much smaller than the typical uncertainty of 100K. We then confirmed that we had reached a minimum χ^2 for each planet.

The integration of the spectral response with the model flux densities is done using the following equation:

$$\bar{F}(\lambda) = \frac{\int_0^\infty F(\lambda)\lambda R(\lambda)d\lambda}{\int_0^\infty \lambda R(\lambda)d\lambda}. \quad (3.2)$$

Here $R(\lambda)$ is the spectral response function at either 3.6 μm or 4.5 μm [e-/photon] taken from Quijada et al. (2004) and $F(\lambda)$ is the flux density of the planet or the star. The output, $\bar{F}(\lambda)$, is the average flux density that would be observed with *Spitzer*/IRAC.

We decided to estimate the uncertainties on the adopted brightness temperatures by taking the minimum and maximum eclipse depth (based on the 1σ uncertainty presented in Table 3.2) and propagating it through Equation 3.1 to calculate a minimum and maximum brightness temperature. The 1σ uncertainty on the brightness temperature is then the mean of these two deviations from the best fit brightness temperature. Since the Rayleigh-Jeans limit is for long wavelengths and high temperatures, the Rayleigh-Jeans formula cannot be simply used

to calculate the uncertainties as the temperatures of the planets are overestimated. However, the formula can be used to get an estimate of the uncertainties provided the temperatures used in the propagation are those calculated using the full Planck function. Our method estimates uncertainties that are equivalent to those calculated using the differentiated and propagated Rayleigh-Jeans law formula.

We test different stellar models to correct the stellar flux contribution when calculating T_B (see Appendix 3.B). We then compare these temperatures to theoretical predictions for the zero albedo full redistribution equilibrium temperature $T_{eq,0}$, irradiation temperature T_0 , and maximum dayside temperature T_{max} . Throughout this paper we fit all correlations with an orthogonal distance regression (ODR), and obtain uncertainties by bootstrapping (see Appendix 3.A.1).

3.3.2 Extracting the planetary flux deviation from a blackbody

We define a new metric that allows us to self-consistently compare how similar these planets are to blackbodies. We do this by first calculating the brightness temperature at $3.6\text{ }\mu\text{m}$ then we propagate this as a blackbody to $4.5\text{ }\mu\text{m}$ and recalculate the expected eclipse depth at $4.5\text{ }\mu\text{m}$. We measure the deviation between this value and the actual $4.5\text{ }\mu\text{m}$ eclipse depth (Observed - Calculated) and call it the deviation from the blackbody (devBB). The mathematical expression for devBB is the following¹:

$$\text{devBB} = \frac{B_{4.5}(T_{B_{3.6}})}{F_{S_{4.5}}} \left(\frac{R_P}{R_S} \right)^2 - (F_P/F_S)_{4.5\text{ observed}}, \quad (3.3)$$

where $B_\lambda(T)$ is the Planck blackbody function of temperature T calculated at wavelength λ . In this case T is the brightness temperature calculated from the observed Spitzer eclipse depth over the $3.6\mu\text{m}$ Spitzer bandpass and λ is the $4.5\mu\text{m}$ Spitzer bandpass. $F_{S_{4.5}}$ is the PHOENIX model stellar flux over the $4.5\mu\text{m}$ Spitzer bandpass, $(R_P/R_S)^2$ is the transit depth, and $(F_P/F_S)_{4.5\text{ observed}}$ is the observed Spitzer eclipse depth at $4.5\mu\text{m}$. Each of the fluxes are integrated with the Spitzer spectral response function using equation 3.2.

A positive deviation means that the $4.5\text{ }\mu\text{m}$ eclipse depth is greater than expected. Uncertainties are fully propagated from the uncertainties on the eclipse depths at 3.6 and $4.5\text{ }\mu\text{m}$. Results are displayed in Table 3.2. Since devBB is the difference of flux ratios it is unitless, but for convenience we express it as the difference in percentages. We also note that using the Rayleigh-Jeans law, we can demonstrate that the deviation from the blackbody is equivalent to the normalized difference in the brightness temperatures. However, it has the advantage that it is derived directly from an observable quantity, the planet-to-star flux ratio.

¹This section has been edited from the original publication to contain the mathematical expression of the deviation from the blackbody

3.3.3 Irradiation, equilibrium, effective, and max dayside temperatures definitions

Following Hansen (2008), we define the irradiation temperature (T_0) as the temperature of the planetary atmosphere at the substellar point caused by the irradiation received from the host star at the distance of the planetary orbit $T_0 = T_{eff} \sqrt{R_*/a}$, where T_{eff} is the stellar effective temperature, R_* is the stellar radius, and a is the semi-major axis of the orbit (assuming a circular orbit). The equilibrium temperature is another theoretical calculation that takes into account the albedo of the planet and the amount of redistribution over the planet's surface. The equilibrium temperature for isotropic (full) redistribution of incoming irradiation is thus defined as $T_{eq} = T_{eff}(1 - A_B)^{1/4} \sqrt{R_*/2a}$, where A_B is the planetary Bond albedo. When we take the Bond albedo to be zero and assume full redistribution, the equilibrium temperature can be written in terms of the irradiation temperature: $T_{eq,0} = (1/4)^{1/4} T_0$. Subsequently, we define the disk integrated apparent maximum dayside temperature (Schwartz et al. 2017) as the equilibrium temperature where the incoming radiation is immediately re-radiated (i.e., no redistribution: $T_{eq,max} = (2/3)^{1/4} T_0$). We do not expect any planets to have temperatures hotter than this as we do not expect any heat from contraction since most of these stars have ages $\gtrsim 1$ Gyr. Furthermore, since temperatures add to the fourth power, even planets with a substantially high internal temperature (e.g., Thorngren et al. 2019) would be within the noise for this study. The uncertainties on these temperatures are calculated through full propagation of uncertainties from the stellar and orbital parameters.

The final temperature used in our analysis is the planetary effective temperature used in Appendix 3.C. We calculate the average brightness temperature, which we take as the error weighted mean of the two brightness temperatures, such that $\langle T_B \rangle = (T_{b_{3.6}}/\sigma_{3.6}^2 + T_{b_{4.5}}/\sigma_{4.5}^2)/2$, where T_{b_λ} is the brightness temperature at wavelength λ and σ_λ is the corresponding error on this measurement. $\langle T_B \rangle$ is algebraically the same as T_{eff} defined in Schwartz & Cowan (2015) and Cowan & Agol (2011b).

3.3.4 Grid of forward emission models to interpret observations

We utilize a new grid of cloud-free self-consistent radiative-convective thermochemical-equilibrium grid models, ScCHIMERA, originally developed and validated against analytical solutions and previously published brown dwarf models in Piskorz et al. (2018) and subsequently applied to the UHJ datasets presented in Arcangeli et al. (2018); Mansfield et al. (2018a) and Kreidberg et al. (2018b). These new models are a successor to the Fortney et al. (2008) models.

Briefly, the model solves for the temperature profile through a vertical flux divergence minimizing via the Newton-Raphson iteration (McKay et al. 1989) utilizing the two stream source function technique for the radiative fluxes (Toon et al. 1989). Mixing length theory is used to compute the convective fluxes as prescribed in Hubeny (2017). Opacities (at R=100, 0.3 - 200 μm , where available) are treated within the correlated-K resort-rebin mixing frame-

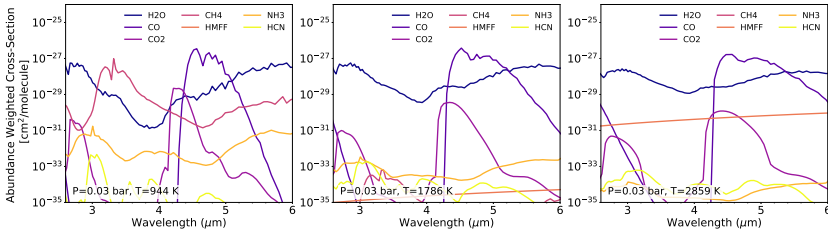


Fig. 3.1: Abundance weighted cross sections for a selection of the emission model grid described in Section 3.3.4, (Piskorz et al. 2018). Each panel presents the abundance weighted cross sections for planets with equilibrium temperatures of 1000K, 1800K, and 3000K. Each TP profile is for a planet around a 5300K star with C/carbon to oxygen (O =) 0.54, $[M/H] = 0.0$, $\log g = 3.0$; the full grid is shown in the first panel of Figure 3.2. The plotted abundances are taken from a pressure of 30mbar, resulting in probing temperatures of 944K, 1786K, and 2859K in each of the respective TP profiles.

work (Lacis & Oinas 1991; Amundsen et al. 2017) and include hot Jupiter-to-UHJ relevant atoms/molecules/ions: H_2 - H_2 /He collision induced absorption, H_2O , CO, CO_2 , CH_4 , NH_3 , H_2S , HCN, C_2H_2 , Na, K, TiO, VO, FeH, H^- free-free/bound-free, PH_3 , Fe, Fe^+ , Ca, and Mg, obtained from a variety of sources (ExoMol, Freedman et al. (2008, 2014) and Kurucz & Bell (1995)). Figure 3.1 demonstrates a selection of the abundance weighted opacities extracted at the approximate pressure of the *Spitzer* contribution functions for three example planets (1000K, 1800K, and 3000K). Atom/Molecule/Ion abundances are computed using the Gibbs free energy minimization routine, NASA CEA2 (Gordon & McBride 1994), given the specified scaling to the Lodders et al. (2009) elemental abundances. This approach also accounts for vertically varying abundances from thermal dissociation. The model assumes full redistribution at a given irradiation temperature, and an internal temperature of 150K (however, see Thorngren et al. (2019)). We utilize the PHOENIX (Allard et al. 2011) models derived from the STScI pysynphot routine for the incident stellar flux (assuming a hemispheric mean incident flux– $u=0.5$).

The model grid consists of 297 spectra and spans a range of carbon to oxygen ratios ($C/O = 0.1, 0.54, 0.84$), planetary surface gravities ($\log(g) = 2.5, 3.0, 3.5, 4.0$), metallicity ($[M/H] = -1, 0, 1, 1.5$), stellar temperatures ($T_{eff} = 4300, 5300, 6300$ K), and planetary equilibrium temperatures ($T_{eq,0} = 1000-3600$ K in steps of 100K). Figure 3.2 demonstrates a selection of the emission spectra at the *Spitzer* wavelengths, where F_p/F_s is calculated using $R_s/R_p = 9.95$. We show three tracks corresponding to the three different stellar temperatures. For 4300K and 6300K we fix $[M/H] = 0$, $C/O = 0.54$, and $\log(g) = 3$, whereas for 5300K we show $[M/H] = 1.5$, $C/O = 0.54$, and $\log(g) = 3$. The right panel contains the temperature pressure profile, which shows the atmosphere turning isothermal very briefly for planetary atmospheres with an equilibrium temperature of 1900K and the temperature inversion appearing for models with equilibrium temperature of 2200K. The left panel demonstrates the emission spectra: carbon monoxide can be seen clearly in emission for the hottest temperatures where the inversion exists.

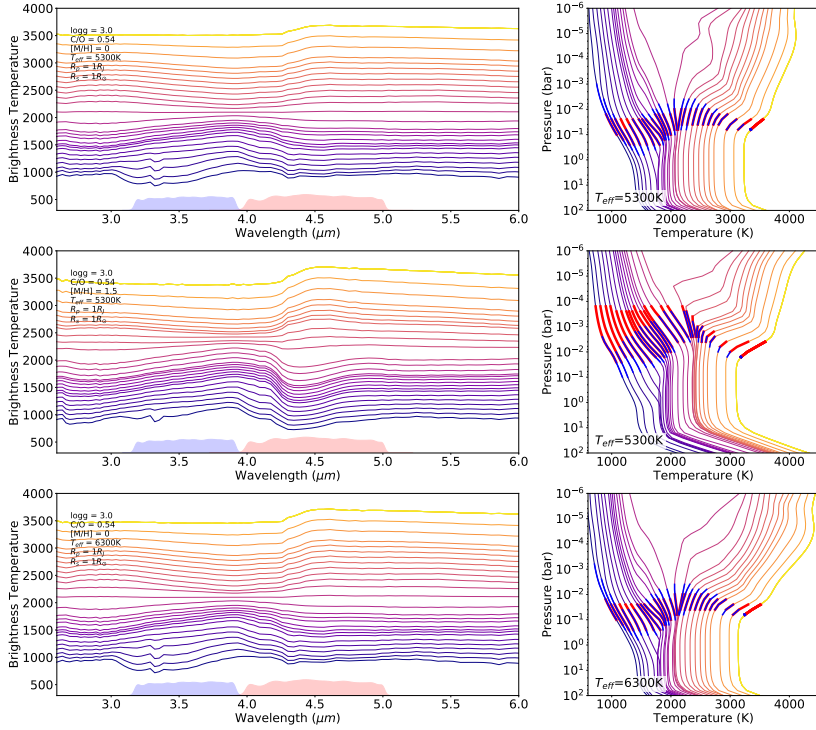


Fig. 3.2: ScCHIMERA model emission spectra for hot Jupiters (Piskorz et al. 2018) for a set of models of varying equilibrium temperature with $\log(g) = 3.0$, C/O = 0.54, [M/H] = 0, $R_p = 1R_J$, and $R_* = 1R_\odot$. In each row we show the flux ratio (left) and temperature pressure profiles (right) for the 1D atmospheres of planets with colors indicating the increasing equilibrium temperatures ranging from 1000K to 3600K (in 100K increments). Top, middle, and bottom rows show the grid for planets around a 4300K, 5300K, and a 6300K star, respectively. Blue and red shaded regions in the left panel indicate the *Spitzer*/IRAC 3.6 μm and 4.5 μm bandpasses, respectively. Blue and red bold lines on the TP profiles correspond to the FWHM of the weighting functions for the 3.6 μm and 4.5 μm channels.

3.4 Results

3.4.1 Deviation between equilibrium and brightness temperatures

In Figure 3.3 we present the measured brightness temperatures plotted against $T_{eq,0}$ for the two IRAC bandpasses. We fit linear functions using an orthogonal distance regression (ODR), see Appendix 3.A.1). If the brightness temperature is the same as $T_{eq,0}$ then the gradient

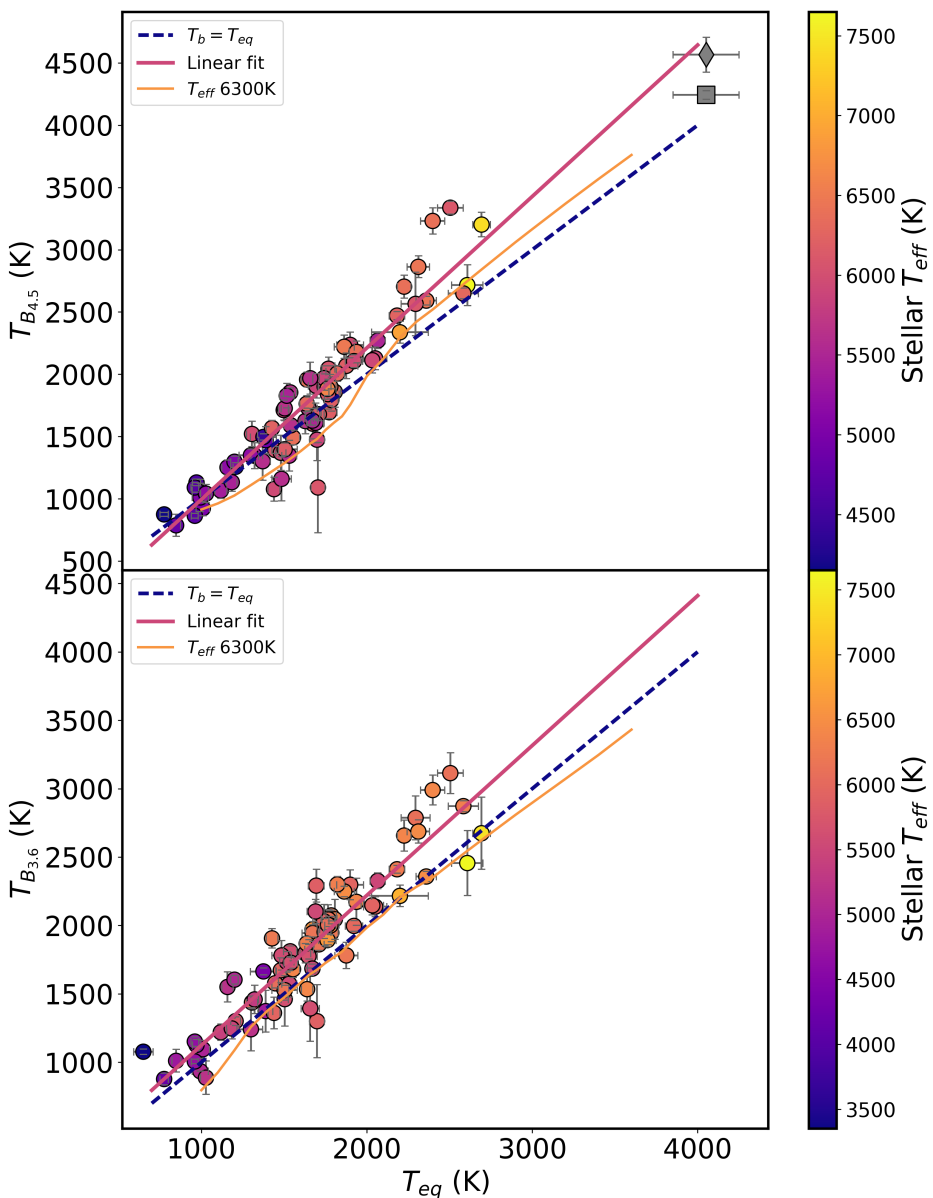


Fig. 3.3: Brightness temperatures vs $T_{eq,0}$ (full redistribution, 0 albedo) at 3.6 μm (bottom panel) and 4.5 μm (top panel). Magenta trend lines show a linear ODR fit to the data (gradient in the legends) and the blue dashed line shows the $T_B = T_{eq,0}$ slope (gradient of 1). The gray points are the 4.5 μm brightness temperatures of KELT-9b: the square is our analysis presented in Appendix 3.D, and the diamond is the analysis presented in Mansfield et al. (2020). Forward ScCHIMERA models are displayed in orange for one stellar effective temperature of 6300K

of the slope will be unity. The measured gradients at $3.6\text{ }\mu\text{m}$ and $4.5\text{ }\mu\text{m}$ are 1.09 ± 0.06 and 1.19 ± 0.06 , respectively. At $4.5\text{ }\mu\text{m}$, this is a statistically significant (3.2σ) deviation from $T_{eq,0}$. On the other hand, at $3.6\text{ }\mu\text{m}$ the brightness temperatures are consistent with the equilibrium temperature (1.5σ). Thus, the source of this deviation exhibits a stronger effect at $4.5\text{ }\mu\text{m}$ compared to $3.6\text{ }\mu\text{m}$. Furthermore, comparing to the grid of forward models demonstrates that the different stellar temperature model grids converge at lower temperatures and diverge at higher temperatures. We measure the residuals and standard deviations of the brightness temperatures to the best fit lines in three equally spaced temperature regimes (649K-1330K, 1330K-2012K, 2012K-2693K). At $4.5\text{ }\mu\text{m}$ the standard deviation of the residuals is 83K, 193K, and 258K, respectively, for the low, medium, and high temperature bins. At $3.6\text{ }\mu\text{m}$ they are 157K, 187K, and 242K. The standard deviation of the residuals increases with increasing temperature, following the trends predicted by the models with temperature inversions in Figure 3.3.

Despite doing an eccentricity cut at an eccentricity of 0.2, there are still some planets with a nonzero eccentricity; these planets are typically outliers in Figure 3.3. Eccentric orbits result in stellar insolation changing throughout the planets orbit, and thus it is expected that their measured brightness temperatures deviate from standard equilibrium temperature calculations (which assumes a circular orbit).

3.4.2 Increasing trend in brightness temperature ratio versus equilibrium temperature

We demonstrate an increasing trend in the brightness temperature ratio with the $T_{eq,0}$ (Figure 3.4). This is a manifestation of the $4.5\text{ }\mu\text{m}$ individual brightness temperatures deviating more from equilibrium than $3.6\text{ }\mu\text{m}$ as seen in Figure 3.3. We fit the increasing trend, and find a slope of 95 ± 31 ppm per Kelvin for the PHOENIX models, which is significant to 3.1σ . In addition to the linear fit we also test a bilinear model, but we find that the change in the BIC does not favor this scenario. Finally, we make a comparison with our grid of forward models and find that they are consistent with the data.

3.4.3 Increasing trend in planetary deviation from a blackbody

Assuming that the planetary flux is a blackbody set at $3.6\text{ }\mu\text{m}$, we calculate the predicted eclipse depth at $4.5\text{ }\mu\text{m}$ and then calculate the deviation from the measured eclipse depth. Figure 3.5 presents this deviation as a function of the equilibrium temperature. We fit three different trend lines to the data and compare their Bayesian information criteria (BIC). First, we fit a simple linear function (two free parameters), then we fit a bilinear model (four free parameters), and finally a bilinear model with the slope of the first line segment fixed to zero (three free parameters). The χ^2_{red} for the three models are 3.77, 3.51, and 3.50 and the BICs are 279, 261, and 259 for the straight line, bilinear, and fix bilinear, respectively. According to the ΔBIC and χ^2_{red} , the fixed bilinear model provides the best fit. This model captures

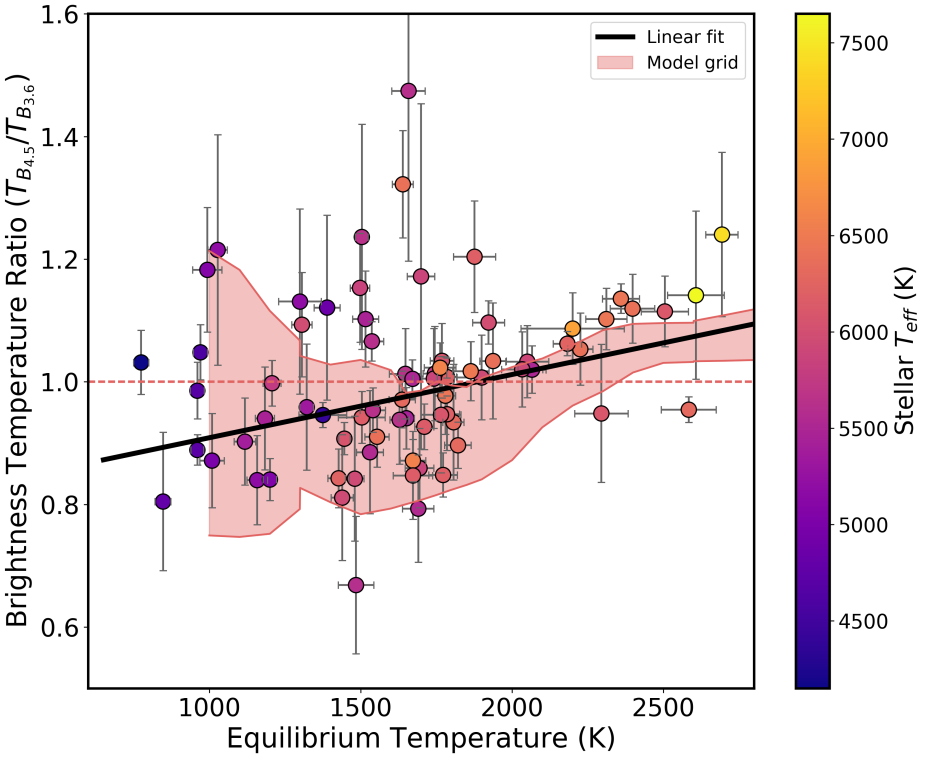


Fig. 3.4: Brightness temperature ratio ($T_{B_{4.5}}/T_{B_{3.6}}$) vs the equilibrium temperature ($T_{eq,0}$) of all of the available planets with secondary eclipses measured with *Spitzer*/IRAC. The blue line shows an ODR fit to the data with a slope significance of 3.1σ . Several functions were tested (see Section 3.4.2) and the model with the lowest BIC is plotted as a straight line. The orange shaded area shows the span of the ScCHIMERA model grid described in Section 3.3.4. The color scale is the effective temperature of the star.

a transition to the UHJs with an intercept of 1660 ± 100 K. We also show that the grid of emission models are consistent with the data and predict these trends.

3.5 Discussion

3.5.1 Summary of our main results

The $3.6\mu\text{m}$ brightness temperatures are statistically consistent with $T_{eq,0}$ (Figure 3.3), but $4.5\mu\text{m}$ shows a statistically significant increase in T_B compared to $T_{eq,0}$, which is seen as a continuum between the hot and ultra-hot planets. Additionally, the $T_{B_{4.5}}/T_{B_{3.6}}$ ratio also demonstrates a smooth continuous increase with $T_{eq,0}$ (Figure 3.4). We note that, with our larger sample size, different uncertainty calculation, and different stellar model correction,

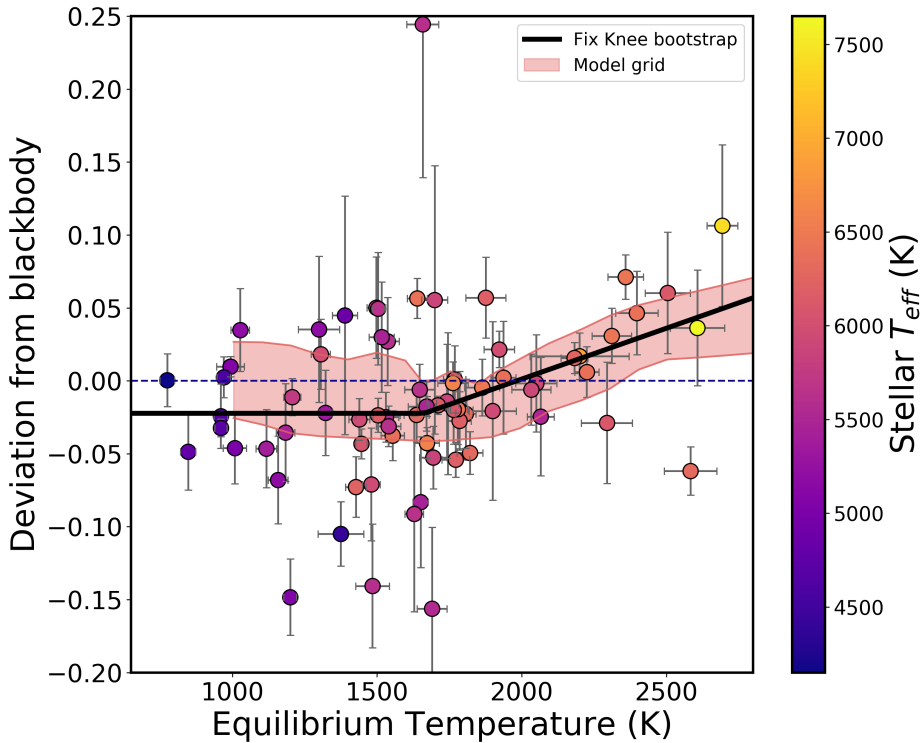


Fig. 3.5: Deviation of the $4.5 \mu\text{m}$ eclipse depth from the $3.6 \mu\text{m}$ blackbody propagated to $4.5 \mu\text{m}$ vs equilibrium temperature (computed with zero albedo and full redistribution). Several functions were tested (see Section 3.4.3) and the model with the lowest BIC is plotted as a bilinear with a knee. The color bar presents the stellar effective temperature. The dashed horizontal line indicates a zero deviation, meaning that the eclipses are consistent with a blackbody. The orange shaded area represents the span of the fiducial forward ScCHIMERA models described in Section 3.3.4.

we support the results of the linear fit of the $T_{B_{4.5}}/T_{B_{3.6}}$ ratio in Garhart et al. (2020) to better than 0.3σ .

However, in addition to the metrics in previous studies, our work includes the deviation from a blackbody which shows evidence of a transition between the hot and the ultra-hot Jupiters (Figure 3.5) that is not captured in the brightness temperature ratio (Figure 3.4). The deviation from a blackbody is proportional to the difference between the two brightness temperatures, whereas Garhart et al. (2020) present the ratio of the brightness temperatures. The ratio of two constantly increasing values is also a constant, but their difference is not. This subtle mathematical difference between the two metrics is the reason why a transition is not captured by the brightness temperature ratio. A bilinear fit of the deviation from a blackbody is statistically favored, indicating that the UHJs are driving the transition. This transition is

also captured in our new grid of 1D self-consistent models (see Section 3.5.3). The 3.6 and 4.5 μm phase curve results of 12 hot Jupiters presented in Keating et al. (2019) tentatively support this transition in thermal structure. They visually demonstrate a difference in the temperature structures between the coolest and the hottest planets by plotting the difference in the two dayside brightness temperatures. We interpret below these trends and transitions in terms of temperature inversions and efficiency of redistribution.

3.5.2 Expected opacities at 3.6 μm and 4.5 μm

The dominant absorbers at the wavelengths probed by *Spitzer*/IRAC are methane (3.6 μm), carbon monoxide (4.5 μm), and water (both wavelengths). Parmentier et al. (2018) and Lee et al. (2012) provide temperature–pressure profiles and the corresponding contribution functions for their analysis of emission spectra of WASP-121b (2400 K) and HD189733b (1200 K). Despite the different temperature regimes, the 4.5 μm contribution function probes lower pressures than 3.6 μm . This is driven by the bimodality at 4.5 μm caused by the H₂O deeper in the atmosphere (\sim 30 mbar) and higher CO/CO₂ at lower pressures (\sim 2-3 mbar), whereas 3.6 μm probes \sim 40 mbar.

The transition between the dominating carbon-bearing species in hot Jupiters is expected to occur at around 1000K (e.g., Zahnle & Marley 2014; Ebbing & Gammon 2016; Molaverdikhani et al. 2019), with hotter atmospheres becoming dominated by CO. Consequently, any changes in the structure of the T-P profile would be seen at 4.5 μm due to the presence of CO (Fortney et al. 2008; Parmentier et al. 2018; Arcangeli et al. 2018). Specifically, a temperature inversion would result in CO in emission, increasing the 4.5 μm brightness temperature compared to 3.6 μm . As the planets approach the ultra-hot temperature regime, water and most other molecular species should begin to dissociate, except the CO. This will further increase the difference in the two pressures probed by *Spitzer*, making our observations even more sensitive to possible temperature inversions.

More generally, the peak of the Planck function corresponding to the thermal emission of the planet shifts at shorter wavelengths when the effective temperature of the planet day-side increases. Since the opacities generally increase with increasing wavelength, the difference between the opacities at the continuum and either of the *Spitzer* wavelengths then increases with increasing equilibrium temperature. The overall opacity of an atmosphere increases from $\sim 1 \mu\text{m}$ to $10 \mu\text{m}$, mostly due to water. Therefore, any difference (positive or negative) between our measured T_B and $T_{eq,0}$ will be larger for hotter planets, as demonstrated in Figure 3.3. However, the relative difference in the water opacity between the two *Spitzer* wavelengths is small enough that we do not expect the Planck function shift to be playing a role when comparing the brightness temperatures to each other (e.g., Figures 3.4 and 3.5). Differences between the two *Spitzer* wavelengths are dominated by the CO opacity at 4.5 μm .

3.5.3 Grid of forward models

In Figure 3.2 we plot the range of 1D models from the emission model grid for three different stellar temperatures (4300K top row, 5300K middle row, and 6300K bottom row). We can see that, for each model track, as the equilibrium temperature increases, the atmosphere switches from being non-inverted to being inverted. This causes the strong CO emission feature in the $4.5 \mu\text{m}$ bandpass to emerge. The hotter the equilibrium temperature of the planet, the stronger the temperature inversion, and the stronger the CO emission feature. We note that we also see the CH_4 absorption feature appearing as a dip in the brightness temperatures at $3.6 \mu\text{m}$ for the coolest (non-inverted) models. The trend from hot to cold is from a weakening inversion until finally the TiO and VO condense out, with a very small isothermal transition region, as can be seen in the grid model T-P profiles displayed in Figure 3.2.

Additionally, Figure 3.2 demonstrates that as the effective temperature of the star increases, the atmosphere of the planet with a given equilibrium temperature has a stronger inversion than a planet with the same temperature does around a cooler star. This is in part because at a given planetary temperature, the wavelength separation between the stellar spectrum and the planetary spectrum increases for hotter stars, which results in a higher effective visible-to-infrared Planck mean opacity. The atmosphere of the planet may respond differently to these fluxes, resulting in different temperature pressure profiles.

We compare the complete sample of eclipses to our grid of 1D emission models for the individual planetary brightness temperatures, for which a subset is plotted in Figure 3.2. We highlight that since most of the hottest ($T_{eq,0} > 2000\text{K}$) planets in our sample have stellar temperatures $> 5900\text{K}$ they should be modeled by the 6300K track. We plot modeled tracks corresponding to planets around a 6300K star on Figure 3.3. We find that the temperatures we measured for our survey planets are higher than expected from the model tracks. We interpret this as being due to the model equilibrium temperature assuming full uniform redistribution, whereas these planets are likely tidally locked and thus will have hotter daysides. However, we do find that the models capture the stronger deviation between brightness and equilibrium temperatures at $4.5 \mu\text{m}$ compared to $3.6 \mu\text{m}$ for hotter planets.

We use the full grid of emission models (see Section 3.3.4) for comparison with the deviation measured in channel 2 ($4.5 \mu\text{m}$) from the blackbody estimated from channel 1 ($3.6 \mu\text{m}$) and with the brightness temperature ratio (Figure 3.5 and Figure 3.4 respectively). First, we find that the model grid is consistent with both of the trends we measured from the data. The models show a clear transition at $\sim 1700\text{K}$, which is consistent with the transition temperature we fit from the data in Figure 3.5. Second, the envelope of models do not show the same abrupt transition at $\sim 1700\text{K}$ in the brightness temperature ratio (Figure 3.4) as they do in the deviation from the blackbody. Instead, they show a continuous increase with equilibrium temperature, with significant variations at the lower temperatures, which is in agreement with the data and the straight line we fit in Section 3.4.2.

We find that the spread in the models for both the deviation from the blackbody (Figure 3.5) and the brightness temperature ratio (Figure 3.4) is primarily caused by differences in

metallicity and C/O ratio, with surface gravity and stellar temperature having little effect here. Thus, using the grids of different C/O ratios we are able to evaluate trends from the whole population. We find that we can rule out tracks with a high C/O ratio of 0.85 (ΔBIC of ~ 270), meaning that the population of hot Jupiters statistically favors low or solar C/O ratios ($\text{C}/\text{O} \leq 0.54$). This means that high C/O planets are rare ($\text{C}/\text{O} \geq 0.85$).

3.5.4 Interpretation of the transition from hot Jupiters to ultra-hot Jupiters

3.5.4.1 Assumptions on albedo, redistribution, clouds, and thermal structure

We compute the equilibrium temperature ($T_{eq,0}$) assuming full redistribution and null Bond albedo, see Section 3.3.3. Changing these assumptions would have an effect on our results. A nonzero albedo would result in the predicted theoretical equilibrium temperature being lower than $T_{eq,0}$, and relaxing the full redistribution assumption would increase the predicted equilibrium temperature toward $T_{eq,max}$ (no redistribution). This likely explains the few cooler planets whose brightness temperatures are lower than the equilibrium temperature (Figure 3.3).

In Figures 3.3 and 3.4, we find a continuous increase in the brightness temperature with $T_{eq,0}$, with the hottest planets being even hotter than the predicted equilibrium temperature, especially at $4.5\ \mu\text{m}$. Empirical estimates of the Bond albedo for hot Jupiters and ultra-hot Jupiters range from 0 to 0.3 (Schwartz & Cowan 2015; Schwartz et al. 2017). A nonzero albedo would statistically lower T_{eq} below $T_{eq,0}$, which in turn would strengthen the deviation seen. Furthermore, Figure 3.3 demonstrates that the increase in brightness temperatures with equilibrium temperature is also predicted by the models that assume zero albedo and full redistribution. Increasing the albedo in the models would also strengthen this deviation. We thus do not think our zero albedo assumption changes these trends.

On the other hand, a lower redistribution efficiency for the hottest planets would increase their T_{eq} , resulting in hotter brightness temperatures. However, a compilation of *Spitzer* phase curves shows no trend with the difference of the phase curve offsets at the two *Spitzer* wavelengths (Beatty et al. 2019; Zhang et al. 2018). This provides no evidence for potential different redistribution in the two IRAC bandpasses, and we would thus expect the deviation to be equal at the two wavelengths; however, this is not observed (Figure 3.3). We hypothesize that a broader range of redistribution efficiencies for the hotter planets could explain the increasing scatter with increasing $T_{eq,0}$ in Figure 3.3. The degree to which hot Jupiters redistribute heat has been known to vary from planet to planet (Showman & Guillot 2002; Cowan et al. 2007; Cowan & Agol 2011b; Knutson et al. 2007; Showman & Polvani 2011).

Figure 3.5 shows a transition at $T_{eq} \simeq 1700\text{K}$ in the dayside emission of our sample of 78 hot Jupiters. We find a similar transition in the new model grid described in Section 3.3.4. Dayside clouds made of large particles could, in theory, equalize the brightness temperature at 3.6 and $4.5\ \mu\text{m}$; however, we do not think that a transition from cloudy to cloud-free is a likely explanation for the trend seen in Figure 3.5. The main reason for this is that a large majority of

hot Jupiters show very low geometric albedos in optical wavelengths, indicative of daysides that are not significantly dominated by cloud opacity. Second, if clouds made of small particles ($\sim 1\mu\text{m}$) were dominating the opacity structure in the *Spitzer* bandpasses, they would be even more dominant in the Hubble Space Telescope wide field camera 3 (HST/WFC3) bandpass. However, the two emission spectra of hot Jupiters (not ultra-hot) taken with the HST/WFC3 and with a good enough signal to noise ratio (HD209458b and WASP-43b) show evidence of water absorption and not the blackbody emission expected from a cloudy day-side (Line & Parmentier 2016; Stevenson et al. 2014a). Additionally, clouds composed of reflective species would create large shifts in the optical phase curves Shporer & Hu (2015). In searching for these large shifts in phase curves measured with the Kepler telescope, there is evidence that clouds could be present in only a tiny fraction of the day-side (Parmentier et al. 2016). Based on this range of evidence, we consider it reasonable in this paper to model the daysides of planets with $T_{eq}>1400\text{K}$ as being cloud-free.

We conclude that the main cause of the increase in brightness temperature with equilibrium temperature and of the increasing deviation from a blackbody is indeed physical, and is not due to our assumptions of the albedo, redistribution, or cloud-free atmosphere when calculating the equilibrium temperature.

3.5.4.2 Transition in thermal inversions

The strength of the deviation from blackbody calculation (Figure 3.5) is that it is free of re-distribution and albedo assumptions; it simply compares $4.5\ \mu\text{m}$ to $3.6\ \mu\text{m}$. Theoretically, the positive deviation from blackbody could be emission by CO at $4.5\ \mu\text{m}$ (inverted T-P profile) or absorption by methane at $3.6\ \mu\text{m}$ (non-inverted T-P profile). However, given equilibrium chemistry, methane is very unlikely to be in the hottest atmospheres. Moreover, three of our hottest planets have already been shown to have temperature inversions: WASP-33b, WASP-121b, and WASP-18b (Haynes et al. 2015; von Essen et al. 2015; Evans et al. 2017; Arcangeli et al. 2018; Kreidberg et al. 2018b). Furthermore, the best fitting model is bilinear with an intercept of $1660\pm100\text{K}$, highlighting the statistical power of the UHJ deviation. Our grid of forward models also predict a curve that is similar to this bilinear fit, capturing the location of the intercept of the two lines at $\sim 1700\text{K}$.

Interestingly, this corresponds to the condensation temperatures of TiO and VO, which could be the origins of thermal inversions (Hubeny et al. 2003; Burrows et al. 2007b; Fortney et al. 2008). We thus interpret that this deviation represents the transition to a different physical realm in these atmospheres, for example as the temperature approaches that of the UHJs, atmospheres transition from non-inverted to inverted. For the cooler hot Jupiters, temperature inversions are suggested to be caused by the absorption of optical incoming stellar irradiation by gas phase TiO and VO (Hubeny et al. 2003; Fortney et al. 2008). On the other hand, for UHJs, inversions can form through other absorbers such as Na/FeH/Fe/Fe+/Mg (e.g Lothringer et al. 2018; Pino et al. 2020) or from lack of cooling due to molecular dissociation (Parmentier et al. 2018). As molecular dissociation occurs, H^- becomes an important opacity

source, leading to blackbody-like emission spectra, as seen in HST/WFC3 near $1.4\text{ }\mu\text{m}$ (e.g., Arcangeli et al. 2018). WASP-12b is the biggest outlier in Figure 3.5 (it has the lowest deviation from a blackbody for planets with $T_{eq} > 2500$), but this planet is thought to have potential mass loss, and so our considerations may not apply to it directly (Cowan et al. 2012a; Bell et al. 2019).

In Figure 3.3 we observe a stronger deviation from equilibrium temperature at $4.5\text{ }\mu\text{m}$ compared to $3.6\text{ }\mu\text{m}$. We interpret that at $4.5\text{ }\mu\text{m}$ we see CO in emission, whereas at $3.6\text{ }\mu\text{m}$ there is a weaker emission feature from non-dissociated H_2O originating deeper and cooler in the atmosphere. This is also captured by the grid of models, especially for the hot stars which represent the majority of the deviating planets. However, in Figure 3.3 there is a systematic discrepancy between the models and the data which is not captured in Figure 3.5 (i.e., our fitted lines lie lower than the models predict). Our interpretation for this discrepancy and for the intrinsic scatter of the brightness temperatures is that it is either due to the difference in strength of the inversions or that the models are not capturing all of the underlying physics. For example, these models do not account for atmospheric drag (e.g., Arcangeli et al. 2019) or assume that stratospheres are cloud-free. Moreover, whatever the effect is, it does not appear to correlate uniquely with stellar insolation since planets with similar equilibrium temperatures can exhibit different strengths of deviation.

KELT-9b is the hottest known transiting exoplanet and is thus a great probe of the extreme scenarios that we have already discussed above. In Appendix 3.D we measure the $4.5\text{ }\mu\text{m}$ eclipse depth of KELT-9b from an observation centered around eclipse and lasting three times the eclipse duration. We compare this with the results of Mansfield et al. (2020) who use the full phase curve observation. Our brightness temperature is 4.6σ lower than the value calculated in Mansfield et al. (2020), which is likely due to the underestimation of the eclipse depth in our modeling since we approximate the concave down phase variation with a linear function; this discrepancy has been studied before (e.g., Bell et al. 2019). Nevertheless, we plot both T_B on Figure 3.3 and find that both follow the trend of increasing T_B with T_{eq} . In particular, the brightness temperatures calculated from the phase curve in Mansfield et al. (2020) agree with our fitted trend line to $<1\sigma$. However, both brightness temperature calculations are cooler than an extrapolation of the model grid might suggest. We hypothesize that this is due to possible partial CO dissociation, given the ultra-hot equilibrium temperature of KELT-9b, resulting in lower CO emission in the $4.5\text{ }\mu\text{m}$ dayside observation (e.g., Kitzmann et al. 2018; Lothringer et al. 2018). A dedicated modeling analysis would be necessary to confirm this hypothesis, which is beyond the scope of this work.

In summary, our work demonstrates that a transition exists in the infrared emission spectra between hot Jupiters and ultra-hot Jupiters and that this is likely due to a change between non-inverted and inverted temperature-pressure profiles as the stellar irradiation increases on these planets.

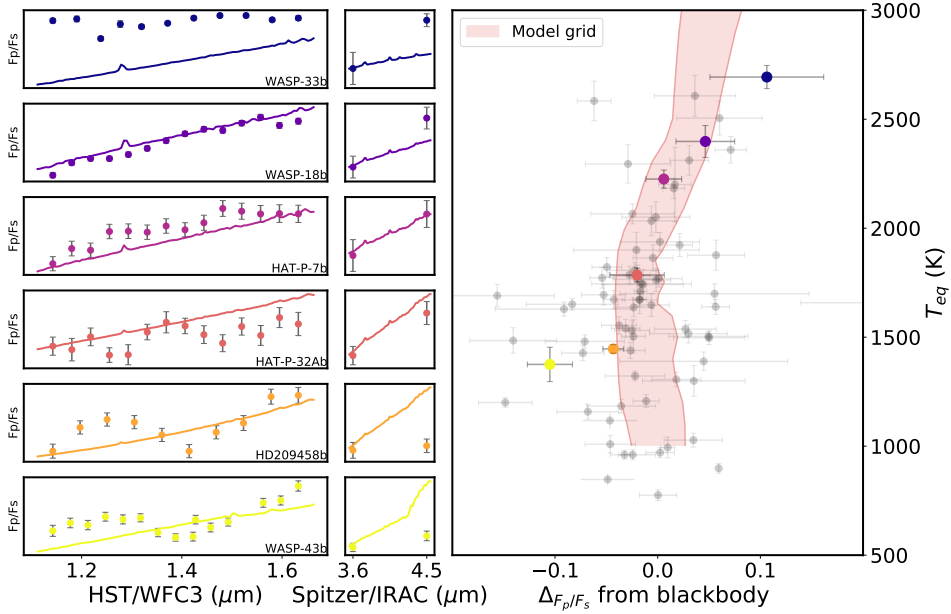


Fig. 3.6: Right panel: Deviation from the blackbody in the *Spitzer* bandpass against equilibrium temperature. Planets here demonstrate the continuous transition between the hot and the ultra-hot planets. Several planet with available HST spectra are highlighted and their spectra are plotted in the left (HST/WFC3) and middle (*Spitzer*) panels. These planets are color-coded by increasing temperature. For simplicity and clarity, we show only six of the HST spectra as examples. The models shown in the left and middle panels are the blackbody at $T_{b3.6}$ and PHOENIX model ratio emission spectra. The model overplotted on the rightmost panel is the emission model grid described in Section 3.3.4.

3.6 Clues from HST/WFC3

Our knowledge of the physics occurring at the IRAC bandpass is deeply influenced by our knowledge of the spectrally resolved HST/WFC3 bandpass. We combine our *Spitzer* survey with available HST/WFC3 data from the literature and discuss the deviation from the blackbody in the context of the water feature at $1.4\ \mu\text{m}$ in the HST/WFC3 spectral band. Figure 3.6 shows the deviation from the blackbody calculated at the *Spitzer* wavelengths (right panel). This is combined with the individual *Spitzer* emission photometry and the HST emission spectra for a subsample of the available planets (middle and left panels respectively).

We see a continuum between the coolest and the hottest hot Jupiters. The hottest planets in our sample (WASP-33b and WASP-18b) have blackbody-like spectra in HST/WFC3 caused by the H^- opacity (Arcangeli et al. 2018), and they show signs of a temperature inversion in *Spitzer*. HAT-P-32Ab is centered in the middle of the deviation from a blackbody plot, exhibiting no absorption or emission of CO, and shows a similar (albeit noisier) blackbody

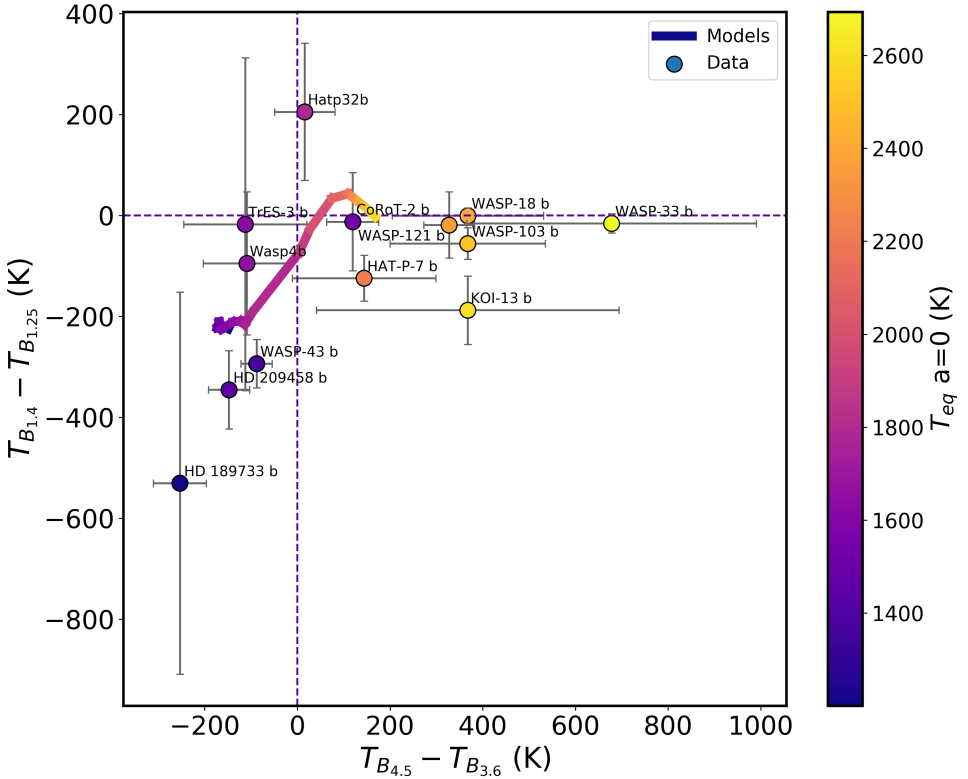


Fig. 3.7: Color-color plot of the planets with available HST spectra. We calculate the color as the difference between the brightness temperatures in and out of the water feature in HST and as the difference between the brightness temperatures in the *Spitzer* bandpass.

emission spectrum with WFC3 (Nikolov et al. 2018). Finally, as we approach the coolest planets in HST (HD209458b and WASP-43b $\sim 1500\text{K}$), we see the water feature appearing strongly in absorption. For these planets we see a negative deviation from the blackbody in *Spitzer*. We interpret this negative deviation as CO in absorption at $4.5\text{ }\mu\text{m}$ since at these cooler temperatures we expect to have non-inverted TP profiles. We highlight that our grid of models predicts these observations.

Building on the color-magnitude work of Triaud et al. (2014) we also create a color-color diagram, where we use the difference between two brightness temperatures. Figure 3.7 shows the *Spitzer* color plotted against the HST color. The HST/WFC3 color is designed to capture inside and outside the water feature at $1.25\text{ }\mu\text{m}$ and $1.4\text{ }\mu\text{m}$. We also show horizontal and vertical dashed lines representing blackbodies for each regime as well as the fiducial model track from our forward model grid ($T_{eff} = 5300\text{K}$, C/O=0.54, [M/H] = 0, $\log(g)=3.0$). Following the increasing temperature of the model track demonstrates the manifestation of the changing TP profiles (seen in Figure 3.2). The *Spitzer* color (horizontal axis), becomes larger

as the models switch from exhibiting CO in absorption to CO in emission, whereas the HST color is slightly more complicated (vertical axis). First, there is a group of models around -200K (both axes) with negative colors, capturing the strong water absorption feature. This is followed by an increase toward a blackbody as the strength of the water feature decreases (-120K to +50K on the X-axis) and the atmospheres begin to transition toward thermally inverted with a slightly positive HST color, up to ~ 50 K. Finally, beyond a mid-IR color of +100K, the model HST colors become consistent with blackbodies again as the water feature disappears as the H⁻ opacity takes over.

In the available data, we note a clear gap in measured planetary temperatures (between HAT-P-7b (2225K) and HAT-P-32Ab (1785K)) where we expect to be probing the transition, which allows us to split the data into two families. The hotter sample planets (> 1785 K) have an average *Spitzer* color of 350K and exhibit less variance in the HST color, which captures the CO in emission at $4.5 \mu\text{m}$ and of their blackbody-like features in HST. Instead, the cooler sample planets (≤ 1785 K) have an average *Spitzer* color of ~ 80 K, indicative of CO in absorption at $4.5 \mu\text{m}$. Furthermore, the cooler sample follows the increasing model track as the strength of the water feature becomes less strong. Thus, our data largely follow the trends predicted by the models in both HST and *Spitzer* wavelengths, and we find that the published sample of HST data supports our claim of a continuum to the ultra-hot Jupiters. An analysis of an expanded dataset including new HST/WFC3 emission spectra for transiting giant planets will be presented in a forthcoming paper (Mansfield et al., in prep.).

3.7 Conclusions

We present our analysis of a literature survey of 78 hot Jupiters with secondary eclipses observed with *Spitzer* at $3.6 \mu\text{m}$ and $4.5 \mu\text{m}$. Our survey spans equilibrium temperatures (zero albedo and full redistribution) between 800K and 2700K. We tested different stellar models (blackbody, ATLAS, PHOENIX) in order to correct the stellar flux from the secondary eclipse depths, and found that improper treatment of the star could bias results, particularly for planets around hotter stars. We then calculated the brightness temperatures at the two *Spitzer* wavelengths by using PHOENIX models to correct the stellar flux, by inverting the Planck function and integrating over the *Spitzer* spectral responses.

We find that the brightness temperatures at $4.5 \mu\text{m}$ are increasingly hotter than equilibrium temperature predictions for the hotter planets, which we interpret as a result of seeing CO in emission at $4.5 \mu\text{m}$ due to the temperature inversions in combination with the Planck function shift. The Planck function of a planetary atmosphere shifts to shorter wavelengths for higher temperatures, increasing the difference between the pressures probed by the equilibrium temperature and the pressures probed by *Spitzer*, and thus the magnitude of the difference between the brightness temperature and equilibrium temperature will be larger for hotter planets. However, we note that any differences between $3.6 \mu\text{m}$ and $4.5 \mu\text{m}$ are going to be dominated by the strong CO band at $4.5 \mu\text{m}$.

We confirm a previous finding that the $T_{B_{4.5}}/T_{B_{3.6}}$ ratio exhibits a smooth continuum increasing with $T_{eq,0}$. However, we also measure, for the first time, the deviation of the data from the blackbody, which we defined as the difference between the observed $4.5\mu\text{m}$ eclipse depth and the eclipse depth expected at $4.5\mu\text{m}$ based on the brightness temperature measured at $3.6\mu\text{m}$. We find a transition at an equilibrium temperature of $1660 \pm 100\text{K}$ in the deviation of the data from a blackbody.

We compare our result to a new grid of 1D self-consistent models (ScCHIMERA) which contain the appropriate physics for temperature inversion formation. We find that the model grid is consistent with both of the trends we measured from the data; in particular, we find an excellent agreement between our measured transition and what is expected from the models. We suggest that this transition is capturing a change in the temperature pressure profile of these atmospheres, from non-inverted to inverted atmospheres as the stellar irradiation increases on these planets.

We find that the spread in the models for the deviation from the blackbody and for the brightness temperature ratio is primarily caused by differences in metallicity and C/O ratio, with surface gravity and stellar temperature having little effect here. We rule out tracks with a high C/O ratio (0.85), meaning that the population of hot Jupiters statistically favors low or solar C/O ratios ($\text{C/O} \leq 0.54$), and that high C/O planets are rare ($\text{C/O} \geq 0.85$).

3.A Details of the data analysis

3.A.1 Fitting correlations with x and y errors

Fitting of linear functions is often done using an ordinary least squares (OLS) or Markov chain Monte Carlo (MCMC) method, both of which assume Gaussian errors. However, our data has errors on both the abscissa and the ordinate, meaning a simple OLS cannot be performed (Hogg et al. 2010). We opted for the `scipy.odr` package, translated from the FORTRAN-77 ODRPACK by Boggs et al. (1989). ODRPACK is a weighted orthogonal distance regression function which takes into account errors on x and on y by minimizing the weighted orthogonal distance between the observations and the model. However, as pointed out in Beatty et al. (2019), ODRPACK uses relative errors between the data points, meaning that the resulting covariance matrix remains the same even when you multiply all of the individual errors by some factor. This has the potential for producing incorrect uncertainties on the parameters. Beatty et al. (2019) use another package, bivariate correlated errors and intrinsic scatter (BCES) (Akritas & Bershady 1996; Nemmen et al. 2012). However, this package only fits a linear model, and so is not suitable for our cases.

Furthermore, these regression methods rely on the assumption that the model perfectly captures the data and that the data are drawn from a purely Gaussian distribution (e.g., Galton 1886; Zhang 2004). In our case, we know that both of these assumptions are not true, and that estimating errors from the covariance matrix could result in underestimated uncertainties.

We thus decide to sample the parameter space using bootstrapping. Bootstrapping estimates posterior distributions by repeatedly resampling with replacement and refitting the function (Efron & Tibshirani 1993). We use ODR to fit the function, accounting for errors on x and y, and then we bootstrap to obtain parameter distributions. Our parameter estimates are then quoted as the 16th, 50th, and 84th percentiles on the marginalized parameter distributions.

When measuring the slope of brightness temperature ratio against equilibrium temperature, we find a slope of 95 ± 31 ppm, which has a significance of 3.1σ , see Section 3.4.2. This is consistent but slightly less significant than 4σ the result presented in Garhart et al. (2020) (98 ± 26), despite our larger sample size. We test our method with their sample and still cannot reproduce their accuracy. We thus expect that the difference is simply due to the fitting and sampling methods chosen. Garhart et al. (2020) use a Gibbs MCMC sampler assuming Gaussian errors based on methods described in Kelly (2007), whereas our bootstrap method does not assume that the errors are Gaussian, and thus end up with broader posterior distributions for our parameters.

3.B Importance of using stellar models

The calculation of the brightness temperature requires an assumption of the stellar model in order to disentangle the planetary flux from the measured planet-to-star flux ratio (F_p/F_s). The simplest assumption is to model the star as a blackbody using the Planck function; however, it is also possible to use a grid of synthetic stellar models. For the first time, to our knowledge, we use our survey to test three different types of models for the star: blackbodies, ATLAS models (Kurucz 1979), and PHOENIX models (Allard & Hauschildt 1995; Husser et al. 2013).

For ATLAS models we use the ATLAS9 version of the code (Castelli & Kurucz 2003). This assumes steady-state plane-parallel layers in local thermodynamic equilibrium (LTE), and opacities that are treated by averaging the contribution of different molecular and/or atomic species resulting in a line blanketing effect. Conversely, the PHOENIX models assume spherical geometry and direct opacity sampling of molecular and atomic species. They are also computed under the LTE assumption; however, non-local thermodynamic equilibrium (NLTE) effects are included for the spectral line profiles of selected important species (Li I, Na I, K I, Ca I, Ca II).

3.B.1 Effect of different stellar models on measured temperature

Comparing the gradients (presented in Table 3.1) of each set of brightness and effective temperatures quantifies the difference between the stellar models. For the effective temperature we can see that the ATLAS and PHOENIX models are consistent with each other at better than 1σ level; however, blackbodies are systematically $\sim 2\sigma$ above the stellar models. This larger gradient was also seen in Schwartz & Cowan (2015) with their sample, where they measured a value of 0.87(5) for the effective temperature. If any of these temperature sets

Table 3.1: We measure the gradient of temperature vs irradiation temperatures for three different temperatures: the individual brightness temperatures ($T_{b_{3.6}}$ and $T_{b_{4.5}}$) and the dayside effective temperature (T_{day}), calculated as a weighted mean. Each set of temperatures is calculated using three different stellar models: blackbodies, ATLAS models, and PHOENIX models. Figure 3.3 displays the individual brightness temperatures for PHOENIX models and Figure 3.8 displays the effective temperatures.

	T_{eff}	$T_{b_{3.6}}$	$T_{b_{4.5}}$
BB	0.85±0.03	0.81±0.05	0.92±0.05
ATLAS	0.80±0.03	0.79±0.04	0.84±0.04
PHOENIX	0.80±0.03	0.76±0.05	0.84±0.05

were to be representative of the equilibrium temperature then the expected gradient would be 0.71 ($T_{eq} = (1/4)^{1/4}T_0 = 0.71T_0$). The Schwartz & Cowan (2015) of 0.87(5) is statistically significantly steeper than 0.71, which they interpreted as hotter planets having a low Bond albedo and/or less efficient heat transport in their atmospheres. However, the gradient displayed in Table 3.1 shows that this could also be an effect of the use of blackbodies to correct the stellar flux, and thus blackbodies cannot be excluded as the cause of their deviation.

A similar result is seen in the individual brightness temperatures, whereby ATLAS and PHOENIX models are consistent with each other. Thus, for statistical studies of the planets with a wide range of temperatures, using blackbodies for the star can be misleading. We therefore decided to use stellar models to correct the stellar flux from eclipse measurements of our sample of hot and ultra-hot Jupiters. PHOENIX models have some advantages over other stellar models; they are computed at a higher resolution, span a larger range of temperatures, and contain direct opacity sampling. Additionally, PHOENIX models also account for some NLTE effects, which has been shown to be important for ultra-hot planets (Lothringer & Barman 2019). Thus, we decided to use PHOENIX models instead of ATLAS for the remainder of the analysis.

We also found that integrating over the spectral response increases the measured flux compared to taking the exact flux density at the average wavelength of the *Spitzer* band pass, as is done in Schwartz & Cowan (2015). This is due to the nonlinear slope of both the stellar and planetary models over the bandpass, see Figure 3.B. We calculate that ignoring this effect could lead to planetary brightness temperatures overestimated by as much as 115K at 3.6 μm . This effect is more prominent where the slope of the spectra are steeper (e.g., at 3.6 μm compared to 4.5 μm or for hotter planets and stars). On average, for the whole sample, without integration we calculate overestimation of 32K at 3.6 μm and 14K at 4.5 μm . Thus, if not accounted for, this could enhance or diminish any statistical differences seen when comparing 3.6 μm and 4.5 μm . Additionally, we find the hottest planets in our survey around the hotter stars. Thus, when looking for trends throughout a wide range of temperatures, it is imperative to carefully correct for the stellar flux to ensure that what we are seeing is a result of the planetary atmosphere.

We find the trend in the brightness temperature ratio with equilibrium temperature to be 99 ± 37 ppm with blackbodies 97 ± 35 ppm with ATLAS models and 95 ± 31 ppm with

PHOENIX models (Section 3.4.2). The maximum difference between the significance of these slopes for all of three stellar models is negligible, which suggests that any importance of stellar models vanishes somewhat when looking at the ratios. Nevertheless, we keep the results from the PHOENIX models (Section 3.4.2).

3.C Comparing effective temperatures with Schwartz & Cowan (2015)

Schwartz & Cowan (2015) measure the slope of the effective dayside temperature against the irradiation temperature. They note that their slope 0.87 ± 0.05 is significantly steeper than equilibrium temperature predictions (0.71), and that this increasing deviation could lower redistribution efficiencies in the hottest planets. We recreate their results with our expanded survey. We follow their method for calculating the effective temperature, which is the weighted mean of the brightness temperatures, and thus we call it $\langle T_B \rangle = (T_{b_{3.6}}/\sigma_{3.6}^2 + T_{b_{4.5}}/\sigma_{4.5}^2)/2$. We then fit the resulting trends with an ODR (see Section 3.A.1). However, first we test their method of brightness temperature calculation of inverting the Planck function and using a blackbody for the star. Then we test our method using a stellar model and fully integrating the Planck function.

Figure 3.8 presents the results for weighted mean effective temperature using the PHOENIX model calculations of the brightness temperatures. We find a slope of 0.76 ± 0.05 , which is consistent with equilibrium temperature (1σ) and inconsistent with the 0.87 ± 0.05 of Schwartz & Cowan (2015). However, with brightness temperatures calculated without integration over the bandpass and with blackbodies for the star we are able to retrieve a slope of 0.81 ± 0.05 , which is in statistical agreement (0.9σ) with their trend.

Since we are able to retrieve the results using blackbodies, we conclude that the discrepancy is a result of careful use of stellar models and integration over the bandpasses and not of the differences in the sample sizes. More importantly, our findings do not support the findings presented in Schwartz & Cowan (2015) as we do not find that the effective temperature trend with irradiation temperature increases disproportionately. This means that we do not think the effective temperature calculated in this way tells us anything about the redistribution in the hottest planets. On the other hand, in Figure 3.3, we find that the $4.5 \mu\text{m}$ brightness temperature is deviating from equilibrium, likely due to the strong CO opacity appearing in emission. This does support the hypothesis that these hottest planets are exhibiting different behaviors, but it is not expected to be captured in the effective temperatures since the weighted mean of the two brightness temperatures is likely muting this deviation.

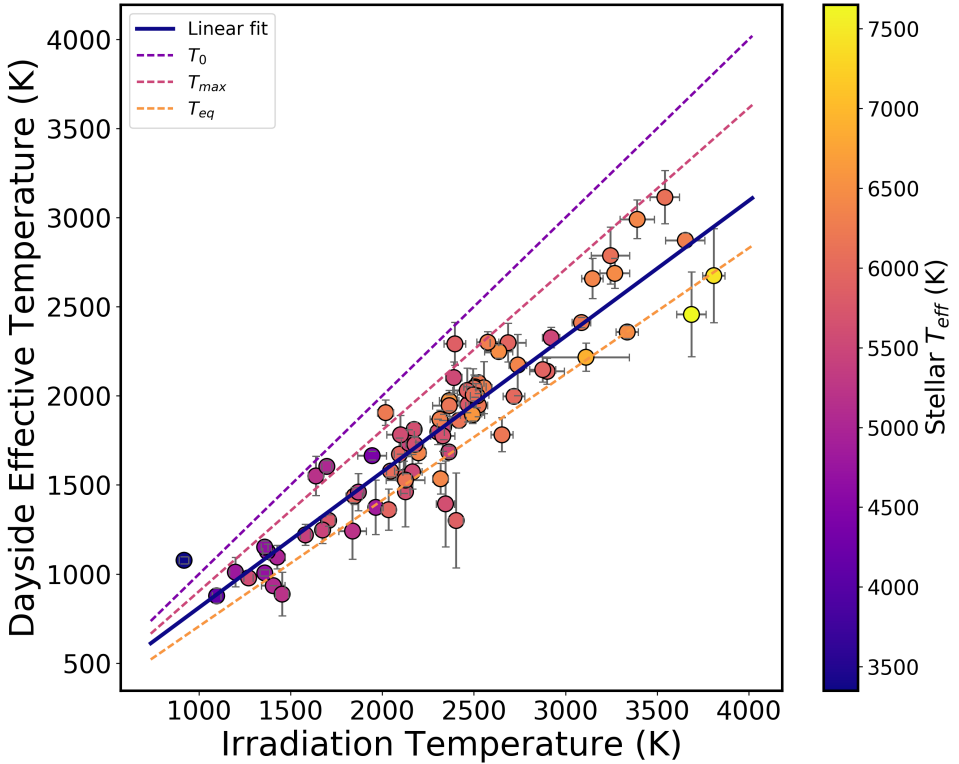


Fig. 3.8: Dayside effective temperature ($< T_B >$) vs the theoretical irradiation temperature (T_{eq}) with zero albedo and full redistribution, similar to Schwartz & Cowan (2015), but with 28 more planets. We also plot the expected irradiation temperature (T_0), the equilibrium temperature with zero albedo (T_{eq}), and the maximum dayside temperature (T_{max}). The color scale is the effective temperature of the host star in Kelvin.

3.D KELT-9b Eclipse: the hottest of the UHJs

A question arises of whether the trends presented in Section 3.5 hold at even higher temperatures. To test this we include the $4.5 \mu\text{m}$ eclipse depth of the hottest of the UHJs, KELT-9b (Gaudi et al. 2017). Significantly hotter than any other ultra-hot Jupiter, KELT-9b is the hottest gas giant planet known. A 1.48-day orbital period around its A-type host star of 10170K makes it the most highly irradiated planet with an equilibrium temperature of 4050K (Gaudi et al. 2017). At these temperatures, the planet itself is similar to a K4 star; its atmosphere is subject to molecular dissociation, leaving behind atomic metals such as iron and titanium (Hoeijmakers et al. 2018, 2019).

We analyse two $4.5 \mu\text{m}$ eclipses of KELT-9b. The data were taken from the phase curve survey, program ID 14059 lead by PI J Bean. We extracted the two secondary eclipses from

the available phase curves. The analysis from raw data to eclipse depth values was done using our custom pipeline described in Baxter et al. (in prep.). In summary, we allow for different background correction methods, different centroiding methods, and different aperture radii to find the combination that gives the lowest χ^2 . We correct for the strong *Spitzer* systematics using Pixel Level Decorrelation (Deming et al. 2015) and perform a full MCMC analysis using Batman (Kreidberg 2015) to fit for the eclipse parameters on the best photometric lightcurve. The raw photometry, the corrected lightcurves, and one of our statistical tests (RMS vs binsize, which characterizes how well we correct red noise) are presented in Figure 3.9. The two eclipse depths (F_p/F_s) are calculated to be 2793 ± 44 (ppm) and 2809 ± 48 (ppm) for AORs r67667712 and r67667968, respectively. The eclipse depth used in the analysis is the mean of these two values 2801 ± 33 (ppm). This eclipse depth is used to calculate the brightness temperatures shown in Figure 3.3.

Our results disagree with the $4.5\text{ }\mu\text{m}$ eclipse depths presented in Mansfield et al. (2020) by 4.6σ . This significant difference is likely not due to any problems with the systematic correction algorithm, but is rather a result of the choice of baseline between eclipse and phase curve observations. Eclipse-only observations ignore phase variations, and can thus underestimate eclipse depths when the real phase variations are concave over the secondary eclipse (e.g., Bell et al. 2019). Since the large phase amplitude (0.601) presented in Mansfield et al. (2020) clearly demonstrates a concave phase variation around the ellipse, this is likely the cause of the discrepancy between the two sets of data analyses. However, since we do not see any trend with the phase curve offsets between the two *Spitzer* bandpasses (discussed in Section 3.5.4.1) we expect that any underestimation of the eclipse depth will apply to both $3.6\text{ }\mu\text{m}$ and $4.5\text{ }\mu\text{m}$, and thus the deviation from the blackbody will be largely unaffected. Nevertheless, such an effect could be relevant for higher precision measurements with the James Webb Space Telescope.

Since we only have the available $4.5\text{ }\mu\text{m}$ measurement of KELT-9b, this data point is excluded from any of the fits in our analysis. Nevertheless, we can see that the brightness temperature deviates positively from equilibrium at $4.5\text{ }\mu\text{m}$. However, like several of the hottest planets, the deviation is smaller than expected compared to the model predictions in Figure 3.3. We interpret this as indicative of more complex physical processes happening in the atmosphere of this extreme object (Bell & Cowan 2018; Komacek & Tan 2018; Lothringer et al. 2018; Kitzmann et al. 2018; Mansfield et al. 2020). For example, due to the high temperature on the dayside of KELT-9b, there could be less carbon monoxide available in the atmosphere due to it being dissociated (Kitzmann et al. 2018).

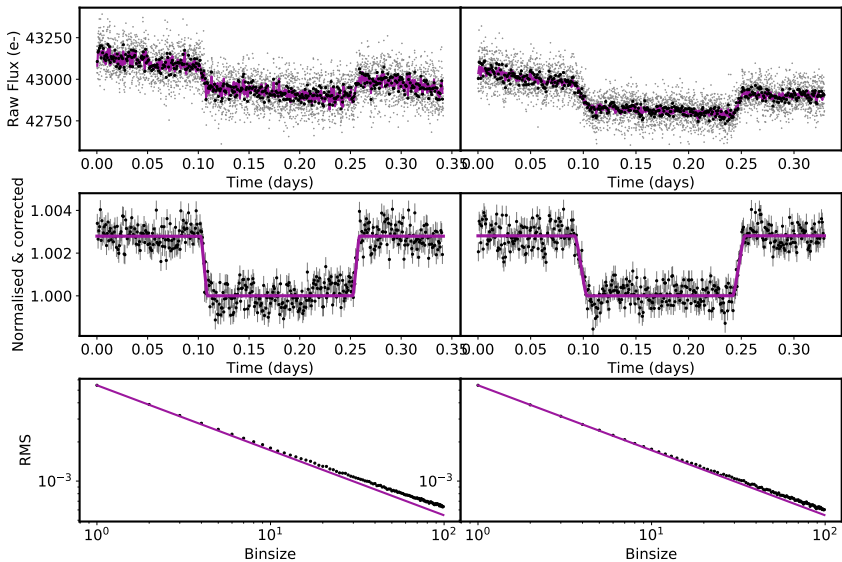


Fig. 3.9: Eclipses of KELT-9b for AORs r67667712 (left panel) and r67667968 (right panel). The top row shows the raw photometric lightcurve with our best fit PLD model. The middle row shows the corrected lightcurves with the best fit eclipse model. The bottom row shows the RMS vs binsize of the data; since this closely follows the photon noise line (\sqrt{N}) we can see that we are capturing the systematics well.

Table 3.2: Planetary eclipse depths from the literature, calculated equilibrium temperatures, calculated brightness temperatures, and deviations from blackbody using PHOENIX models and stellar parameters used to obtain the correct stellar models.

Planet	$(F_p/F_s)_{3.6}$	$(F_p/F_s)_{4.5}$	$T_{eq,i=0}$	T_{eff}	log (cgs)	[Fe/H] (dex)	$T_{B_{3.6}}$ (K)	$T_{B_{4.5}}$ (K)	devBB (%)	Ref.
	(ppm)	(ppm)	(K)	(K)						
HAT-P-32b	3640±160	4380±200	1785±32	6207±88	4.33±0.01	-0.04±0.08	2073±40	2023±46	0.006±0.026	1
XO-1b	860±70	1220±90	1207±30	5750±75	4.5±0.01	0.02±0.08	1301±32	1257±34	-0.001±0.012	2
HAT-P-1b	800±80	1350±220	1306±33	5980±49	4.36±0.01	0.13±0.01	1437±47	1521±103	0.026±0.024	3
WASP-39b	880±150	960±180	1118±35	5400±150	4.4±0.2	-0.12±0.1	1220±60	1066±63	-0.034±0.026	4
HAT-P-18b	437±145	326±146	847±26	4803±80	4.57±0.04	0.1±0.08	1011±83	787±88	-0.04±0.025	5
TrES2b	1270±210	2300±240	1498±32	5850±50	4.43±0.02	-0.15±0.1	1543±90	1712±81	0.063±0.034	6
WASP-4b	3190±310	3430±270	1651±27	5436±34	4.46±0.05	-0.05±0.04	1825±72	1650±57	-0.049±0.042	7
XO-2b	810±170	980±200	1322±23	5340±32	4.48±0.05	0.45±0.02	1460±104	1346±104	-0.011±0.028	8
WASP-1b	1170±160	2120±210	1876±69	6200±200	4.3±0.3	0.1±0.2	1781±95	2067±103	0.066±0.027	9
HAT-P-26b	85±0	265±70	994±48	5079±88	4.56±0.06	-0.04±0.08	935±0	1067±90	0.011±0.007	5
CoRoT-1 b	4150±420	4820±420	1900±81	5950±150	4.25±0.3	-0.3±0.25	2298±109	2236±102	0.006±0.06	10
CoRoT-2 b	3550±200	5000±200	1537±40	5625±120	4.53±0.02	0.03±0.06	1811±40	1854±36	0.062±0.029	10
HAT-P-17 b	118±39	149±...	779±17	5246±80	4.53±0.02	0.0±0.08	807±54	704±...	-0.009±...	5
HAT-P-19 b	620±140	620±140	1009±40	4990±130	4.54±0.05	0.23±0.08	1095±66	924±59	-0.036±0.023	4
HAT-P-2 b	996±72	1031±61	1428±57	6290±60	4.16±0.08	0.14±0.08	2256±76	2065±62	-0.012±0.01	11
HAT-P-20 b	615±82	1096±77	971±24	4595±80	4.63±0.02	0.35±0.08	1127±40	1131±26	0.014±0.013	12
HAT-P-23 b	2480±190	3090±260	2051±71	5905±80	4.33±0.05	0.15±0.04	2137±73	2128±92	0.018±0.032	13
HAT-P-3 b	1120±225	940±125	1158±34	5185±80	4.56±0.03	0.27±0.08	1550±110	1252±60	-0.053±0.028	14
HAT-P-4 b	1420±160	1220±130	1694±47	5860±80	4.36±0.11	0.24±0.08	2291±120	1906±98	-0.041±0.021	14
HAT-P-6 b	1170±80	1060±60	1673±42	6570±80	4.22±0.03	-0.13±0.08	1973±57	1681±43	-0.035±0.01	15
HAT-P-7 b	1560±130	1900±110	2225±41	6389±17	4.7±0.06	0.26±0.08	2657±113	2704±92	0.016±0.017	16
HAT-P-8 b	1310±85	1110±75	1772±48	6200±80	4.15±0.03	0.01±0.08	2050±58	1695±52	-0.045±0.012	15
HD 149026 b	400±30	340±60	1673±65	6160±50	4.28±0.05	0.36±0.08	1945±61	1603±122	-0.014±0.007	17

Table 3.2: continued.

Planet	$(F_p/F_s)_{3.6}$	$(F_p/F_s)_{4.5}$	$T_{eq_{eff=0}}$	T_{eff}	logg	[Fe/H]	$T_{B_{3.6}}$	$T_{B_{4.5}}$	devBB	Ref.
	(ppm)	(ppm)	(K)	(K)	(cgs)	(dex)	(K)	(K)	(%)	
HD 189733 b	2560±140	2140±200	1200±22	5040±50	4.59±0.01	-0.03±0.08	1604±32	1298±45	-0.115±0.025	18
HD 209458 b	1190±70	1230±60	1446±19	6065±50	4.36±0.01	0.0±0.05	1577±33	1392±27	-0.033±0.01	19
Kepler-12 b	1370±200	1160±310	1481±31	5947±100	4.18±0.01	0.07±0.04	1672±91	1369±142	-0.058±0.038	20
Kepler-17 b	2500±300	3100±350	1745±39	5781±85	4.53±0.12	0.26±0.1	1952±98	1902±102	0.008±0.047	21
Kepler-5 b	1030±170	1070±150	1807±35	6297±60	3.96±0.1	0.04±0.06	2045±146	1859±124	-0.016±0.023	23
Kepler-6 b	690±270	1510±190	1504±21	5647±44	4.24±0.01	0.34±0.04	1462±196	1726±98	0.058±0.036	23
KOI-13 b	1560±310	2220±230	2607±94	7650±250	4.2±0.5	0.2±0.2	2456±238	2716±164	0.044±0.039	24
Qatar-1 b	1490±510	2730±490	1389±43	4861±125	4.54±0.02	0.2±0.1	1374±153	1470±108	0.068±0.077	25
TrES-3 b	3460±350	3720±540	1629±32	5650±75	4.58±0.01	-0.19±0.08	1797±72	1624±103	-0.056±0.066	26
TrES-4 b	1370±110	1480±160	1785±41	6200±75	4.06±0.02	0.14±0.09	1947±65	1793±90	-0.017±0.02	27
WASP-10 b	1000±110	1460±160	960±24	4675±100	4.4±0.2	0.03±0.2	1151±35	1091±39	-0.007±0.021	11
WASP-103 b	4458±383	5686±138	2505±78	6110±160	4.22±0.08	0.06±0.13	3114±149	3337±52	0.088±0.04	28
WASP-12 b	4210±110	4280±120	2584±91	6300±150	4.38±0.1	0.3±0.1	2872±40	2649±43	-0.034±0.016	29
WASP-121 b	3150±103	4510±107	2359±61	6459±140	4.24±0.01	0.13±0.09	2358±36	2591±35	0.09±0.015	25
WASP-14 b	1870±70	2240±180	1864±60	6475±100	4.07±0.2	0.0±0.2	2248±39	2221±93	0.007±0.019	30
WASP-18 b	3000±200	3900±200	2398±73	6400±100	4.37±0.04	0.0±0.09	2990±109	3231±104	0.063±0.028	31
WASP-19 b	4830±250	5720±300	2066±46	5500±100	4.5±0.2	0.02±0.09	2326±57	2270±63	0.02±0.039	32
WASP-2 b	830±350	1690±170	1300±71	5200±200	4.54±0.04	0.1±0.2	1241±158	1350±51	0.048±0.046	9
WASP-24 b	1590±130	2020±180	1769±39	6075±100	4.26±0.17	0.0±0.1	2044±73	2044±92	0.013±0.022	33
WASP-33 b	2600±500	4100±200	2694±53	7430±100	4.3±0.2	0.1±0.2	2674±264	3202±98	0.119±0.054	34
WASP-43 b	3460±130	3820±150	1375±79	4400±200	4.65±0.05	-0.05±0.17	1664±24	1497±24	-0.053±0.02	35
WASP-48 b	1760±130	2140±200	2033±68	5920±150	4.03±0.03	-0.12±0.12	2147±70	2113±101	0.008±0.024	13
WASP-5 b	1970±280	2370±240	1742±68	5880±150	4.4±0.04	0.9±0.09	2030±125	1969±98	0.0024±0.038	36
WASP-6 b	940±190	1150±220	1184±32	5450±100	4.6±0.2	-0.2±0.09	1247±75	1134±72	-0.022±0.032	4

Table 3.2: continued.

Planet	$(F_p/F_s)_{3.6}$	$(F_p/F_s)_{4.5}$	$T_{eq_{a=0}}$	T_{eff}	logg (cgs)	[Fe/H] (dex)	$T_{B_{3.6}}$ (K)	$T_{B_{4.5}}$ (K)	devBB (%)	Ref.
WASP-67 b	220±130	800±180	1028±32	5200±100	4.35±0.15	-0.07±0.09	887±122	1042±73	0.039±0.027	4
WASP-69 b	421±29	463±39	961±21	4700±50	4.5±0.15	0.15±0.08	1006±17	864±19	-0.024±0.006	5
WASP-8 b	1130±180	690±70	927±27	5600±80	4.5±0.1	0.17±0.07	1573±90	1144±39	-0.078±0.021	37
WASP-80 b	455±100	944±65	775±25	4150±100	4.6±0.2	-0.14±0.16	878±42	875±16	0.01±0.016	38
XO-3 b	1010±40	1580±36	2046±40	6429±50	3.95±0.06	-0.18±0.03	1814±29	1972±21	0.033±0.006	39
XO-4 b	560±90	1350±85	1639±35	6397±70	4.18±0.07	-0.04±0.03	1535±86	1957±60	0.061±0.013	15
HAT-P-13 b	851±107	1090±124	1648±53	5655±90	4.13±0.04	0.41±0.08	1775±87	1728±89	0.003±0.017	25
HAT-P-30 b	1584±107	1825±147	1637±43	6304±88	4.36±0.3	0.13±0.08	1868±51	1763±65	-0.012±0.019	25
HAT-P-33 b	1603±127	1835±199	1780±34	6446±88	4.15±0.01	0.05±0.08	2000±67	1901±98	-0.009±0.024	25
HAT-P-40 b	988±168	1057±145	1765±66	6080±100	3.93±0.02	0.22±...	2005±146	1840±119	-0.012±0.023	25
HAT-P-41 b	1829±319	2278±177	1937±44	6390±100	4.14±0.02	0.21±0.1	2173±172	2179±88	0.014±0.037	25
KELT-2 A b	650±38	678±47	1710±31	6151±50	4.03±0.02	-0.02±0.07	1862±44	1679±52	-0.012±0.006	25
KELT-3 b	1766±97	1656±104	1822±44	6304±49	4.2±0.03	0.05±0.08	2300±59	2006±62	-0.038±0.014	25
WASP-100 b	1267±98	1720±119	2200±171	6900±120	4.35±0.17	-0.03±0.1	2216±79	2337±88	0.024±0.016	25
WASP-101 b	1161±111	1194±113	1554±40	6380±120	4.31±0.08	0.2±0.12	1680±61	1492±58	-0.029±0.017	25
WASP-104 b	1709±195	2643±303	1516±43	5475±127	4.5±0.02	0.32±0.09	1734±76	1828±98	0.05±0.037	25
WASP-131 b	364±97	282±78	1439±36	5950±100	3.9±0.1	-0.18±0.08	1361±115	1077±96	-0.023±0.014	25
WASP-36 b	913±578	1948±544	1699±45	5881±136	4.5±0.01	-0.31±0.12	1300±267	1475±168	0.064±0.089	25
WASP-46 b	1360±701	4446±589	1658±55	5620±160	4.49±0.02	-0.37±0.13	1394±241	1968±129	0.258±0.101	25
WASP-62 b	1616±146	1359±130	1427±35	6230±80	4.45±0.1	0.04±0.06	1906±71	1568±63	-0.061±0.02	25
WASP-63 b	552±95	533±128	1531±45	5550±100	4.01±0.03	0.08±0.07	1573±97	1347±123	-0.018±0.017	25
WASP-64 b	2859±270	2071±471	1690±52	5550±150	4.39±0.02	-0.08±0.11	2102±87	1610±159	-0.129±0.055	25
WASP-65 b	1587±245	724±318	1485±59	5600±100	4.25±0.1	-0.07±0.07	1781±108	1160±177	-0.125±0.041	25
WASP-74 b	1446±66	2075±100	1923±53	5990±110	4.39±0.07	0.39±0.13	1997±39	2106±51	0.034±0.012	25

Table 3.2: continued.

Planet	$(F_p/F_s)_{3.6}$	$(F_p/F_s)_{4.5}$	$T_{eq_{\text{at}0}}$	T_{eff}	logg	[Fe/H]	$T_{B_{3.6}}$	$T_{B_{4.5}}$	devBB	Ref.
	(ppm)	(ppm)	(K)	(K)	(cgs)	(dex)	(K)	(K)	(%)	
WASP-76 b	2645±63	3345±82	2183±47	6250±100	4.4±0.1	0.23±0.1	2411±28	2471±33	0.034±0.01	25
WASP-77 A b	1845±94	2362±127	1671±31	5500±80	4.33±0.08	0.0±0.11	1685±32	1628±37	0.002±0.016	25
WASP-78 b	2001±218	2013±351	2295±88	6100±150	4.1±0.2	-0.35±0.14	2787±160	2565±255	-0.019±0.041	25
WASP-79 b	1394±88	1783±106	1762±53	6600±100	4.2±0.15	0.03±0.1	1893±49	1882±54	0.008±0.014	25
WASP-87 b	2077±127	2705±137	2311±68	6450±120	4.32±0.21	-0.41±0.1	2687±85	2863±87	0.04±0.019	25
WASP-94 A b	867±59	995±93	1504±77	6170±80	4.27±0.07	0.26±0.15	1527±36	1398±50	-0.016±0.011	25
WASP-97 b	1359±84	1534±101	1540±42	5640±100	4.45±0.08	0.23±0.11	1727±40	1590±44	-0.017±0.014	25
KELT-9 b	...±...	2802±33	4051±199	10170±450	4.09±0.01	-0.03±0.2	...±...	...±...	...±...	40

- (1) Zhao et al. (2014); (2) Machalek et al. (2008); (3) Todorov et al. (2010); (4) Kammer et al. (2015); (5) Wallack et al. (2019); (6) O'Donovan et al. (2010); (7) Beerer et al. (2011); (8) Machalek et al. (2009); (9) Wheatley et al. (2010); (10) Deming et al. (2011); (11) Lewis et al. (2013); (12) Deming et al. (2015); (13) O'Rourke et al. (2014); (14) Todorov et al. (2012); (16) Christiansen et al. (2010); (17) Stevenson et al. (2012); (18) Charbonneau et al. (2008); (19) Diamond-Lowe et al. (2014); (20) Fortney et al. (2011); (21) Désert et al. (2011a); (22) Désert et al. (2011b); (24) Shporer et al. (2014); (25) Garhart et al. (2020); (26) Fressin et al. (2010); (27) Knutson et al. (2009a); (28) Kreidberg et al. (2018b); (29) Stevenson et al. (2014a); (30) Bleicic et al. (2013); (31) Nymeyer et al. (2011); (32) Anderson et al. (2013); (33) Smith et al. (2012); (34) Deming et al. (2012); (35) Bleicic et al. (2014); (36) Baskin et al. (2013); (37) Cubillos et al. (2013); (38) Triaud et al. (2015); (39) Machalek et al. (2010); (40) This work.;

4

PERIODIC VARIABILITY IN THE BRIGHTNESS OF AN ULTRA-HOT JUPITER ATMOSPHERE

Claire Baxter & Jean-Michel Désert

Astronomy & Astrophysics, (to be submitted)

Abstract

Context With close-in orbits and strong stellar irradiation on tidally locked daysides, hot Jupiter atmospheres are predicted to form large-scale weather structures. Observing the variability of a hot Jupiter is a key probe of such weather patterns as well as probing the atmospheric dynamics and temperature structures.

Aims We aim to characterize the brightness variability of the ultra-hot Jupiter WASP-18b by analyzing ten secondary eclipses at $4.5\text{ }\mu\text{m}$ with *Spitzer*/IRAC.

Methods Our observations span a time frame of 21.6 days which covers 23 planetary orbits. We search for temporal variability by robustly analyzing each of the lightcurves using our custom pipeline which implements pixel level decorrelation. We benchmark our results against the well-studied XO-3b.

Results We observe variability in the eclipse depth with time, which is the first infrared temporal variability in secondary eclipse observations of hot Jupiters. Using a sinusoidal model, we derive a variability period of 23.12 ± 1.66 days and a peak-to-trough amplitude of 456 ± 71 ppm, corresponding to $\sim 12\%$ variability. We discuss possible causes of this variability, such as stellar variability, variable wind speeds, clouds, changes in atmospheric composition, and magnetic field coupling. We find that a 12% variability signal would not be detected in the four available sectors of TESS containing WASP-18b, or with the 5 available HST/WFC3 eclipses, and that future observatories would be required for follow-up.

4.1 Introduction

Hot Jupiters are ideal targets for precise atmospheric characterization due to their large planet-to-star flux ratios. There have now been many secondary eclipse observations of hot Jupiters in the infrared, ranging from individual studies (e.g., Charbonneau et al. 2005; Deming et al. 2005) to large-scale survey programs (e.g., Schwartz et al. 2017; Baxter et al. 2020; Garhart et al. 2020). The vast majority of hot Jupiter atmospheres are expected to form clouds and photochemical hazes (Sing et al. 2016; Parmentier et al. 2016; Wakeford et al. 2019). Inhomogeneous coverage of such clouds could lead to brightness variability in time.

Temporal variations have been observed at $5\text{ }\mu\text{m}$ in the equatorial banded structures of Jupiter (Antuñano et al. 2019). Variability in time is also common in cool brown dwarfs, with variability amplitudes of a few percent in more than 50% of L and T brown dwarfs (Metchev et al. 2015). Furthermore, variability has also recently been detected on directly imaged free-floating planetary-mass objects (e.g., Biller et al. 2015). However, observing variability on directly imaged exoplanets is difficult due to the contrast between the host star and planet (Apai et al. 2016).

Nevertheless, atmospheric variability in time has been measured with phase curve observations of 3 hot Jupiters to date: HAT-P-7b (Armstrong et al. 2016), Kepler-76b (Jackson et al. 2019), and WASP-12b (Bell et al. 2019). Armstrong et al. (2016) use 4 years of public *Kepler* data of HAT-P-7b to search for variability. They find temporal variations in the phase curve shape, including the hot-spot offset, such that the hot-spot shifts from one side of the substellar point to the other on timescales of tens to hundreds of days. However, they find only marginal evidence of brightness variability in time, which they note can be explained by systematic noise in their fits. Also using *Kepler* data, Jackson et al. (2019) found similar phase offset variability in Kepler-76b, however, they do measure variability in the phase curve amplitude. Furthermore, two phase-curve observations at $3.6\text{ }\mu\text{m}$ taken 3 years apart of WASP-12b measure the phase curve offset to be $32.6 \pm 6.2^\circ$ eastward to $13.6 \pm 3.8^\circ$ westward (Bell et al. 2019).

To date, there has been no periodic brightness variability measured in secondary eclipse observations of hot Jupiters in the infrared. Agol et al. (2010) place an upper limit of 2.7% at $8\text{ }\mu\text{m}$ on the eclipse depth variability of HD 189733b. Furthermore, Kilpatrick et al. (2020) carried out multi-epoch secondary eclipse observations with *Spitzer*/IRAC in an attempt to constrain the variability of HD 189733b and HD 209458b. They do not find a periodic variability signal, but they can place upper limit constraints on any possible variability to 12% and 1.6% at $4.5\text{ }\mu\text{m}$ for HD 189733b and HD 209458b respectively.

A possible cause of the variability on HAT-P-7b in the optical is variable wind speeds leading to variable cloud coverage (Armstrong et al. 2016). Similarly, Jackson et al. (2019) proposed the advance and retreat of thermal structures on Kepler-76b. This leads to cloud formation on the nightside blowing over to the dayside and creating a feedback loop resulting in periodic variability. Rogers (2017) explored the effect of magnetic fields on HAT-P-7b by incorporating magnetohydrodynamics (MHD) into their global circulation models (GCMs).

They conclude that coupling of the magnetic field with ionized species in the atmosphere can act against the eastward hot spot offset caused by the day-night temperature contrast. Such feedback can settle into an oscillating pattern on timescales of $\sim 10^6$ seconds, creating the observed variability. In the case of WASP-12b, analysis of the 3.6 and 4.5 μm phase curves suggest mass-loss of the planet (Bell et al. 2019). Variability in the mass loss rate could be the cause of the phase offset variability. However, they also note that, following the arguments of Rogers (2017), variability due to magnetic coupling would be expected on WASP-12b.

In this paper, we measure and discuss the atmospheric brightness variability in the infrared of the ultra-hot Jupiter WASP-18b.

4.2 Observations

We observed ten secondary eclipses of WASP-18b at 4.5 μm with *Spitzer* /Infrared array camera (IRAC), program 11099 (PI: Kreidberg). Each observation consisted of 11776 exposures of 2-second integration in sub-array mode, resulting in 6.54 hours per lightcurves. Our observations were preceded with a scheduled 30-minute throw-away "peak-up" observation to obtain accurate pointing before the main observation to minimize the effect of IRACs well known intrapixel sensitivity. The ten eclipses span from 8th-30th September 2015, a total time of 21.65 days, corresponding to 23 orbits of WASP-18b, given its orbital period of 0.94124000 days (Pearson 2019).

Furthermore, we also analyzed the ten eclipses of XO-3b, program 90032 (PI: Knutson), to test the robustness of our pipeline and our results, particularly on the variability. These eclipses were previously part of the repeatability and reliability data challenge presented in Ingalls et al. (2016).

4.3 Data Analysis

4.3.1 *Spitzer*/IRAC photometric lightcurve reduction

We reduce the *Spitzer*/IRAC secondary eclipse lightcurves with our custom pipeline described fully in Baxter et al. (submitted.) which follows the analysis method from (Deming et al. 2015). For clarity, we recall the main steps of our pipeline. In each of the *Spitzer* subarray frames, we correct the dark current, flat field, and convert to flux units before performing aperture photometry using a circular aperture around the calculated centroid position of the star. A full run of our pipeline creates a grid of data reductions and finds the optimum methods and parameters for background subtraction, centroiding, and aperture photometry radius utilizing a lowest reduced χ^2 on the resulting lightcurves. Uncertainties on the photometric points are calculated from photon noise and scaled up such that the reduced χ^2 after an initial least-squares fit is equal to 1.

Our resulting optimum pipeline reduction methods were to centroid using the barycenter

method, with a box size of 3x3, calculate the background using 4 pixels in each of the 4 corners of the image, and to perform aperture photometry with a radius of 2.5 pixels around the star. In each lightcurve, we masked between 0.053% and 0.076% bad pixels at 4σ . We also removed 15 minutes from the beginning of each of the lightcurves to remove the peak-up period of the observations. The best raw normalized photometric lightcurve for each observation is then used in the next step for a complete statistical analysis of the transit/eclipse parameters.

4.3.2 *Spitzer*/IRAC secondary eclipse fitting

To find the eclipse parameters from the raw photometric lightcurve, we fit a batman eclipse model (Kreidberg 2015) in combination with a temporal quadratic function (1 or 2 order) and a pixel-level decorrelation (PLD) systematic model (Deming et al. 2015). In our fit of WASP-18 b, we fix the period to 0.9414529 ± 0.00000234 (Pearson 2019) and the eccentricity and angle of periastron passage to 0.

Typically, the PLD systematic model uses a 3x3 grid of pixels around the centroid of the star to model the systematics. Since WASP-18b is a bright star, a significant portion of the stellar PSF may spread beyond these nine pixels, we, therefore, test the effect of including more pixels with a 5x5 PLD grid. However, we found that a 5x5 PLD box compared to a 3x3 PLD box was not improving the fits.

Furthermore, since assuming a 1 order quadratic (linear) baseline can result in underestimating the eclipse depth for hot planets with large phase amplitudes (e.g., Bell et al. 2019), we also tested a 2 order quadratic baseline in time. However, such a 2 order quadratic coefficient can also be degenerate with the eclipse depth. We tested including a 2 order quadratic baseline (2 free parameters) compared to a 1 order baseline (1 free parameter). We found that it was not statistically significant to have a 2 order quadratic free in each of the fits (mean ΔBIC of 3). However, we also tested fixing the 2 order quadratic co-efficient while still leaving the 1 order co-efficient free. This test was statistically significant (mean ΔBIC of 53) when comparing it with a 1 order quadratic (linear) baseline. We, therefore, opted to fix the 2 order coefficient to the weighted mean value from the first fit, -0.031 ± 0.004 . This method corrects the astrophysical signal from the large phase amplitudes (2 order) without compromising the systematic correction (1 order) and thus leads to accurate results on the eclipse depths.

To achieve our final results we perform two fits of the lightcurves. First, we perform an initial fit with 15 free parameters (a/R_s , inclination, F_p/F_s , $T_{\text{secondary}}$, 9 PLD parameters and a 2 order quadratic baseline in time). Then we fix a/R_s , inclination, and the 2 order quadratic coefficient to the weighted mean of all ten lightcurves. We do this since we do not expect these parameters to be physically changing in time. Our final MCMC fits have 12 free parameters (R_p/R_s , $T_{\text{secondary}}$, 9 PLD parameters and 1 temporal slope). As a sanity check, we compare the brightness temperatures between the first and second fit in Figure 4.4, and find that it still shows variability.

Posterior distributions and uncertainties are calculated on the fitted eclipse parameters by performing a full Markov Chain Monte Carlo (MCMC) exploration of parameter space using emcee (Foreman-Mackey et al. 2013). We run chains with 100 walkers with a typical 500 step burn-in period followed by a 1000 step production run and confirm the convergence of our chains via the auto-correlation time and the mean acceptance fraction.

4.4 Results

4.4.1 *Spitzer*/IRAC secondary eclipse lightcurves

Table 4.1 displays the a/R_s , inclination and 2 order quadratic coefficient from the first fit. We did not find any variability in a/R_s and inclination with time, which is why we fixed these parameters to the weighted mean for the second fit. Regarding the quadratic baseline, we found that the best ΔBIC was obtained by including a non-zero 2 order quadratic coefficient but fixing it to the mean from the first fit as mentioned in Section 4.3.2. The right hand side of Table 4.1 displays F_p/F_s , $T_{\text{secondary}}$ and T_B resulting from the second and final fit. We find that the weighted mean eclipse depth is 3729 ± 56 ppm, which is consistent with the eclipse presented in Nymeyer et al. (2011) and the phase curve presented in Maxted et al. (2013). We also find that the weighted mean secondary eclipse timings are within 1σ agreement with the previously calculated eclipse ephemeris from Maxted et al. (2013). In Figure 4.1, we show the final resulting systematic corrected lightcurves, where a/R_s , inclination and 2 order quadratic coefficient are fixed to the mean of the first fit. Raw lightcurves and residuals are shown in Appendix 4.A.

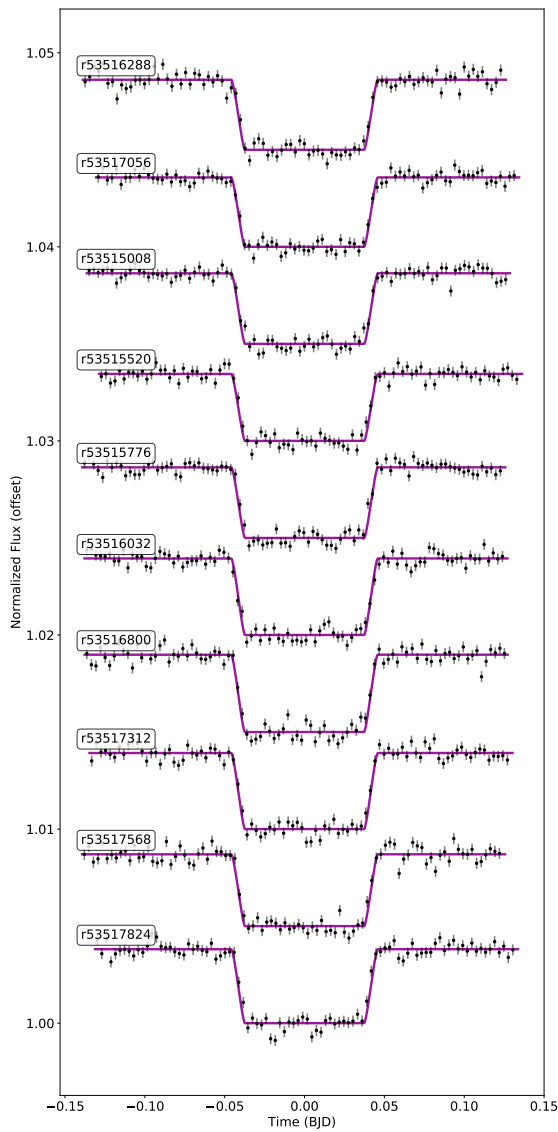


Fig. 4.1: Normalized and corrected eclipse lightcurves of WASP-18b, vertically offset for display purposes. These lightcurves are from the final fit, where we fixed a/R_s , inclination and the 2 quadratic coefficient to their weighted means from the first fit.

Table 4.1: Best fit eclipse and systematic parameters using an MCMC method. The semi-major axis (a/R_s), inclination, and 2nd order quadratic co-efficient (h) are shown from the first fits, they are fixed to the weighted mean in the final fit. The eclipse depth (F_p/F_s), brightness temperature (T_B) and the time of secondary eclipse ($T_{\text{secondary}}$) are shown from the final fits.

AOR	a/R_s	Inclination Degrees	h	F_p/F_s ppm	T_B Kelvin	$T_{\text{secondary}}$ BJD
r53517824	3.48 ± 0.15	83.29 ± 2.05	-0.03 ± 0.008	3810 ± 68	3079 ± 37	2457274.14104 ± 0.00029
r53517568	3.46 ± 0.14	83.38 ± 1.95	-0.039 ± 0.008	3700 ± 68	3011 ± 37	2457275.08202 ± 0.0003
r53517312	3.43 ± 0.16	83.09 ± 2.22	-0.035 ± 0.01	3919 ± 78	3166 ± 41	2457278.84855 ± 0.00028
r53516800	3.34 ± 0.15	82.04 ± 1.94	-0.038 ± 0.008	3984 ± 66	3163 ± 36	2457279.78877 ± 0.00026
r53516032	3.15 ± 0.15	80.42 ± 1.75	-0.011 ± 0.009	3954 ± 69	3147 ± 37	2457283.55482 ± 0.00028
r53515776	3.48 ± 0.14	83.27 ± 1.85	-0.041 ± 0.008	3640 ± 68	2984 ± 38	2457286.37946 ± 0.00028
r53515520	3.28 ± 0.18	81.15 ± 2.26	-0.046 ± 0.009	3454 ± 70	2890 ± 37	2457288.26257 ± 0.00029
r53515008	3.06 ± 0.18	78.70 ± 2.09	-0.028 ± 0.009	3633 ± 67	2988 ± 35	2457289.2035 ± 0.00029
r53517056	3.32 ± 0.19	82.08 ± 2.41	-0.025 ± 0.008	3585 ± 71	2943 ± 37	2457293.91153 ± 0.00031
r53516288	3.38 ± 0.18	82.32 ± 2.27	-0.013 ± 0.009	3616 ± 69	2973 ± 38	2457295.79433 ± 0.0003
Weighted Mean	3.45 ± 0.04	81.96 ± 0.49	-0.031 ± 0.004	3729 ± 56	3033 ± 31	
Standard Deviation	0.13	1.43	0.01	169	93	
Mean Error	0.16	2.08	0.01	69	37	

4.4.2 Brightness variability of WASP-18b in time

We plot the secondary eclipse depths of WASP-18b in time (see Figure 4.2), and we find that the eclipse depths are not constant, but instead, they show a level of variability, that isn't random, but that is reproduced by a periodic sinusoidal signal. We find that the eclipse depth measurements deviate from a straight line by more than 7σ . We fit this temporal brightness variability with a sinusoidal function in time (t). We parameterize the sinusoid with four free parameters: semi-amplitude (A), frequency (ν), phase (φ) and an offset (\bar{D}) such that the eclipse depths in time are modeled with $D(t) = A\sin(\nu t) + \bar{D}$. We tested fixing the phase parameter (φ) but this did not significantly improve the fits ($\Delta\text{BIC} = 2.2$). We calculate posterior distributions on these parameters by running an MCMC exploration using emcee (Foreman-Mackey et al. 2013) with 300 walkers, 1000 burn-in steps, and 20000 production steps. We confirm the convergence of the chains using the auto-correlation time and the mean acceptance fraction. We then test the robustness of our sinusoidal fit by comparing it with a straight line using the Bayesian Information Criteria (BIC).

Figure 4.3 shows the posterior distributions from the MCMC sinusoidal fits and the best sinusoidal fit is also shown in Figure 4.2. We find that the sinusoidal fit is statistically significantly favored over a straight line fit where the BIC of the straight line is 62.3 and the BIC of the sinusoid being 18.2. The best fit sinusoidal parameters are: $A = 228 \pm 36$ ppm, $\nu = 0.27 \pm 0.02$, $\varphi = -0.01 \pm 0.23$, $\bar{D} = 3732 \pm 23$ ppm. This corresponds to a 23.1 ± 1.7 days period of variability and a $12.2 \pm 1.9\%$ peak-to-trough brightness variability ($2A$).

We tested for variability and correlations with the other parameters we let free in the fits. The standard deviation is smaller than the mean error over all ten lightcurves for a/R_s and inclination (see Table 4.1). This indicates that there is no variability in these parameters. We also tested for correlations between a/R_s and inclination with F_p/F_s , in both cases they had low Pearson correlation coefficients (0.05 and 0.13 respectively) with high associated chance probabilities (0.9 and 0.7 respectively). These numbers indicate that a/R_s and inclination are not correlated with F_p/F_s .

4.4.3 Testing the method to measure variability

To test the robustness of our analysis and ensure that our method does not introduce any spurious variability, we analyze the ten secondary eclipses of another hot Jupiter, XO-3b, which has been widely studied, and which serves as calibration of our methods. These eclipses were first published in Wong et al. (2014) and later used as part of the extensive repeatability and accuracy post-cryogenic *Spitzer*/IRAC data challenge (Ingalls et al. 2016). Ingalls et al. (2016) test seven different techniques for correcting the correlated noise. Across these seven techniques, they measure an average eclipse depth of 1520 ± 30 ppm. This value is a straight average of the weighted mean and weighted uncertainty over the ten eclipses for each technique. We calculate the weighted mean and weighted uncertainty using the same method (see their eq. 5-9) and find that the weighted mean eclipse depth of our PLD corrected secondary

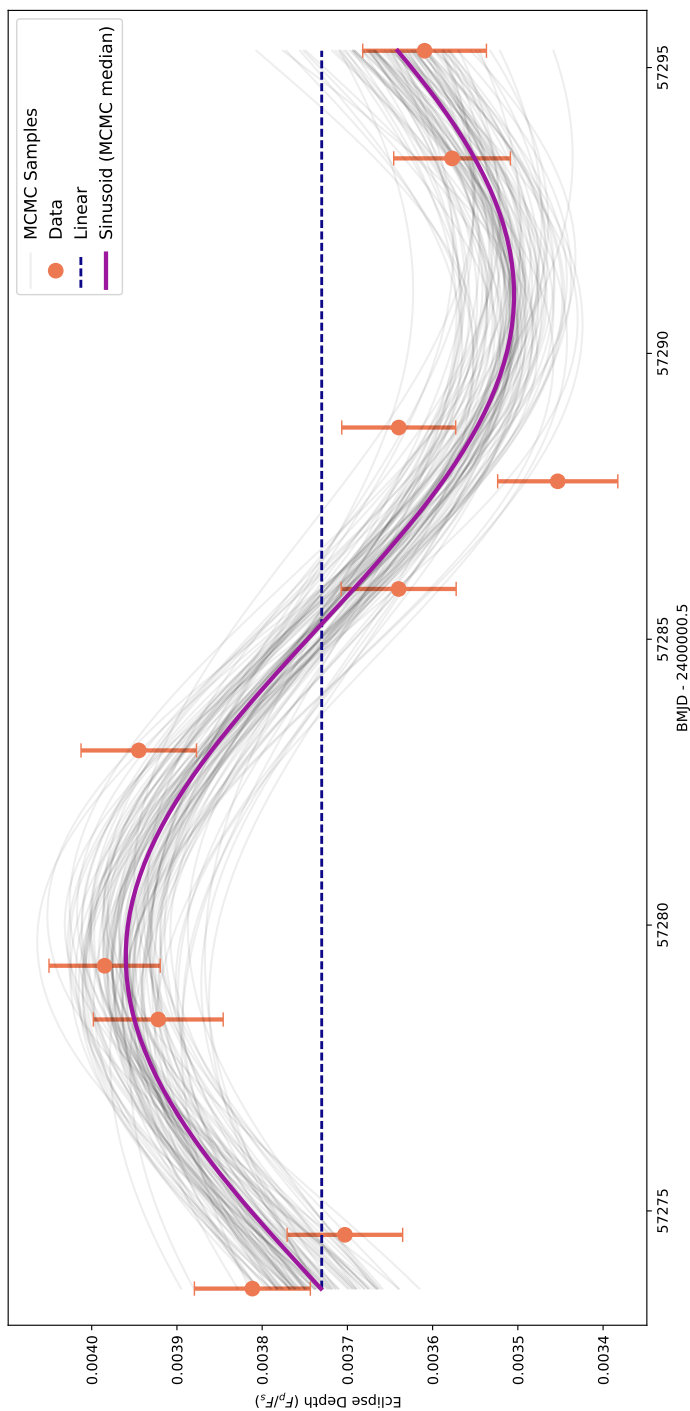


Fig. 4.2: Measured eclipse depths of WASP-18b over time in orange, for the ten semi-consecutive eclipses. Purple solid line shows the median result from the MCMC fit, 100 random samples from the posterior distributions are shown in gray, blue line shows the best fitting straight line.

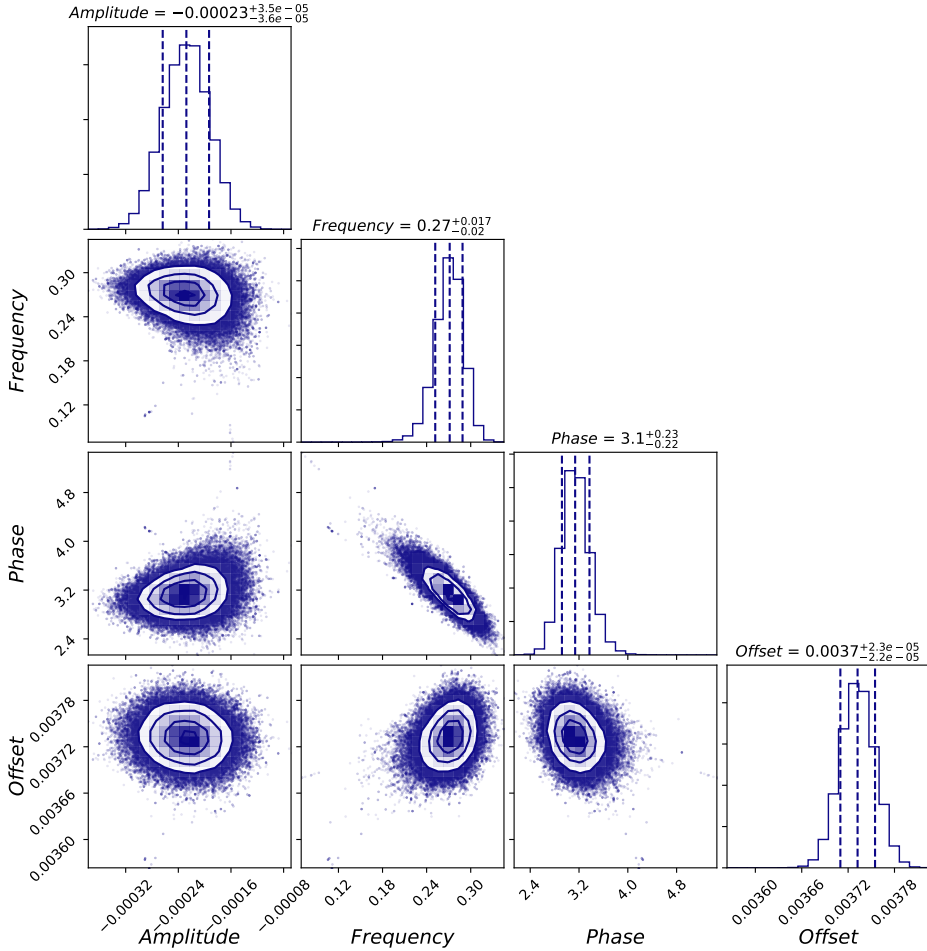


Fig. 4.3: Posterior probability distributions of the free parameters from a periodic sinusoidal MCMC fit to the brightness variability in time of WASP-18b at $4.5\text{ }\mu\text{m}$. In the marginalized confidence intervals the inner dashed line is the median and the outer dashed lines are the 1σ confidence level.

eclipses to be 1520 ± 29 ppm. This is in remarkable agreement with Ingalls et al. (2016) and we conclude that our pipeline produces consistent results.

For XO-3b we measure the mean uncertainty over the ten eclipses to be 84 ppm, which is in agreement with the average precision achieved over the seven different techniques in Ingalls et al. (2016), which was 102 ppm (ranging from 48 ppm to 152 ppm). We also find that the standard deviation of the ten eclipse depths to be 86 ppm. The fact that the mean uncertainty and the standard deviation are the same indicates that the eclipse depths are drawn from a random distribution, and there is no evidence for variability in the eclipses of XO-3b.

On the other hand, for WASP-18b, the mean uncertainty of the ten eclipse depths is 69 ppm, yet the standard deviation is 173 ppm. This indicates that there is variability measured at a significant level in the secondary eclipse measurements of WASP-18b.

4.4.4 Variability of WASP-18b at various wavelengths

WASP-18b was also observed at 3.6 μm with *Spitzer*/IRAC on two occasions: an eclipse was observed in December 2008, $F_p/F_s=3040\pm170$ ppm (Nymeyer et al. 2011), and a phase curve was observed in January 2010, $F_p/F_s=3000\pm200$ ppm (Maxted et al. 2013). These two eclipse depths are consistent to within 1σ and so cannot rule out or confirm variability at 3.6 μm .

Shporer et al. (2019) measure the eclipse depth of WASP-18b with 40 TESS eclipses to be 341^{+17}_{-18} ppm. A $\sim 12\%$ variability in TESS would result in a 21 ppm variability semi-amplitude. The precision on one eclipse measured with TESS would be $18 \times \sqrt{N}$, where N is the number of measurements, resulting in a precision of 113 ppm on each eclipse. Using this precision, we simulate the 40 individual eclipses from Sectors 2 and 3 in Shporer et al. (2019) and the 58 additional unpublished eclipses from Sectors 29 and 30. We then add a 21 ppm sinusoidal variability signal and try to retrieve it using MCMC. We find that TESS does not have the precision to detect the 21 ppm variability to greater than 1σ with the 98 simulated eclipses.

Furthermore, Arcangeli et al. (2018) publish 5 secondary eclipses of WASP-18b with HST/WFC3. Their combined spectrum is measured to ~ 20 ppm precision per bin. Using this, we calculated the precision on the combined white lightcurve to be 38 ppm. This means that the precision on one eclipse is 45 ppm per bin and 86 ppm on the white lightcurve. A $\sim 12\%$ peak-to-trough variability would result in 46–72 ppm semi-amplitudes over the spectral range. Using the same method as above, we found that HST/WFC3 does not have the precision to detect this variability across 5 eclipses in either the white light curve or the individual bins.

4.5 Discussion & Conclusion

We explore the possible origins of the variability in the dayside of an ultra-hot Jupiter atmosphere, these are changes in disk-integrated temperature, compositional changes, the presence of inhomogeneous clouds, magnetic field interactions, or stellar variability.

We first consider whether the periodic change in eclipse depths measured at 4.5 μm could be due to the variability of the atmosphere of the planet itself. Variability in the eclipse depths relates directly to variability in the disc averaged brightness temperatures (see Table 4.1). The peak-to-trough change in the brightness temperature of our sinusoidal fit is ~ 250 K. GCMs of WASP-18b show that the temperature-pressure profiles on the dayside change significantly from the coolest western terminator to the hottest substellar point Helling et al. (2019a). At the millibar level, which corresponds to the pressures probed by *Spitzer*, these temperatures change by almost 1000 K. 250 K variability in the disc averaged temperature could lead to

compositional variability in the atmosphere in time. However, the dominating opacity at the $4.5\text{ }\mu\text{m}$ band of *Spitzer*/IRAC is carbon monoxide and the abundance weighted opacity is relatively constant, even over the 1000 K temperature gradient spanned by the hot spot to the western terminator (e.g., Moses et al. 2013a). It is therefore unlikely that we are detecting changes in the volume mixing ratio of CO at $4.5\text{ }\mu\text{m}$.

However, high levels of H₂ dissociation are expected in the atmospheres of UHJs, atomic hydrogen can be transported to the nightside via eastward winds where it recombines and deposits a large amount of heat (Komacek 2018; Bell & Cowan 2018). Given a fixed wind speed, this will increase the global efficiency of heat redistribution. However, if the wind speeds are variable, the heat re-circulation from H₂ dissociation/recombination will also vary, and so might the measured brightness.

A second possible cause of variability in the atmosphere of WASP-18b is the presence of clouds. A previous theoretical study has examined cloud formation on WASP-18b using GCMs (Helling et al. 2019a). They extract 1D profiles to use as inputs in their kinetic cloud formation modeling. They find that, due to high temperatures, the dayside of WASP-18b has no seed formation and is almost completely cloud-free, with the exception of the coolest mid-latitude western terminator region. However, the seed formation occurs much deeper than the observable pressures. We, therefore, do not think that in-situ cloud formation is causing the $\sim 12\%$ variability. It is also possible that small cloud particles could be transferred from the nightside to the dayside and act as condensation seeds, however, the dayside temperature is too hot for sufficient supersaturation of the gas phase required for condensation (Helling et al. 2019a), thus it is unlikely that the $\sim 12\%$ peak-to-trough brightness variability is due to clouds.

The temperature of WASP-18b dayside is so hot that it is expected that many of the atoms are in their second ionization state (Helling et al. 2019a). The predicted degree of ionization ($f_e > 10^{-7}$) is sufficiently high for the atmosphere to couple the planetary magnetic field. This results in electromagnetic hydrodynamic waves called Alfvén waves (Alfvén 1942). MHD GCMs of HAT-P-7b with a 10G magnetic field shows zonal wind oscillations on a timescale of $\sim 10^6$ seconds (11.5 days), which is consistent with the Alfvén time ($\tau_A = \sqrt{4\pi\rho\lambda/B}$) (Rogers 2017). Scaling this Alfvén time to the mass and size of WASP-18b, and maintaining a 10G field, leads to a scaling factor of 2.5. This results in ~ 28 day oscillations, which is in good agreement with our measured infrared variability period. The 23 day period of WASP-18b's variability can be matched with a 12G magnetic field injected in this equation. Meaning that our observations can be explained with a relatively small magnetic field. Simulations specific to WASP-18b would be necessary to constrain the magnetic field further.

Stellar variability can alter the interpretation of transiting planets (e.g., Pont et al. 2008; Oshagh et al. 2014; Désert et al. 2011c), however, stellar variability affects transits more than secondary eclipses (Zellem et al. 2017). WASP-18 has been shown to have suppressed stellar activity, with a low $\log(R'_{HK})$ of -5.15 (Lanza 2014) and a far UV spectrum representing that of an old ($>5\text{Gyr}$) inactive star (Fossati et al. 2018). We, therefore, do not think the brightness variability of WASP-18b is caused by stellar variability. Our finding is similar to HD189733,

which is known to be more active than WASP-18. Kilpatrick et al. (2020) measured the stellar variability amplitudes of HD189733 and find no statistically significant effect on the measured eclipse depths, even though the eclipses have 2x higher precision than WASP-18b.

Multiple epoch observations at different wavelengths would also be necessary to further disentangle the story behind WASP-18b's variability. However, WASP-18b is the fourth ultra-hot Jupiter to exhibit variability and the first to exhibit periodic infrared brightness variability in time. It is thus clear that planetary variability cannot be ignored going forward with JWST observations of ultra-hot Jupiters. JWST will be able to measure phase curves of ultra-hot Jupiters to unprecedented precision. This will help determine longitudinal changes in chemical composition and measure the brightness phase variations and hot-spot offsets. This, when coupled with MHD atmospheric models, could help constrain the planetary magnetic field strength.

4.A Supplementary plots

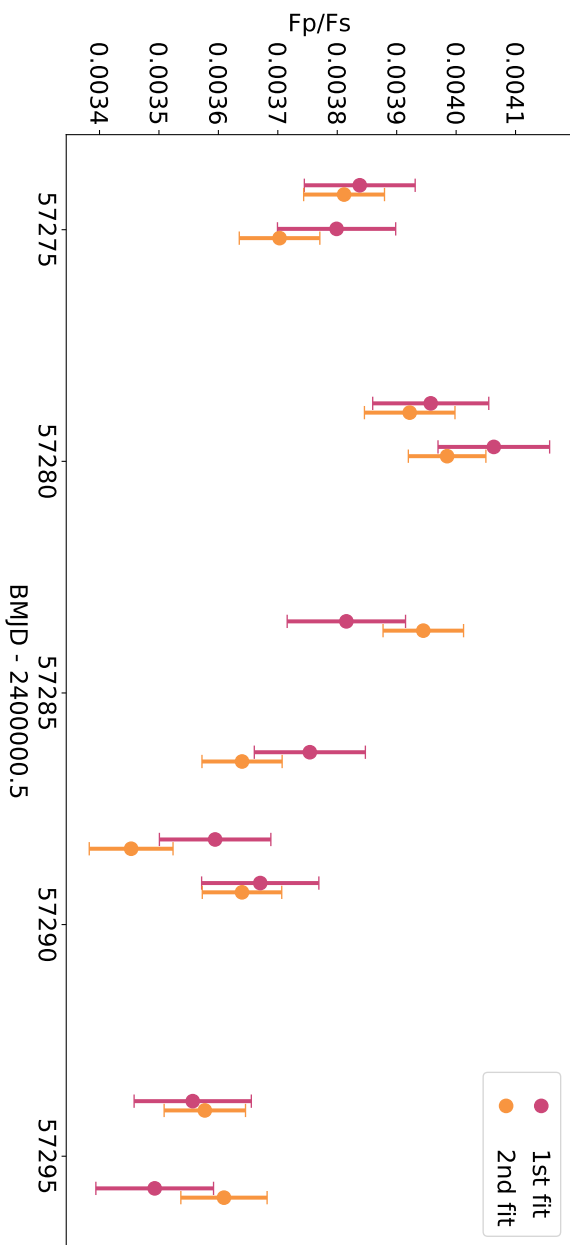


Fig. 4.4: Measured eclipse depths of WASP-18b over time in orange, for the ten semi-consecutive eclipses. Pink shows the eclipse depths from the first fit, where all parameters are free. Orange show the eclipse depths from the second fit, where the orbital distance, inclination and 2 order quadratic term are fixed to the weighted mean from the first fit.

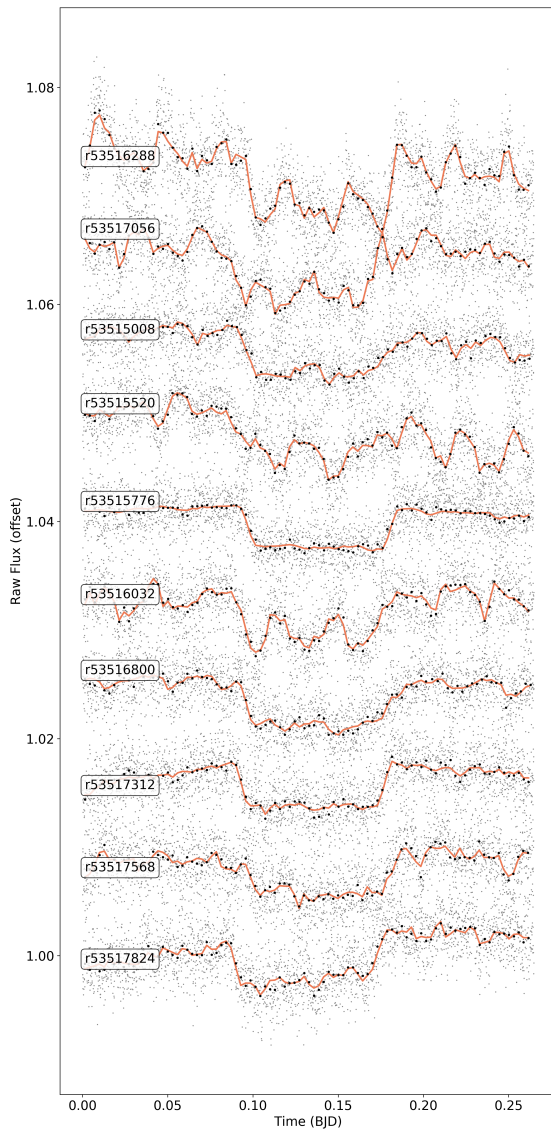


Fig. 4.5: Raw eclipse lightcurves of WASP-18b with best fit systematic and eclipse model in orange.

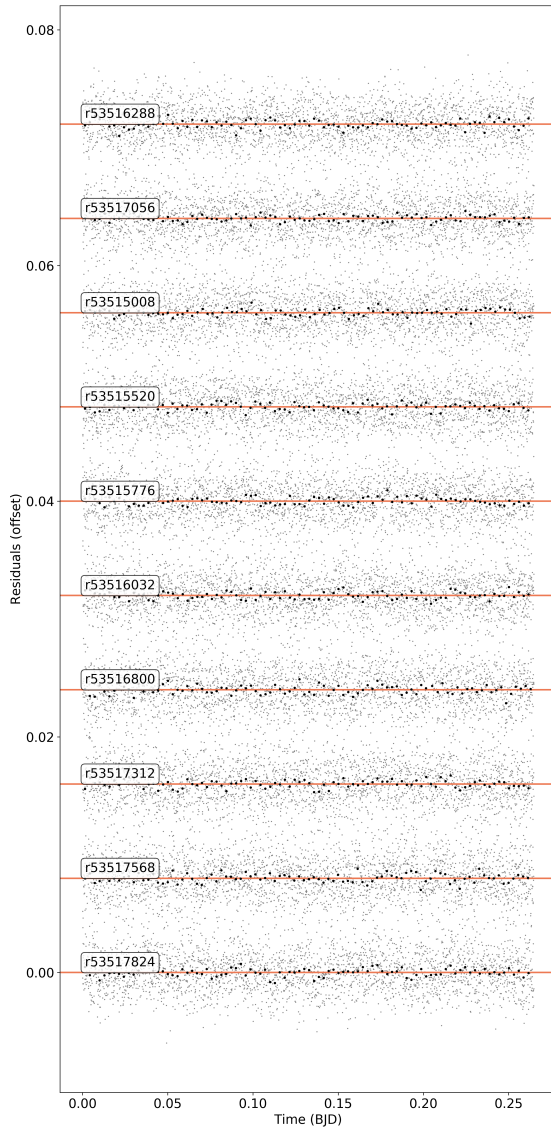
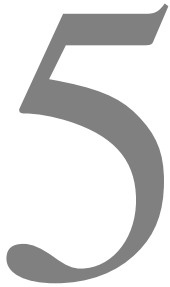


Fig. 4.6: Residuals of WASP-18b eclipses with best fit systematic and eclipse model subtracted.

**TRANSIT TIMING VARIATIONS OF COOL KEPLER PLANETS
FROM SPITZER/IRAC ANALYSIS**

Claire Baxter, Jean-Michel Désert, Daniel Fabrycky

in preparation

Abstract

Here we present the analysis of forty-eight transits of three multi-planet systems (Kepler-9, Kepler-18 and Kepler-32) and one circumbinary system (Kepler-16b) using *Spitzer*/IRAC 3.6 and 4.5 μm photometric bandpasses. We analyze the lightcurves using our custom pipeline, which implements pixel level decorrelation to correct for the strong *Spitzer* systematics. We present the resulting transit parameters and transit times for each lightcurve. For the multi-planet systems we are able to constrain the transit times to around 8-minute precision for Kepler-9 and -18 and to around 40 minutes for Kepler-32. The flux from Kepler-16 is two orders of magnitude higher resulting in much better precision on the transit parameters, the transit times are constrained to the sub-minute level. We compare the transit times of the multi-planet systems to transit timing variation models which were calculated using *Kepler* data, and find that our times agree with the current predictions. However, the data demonstrates significant scatter compared to the *Kepler* data and so we cannot constrain the models any further. We compare the Kepler-16b *Spitzer* transit times to photodynamical predictions from the *Kepler* data. We find that the transits occur significantly later than predicted. We, therefore, use the *Spitzer* transits in combination with the *Kepler* transits to update the photodynamical model and report the new constraints on the orbital elements of the system.

5.1 Introduction

The *Kepler* mission (Borucki et al. 2010) has provided us with a wealth of information on the exoplanet population. So far, there have been over 2800 planets discovered with *Kepler* and K2. Analysis of this population of planets has revealed that almost 50% of stars in our galaxy are hosts to exoplanets, and that the most common type of planet are those with masses between the Earth and Neptune (Batalha et al. 2013; Batalha 2014; Fressin et al. 2013; Petigura et al. 2013b,a). Out of these many newly discovered exoplanets resulting from the *Kepler* mission, there are more than 700 multi-planet systems.

Prior to the launch of *Kepler*, it was shown that numerically reproducing the dynamical interactions of multi-planet systems can provide constraints on the individual planet masses (Holman & Murray 2005; Agol et al. 2005). Dynamical interactions in multi-planet systems cause deviations from Keplerian orbits resulting in variations in the orbital period which can be detected by measuring transit timing variations (TTVs). This technique was used to confirm the multi-planet system Kepler-9 and to measure the individual masses of the planets (Holman et al. 2010). TTV measurements with *Kepler* have yielded mass and eccentricity measurements for a significant number of planets, which is particularly useful for sub-Jovian planets where radial velocity signals are typically too small (Jontof-Hutter et al. 2016; Hadden & Lithwick 2017). Mass and eccentricity constraints are crucial for understanding planetary formation and evolution.

The Spitzer Space Telescope can also provide excellent precision on the transit times of multi-planetary systems (e.g., Beichman et al. 2016; Gillon et al. 2017; Berardo et al. 2019). Gillon et al. (2017) used the $4.5\mu\text{m}$ bandpass to continuously monitor the TRAPPIST-1 system, detecting 37 transits of the shortest period planet (TRAPPIST-1b) and 1 transit of the longest period planet (TRAPPIST-1h). They were able to measure the transit times of all seven Earth-size exoplanets to better than one minute precision.

In this work, we study three multi-planet systems (Kepler-9, Kepler-18 and Kepler-32) and one circumbinary system (Kepler-16). Kepler-9 is a benchmark system consisting of two planets with relatively deep transits ($\sim 0.5\%$) and one super-Earth orbiting a solar analog star with *Kepler*-magnitude of 13.803 (Holman et al. 2010). Freudenthal et al. (2018) applies a photodynamical model to *Kepler* and ground-based observations of the Kepler-9 system to determine precise densities and predict the future dynamics of the system. Here, we use *Spitzer*/IRAC data to study the two innermost planets, Kepler-9b and Kepler-9c, in an attempt to compare the data to model predictions as well as study their atmospheres. These two planets have orbital periods near a 2:1 mean motion resonance, leading to TTV amplitudes on the order of one day (Freudenthal et al. 2018).

The second system we study is Kepler-18, another 3 planet system around another sun-like star, with a *Kepler*-magnitude of 13.549. In this work, we study the two outermost low-density Neptune mass planets, Kepler-18c and Kepler-18b, which are accompanied by an inner super-Earth planet Cochran et al. (2011). Kepler-18c and Kepler-18d also have orbital periods near a 2:1 mean-motion resonance, resulting in large TTV signals.

The third system is Kepler-32, a five-planet system around an M dwarf (Muirhead et al. 2012) with *Kepler*-magnitude of 15.801. Planet b and c have relatively short orbital periods in a 3:2 mean motion resonance, resulting in detectable TTV amplitudes in *Kepler*. However, have relatively small transit depths ($\sim 0.15\%$), which when combined with a faint star make their transits challenging.

The final planet we study is the circumbinary planet, Kepler-16b, which is on a 229 day orbital period around its two parent stars (Doyle et al. 2011). Kepler-16b now only transits star A, a 0.68 solar mass K-type star with *Kepler*-magnitude 11.762. Here, we analyze two transits of Kepler-16b, at 3.6 and $4.5 \mu\text{m}$, two orbital periods apart. We aim to constrain the dynamics and planet mass using photo-dynamical models.

This paper is organized as follows. We describe the observations in Section 5.2, and the data analysis and lightcurve reduction in Section 5.3. We present the results on the transit times of each of our systems in Section 5.4 and compare to predictions from TTV models in the case of the multi-planet systems and photo-dynamical model for Kepler-16b.

5.2 Observations

Using *Spitzer* /Infrared Array Camera (IRAC), we observed a total of 46 transits at 3.6 and $4.5 \mu\text{m}$ of three multi-planet Kepler systems: Kepler-9, Kepler-18 and Kepler-32. Additionally, we obtained two transit observations of the circumbinary planet Kepler-16b (one at $3.6 \mu\text{m}$ and one at $4.5 \mu\text{m}$). These transits were taken two orbital periods apart with the first ($3.6 \mu\text{m}$) observation taking place on UT 2013 September 23 and the second ($4.5 \mu\text{m}$) on UT 2014 December 18. Our observations are part of the survey program 90092 (PI Desert) and are thus taken during the Post Cryogenic Warm *Spitzer* /IRAC mission, meaning the data are in sub-array mode (32×32 pixels) and only at 3.6 and $4.5 \mu\text{m}$. Furthermore, all observations were taken in "peak-up" mode, which consists of a 30-minute throw-away observation allowing for accurate pointing and precise positioning of the target which reduces the ramp-up caused by the intrapixel sensitivity. Table ?? shows further details of our observations.

Table 5.1: Details of the Spitzer Observations used in our survey analysis showing the UT date of observation, the duration of observation in hours and the program ID of each transit.

Target	λ μm	UT Start Date	Duration Hours	Program ID
Kepler-9b	3.6	2013 Jul 04	7.2	90092
Kepler-9b	3.6	2013 Aug 31	7.2	90092
Kepler-9b	3.6	2013 Dec 05	7.2	90092
Kepler-9b	3.6	2014 Jan 12	7.2	90092
Kepler-9b	4.5	2013 Aug 11	7.2	90092
Kepler-9b	4.5	2013 Sep 19	7.2	90092
Kepler-9b	4.5	2013 Dec 24	7.2	90092
Kepler-9b	4.5	2014 Jul 24	7.2	90092

Table 5.1: continued.

Target	λ $\mu\text{ m}$	UT Start Date	Duration Hours	Program ID
Kepler-9c	3.6	2013 Jan 01	7.7	90092
Kepler-9c	3.6	2013 Nov 09	7.7	90092
Kepler-9c	3.6	2014 Jun 30	7.7	90092
Kepler-9c	3.6	2014 Sep 16	7.7	90092
Kepler-9c	4.5	2013 Oct 01	7.7	90092
Kepler-9c	4.5	2013 Dec 18	7.7	90092
Kepler-9c	4.5	2014 Aug 08	7.7	90092
Kepler-9c	4.5	2014 Dec 02	7.7	90092
Kepler-18c	3.6	2012 Nov 28	6.3	90092
Kepler-18c	3.6	2012 Dec 13	6.3	90092
Kepler-18c	3.6	2013 Oct 22	6.3	90092
Kepler-18c	4.5	2013 Aug 15	6.3	90092
Kepler-18c	4.5	2013 Oct 07	6.3	90092
Kepler-18c	4.5	2014 Jan 07	6.3	90092
Kepler-18d	3.6	2012 Nov 22	6.3	90092
Kepler-18d	3.6	2013 Nov 13	6.3	90092
Kepler-18d	3.6	2013 Dec 28	6.3	90092
Kepler-18d	4.5	2013 Oct 15	6.3	90092
Kepler-18d	4.5	2013 Nov 28	6.3	90092
Kepler-18d	4.5	2014 Jan 27	6.3	90092
Kepler-32b	3.6	2013 Jul 29	4.5	90092
Kepler-32b	3.6	2013 Aug 04	4.5	90092
Kepler-32b	3.6	2013 Nov 18	4.5	90092
Kepler-32b	3.6	2014 Jan 05	4.5	90092
Kepler-32b	3.6	2014 Jan 22	4.5	90092
Kepler-32b	4.5	2013 Aug 22	4.5	90092
Kepler-32b	4.5	2013 Oct 20	4.5	90092
Kepler-32b	4.5	2013 Dec 06	4.5	90092
Kepler-32b	4.5	2014 Jan 16	4.5	90092
Kepler-32b	4.5	2014 Feb 09	4.5	90092
Kepler-32c	3.6	2013 Jul 26	4.5	90092
Kepler-32c	3.6	2013 Aug 04	4.5	90092
Kepler-32c	3.6	2013 Oct 22	4.5	90092
Kepler-32c	3.6	2013 Nov 08	4.5	90092
Kepler-32c	4.5	2013 Aug 13	4.5	90092
Kepler-32c	4.5	2013 Aug 30	4.5	90092
Kepler-32c	4.5	2013 Oct 30	4.5	90092

Table 5.1: continued.

Target	λ $\mu\text{ m}$	UT Start Date	Duration	Program ID
			Hours	
Kepler-32c	4.5	2013 Dec 22	4.5	90092
Kepler-16b	3.6	2013 Sep 23	13.6	90092
Kepler-16b	4.5	2014 Dec 18	13.6	90092

5.3 Data Analysis

5.3.1 *Spitzer* /IRAC lightcurve reduction

We reduce the *Spitzer* /IRAC transit observations with our custom pipeline described fully in Baxter et al. (2021) which uses the pixel level decorrelation method from (Deming et al. 2015). The planets in Baxter et al. (2021) were selected for observation due to their high expected signal-to-noise ratio (S/N), these planets had an average K-magnitude of 10 resulting in high precision measurements on transit lightcurve parameters. The multi-planet Kepler systems in this work have a much lower expected S/N with an average K-mag of 12, two orders of magnitude fainter than the Baxter et al. (2021) sample. As an example, the average number of electrons detected in a 2-second exposure was \sim 40,000 e- for all of the planets in Baxter et al. (2021). This number determines the precision on each photometric data point due to photon counting statistics, and therefore determines the overall precision of the resulting parameters from fitting the transit lightcurve. For the multi-planet systems presented in this work, the average number of electrons detected in a 2 second exposure is \sim 5,500 e-, resulting in large uncertainties and poorly constrained transit parameters. Due to the low signal-to-noise ratios (S/N) for all planets except Kepler-16b, we modified our approach in this work. For clarity, we recall the main steps of our pipeline and then note the changes for the low S/N planets.

In each of the Spitzer sub-array frames, we correct the dark current, flat field, and convert them to flux units before performing aperture photometry using a circular aperture around the calculated centroid position of the star. A full run of our original pipeline would create a grid of data reductions and finds the optimum methods and parameters for background subtraction, centroiding, and aperture photometry radius by means of a lowest reduced χ^2 on the resulting lightcurves.

This method was followed for Kepler-16b, with details on the transit fitting below. However, for the other planets (Kepler-9, Kepler-18, and Kepler-32) we found that there was a very large spread in the fit parameters depending on the choice of pipeline parameters, the fit resulted in no transit being detected (transit depth of 0). We, therefore, studied all transit depths for every iteration of the pipeline and manually choose the optimum pipeline parameters (background subtraction, centroiding, and photometry radius). The criteria for the manual selection of the pipeline parameters were to have a non-zero and stable transit depth,

Table 5.2: Transit parameters and the corresponding reference for each of the Kepler planets. We show the semi-major axis (a/R_s), inclination, transit depth (R_p/R_s) and orbital period. Kepler-32 a/R_s were calculated from $R_p(R_J)$ and $a(\text{AU})$.

System	a/R_s	inclination °	R_p/R_s	Period days	Ref.
Kepler-9b	$31.3^{+1.1}_{-1.5}$	$88.982^{+0.007}_{-0.005}$	$0.0776^{+0.0019}_{-0.0015}$	19.23891 ± 0.00006	1
Kepler-9c	$49.8^{+1.7}_{-2.6}$	$89.188^{+0.005}_{-0.006}$	$0.0756^{+0.0018}_{-0.0014}$	38.9853 ± 0.0003	1
Kepler-18c	14.43 ± 0.61	87.68 ± 0.22	0.04549 ± 0.00055	7.64159 ± 0.00003	2
Kepler-18d	22.48 ± 0.96	88.07 ± 0.10	0.05782 ± 0.00069	14.85888 ± 0.00004	2
Kepler-32b*	20.29 ± 2.35	...	0.0389 ± 0.0019	5.90124 ± 0.00010	3
Kepler-32c*	36.52 ± 7.60	...	0.0352 ± 0.0033	8.7522 ± 0.0003	3
Kepler-16b	$228.776^{+0.020}_{-0.037}$	4

(1) Borsato et al. (2019); (2) Cochran et al. (2011); (3) Fabrycky et al. (2012); (4) Doyle et al. (2011);

i.e. small changes in pipeline parameters resulted in small changes in transit depths, then to keep the reduced χ^2 as low as possible. Finally, we opted to use the same parameters for all AORs of each planet for consistency.

Uncertainties on the photometric points are calculated from photon noise and scaled up such that the reduced χ^2 after an initial least-squares fit is equal to 1.

5.3.2 Spitzer /IRAC lightcurve fitting

The *Spitzer* /IRAC transit lightcurves are fit using the same method as in (Baxter et al. 2021). We fit the Spitzer systematics using Pixel Level Decorrelation (Deming et al. 2015) and fit the transit using batman (Kreidberg 2015). Due to the differences in S/N, we treat the multi-planet systems and Kepler-16 differently. However, all the tests performed and the method used to obtain the results on final parameters is a full Markov Chain Monte Carlo (MCMC) with 100 walkers, 500 throwaway burn-in steps, and 1000 production steps. We confirm convergence by looking at the autocorrelation time.

5.3.2.1 Obtaining the best fits of the multi-planet systems

Due to the low signal-to-noise of the multi-planet systems, the final transit times are calculated by fixing the orbital distance (a/R_s), inclinations (i), and transit depths ($(R_p/R_s)^2$) to the literature values. These fixed values are displayed in Table 5.2. We also fix the limb darkening to a linear law with parameters calculated from the 1D ATLAS code presented in (Sing 2010). The stellar parameters use for this calculation are also displayed in Table 5.3.

To determine the optimum transit times for the lightcurves, we performed several different tests when fitting the lightcurves. We compared each of our tests using the Bayesian Information Criterion (BIC) and by studying the precision on the resulting transit times. We

Table 5.3: Stellar parameters and the corresponding reference for each of the Kepler systems. We show the stellar effective temperature (T_{eff}), metallicity ([Fe/H]) and surface gravity ($\log(g)$). Limb darkening co-efficients for a linear limb darkening law calculated from the 1D ATLAS code (Sing 2010) shown for 3.6 and $4.5\mu\text{m}$.

System	T_{eff} Kelvin	[Fe/H] dex	$\log(g)$ $\log_{10}(\text{cm/s}^2)$	$3.6\mu\text{m}$ ld	$4.5\mu\text{m}$ ld	Ref.
Kepler-9	5777 ± 61	0.12 ± 0.04	4.49 ± 0.09	0.202 ± 0.004	0.175 ± 0.003	1
Kepler-18	5345 ± 100	0.19 ± 0.06	4.31 ± 0.12	0.219 ± 0.004	0.186 ± 0.002	2
Kepler-32	3787 ± 117	-0.1 ± 0.1	4.74 ± 0.08	0.165 ± 0.017	0.157 ± 0.010	3
Kepler-16	4450 ± 150	-0.2 ± 0.2	4.6527 ± 0.0017	0.113 ± 0.029	0.107 ± 0.017	4

(1) Torres et al. (2011); (2) Cochran et al. (2011); (3) Dressing & Charbonneau (2013); (4) Doyle et al. (2011)

aimed to have a uniform approach for each planet, so we calculated the average ΔBIC and average improvement in timing precision over all the lightcurves for each planet to determine if the method had a statistically significant improvement on the fit for each planet.

The first test was determining which parameters we could leave free in the fits. When leaving the transit depth, semi-major axis, and inclination as free parameters the transit fits were often unconstrained, with the fits getting stuck at a transit depth of zero. We first tested fixing only the semi-major axis and the inclination (leaving R_p/R_s free), the average ΔBIC for all ten of the Kepler-9 lightcurves was 4, meaning that the difference between having R_p/R_s fixed or free was not statistically significant. However, the precision retrieved on the final transit times of these fits was a factor of 1.5 smaller for R_p/R_s fixed compared to when R_p/R_s is free. For Kepler-32, leaving the transit depth free resulted in completely unconstrained transit parameters, so no information could be gained from these fits. We, therefore, opted to fix the transit parameters to literature values for studying the timing. However, leaving the transit depth free can provide us with information on the atmosphere so we show these results in Table 5.8 and Figure 5.6.

There are several different published values for each of our Kepler systems. For the Kepler-9 system we tested values from Holman et al. (2010) and Borsato et al. (2019), we found that Holman et al. (2010) provided better fits and more precise measured transit times with a ΔBIC of -32 compared to Borsato et al. (2019). However, the more recent parameters from Borsato et al. (2019) resulted in improved precision on the final transit times (average of 8.3 minutes compared to 8.0 minutes), so these are the values presented in Section 5.4. For the Kepler-32 system, we tested transit parameters from Fabrycky et al. (2012) and Muirhead et al. (2012). We found that the ΔBIC between the two sets of parameters was marginally in favor of the Muirhead et al. (2012) parameters ($\Delta\text{BIC} = -4$) and that the results using these parameters had a 5-minute improvement on the precision of the transit times. Therefore, we use the Muirhead et al. (2012) parameters for the remainder of this work. For the Kepler-18 system, there was just one study providing the transit depth, inclination, and semi-major axis, so we used those transit parameters from Cochran et al. (2011).

An additional source of error from the low signal to noise is increased scatter in the centroiding positions. We, therefore, tested fixing the centroiding to the mean over the whole lightcurve. We found that this induced more noise in the photometric lightcurve and resulted in worse fits with the average ΔBIC for fixing the centroid compared to leaving the centroiding free was -0.5, -2.0, and -3.1 for Kepler-9, Kepler-18, and Kepler-32 respectively. This means that fixing the centroid made the fits marginally worse. It also had no significant improvement on the precision of the transit times. Furthermore, we also tried binning the data to improve the S/N, however, we also found that this did not improve the precision of the times.

Finally, we tested Gaussian priors on some of our parameters. First, we tried a prior on the transit depth. We found that the average ΔBIC from having priors was -5.3 with a slight decrease in the precision on the transit times. Secondly, we tried a prior on the transit depth, orbital distance, and inclination, which resulted in a ΔBIC of -8.5. Therefore, it was not helpful to have a prior on either the $(R_p/R_s)^2$ or on the $(R_p/R_s)^2, a/R_s$ and i .

In Section 5.4.2 we compare the final transit times to TTV predictions using Kepler data. As a test, we also tried fixing the time with a prior on this parameter (as well as fixing semi-major axis, inclination, and transit depth as before) and compared the ΔBIC . We found that the ΔBIC was -16.6, meaning that the fits are better when there is no prior on the time.

5.3.2.2 Obtaining the best fits of the Kepler-16 system

Kepler-16 is of similar magnitude ($m_{\text{Ks}} = 8.996 \pm 0.022$) to the planets presented in Baxter et al. (2021), which allows us to use the same data reduction method. Using this method (outlined in Baxter et al. 2021), we determined that the optimum parameters for extracting the light curve were to centroid using a Moffat function, background subtract using a circular annulus centered on the star with a minimum radius of 6 and a maximum radius of 10, and to perform aperture photometry with a radius of 2.5 pixels around the star. We also found that the best fit for correcting the initial ramp-up was to remove the first 15 minutes of the $4.5 \mu\text{m}$ lightcurve. However, the $3.6 \mu\text{m}$ is more complicated since the ingress falls at the very beginning of the observation. We tested cutting the beginning of the lightcurve at 2-minute intervals but determined that the best fits were obtained by using all of the data, therefore, no cut was performed at the beginning of the $3.6 \mu\text{m}$ lightcurve.

Furthermore, the high S/N of the Kepler-16b lightcurves allows us to accurately constrain the transit parameters. Therefore, in our fits we left the transit depth ($(R_p/R_s)^2$), the orbital distance (a/R_s), the inclination (i), the transit time (T_0) and the systematic parameters all free. We fixed the orbital period to $228.776^{+0.020}_{-0.037}$ (Doyle et al. 2011) and the eccentricity and angle of periastron passage to 0. We also tried fixing the eccentricity and angle of periastron passage to 0.0069 and 318.0, respectively, however, we found that this had a negligible effect on the final parameters, with every parameter in every channel being consistent to less than 0.37σ .

We also fix the parameters of a linear limb darkening law with limb darkening parameters

calculated from the 1D ATLAS code presented in (Sing 2010), these parameters and the stellar parameters use for this calculation are displayed in Table 5.3.

5.3.3 TTV predictions of the multi-planet systems

Here we describe the dynamical analysis of the Kepler data, which allowed us to schedule the Spitzer observations originally, as well as determine how the knowledge of the dynamics of the systems are enhanced by the new data.

For the single-star systems (Kepler-9, 18, and 32), transit times are derived from the simple-aperture photometry provided on the Mikulski Archive for Space Telescopes (MAST) data portal. The transits are initially masked, and the coefficients to the first five contending basis vectors are adjusted to best-fit each quarter of data, after which that baseline is subtracted. A common shape model is assumed for all transits, based on the rectilinear motion of a planet across a linear limb-darkened star within the code of Mandel & Agol (2002), times a quadratic baseline covering 3 transits, centered on an initial guess for the transit time. Each transit mid-time is adjusted, simultaneous with the parameters of the shape model by χ^2 minimization, via the Levenberg-Marquardt algorithm, resulting in the data presented in Table 5.4.

An N-body model, described by (Fabrycky 2010), is run with DEMCMC to determine the error bars on orbital elements and masses. A subset of the resulting chain is propagated forward in time to the Spitzer observations, yielding a posterior for the times of transits. These values may be used as priors on the photometric fits, or they may simply be compared with the results of the Spitzer analysis. If the latter, a difference between the Kepler predictions and the Spitzer observations may be interpreted as missing components of the model, e.g. previously unknown perturbers.

5.3.4 Kepler-16b photodynamical model

A photodynamical model was developed in the Ph.D. thesis of S. Mills, where it was applied to both resonant system (Mills et al. 2016) and planets around binary systems (Welsh et al. 2015). This model was applied to the long-cadence photometric data of Kepler-16. The data were prepared by masking the transit times, then de-trending by fitting a cubic polynomial, within a sliding 2-day wide window.

Starting with orbital elements that were optimized to the first 600 days of Kepler photometry (Doyle et al. 2011), a differential-evolution Markov Chain Monte Carlo (DEMCMC; Ter Braak 2005) fit was performed, including the radial velocity values. A run of 40 walkers for 4300 generations yielded a best-fit, which was propagated forward to make photometric predictions for the Spitzer data.

We found that these best-fit times were considerably early (14 min) for the second transit, showing that actually including Spitzer data in the fit would give better constraints on the orbits. We ran the DEMCMC fit with the Kepler and Spitzer data combined. A common limb

Table 5.4: Transit times in units of $\text{BJD}_{\text{TDB}} - 2454900$ measured with *Kepler* for each of the multi-planet systems (Kepler 9, 18 and 32). Showing the first ten transits for each system, full data from the 4 year mission available electronically.

Kepler-9b	Kepler-9c	Kepler-18c
77.249373 ± 0.000796	69.306589 ± 0.001039	60.769501 ± 0.001044
96.483689 ± 0.000700	108.331810 ± 0.001211	68.407929 ± 0.001051
134.955219 ± 0.000674	147.336255 ± 0.001194	76.050937 ± 0.001472
154.191546 ± 0.000534	186.313195 ± 0.001747	83.692455 ± 0.001207
173.434560 ± 0.000907	225.263861 ± 0.000786	91.334704 ± 0.001689
211.926312 ± 0.000935	264.184471 ± 0.001091	106.611826 ± 0.001600
231.172271 ± 0.000391	303.071831 ± 0.001059	114.255395 ± 0.001632
250.430550 ± 0.000580	341.930204 ± 0.001084	121.896125 ± 0.001352
269.681775 ± 0.000945	380.765554 ± 0.000807	129.536438 ± 0.001212
288.946342 ± 0.000416	419.578253 ± 0.000940	137.178077 ± 0.001146
...
Kepler-18d	Kepler-32b	Kepler-32c
61.151516 ± 0.000892	68.993086 ± 0.006401	68.630187 ± 0.009214
76.011567 ± 0.000973	74.909074 ± 0.004925	77.395221 ± 0.010078
90.870969 ± 0.000741	80.791214 ± 0.008591	103.646223 ± 0.010308
105.730819 ± 0.000787	86.685556 ± 0.009716	112.378658 ± 0.013648
120.593162 ± 0.001387	92.606325 ± 0.006081	121.129198 ± 0.009362
135.449711 ± 0.000847	104.400104 ± 0.008117	129.887968 ± 0.010674
150.308328 ± 0.000845	110.293412 ± 0.006943	138.628310 ± 0.006710
165.169560 ± 0.000826	122.101891 ± 0.006287	147.378278 ± 0.008525
180.024765 ± 0.002150	128.019136 ± 0.004992	156.159973 ± 0.009048
194.885133 ± 0.000999	133.907354 ± 0.005382	164.889254 ± 0.009799
...

darkening was used, which allows the fit to correctly adjust to the timing of the Spitzer data, but not the shape. The parameters of the quadratic limb darkening for the Kepler bandpass are 0.652201 and 0.017569 for the 1st and 2nd order coefficients. For display purposes, we have plotted this model with Kepler limb-darkening, for the Spitzer transit we can optimize the limb darkening as a post-processing step.

5.4 Results

5.4.1 Transit times for the multi-planet systems

The final photometric lightcurves of Kepler-9b and -9c, Kepler-18c and -18d and Kepler-32b and -32c are shown in Figure 5.5. The measured transit times for each lightcurve are displayed in Table 5.5. In this table, we also show the error on the transit time in minutes as well as the fraction that the lightcurve was above photon noise. In terms of errors on the transit time, the Kepler-9 and Kepler-18 transit times are significantly better constrained compared with the Kepler-32 transit times. All three stars are of a similar magnitude and we obtain a similar level of precision in terms of the percentage of photon noise for all of the transits. So the lower precision on the transit times of the Kepler-32 planets is likely due to them having a significantly smaller transit depth signal due to the smaller relative size of the planet.

In these transit time results, there are three AORs of Kepler-9 and Kepler-18 (r47029248, r47060992, r47056128) that have very large errors on the transit times. Each of these three transits either has a poor correction of the instrumental systematics or they are almost partial transits, i.e. the ingress or egress falls close to the beginning or end of observation respectively. This can result in the transit timing having very large errors if the shape of the transit is not properly constrained.

Additionally, in Appendix Table 5.8 and Figure 5.6 we also list and plot the results from the fits where the transit depth was also a free parameter of the lightcurves of Kepler-9 and Kepler-18. We calculate the weighted mean of these transit depths for each bandpass following the method outlined in Ingalls et al. (2016). The individual transit depths exhibit significant scatter compared to each other and the weighted means do not demonstrate a significant atmospheric signal between 3.6 and $4.5\mu\text{m}$. We calculate the normalized transit depth difference used in Baxter et al. (2021) ($(\delta_{ch2} - \delta_{ch1})/\delta_{ch1}$) and find that all 4 planets are within 1σ of zero. This could either indicate that these planets are cloudy or that we do not have significant precision to measure the atmospheric signal.

Table 5.5: Table of measured transit times (in BJD_{UTC}) for each of the six Kepler planets. We also show the uncertainty on the time converted to minutes, the fraction above photon noise and the deviation from the TTV predictions.

Planet	AOR	λ μm	T0 BJD_{UTC}	σ_{T0} Minutes	Photon noise	O-C $N\sigma$
Kepler9b	r47043072	3.6	2456670.630 ± 0.003	3.9	2.8	0.66
Kepler9b	r47043584	3.6	2456632.131 ± 0.003	3.7	2.9	2.63
Kepler9b	r47044352	3.6	2456535.881 ± 0.004	5.5	3.2	-8.47
Kepler9b	r47044608	3.6	2456478.207 ± 0.003	4.6	2.9	-3.08
Kepler9b	r47054336	4.5	2456863.317 ± 0.003	4.1	2.9	-0.66
Kepler9b	r47054592	4.5	2456651.375 ± 0.003	4.0	2.6	1.66

Table 5.5: continued.

Planet	AOR	λ μm	T0 BJD _{UTC}	σ_{T0} Minutes	Photon noise	O-C $N\sigma$
Kepler9b	r47054848	4.5	2456555.152 ± 0.004	5.1	2.7	0.04
Kepler9b	r47055104	4.5	2456516.679 ± 0.003	4.4	2.6	-0.57
Kepler9c	r47029248	4.5	2456994.481 ± 0.010	14.2	6.1	-1.50
Kepler9c	r47061760	3.6	2456293.779 ± 0.003	4.6	2.8	3.63
Kepler9c	r47061504	3.6	2456606.048 ± 0.003	4.4	2.8	-3.98
Kepler9c	r47060992	3.6	2456839.407 ± 0.033	47.5	2.9	2.44
Kepler9c	r47060480	3.6	2456916.899 ± 0.004	5.3	3.8	-3.94
Kepler9c	r47030016	4.5	2456567.072 ± 0.004	5.1	2.7	-2.58
Kepler9c	r47029760	4.5	2456645.005 ± 0.005	7.2	2.7	-1.13
Kepler9c	r47029504	4.5	2456878.118 ± 0.003	4.4	3.1	-2.09
Kepler18c	r46858496	3.6	2456259.836 ± 0.005	7.8	2.4	-0.06
Kepler18c	r47045376	3.6	2456275.121 ± 0.005	7.4	2.3	0.33
Kepler18c	r47045120	3.6	2456588.422 ± 0.005	7.0	2.3	0.33
Kepler18c	r47056640	4.5	2456519.646 ± 0.004	6.2	2.0	-0.95
Kepler18c	r47056384	4.5	2456573.156 ± 0.004	6.0	2.0	4.18
Kepler18c	r47056128	4.5	2456664.876 ± 0.066	94.5	2.0	0.67
Kepler18d	r46867456	3.6	2456253.880 ± 0.003	4.1	2.3	1.04
Kepler18d	r47063808	3.6	2456610.491 ± 0.002	2.5	2.2	-2.32
Kepler18d	r47063552	3.6	2456655.057 ± 0.003	4.8	2.1	-4.97
Kepler18d	r47033600	4.5	2456580.774 ± 0.005	6.9	2.0	-0.14
Kepler18d	r47033344	4.5	2456625.344 ± 0.003	4.0	2.1	-3.68
Kepler18d	r47033088	4.5	2456684.785 ± 0.003	3.8	2.1	-2.10
Kepler32b	r47032320	3.6	2456503.279 ± 0.040	57.4	3.5	-1.23
Kepler32b	r47031808	3.6	2456509.223 ± 0.006	8.3	3.8	-0.99
Kepler32b	r47031296	3.6	2456615.503 ± 0.058	83.2	3.0	0.77
Kepler32b	r47030528	3.6	2456662.613 ± 0.028	40.0	3.1	-2.05
Kepler32b	r47030272	3.6	2456680.310 ± 0.027	38.2	3.8	-2.37
Kepler32b	r47042560	4.5	2456526.904 ± 0.033	47.8	2.9	-0.89
Kepler32b	r47042048	4.5	2456585.975 ± 0.030	43.8	2.7	0.78
Kepler32b	r47041536	4.5	2456633.170 ± 0.007	10.4	2.7	0.87
Kepler32b	r47040768	4.5	2456674.474 ± 0.017	23.9	2.8	0.11
Kepler32b	r47040256	4.5	2456698.079 ± 0.033	47.8	2.9	0.14
Kepler32c	r47048192	3.6	2456500.226 ± 0.012	16.6	3.4	-2.15
Kepler32c	r47047936	3.6	2456509.010 ± 0.007	9.5	3.9	1.00
Kepler32c	r47047680	3.6	2456587.767 ± 0.016	23.5	3.3	0.10
Kepler32c	r47047424	3.6	2456605.238 ± 0.026	37.7	3.0	-1.11
Kepler32c	r47059968	4.5	2456517.709 ± 0.038	54.0	2.9	-1.24

Table 5.5: continued.

Planet	AOR	λ μm	T0 BJD _{UTC}	σ_{T0} Minutes	Photon noise	O-C $N\sigma$
Kepler32c	r47059712	4.5	2456535.252 ± 0.021	29.6	2.9	-0.31
Kepler32c	r47059456	4.5	2456596.483 ± 0.049	71.2	2.8	-0.69
Kepler32c	r47059200	4.5	2456649.088 ± 0.047	67.5	2.7	1.33

5.4.2 Comparing multi-planet system transit times to predictions

In Figure 5.1 we compare the *Spitzer* transit times to predictions from the Kepler data, described in Section 5.3.3. We calculate the Observed - Calculated times by fitting a straight line to the Kepler observations ($O_E = P * E + T_0$) where O_E are the observed times, P is the period, T_0 is the ephemeris and E is the integer transit number ($E = 0$ is set to the closest value to T_0). This yields values for P and T_0 which can be propagated to create C_E , a list of calculated transit times. These times are then subtracted from the observed *Kepler* times (O_E), as well as the model prediction and the *Spitzer* times.

In Table 5.5 we show the number of standard deviations between the measured transit times and the TTV predictions. In absolute value, these planets are on average not significantly deviating from the TTV predictions (average $N\sigma$ is 1.7σ) and are thus not constraining to the TTV models.

5.4.3 Kepler-16b lightcurves and transit parameters

The raw transit lightcurves, corrected lightcurves, best-fit models, residuals, and root mean squared (RMS) vs bin size of Kepler-16b are shown in Figure 5.2 for channel 1 and channel 2 respectively. Before scaling up the uncertainties, we found that the $3.6 \mu\text{m}$ and $4.5 \mu\text{m}$ errors were 1.3 and 1.24 times photon noise respectively. This is standard for warm Spitzer/IRAC lightcurves, e.g. see Baxter et al. (2021).

The RMS vs bin size plot demonstrates how well the correlated noise is corrected by comparing with the Poisson expectation (\sqrt{N}). For channel 1 there is a deviation from Poisson, indicating there is some red noise remaining in the lightcurve, this can also be seen in the residuals and is likely due to the extremely short-out-of-transit baseline before the transit. We tested cutting different amounts of time in 2-minute intervals from the beginning of the lightcurve. We found that there was a degeneracy with the amount of time cut off and the transit parameters (R_p/R_s , a/R_s and inclination). In particular, we noted that the more time we cut off the smaller the measured transit depth. In a typical Spitzer observation, failing to remove the ramp-up at the beginning of the lightcurve has the effect of reducing the measured transit depth. Therefore, we should see a positive correlation with an increasing amount of time cut off at the beginning of the observation and the measured transit depth. However, in our case, we see that cutting the beginning of the observation also reduces the transit depth. We conclude that this is because we are cutting off too much of the ingress, which would also

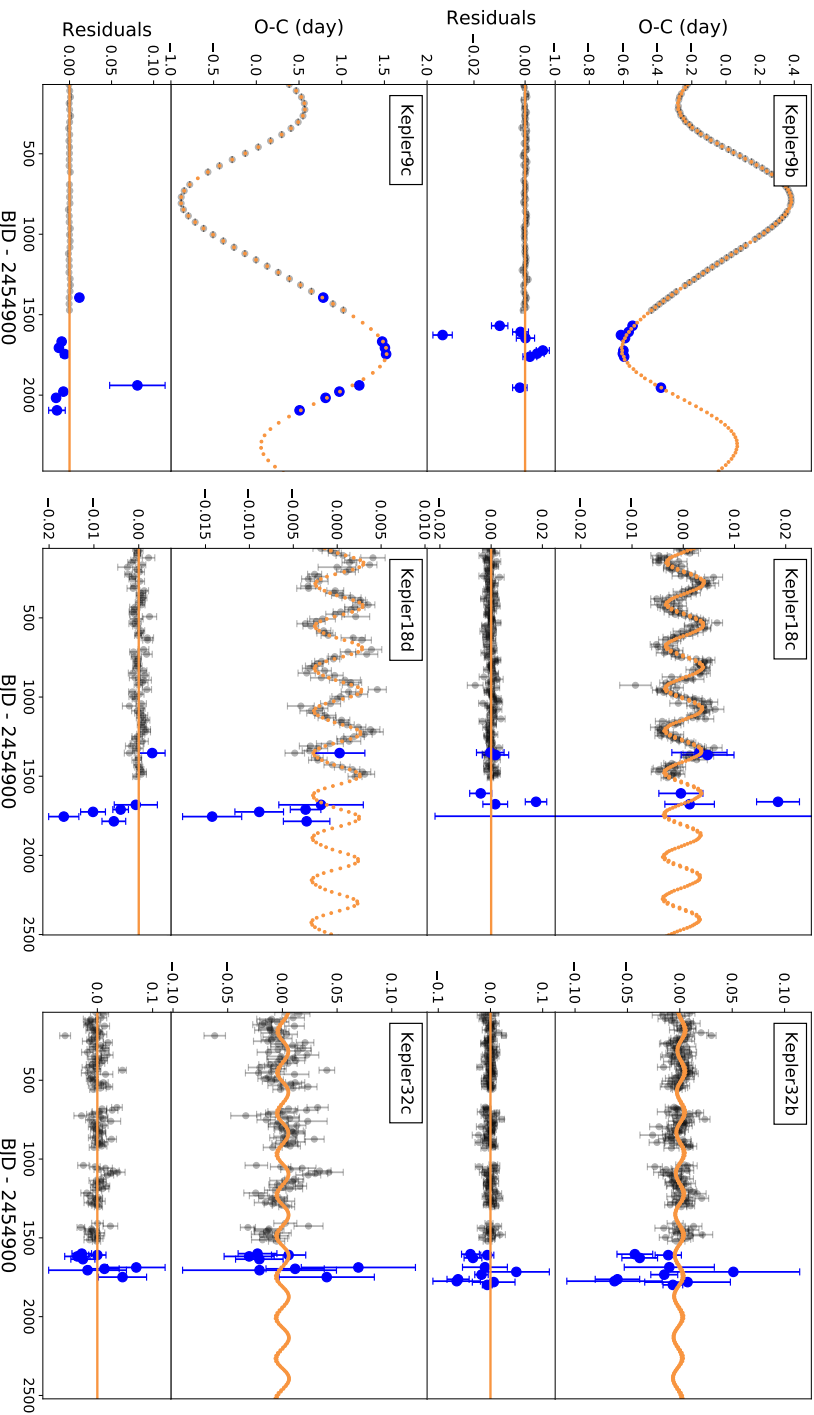


Fig. 5.1: First and third rows: The O-C diagrams of transit times and predictions from the *Kepler* data and the newly analyzed *Spitzer* data for Kepler-9b, Kepler-9c, Kepler-18c, Kepler-18d, Kepler-32b and Kepler-32c. Calculated times are from a linear ephemeris fit to the *Kepler* data. Second and fourth rows: The residuals for the O-C diagrams.

Table 5.6: Table of the best-fit transit parameters for each of the two Spitzer/IRAC lightcurves of Kepler-16b. We show the transit depth (R_p^2/R_s^2), the orbital distance (a/R_s), the inclination, and the transit time in BJD.

Parameter	$3.6\mu\text{m}$	$4.5\mu\text{m}$
$(R_p/R_s)^2$	0.11783 ± 0.00051	0.11566 ± 0.00036
a/R_s	260.2776 ± 2.96	256.016 ± 3.44
inc (deg)	89.89 ± 0.005	89.86 ± 0.005
T_0 (BJD)	$2456559.0059831^{+0.0002152}_{-0.0002144}$	$2457010.7655917^{+0.0002496}_{-0.00025368}$

reduce the transit depth, and so we opted to keep all of the data. In Appendix Figures 5.7 and 5.8 we show the corner plots resulting from the MCMC calculation of Kepler-16b. Due to the $3.6\mu\text{m}$ lightcurve observation starting very close to ingress, the corner plot shows that there is also a slight degeneracy with the transit depth and the temporal ramp parameter (g). In the end, this results in the uncertainty on the transit depth (R_p^2/R_s^2) at $3.6\mu\text{m}$ being larger.

Additionally, both corner plots demonstrate the degeneracy between the semi-major axis and inclination, which is a common degeneracy when fitting the transit. Typically, we would fix these parameters either to literature values or to the mean of the two Spitzer transit lightcurves (e.g., see Baxter et al. (2021)). However, Kepler-16b has undergone significant precession over the duration between the two observations (two orbital periods) and so these parameters need to be left free in our fits. We are therefore able to use this information to constrain the photometric models.

In Table 5.6 we display the resulting best fit transit parameters for 3.6 and $4.5\mu\text{m}$. We measure the exquisite precision on the transit time of both transits, with uncertainties of 17 and 22 seconds for 3.6 and $4.5\mu\text{m}$ respectively.

5.4.4 Comparing Kepler-16b to photodynamical model

In Figure 5.3 we plot the results of the photodynamical modeling of the last two Kepler-16b transits and compare it to the Spitzer data. We first performed the photodynamical fit with just the Kepler data and propagated the results forward in time to the Spitzer observations. These predictions are shown in blue on Figure 5.3. We found that the $3.6\mu\text{m}$ transit time measured with Spitzer (on 23rd September 2013) was in agreement with the Kepler predictions, with a deviation of just 1.6σ . However, there was a gap of two orbital periods until the $4.5\mu\text{m}$ Spitzer transit and we found that during this time the observation significantly deviated from the prediction. The $4.5\mu\text{m}$ transit arrived 14 minutes (37σ) early. Additionally, there is a significant deviation in the depth and duration of the transit at $4.5\mu\text{m}$, which indicates that these transits can be used to constrain the orbital elements of the photodynamical model and the precession of the circumbinary orbit in time.

In our second fit, we incorporated the Spitzer data into the fit of the photodynamical model. The resulting lightcurves are shown in green on Figure 5.3. Additionally, in Figure 5.4 we plot the resulting lightcurve of the photodynamical model of Kepler-16b over the

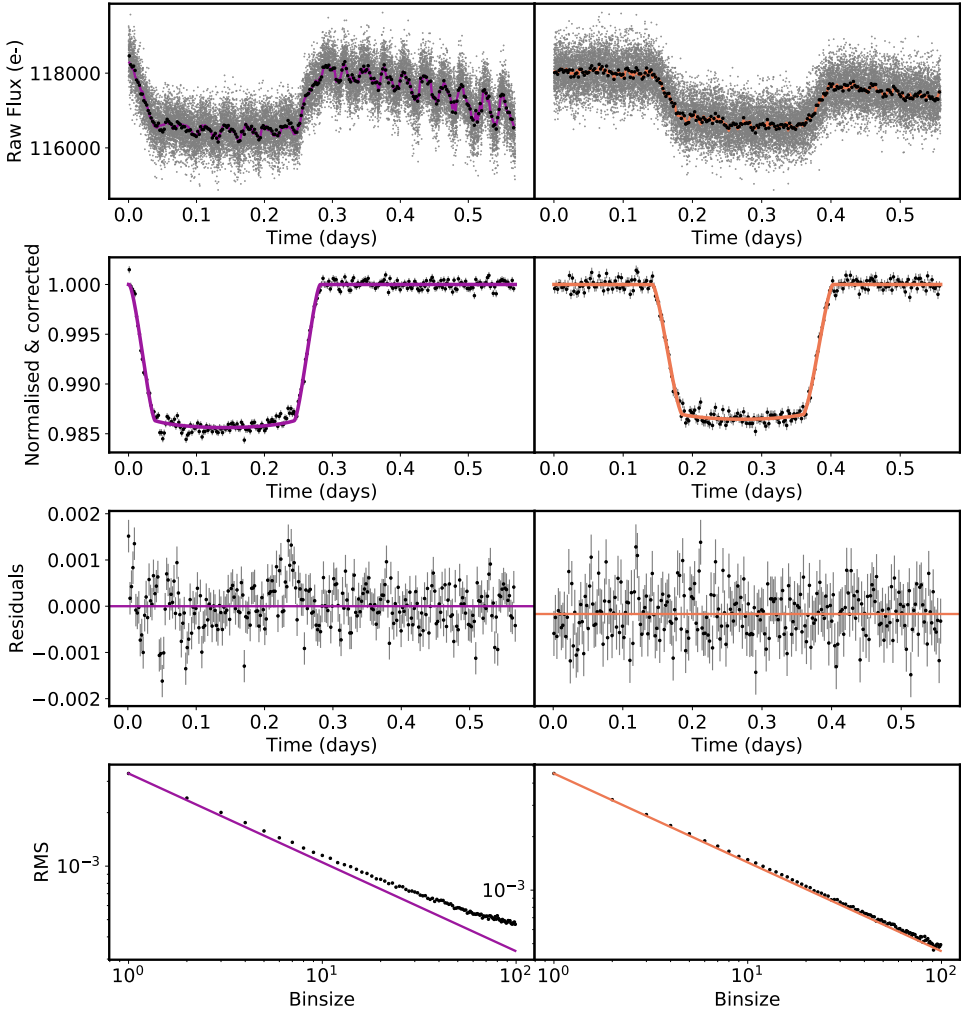


Fig. 5.2: Left and right columns show the 3.6 and 4.5 μm Spitzer/IRAC lightcurves for Kepler-16b respectively. Top panel: Raw flux of the transit lightcurve against time, overlaid with the best fit systematic and transit model. Second panel: Normalized and systematic corrected lightcurve, binned to roughly 5-minute intervals with the best fit transit model. Third panel: Residuals (data - model). Bottom panel: root mean squared of residuals vs bin size.

entire baseline (Kepler + Spitzer). The model contains 4 types of transits/occultations in total: star B eclipsing star A, star A occulting star B, planet b transiting star A and planet b transiting star B. The two last transits in the Figure (in dark blue) show the *Spitzer* transits of planet b transiting star A. There are 153 days between the last *Kepler* observation and the first *Spitzer* observation. Given that the orbital period of planet b is around 219 days, this means that the 3.6 μm *Spitzer* lightcurve contains the next transit of planet b after the last one in the *Kepler* data. Additionally, there are then two orbital periods between the 3.6 and 4.5 μm *Spitzer*

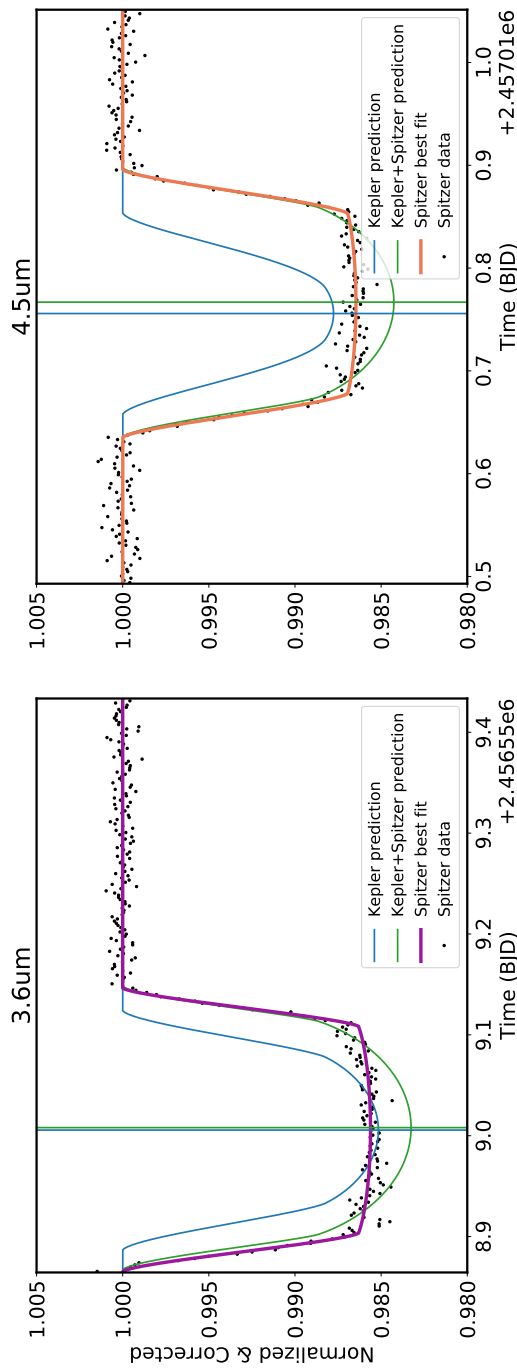


Fig. 5.3: We show the Kepler-16b transits at $3.6\mu\text{m}$ (left) and $4.5\mu\text{m}$ (right) with the photodynamical predictions. These photodynamical transit predictions are computed with Kepler transit depths and Kepler limb darkening predictions, we are interested in comparing the timing. The blue line shows the photodynamical predictions made with the Kepler data alone and propagated into the future for the Spitzer observations. The green line shows the results from the photodynamical fit with Kepler plus Spitzer data.

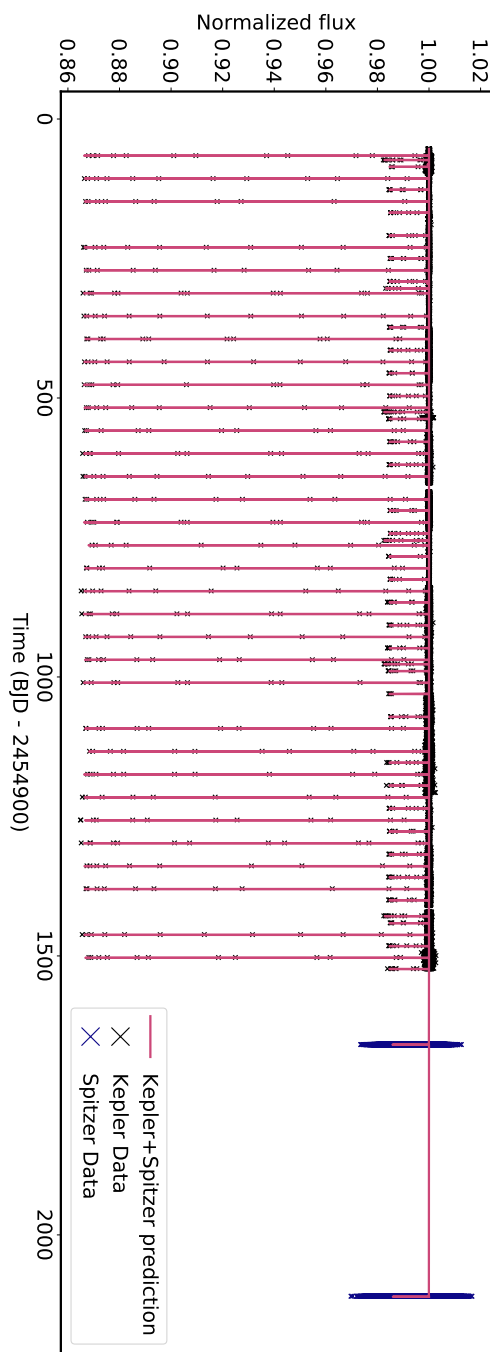


Fig 5.4: We show the results from the photodynamical mode fitting of the Kepler and Spitzer data. These photodynamical transit predictions are computed with Kepler transit depths and Kepler limb darkening predictions. The pink shows the photodynamical predictions, the black and dark blue markers show the Kepler and Spitzer data respectively.

Table 5.7: Table of orbital elements resulting from photodynamical fit of Kepler + Spitzer data. We show the results for the secondary star (Kepler-16B) and the circumbinary planet (Kepler-16b). For each body we show the orbital period, the ephemeris (T_0 in BJD-2454900), eccentricity (e), inclination (i), longitude of ascending node (Ω), angle of periaxis (ω), mass of the planet or star (M_p) and the radius ratio to the primary (R_p/R_s).

Planet	Period days	T_0 BJD-2454900	e	i deg	Ω deg	ω deg	M_p M_{jup}	R_p/R_s
Kepler-16B	41.0790347	312.1245095	0.163	90.339	0.0	-96.381	211.990	0.347
Kepler-16b	228.7817675	530.0330639	0.008	90.029	-0.016	-41.445	0.291	0.118

transits, which provides a significant extension to the baseline.

The best-fitting parameters for the secondary star (Kepler-16B) and the circumbinary planet (Kepler-16b) from the joint fit are given in Table 5.7. We also obtain a primary (Kepler-16A) mass of $0.688 M_\odot$ and radius of $0.648 R_\odot$.

5.5 Discussion and Conclusion

We have presented an analysis of 46 lightcurves using Spitzer/IRAC of 3 multi-planet systems (Kepler-9b, -9c, -18c, -18d, -32b and -32c) in an effort to constrain current TTV models. We found that the sub-array observations resulting from Spitzer entering the warm mission lead to significantly lower signal-to-noise ratios in the photometric lightcurves than predicted. These faint stars have ten times less flux than the stars of the planets studied in our previous works (e.g., see Baxter et al. 2021), which results in very noisy lightcurves. Nevertheless, we performed a thorough analysis of the raw data by testing and visually inspecting all iterations of our pipeline parameters (photometry, centroiding, and background subtracting). We also tested combinations of fixed parameters from the literature, free parameters, and priors on parameters to extract the transit times from the photometric lightcurves. We present the best resulting lightcurves and the extracted transit times. Additionally, we present a version of the analysis where the transit depth is a free parameter and calculated that we do not have the precision to detect a molecular signature in the atmosphere.

We derived the transit times from Kepler data of these same planets and used an N-body model to determine the orbital elements and masses. We propagated the orbital elements forward in time to obtain posterior transit times for the times of the Spitzer transits. We compared the Kepler predictions to the Spitzer data in the hopes of constraining the TTV model. However, we found no significant deviation from the TTV predictions and the O-C plots demonstrated significant scatter. We conclude that the transits of these multi-planet systems measured with Spitzer/IRAC are consistent with but are not offering any additional constraints to current TTV models.

Additionally, we present the analysis of two Spitzer transits of the circumbinary planet Kepler-16b, one at $3.6\mu\text{m}$ and one at $4.5\mu\text{m}$. These transits provide exquisite precision on the transit parameters. In particular, the transit times are measured to 22- and 17-second

precision respectively. Using archival Kepler data, we created a photodynamical model of the system and propagated it to the time of the Spitzer observations. We found a significant deviation (37σ) between the second Spitzer transit and the predictions, suggesting that the Spitzer observations could be used to update the model and constrain the orbital elements. We then ran a DEMCMC fit of the photodynamical model with Kepler plus Spitzer data and present the updated orbital elements of the circumbinary Kepler-16 system.

5.A Supplementary plots

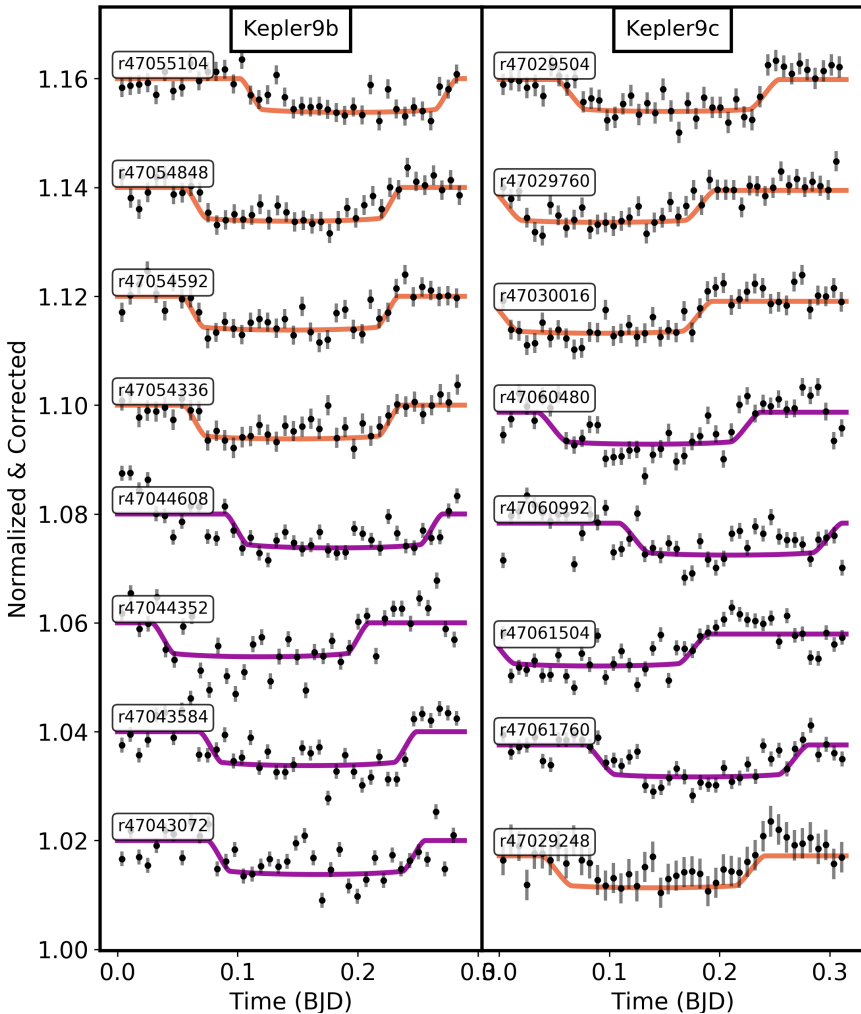


Fig. 5.5: Normalized and systematic corrected transit lightcurves for each planet in the Kepler-9 system. Left panel shows Kepler-9b and right panel shows Kepler-9c. Continuous curves show the best fit transit models, 3.6 μm in orange and 4.5 μm in purple. 1 σ uncertainties on each photometric point are calculated from scaled photon noise. The data and these uncertainties are binned in 10 minute intervals for display purposes.

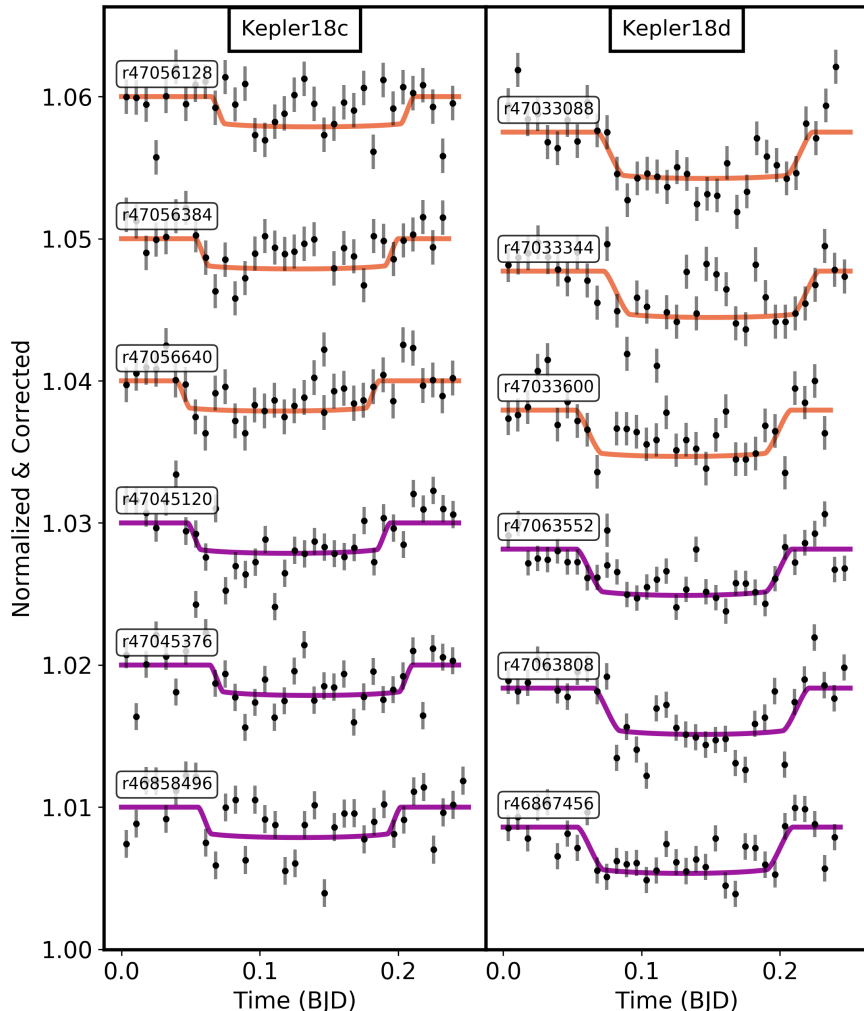


Fig. 5.5: Continued. Left panel shows Kepler-18c and right panel shows Kepler-18d.

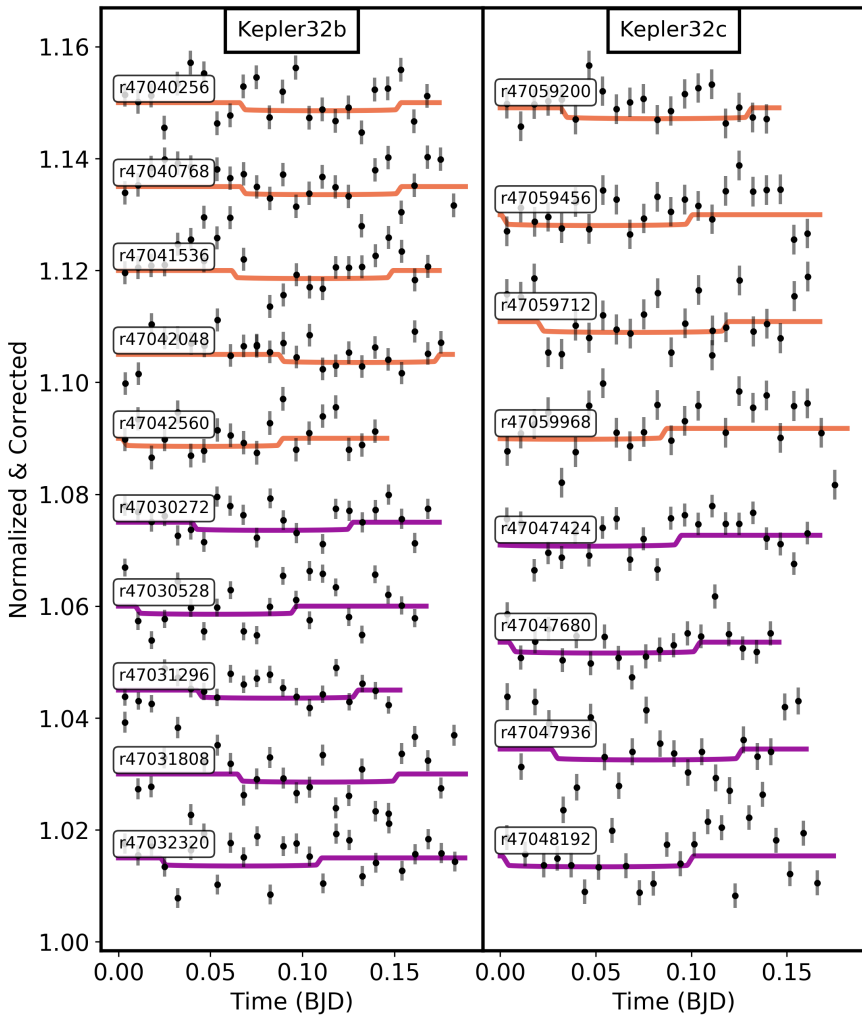


Fig. 5.5: Continued. Left panel shows Kepler-32b and right panel shows Kepler-32c.

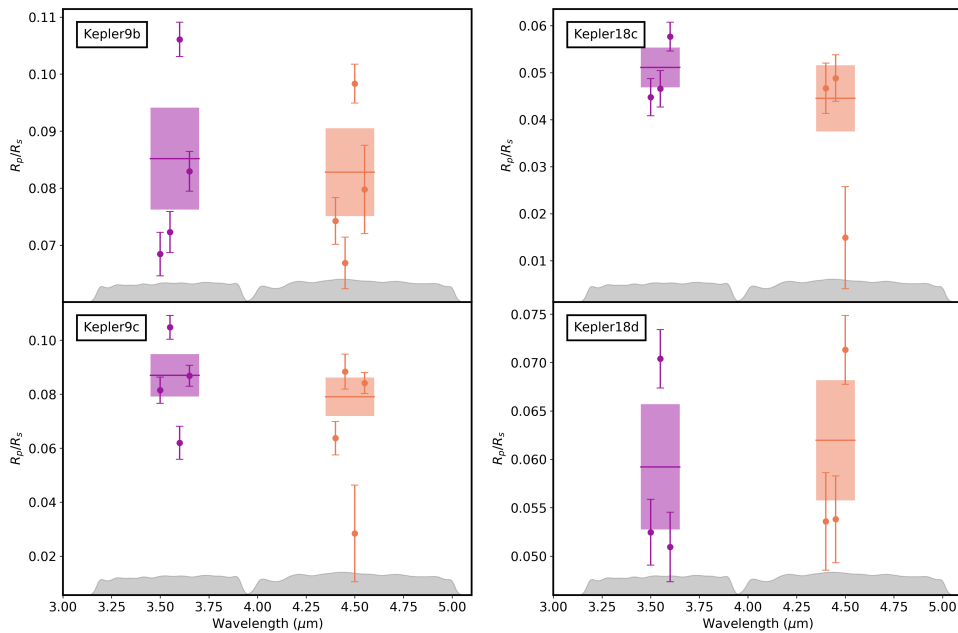


Fig. 5.6: Transit depths and their 1σ uncertainties of each observation of Kepler-9b, Kepler-9c, Kepler-18c and Kepler-18d. Spitzer response functions are plotted in gray and the weighted mean and weighted error of the transit depths (R_p^2/R_s^2) for each channel are shown with the colored shaded region. 3.6 μm in purple and 4.5 μm in orange.

Table 5.8: Table of measured transit times and transit depths for Kepler-9 and Kepler-18 planets. We show the time and uncertainty in BJD_{UTC}, the uncertainty converted to minutes and the transit depth (R_p^2/R_s^2).

Planet	AOR	λ	T0 μm	BJD _{UTC}	σ_{T0} Minutes	$(R_p/R_s)^2$
Kepler9b	r47043072	3.6	2.456671e+06	± 0.003107	4.473655	0.068431 ± 0.003821
Kepler9b	r47043584	3.6	2.456632e+06	± 0.002756	3.968588	0.072281 ± 0.003617
Kepler9b	r47044352	3.6	2.456536e+06	± 0.001378	1.984667	0.106083 ± 0.003005
Kepler9b	r47044608	3.6	2.456478e+06	± 0.003905	5.623396	0.082942 ± 0.003496
Kepler9b	r47054336	4.5	2.456863e+06	± 0.003636	5.236191	0.074248 ± 0.004110
Kepler9b	r47054592	4.5	2.456651e+06	± 0.004495	6.472122	0.066890 ± 0.004531
Kepler9b	r47054848	4.5	2.456555e+06	± 0.001817	2.616881	0.098337 ± 0.003420
Kepler9b	r47055104	4.5	2.456517e+06	± 0.004150	5.976012	0.079762 ± 0.007760
Kepler9c	r47029248	4.5	2.456994e+06	± 0.004427	6.374814	0.063701 ± 0.006222
Kepler9c	r47061760	3.6	2.456294e+06	± 0.002448	3.525807	0.081451 ± 0.004860
Kepler9c	r47061504	3.6	2.456606e+06	± 0.002054	2.957437	0.104802 ± 0.004421
Kepler9c	r47060992	3.6	2.456839e+06	± 0.030353	43.708638	0.061969 ± 0.006118
Kepler9c	r47060480	3.6	2.456917e+06	± 0.002838	4.087393	0.086838 ± 0.003902
Kepler9c	r47030016	4.5	2.456567e+06	± 0.002927	4.215005	0.088371 ± 0.006494
Kepler9c	r47029760	4.5	2.456645e+06	± 0.069111	99.520470	0.028413 ± 0.017901
Kepler9c	r47029504	4.5	2.456878e+06	± 0.002770	3.988523	0.084158 ± 0.003908
Kepler18d	r46867456	3.6	2.456254e+06	± 0.003540	5.097910	0.052459 ± 0.003396
Kepler18d	r47063808	3.6	2.456610e+06	± 0.001513	2.178499	0.070387 ± 0.003015
Kepler18d	r47063552	3.6	2.456655e+06	± 0.003871	5.573921	0.050935 ± 0.003587
Kepler18d	r47033600	4.5	2.456581e+06	± 0.005868	8.450013	0.053577 ± 0.005039
Kepler18d	r47033344	4.5	2.456625e+06	± 0.002928	4.216482	0.053800 ± 0.004481
Kepler18d	r47033088	4.5	2.456685e+06	± 0.002511	3.616499	0.071315 ± 0.003559
Kepler18c	r46858496	3.6	2.456260e+06	± 0.005614	8.084660	0.044786 ± 0.003964
Kepler18c	r47045376	3.6	2.456275e+06	± 0.005766	8.302904	0.046585 ± 0.003877
Kepler18c	r47045120	3.6	2.456588e+06	± 0.003746	5.394609	0.057670 ± 0.003047
Kepler18c	r47056640	4.5	2.456520e+06	± 0.004408	6.347335	0.046707 ± 0.005354
Kepler18c	r47056384	4.5	2.456573e+06	± 0.004130	5.947279	0.048846 ± 0.004948
Kepler18c	r47056128	4.5	2.456665e+06	± 0.064899	93.454854	0.014911 ± 0.010858

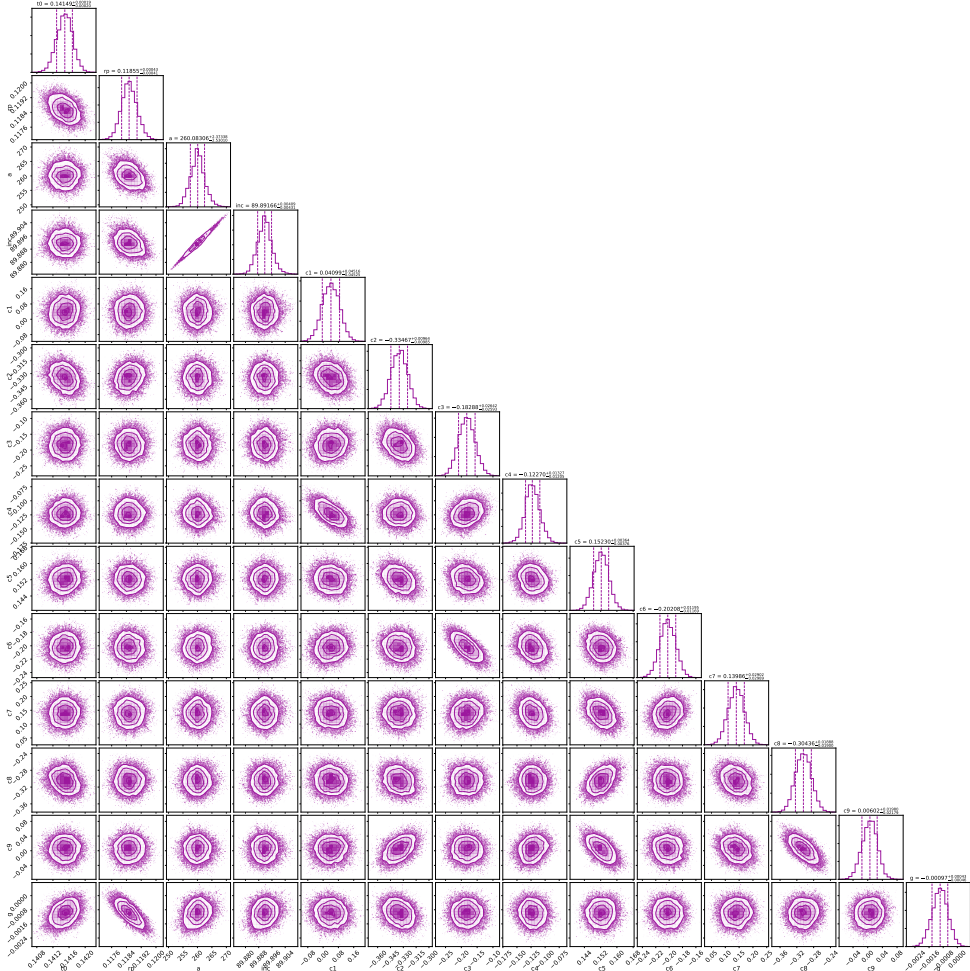


Fig. 5.7: Corner plot of the posterior distributions resulting from the MCMC fit to the $3.6\text{ }\mu\text{m}$ Spitzer/IRAC lightcurve for Kepler-16b.

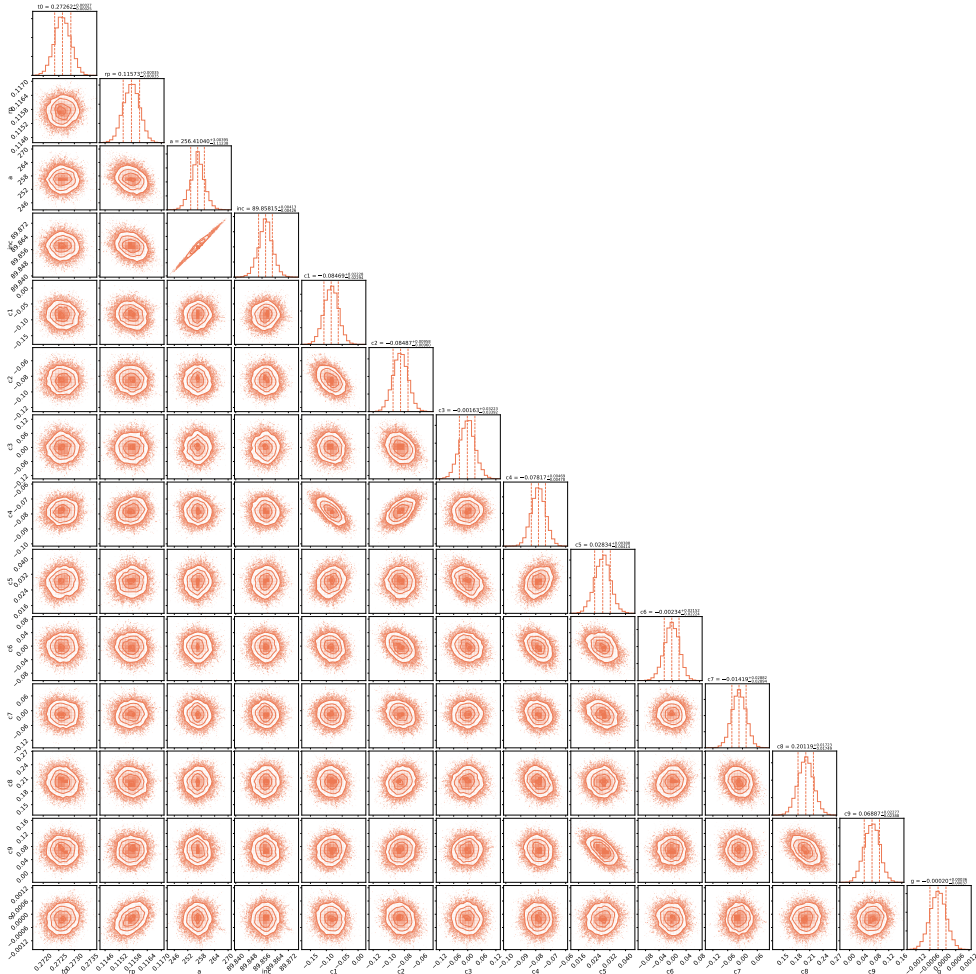


Fig. 5.8: Corner plot of the posterior distributions resulting from the MCMC fit to the $4.5\ \mu\text{m}$ Spitzer/IRAC lightcurve for Kepler-16b.

BIBLIOGRAPHY

- Agol, E., Cowan, N. B., Knutson, H. A., et al. 2010, *ApJ*, 721, 1861
- Agol, E., Steffen, J., Sari, R., et al. 2005, *MNRAS*, 359, 567
- Agúndez, M., Venot, O., Iro, N., et al. 2012, *A&A*, 548, A73
- Agúndez, M., Venot, O., Selsis, F., et al. 2014, *ApJ*, 781, 68
- Akritas, M. G., & Bershady, M. A. 1996, *ApJ*, 470, 706
- Alfvén, H. 1942, *Nature*, 150, 405
- Allard, F., & Hauschildt, P. H. 1995, *ApJ*, 445, 433
- Allard, F., Homeier, D., & Freytag, B. 2011, in Astronomical Society of the Pacific Conference Series, Vol. 448, 16th Cambridge Workshop on Cool Stars, Stellar Systems, and the Sun, ed. C. Johns-Krull, M. K. Browning, & A. A. West, 91
- Amundsen, D. S., Tremblin, P., Manners, J., et al. 2017, *A&A*, 598, A97
- Anderson, D. R., Smith, A. M. S., Lanotte, A. A., et al. 2011a, *MNRAS*, 416, 2108
- Anderson, D. R., Collier Cameron, A., Hellier, C., et al. 2011b, *A&A*, 531, A60
- Anderson, D. R., Smith, A. M. S., Madhusudhan, N., et al. 2013, *MNRAS*, 430, 3422
- Anderson, D. R., Collier Cameron, A., Delrez, L., et al. 2014, *MNRAS*, 445, 1114
- Antuñano, A., Fletcher, L. N., Orton, G. S., et al. 2019, *AJ*, 158, 130
- Apai, D., Kasper, M., Skemer, A., et al. 2016, *ApJ*, 820, 40
- Arcangeli, J., Désert, J. M., Parmentier, V., et al. 2021, *A&A*, 646, A94
- Arcangeli, J., Désert, J.-M., Line, M. R., et al. 2018, *ApJ*, 855, L30
- Arcangeli, J., Désert, J.-M., Parmentier, V., et al. 2019, *A&A*, 625, A136
- Armstrong, D. J., de Mooij, E., Barstow, J., et al. 2016, *Nature Astronomy*, 1, 0004
- Astropy Collaboration, Price-Whelan, A. M., Sipőcz, B. M., et al. 2018, *AJ*, 156, 123
- Bailer-Jones, C. A. L., Rybizki, J., Fouesneau, M., et al. 2018, *AJ*, 156, 58
- Baines, K. H., Delitsky, M. L., Momary, T. W., et al. 2009, *Planet. Space Sci.*, 57, 1650
- Bakos, G. Á., Penev, K., Bayliss, D., et al. 2015, *ApJ*, 813, 111
- Ballard, S., Charbonneau, D., Deming, D., et al. 2010, *PASP*, 122, 1341
- Ballard, S., Fabrycky, D., Fressin, F., et al. 2011, *ApJ*, 743, 200
- Barros, S. C. C., Pollacco, D. L., Gibson, N. P., et al. 2012, *MNRAS*, 419, 1248
- Barstow, J. K., Aigrain, S., Irwin, P. G. J., et al. 2017, *ApJ*, 834, 50
- Baskin, N. J., Knutson, H. A., Burrows, A., et al. 2013, *ApJ*, 773, 124
- Batalha, N. M. 2014, *Proceedings of the National Academy of Science*, 111, 12647
- Batalha, N. M., Rowe, J. F., Bryson, S. T., et al. 2013, *ApJS*, 204, 24

BIBLIOGRAPHY

- Batygin, K., & Stevenson, D. J. 2010, ApJ, 714, L238
- Baxter, C., Désert, J.-M., Parmentier, V., et al. 2020, A&A, 639, A36
- Baxter, C., Désert, J.-M., Tsai, S.-M., et al. 2021, A&A, 648, A127
- Beatty, T. G., Marley, M. S., Gaudi, B. S., et al. 2019, AJ, 158, 166
- Beatty, T. G., Collins, K. A., Fortney, J., et al. 2014, ApJ, 783, 112
- Beaulieu, J. P., Tinetti, G., Kipping, D. M., et al. 2011, ApJ, 731, 16
- Beerer, I. M., Knutson, H. A., Burrows, A., et al. 2011, ApJ, 727, 23
- Beichman, C., Livingston, J., Werner, M., et al. 2016, ApJ, 822, 39
- Bell, T. J., & Cowan, N. B. 2018, ApJ, 857, L20
- Bell, T. J., Nikolov, N., Cowan, N. B., et al. 2017, ApJ, 847, L2
- Bell, T. J., Zhang, M., Cubillos, P. E., et al. 2019, MNRAS, 489, 1995
- Benneke, B., Knutson, H. A., Lothringer, J., et al. 2019, Nature Astronomy, 3, 813
- Berardo, D., Crossfield, I. J. M., Werner, M., et al. 2019, AJ, 157, 185
- Berta, Z. K., Charbonneau, D., Désert, J.-M., et al. 2012, ApJ, 747, 35
- Biddle, L. I., Pearson, K. A., Crossfield, I. J. M., et al. 2014, MNRAS, 443, 1810
- Biller, B. A., Vos, J., Bonavita, M., et al. 2015, ApJ, 813, L23
- Blecic, J., Harrington, J., Madhusudhan, N., et al. 2013, ApJ, 779, 5
- Blecic, J., Harrington, J., Madhusudhan, N., et al. 2014, ApJ, 781, 116
- Bodenheimer, P., Lin, D. N. C., & Mardling, R. A. 2001, ApJ, 548, 466
- Boggs, P. T., Donaldson, J. R., Byrd, R. h., et al. 1989, ACM Trans. Math. Softw., 15, 348
- Borsato, L., Malavolta, L., Piotto, G., et al. 2019, MNRAS, 484, 3233
- Borucki, W. J., & Summers, A. L. 1984, Icarus, 58, 121
- Borucki, W. J., Koch, D., Jenkins, J., et al. 2009, Science, 325, 709
- Borucki, W. J., Koch, D., Basri, G., et al. 2010, Science, 327, 977
- Borucki, W. J., Koch, D. G., Basri, G., et al. 2011, ApJ, 736, 19
- Bouchy, F., Hebb, L., Skillen, I., et al. 2010, A&A, 519, A98
- Brooke, T. Y., Knacke, R. F., Encrenaz, T., et al. 1998, Icarus, 136, 1
- Brown, M. E., Bouchez, A. H., & Griffith, C. A. 2002, Nature, 420, 795
- Brown, T. M. 2001, ApJ, 553, 1006
- Bryson, S., Coughlin, J., Batalha, N. M., et al. 2020, AJ, 159, 279
- Buchhave, L. A., Bizzarro, M., Latham, D. W., et al. 2014, Nature, 509, 593
- Burke, C. J., McCullough, P. R., Valenti, J. A., et al. 2007, ApJ, 671, 2115
- Burke, C. J., McCullough, P. R., Bergeron, L. E., et al. 2010, ApJ, 719, 1796
- Burrows, A., Hubeny, I., Budaj, J., et al. 2007a, ApJ, 661, 502
- Burrows, A., Hubeny, I., Budaj, J., et al. 2007b, ApJ, 668, L171
- Buzasi, D. L., Carboneau, L., Hessler, C., et al. 2015, in IAU General Assembly, Vol. 29, 2256843
- Carone, L., Mollière, P., Zhou, Y., et al. 2021, A&A, 646, A168
- Carter, J. A., Agol, E., Chaplin, W. J., et al. 2012, Science, 337, 556
- Castelli, F., & Kurucz, R. L. 2003, in Modelling of Stellar Atmospheres, ed. N. Piskunov, W. W. Weiss, & D. F. Gray, Vol. 210, A20

- Chabrier, G., Saumon, D., & Winisdoerffer, C. 2007, *Ap&SS*, 307, 263
- Chachan, Y., Knutson, H. A., Gao, P., et al. 2019, *AJ*, 158, 244
- Charbonneau, D., Brown, T. M., Noyes, R. W., et al. 2002, *ApJ*, 568, 377
- Charbonneau, D., Knutson, H. A., Barman, T., et al. 2008, *ApJ*, 686, 1341
- Charbonneau, D., Allen, L. E., Megeath, S. T., et al. 2005, *ApJ*, 626, 523
- Christiansen, J. L., Ballard, S., Charbonneau, D., et al. 2010, *ApJ*, 710, 97
- Cochran, W. D., Fabrycky, D. C., Torres, G., et al. 2011, *ApJS*, 197, 7
- Collier Cameron, A., Bouchy, F., Hébrard, G., et al. 2007, *MNRAS*, 375, 951
- Cowan, N. B., & Agol, E. 2008, *ApJ*, 678, L129
- Cowan, N. B., & Agol, E. 2011a, *ApJ*, 726, 82
- Cowan, N. B., & Agol, E. 2011b, *ApJ*, 729, 54
- Cowan, N. B., Agol, E., & Charbonneau, D. 2007, *MNRAS*, 379, 641
- Cowan, N. B., Machalek, P., Croll, B., et al. 2012a, *ApJ*, 747, 82
- Cowan, N. B., Voigt, A., & Abbot, D. S. 2012b, *ApJ*, 757, 80
- Crossfield, I. J. M. 2015, *PASP*, 127, 941
- Crossfield, I. J. M., Knutson, H., Fortney, J., et al. 2012, *ApJ*, 752, 81
- Crossfield, I. J. M., & Kreidberg, L. 2017, *AJ*, 154, 261
- Cubillos, P., Harrington, J., Madhusudhan, N., et al. 2013, *ApJ*, 768, 42
- Cutri, R. M., & et al. 2012, VizieR Online Data Catalog, II/311
- Dang, L., Cowan, N. B., Schwartz, J. C., et al. 2018, *Nature Astronomy*, 2, 220
- Delrez, L., Santerne, A., Almenara, J. M., et al. 2016, *MNRAS*, 458, 4025
- Deming, D., Harrington, J., Laughlin, G., et al. 2007, *ApJ*, 667, L199
- Deming, D., Seager, S., Richardson, L. J., et al. 2005, *Nature*, 434, 740
- Deming, D., Knutson, H., Agol, E., et al. 2011, *ApJ*, 726, 95
- Deming, D., Fraine, J. D., Sada, P. V., et al. 2012, *ApJ*, 754, 106
- Deming, D., Knutson, H., Kammer, J., et al. 2015, *ApJ*, 805, 132
- Deming, L. D., & Seager, S. 2017, *Journal of Geophysical Research (Planets)*, 122, 53
- Demory, B.-O., & Seager, S. 2011, *ApJS*, 197, 12
- Demory, B. O., Gillon, M., Barman, T., et al. 2007, *A&A*, 475, 1125
- Désert, J. M., Vidal-Madjar, A., Lecavelier Des Etangs, A., et al. 2008, *A&A*, 492, 585
- Désert, J.-M., Bean, J., Miller-Ricci Kempton, E., et al. 2011a, *ApJ*, 731, L40
- Désert, J.-M., Charbonneau, D., Fortney, J. J., et al. 2011b, *ApJS*, 197, 11
- Désert, J.-M., Charbonneau, D., Demory, B.-O., et al. 2011c, *ApJS*, 197, 14
- Diamond-Lowe, H., Stevenson, K. B., Bean, J. L., et al. 2014, *ApJ*, 796, 66
- Doyle, L. R., Carter, J. A., Fabrycky, D. C., et al. 2011, *Science*, 333, 1602
- Dransfield, G., & Triaud, A. H. M. J. 2020, *MNRAS*, 499, 505
- Dressing, C. D., & Charbonneau, D. 2013, *ApJ*, 767, 95
- Drummond, B., Tremblin, P., Baraffe, I., et al. 2016, *A&A*, 594, A69
- Dupuy, T. J., & Liu, M. C. 2012, *ApJS*, 201, 19
- Ebbing, D., & Gammon, S. D. 2016, General chemistry (Cengage Learning)
- Efron, B., & Tibshirani, R. J. 1993, An introduction to the bootstrap, Mono. Stat. Appl.

BIBLIOGRAPHY

- Probab. (London: Chapman and Hall)
- Ehrenreich, D., Lovis, C., Allart, R., et al. 2020, *Nature*, 580, 597
- Eistrup, C., Walsh, C., & van Dishoeck, E. F. 2018, *A&A*, 613, A14
- Elkins-Tanton, L. T. 2012, *Annual Review of Earth and Planetary Sciences*, 40, 113
- Espinoza, N., Fortney, J. J., Miguel, Y., et al. 2017, *ApJ*, 838, L9
- Esteves, L. J., De Mooij, E. J. W., & Jayawardhana, R. 2015, *ApJ*, 804, 150
- Evans, T. M., Aigrain, S., Gibson, N., et al. 2015, *MNRAS*, 451, 680
- Evans, T. M., Sing, D. K., Kataria, T., et al. 2017, *Nature*, 548, 58
- Fabrycky, D. C. 2010, *Non-Keplerian Dynamics of Exoplanets*, ed. S. Seager, 217
- Fabrycky, D. C., Ford, E. B., Steffen, J. H., et al. 2012, *ApJ*, 750, 114
- Faedi, F., Barros, S. C. C., Anderson, D. R., et al. 2011, *A&A*, 531, A40
- Fazio, G. G., Hora, J. L., Allen, L. E., et al. 2004, *ApJS*, 154, 10
- Foreman-Mackey, D., Hogg, D. W., Lang, D., et al. 2013, *PASP*, 125, 306
- Fortney, J. J. 2005, *MNRAS*, 364, 649
- Fortney, J. J., Cooper, C. S., Showman, A. P., et al. 2006, *ApJ*, 652, 746
- Fortney, J. J., Lodders, K., Marley, M. S., et al. 2008, *ApJ*, 678, 1419
- Fortney, J. J., Mordasini, C., Nettelmann, N., et al. 2013, *ApJ*, 775, 80
- Fortney, J. J., Shabram, M., Showman, A. P., et al. 2010, *ApJ*, 709, 1396
- Fortney, J. J., Sudarsky, D., Hubeny, I., et al. 2003, *ApJ*, 589, 615
- Fortney, J. J., Visscher, C., Marley, M. S., et al. 2020, *AJ*, 160, 288
- Fortney, J. J., Demory, B.-O., Désert, J.-M., et al. 2011, *ApJS*, 197, 9
- Fossati, L., Koskinen, T., France, K., et al. 2018, *AJ*, 155, 113
- Fraine, J. D., Deming, D., Gillon, M., et al. 2013, *ApJ*, 765, 127
- France, K., Loyd, R. O. P., Youngblood, A., et al. 2016, *ApJ*, 820, 89
- Freedman, R. S., Lustig-Yaeger, J., Fortney, J. J., et al. 2014, *ApJS*, 214, 25
- Freedman, R. S., Marley, M. S., & Lodders, K. 2008, *ApJS*, 174, 504
- Fressin, F., Knutson, H. A., Charbonneau, D., et al. 2010, *ApJ*, 711, 374
- Fressin, F., Torres, G., Charbonneau, D., et al. 2013, *ApJ*, 766, 81
- Freudenthal, J., von Essen, C., Dreizler, S., et al. 2018, *A&A*, 618, A41
- Fu, G., Deming, D., Knutson, H., et al. 2017, *ApJ*, 847, L22
- Fulton, B. J., Petigura, E. A., Howard, A. W., et al. 2017, *AJ*, 154, 109
- Gaia Collaboration, Brown, A. G. A., Vallenari, A., et al. 2018, *A&A*, 616, A1
- Galton, F. 1886, *The Journal of the Anthropological Institute of Great Britain and Ireland*, 15, 246
- Gandhi, S., & Madhusudhan, N. 2019, *MNRAS*, 485, 5817
- Gao, P., Thorngren, D. P., Lee, G. K. H., et al. 2020, *Nature Astronomy*, 4, 951
- Garhart, E., Deming, D., Mandell, A., et al. 2020, *AJ*, 159, 137
- Gaudi, B. S., Stassun, K. G., Collins, K. A., et al. 2017, *Nature*, 546, 514
- Gelman, A., & Rubin, D. B. 1992, *Statistical Science*, 7, 457
- Gibson, N. P., Aigrain, S., Roberts, S., et al. 2012, *MNRAS*, 419, 2683
- Gibson, N. P., Nikolov, N., Sing, D. K., et al. 2017, *MNRAS*, 467, 4591

- Gillon, M., Demory, B. O., Barman, T., et al. 2007a, A&A, 471, L51
- Gillon, M., Pont, F., Demory, B. O., et al. 2007b, A&A, 472, L13
- Gillon, M., Demory, B. O., Lovis, C., et al. 2017, A&A, 601, A117
- Gordon, S., & McBride, B. J. 1994, NASRP, 1311
- Gould, A., Udalski, A., An, D., et al. 2006, ApJ, 644, L37
- Guillot, T. 2010, A&A, 520, A27
- Guillot, T., Burrows, A., Hubbard, W. B., et al. 1996, ApJ, 459, L35
- Guilluy, G., Sozzetti, A., Brogi, M., et al. 2019, A&A, 625, A107
- Guo, X., Crossfield, I. J. M., Dragomir, D., et al. 2020, AJ, 159, 239
- Hadden, S., & Lithwick, Y. 2017, AJ, 154, 5
- Han, E., Wang, S. X., Wright, J. T., et al. 2014, PASP, 126, 827
- Hansen, B. M. S. 2008, ApJS, 179, 484
- Hansen, J. E., & Hovenier, J. W. 1974, Journal of Atmospheric Sciences, 31, 1137
- Hartman, J. D., Bakos, G. Á., Torres, G., et al. 2009, ApJ, 706, 785
- Hartman, J. D., Bakos, G. Á., Sato, B., et al. 2011a, ApJ, 726, 52
- Hartman, J. D., Bakos, G. Á., Kipping, D. M., et al. 2011b, ApJ, 728, 138
- Hartman, J. D., Bakos, G. Á., Torres, G., et al. 2011c, ApJ, 742, 59
- Haynes, K., Mandell, A. M., Madhusudhan, N., et al. 2015, ApJ, 806, 146
- Hellier, C., Anderson, D. R., Collier Cameron, A., et al. 2010, ApJ, 723, L60
- Hellier, C., Anderson, D. R., Collier Cameron, A., et al. 2012, MNRAS, 426, 739
- Hellier, C., Anderson, D. R., Collier Cameron, A., et al. 2017, MNRAS, 465, 3693
- Helling, C., Gourbin, P., Woitke, P., et al. 2019a, A&A, 626, A133
- Helling, C., Lee, G., Dobbs-Dixon, I., et al. 2016, MNRAS, 460, 855
- Helling, C., Iro, N., Corrales, L., et al. 2019b, A&A, 631, A79
- Heng, K. 2016, ApJ, 826, L16
- Heng, K., Mendonça, J. M., & Lee, J.-M. 2014, ApJS, 215, 4
- Henry, G. W., & Winn, J. N. 2008, AJ, 135, 68
- Herrero, E., Morales, J. C., Ribas, I., et al. 2011, A&A, 526, L10
- Hoeijmakers, H. J., Ehrenreich, D., Heng, K., et al. 2018, Nature, 560, 453
- Hoeijmakers, H. J., Ehrenreich, D., Kitzmann, D., et al. 2019, A&A, 627, A165
- Hogg, D. W., Bovy, J., & Lang, D. 2010, arXiv e-prints, arXiv:1008.4686
- Holman, M. J., & Murray, N. W. 2005, Science, 307, 1288
- Holman, M. J., Fabrycky, D. C., Ragozzine, D., et al. 2010, Science, 330, 51
- Howard, A. W., Marcy, G. W., Bryson, S. T., et al. 2012, ApJS, 201, 15
- Hoyer, S., López-Morales, M., Rojo, P., et al. 2013, MNRAS, 434, 46
- Hu, R., Seager, S., & Yung, Y. L. 2015, ApJ, 807, 8
- Hubeny, I. 2017, MNRAS, 469, 841
- Hubeny, I., Burrows, A., & Sudarsky, D. 2003, ApJ, 594, 1011
- Husser, T. O., Wende-von Berg, S., Dreizler, S., et al. 2013, A&A, 553, A6
- Ingalls, J. G., Krick, J. E., Carey, S. J., et al. 2016, AJ, 152, 44
- Jackson, B., Adams, E., Sandidge, W., et al. 2019, AJ, 157, 239

BIBLIOGRAPHY

- Johnson, J. A., Gazak, J. Z., Apps, K., et al. 2012, AJ, 143, 111
- Jontof-Hutter, D., Ford, E. B., Rowe, J. F., et al. 2016, ApJ, 820, 39
- Kammer, J. A., Knutson, H. A., Line, M. R., et al. 2015, ApJ, 810, 118
- Kataria, T., Showman, A. P., Fortney, J. J., et al. 2015, ApJ, 801, 86
- Kawashima, Y., & Ikoma, M. 2019, ApJ, 877, 109
- Keating, D., Cowan, N. B., & Dang, L. 2019, Nature Astronomy, 3, 1092
- Kelly, B. C. 2007, ApJ, 665, 1489
- Kempton, E. M. R., Bean, J. L., & Parmentier, V. 2017a, ApJ, 845, L20
- Kempton, E. M. R., Lupu, R., Owusu-Asare, A., et al. 2017b, PASP, 129, 044402
- Kilpatrick, B. M., Kataria, T., Lewis, N. K., et al. 2020, AJ, 159, 51
- Kirkpatrick, J. D., Cushing, M. C., Gelino, C. R., et al. 2011, ApJS, 197, 19
- Kitzmann, D., Heng, K., Rimmer, P. B., et al. 2018, ApJ, 863, 183
- Knutson, H. A., Benneke, B., Deming, D., et al. 2014, Nature, 505, 66
- Knutson, H. A., Charbonneau, D., Allen, L. E., et al. 2008, ApJ, 673, 526
- Knutson, H. A., Charbonneau, D., Burrows, A., et al. 2009a, ApJ, 691, 866
- Knutson, H. A., Charbonneau, D., Cowan, N. B., et al. 2009b, ApJ, 703, 769
- Knutson, H. A., Howard, A. W., & Isaacson, H. 2010, ApJ, 720, 1569
- Knutson, H. A., Charbonneau, D., Allen, L. E., et al. 2007, Nature, 447, 183
- Knutson, H. A., Madhusudhan, N., Cowan, N. B., et al. 2011, ApJ, 735, 27
- Knutson, H. A., Lewis, N., Fortney, J. J., et al. 2012, ApJ, 754, 22
- Koll, D. D. B., Malik, M., Mansfield, M., et al. 2019, ApJ, 886, 140
- Komacek, T. D. 2018, PhD thesis, The University of Arizona
- Komacek, T. D., Showman, A. P., & Parmentier, V. 2019, ApJ, 881, 152
- Komacek, T. D., & Tan, X. 2018, Research Notes of the American Astronomical Society, 2, 36
- Kreidberg, L. 2015, PASP, 127, 1161
- Kreidberg, L., Line, M. R., Thorngren, D., et al. 2018a, ApJ, 858, L6
- Kreidberg, L., Line, M. R., Parmentier, V., et al. 2018b, AJ, 156, 17
- Krick, J. E., Ingalls, J., Carey, S., et al. 2016, ApJ, 824, 27
- Kurucz, R. L. 1979, ApJS, 40, 1
- Kurucz, R. L., & Bell, B. 1995, Atomic line list
- Kuzuhara, M., Tamura, M., Kudo, T., et al. 2013, ApJ, 774, 11
- Lacis, A. A., & Oinas, V. 1991, J. Geophys. Res., 96, 9027
- Lagrange, A. M., Bonnefoy, M., Chauvin, G., et al. 2010, Science, 329, 57
- Lanotte, A. A., Gillon, M., Demory, B. O., et al. 2014, A&A, 572, A73
- Lanza, A. F. 2014, A&A, 572, L6
- Laughlin, G., Crismani, M., & Adams, F. C. 2011, ApJ, 729, L7
- Lecavelier Des Etangs, A., Vidal-Madjar, A., Désert, J. M., et al. 2008, A&A, 485, 865
- Lee, J. M., Fletcher, L. N., & Irwin, P. G. J. 2012, MNRAS, 420, 170
- Léger, A., Grasset, O., Fegley, B., et al. 2011, Icarus, 213, 1
- Leggett, S. K., Tremblin, P., Esplin, T. L., et al. 2017, ApJ, 842, 118

- Lewis, N. K., Knutson, H. A., Showman, A. P., et al. 2013, *ApJ*, 766, 95
- Line, M. R., Knutson, H., Deming, D., et al. 2013a, *ApJ*, 778, 183
- Line, M. R., & Parmentier, V. 2016, *ApJ*, 820, 78
- Line, M. R., Vasish, G., Chen, P., et al. 2011, *ApJ*, 738, 32
- Line, M. R., Wolf, A. S., Zhang, X., et al. 2013b, *ApJ*, 775, 137
- Lodders, K. 2004, *ApJ*, 611, 587
- Lodders, K., Palme, H., & Gail, H. P. 2009, *Landolt Börnstein*, 4B, 712
- Lothringer, J., & Barman, T. 2019, in American Astronomical Society Meeting Abstracts, Vol. 233, American Astronomical Society Meeting Abstracts #233, 404.05
- Lothringer, J. D., Barman, T., & Koskinen, T. 2018, *ApJ*, 866, 27
- Lupu, R. E., Zahnle, K., Marley, M. S., et al. 2014, *ApJ*, 784, 27
- Lyons, L. 1992, *Journal of Physics A Mathematical General*, 25, 1967
- Machalek, P., Greene, T., McCullough, P. R., et al. 2010, *ApJ*, 711, 111
- Machalek, P., McCullough, P. R., Burke, C. J., et al. 2008, *ApJ*, 684, 1427
- Machalek, P., McCullough, P. R., Burrows, A., et al. 2009, *ApJ*, 701, 514
- Maciejewski, G., Ohlert, J., Dimitrov, D., et al. 2014, *Acta Astron.*, 64, 11
- Maciejewski, G., Dimitrov, D., Mancini, L., et al. 2016, *Acta Astron.*, 66, 55
- Madhusudhan, N. 2012, *ApJ*, 758, 36
- Madhusudhan, N. 2019, *ARA&A*, 57, 617
- Madhusudhan, N., Mousis, O., Johnson, T. V., et al. 2011, *ApJ*, 743, 191
- Madhusudhan, N., & Seager, S. 2010, *ApJ*, 725, 261
- Mancini, L., Kemmer, J., Southworth, J., et al. 2016, *MNRAS*, 459, 1393
- Mandel, K., & Agol, E. 2002, *ApJ*, 580, L171
- Mansfield, M., Bean, J. L., Line, M. R., et al. 2018a, *AJ*, 156, 10
- Mansfield, M., Bean, J. L., Oklopčić, A., et al. 2018b, *ApJ*, 868, L34
- Mansfield, M., Bean, J. L., Stevenson, K. B., et al. 2020, *ApJ*, 888, L15
- Marley, M. S., Ackerman, A. S., Cuzzi, J. N., et al. 2013, *Clouds and Hazes in Exoplanet Atmospheres*, ed. S. J. Mackwell, A. A. Simon-Miller, J. W. Harder, & M. A. Bullock, 367
- Marois, C., Macintosh, B., Barman, T., et al. 2008, *Science*, 322, 1348
- Marois, C., Zuckerman, B., Konopacky, Q. M., et al. 2010, *Nature*, 468, 1080
- Maxted, P. F. L., Anderson, D. R., Doyle, A. P., et al. 2013, *MNRAS*, 428, 2645
- Mayor, M., & Queloz, D. 1995, *Nature*, 378, 355
- McKay, C. P., Pollack, J. B., & Courtin, R. 1989, *Icarus*, 80, 23
- McMurtry, C. W., Pipher, J. L., & Forrest, W. J. 2006, in Society of Photo-Optical Instrumentation Engineers (SPIE) Conference Series, Vol. 6265, Society of Photo-Optical Instrumentation Engineers (SPIE) Conference Series, ed. J. C. Mather, H. A. MacEwen, & M. W. M. de Graauw, 626508
- Melville, G., Kedziora-Chudczer, L., & Bailey, J. 2020, *MNRAS*, 494, 4939
- Metchev, S. A., Heinze, A., Apai, D., et al. 2015, *ApJ*, 799, 154
- Miles, B. E., Skemer, A. J. I., Morley, C. V., et al. 2020, *AJ*, 160, 63
- Miller, N., & Fortney, J. J. 2011, *ApJ*, 736, L29

BIBLIOGRAPHY

- Mills, S. M., Fabrycky, D. C., Migaszewski, C., et al. 2016, *Nature*, 533, 509
- Molaverdikhani, K., Henning, T., & Mollière, P. 2019, *ApJ*, 873, 32
- Molaverdikhani, K., Henning, T., & Mollière, P. 2020, *ApJ*, 899, 53
- Mollière, P., van Boekel, R., Dullemond, C., et al. 2015, *ApJ*, 813, 47
- Morello, G. 2015, *ApJ*, 808, 56
- Morello, G., Waldmann, I. P., Tinetti, G., et al. 2015, *ApJ*, 802, 117
- Morley, C. V., Fortney, J. J., Marley, M. S., et al. 2015, *ApJ*, 815, 110
- Morley, C. V., Knutson, H., Line, M., et al. 2017, *AJ*, 153, 86
- Morton, T. D., & Swift, J. 2014, *ApJ*, 791, 10
- Moses, J. I., Madhusudhan, N., Visscher, C., et al. 2013a, *ApJ*, 763, 25
- Moses, J. I., Visscher, C., Fortney, J. J., et al. 2011, *ApJ*, 737, 15
- Moses, J. I., Line, M. R., Visscher, C., et al. 2013b, *ApJ*, 777, 34
- Močnik, T., Hellier, C., Anderson, D. R., et al. 2017, *MNRAS*, 469, 1622
- Muirhead, P. S., Hamren, K., Schlawin, E., et al. 2012, *ApJ*, 750, L37
- Nemmen, R. S., Georganopoulos, M., Guiriec, S., et al. 2012, *Science*, 338, 1445
- Neveu-VanMalle, M., Queloz, D., Anderson, D. R., et al. 2014, *A&A*, 572, A49
- Nikolov, N., Sing, D. K., Pont, F., et al. 2014, *MNRAS*, 437, 46
- Nikolov, N., Sing, D. K., Goyal, J., et al. 2018, *MNRAS*, 474, 1705
- Nymeyer, S., Harrington, J., Hardy, R. A., et al. 2011, *ApJ*, 742, 35
- Öberg, K. I., Murray-Clay, R., & Bergin, E. A. 2011, *ApJ*, 743, L16
- O'Donovan, F. T., Charbonneau, D., Harrington, J., et al. 2010, *ApJ*, 710, 1551
- O'Rourke, J. G., Knutson, H. A., Zhao, M., et al. 2014, *ApJ*, 781, 109
- Oshagh, M., Santos, N. C., Ehrenreich, D., et al. 2014, *A&A*, 568, A99
- Parmentier, V., Fortney, J. J., Showman, A. P., et al. 2016, *ApJ*, 828, 22
- Parmentier, V., & Guillot, T. 2014, *A&A*, 562, A133
- Parmentier, V., Showman, A. P., & Fortney, J. J. 2021, *MNRAS*, 501, 78
- Parmentier, V., Showman, A. P., & Lian, Y. 2013, *A&A*, 558, A91
- Parmentier, V., Line, M. R., Bean, J. L., et al. 2018, *A&A*, 617, A110
- Pearson, K. A. 2019, *AJ*, 158, 243
- Perez-Becker, D., & Showman, A. P. 2013, *ApJ*, 776, 134
- Perna, R., Heng, K., & Pont, F. 2012, *ApJ*, 751, 59
- Petigura, E. A., Howard, A. W., & Marcy, G. W. 2013a, *Proceedings of the National Academy of Science*, 110, 19273
- Petigura, E. A., Marcy, G. W., & Howard, A. W. 2013b, *ApJ*, 770, 69
- Petigura, E. A., Marcy, G. W., Winn, J. N., et al. 2018, *AJ*, 155, 89
- Petrucci, R., Jofré, E., Schwartz, M., et al. 2013, *ApJ*, 779, L23
- Pino, L., Désert, J.-M., Brogi, M., et al. 2020, *ApJ*, 894, L27
- Piskorz, D., Buzard, C., Line, M. R., et al. 2018, *AJ*, 156, 133
- Pont, F., Knutson, H., Gilliland, R. L., et al. 2008, *MNRAS*, 385, 109
- Pont, F., Sing, D. K., Gibson, N. P., et al. 2013, *MNRAS*, 432, 2917
- Quijada, M. A., Marx, C. T., Arendt, R. G., et al. 2004, in *Society of Photo-Optical Instrumentation Engineers (SPIE) Conference Series*, 5485, 103

- mentation Engineers (SPIE) Conference Series, Vol. 5487, Optical, Infrared, and Millimeter Space Telescopes, ed. J. C. Mather, 244
- Rages, K., & Pollack, J. B. 1992, *Icarus*, 99, 289
- Rameau, J., Chauvin, G., Lagrange, A. M., et al. 2013, *ApJ*, 779, L26
- Rasio, F. A., Tout, C. A., Lubow, S. H., et al. 1996, *ApJ*, 470, 1187
- Reach, W. T., Megeath, S. T., Cohen, M., et al. 2005, *PASP*, 117, 978
- Rogers, T. M. 2017, *Nature Astronomy*, 1, 0131
- Romani, P. N., & Atreya, S. K. 1988, *Icarus*, 74, 424
- Rothman, L. S., Gordon, I. E., Barber, R. J., et al. 2010, *J. Quant. Spec. Radiat. Transf.*, 111, 2139
- Rugheimer, S., Kaltenegger, L., Zsom, A., et al. 2013, *Astrobiology*, 13, 251
- Sagan, C., Thompson, W. R., & Khare, B. N. 1992, in *ESA Special Publication*, Vol. 338, Symposium on Titan, ed. B. Kaldeich, 161
- Sainsbury-Martinez, F., Wang, P., Fromang, S., et al. 2019, *A&A*, 632, A114
- Santerne, A., Díaz, R. F., Moutou, C., et al. 2012, *A&A*, 545, A76
- Schneider, J. 2003, in SF2A-2003: Semaine de l’Astrophysique Francaise, ed. F. Combes, D. Barret, T. Contini, & L. Pagani, 149
- Schneider, J., Dedieu, C., Le Sidaner, P., et al. 2011, *A&A*, 532, A79
- Schwartz, J. C., & Cowan, N. B. 2015, *MNRAS*, 449, 4192
- Schwartz, J. C., Kashner, Z., Jovmir, D., et al. 2017, *ApJ*, 850, 154
- Seager, S. 1999, PhD thesis, HARVARD UNIVERSITY
- Seager, S., & Deming, D. 2010, *ARA&A*, 48, 631
- Seager, S., & Sasselov, D. D. 2000, *ApJ*, 537, 916
- Seager, S., Whitney, B. A., & Sasselov, D. D. 2000, *ApJ*, 540, 504
- Seeliger, M., Kitze, M., Errmann, R., et al. 2015, *MNRAS*, 451, 4060
- Sheppard, K. B., Mandell, A. M., Tamburo, P., et al. 2017, *ApJ*, 850, L32
- Showman, A. P., Cooper, C. S., Fortney, J. J., et al. 2008, *ApJ*, 682, 559
- Showman, A. P., Fortney, J. J., Lian, Y., et al. 2009, *ApJ*, 699, 564
- Showman, A. P., & Guillot, T. 2002, *A&A*, 385, 166
- Showman, A. P., & Polvani, L. M. 2011, *ApJ*, 738, 71
- Shporer, A., & Hu, R. 2015, *AJ*, 150, 112
- Shporer, A., O’Rourke, J. G., Knutson, H. A., et al. 2014, *ApJ*, 788, 92
- Shporer, A., Wong, I., Huang, C. X., et al. 2019, *AJ*, 157, 178
- Silburt, A., Gaidos, E., & Wu, Y. 2015, *ApJ*, 799, 180
- Sing, D. K. 2010, *A&A*, 510, A21
- Sing, D. K., Désert, J. M., Fortney, J. J., et al. 2011, *A&A*, 527, A73
- Sing, D. K., Wakeford, H. R., Showman, A. P., et al. 2015, *MNRAS*, 446, 2428
- Sing, D. K., Fortney, J. J., Nikolov, N., et al. 2016, *Nature*, 529, 59
- Skillen, I., Pollacco, D., Collier Cameron, A., et al. 2009, *A&A*, 502, 391
- Smith, A. M. S., Anderson, D. R., Madhusudhan, N., et al. 2012, *A&A*, 545, A93
- Snellen, I. A. G., de Mooij, E. J. W., & Albrecht, S. 2009, *Nature*, 459, 543

BIBLIOGRAPHY

- Southworth, J. 2008, MNRAS, 386, 1644
- Sozzetti, A., Torres, G., Charbonneau, D., et al. 2007, ApJ, 664, 1190
- Spake, J. J., Sing, D. K., Evans, T. M., et al. 2018, Nature, 557, 68
- Sromovsky, L. A., Fry, P. M., & Kim, J. H. 2011, Icarus, 215, 292
- Stassun, K. G., Collins, K. A., & Gaudi, B. S. 2017, AJ, 153, 136
- Stassun, K. G., Corsaro, E., Pepper, J. A., et al. 2018, AJ, 155, 22
- Stassun, K. G., Oelkers, R. J., Paegert, M., et al. 2019, AJ, 158, 138
- Steinrueck, M. E., Parmentier, V., Showman, A. P., et al. 2019, ApJ, 880, 14
- Stevenson, K., Harrington, J., Nymeyer, S., et al. 2010a, in AAS/Division for Planetary Sciences Meeting Abstracts, Vol. 42, AAS/Division for Planetary Sciences Meeting Abstracts #42, 27.13
- Stevenson, K. B. 2016, ApJ, 817, L16
- Stevenson, K. B., Bean, J., Line, M. R., et al. 2016, in American Astronomical Society Meeting Abstracts, Vol. 227, American Astronomical Society Meeting Abstracts #227, 224.02
- Stevenson, K. B., Bean, J. L., Madhusudhan, N., et al. 2014a, ApJ, 791, 36
- Stevenson, K. B., Bean, J. L., Seifahrt, A., et al. 2014b, AJ, 147, 161
- Stevenson, K. B., Harrington, J., Nymeyer, S., et al. 2010b, Nature, 464, 1161
- Stevenson, K. B., Harrington, J., Fortney, J. J., et al. 2012, ApJ, 754, 136
- Stevenson, K. B., Désert, J.-M., Line, M. R., et al. 2014c, Science, 346, 838
- Stevenson, K. B., Line, M. R., Bean, J. L., et al. 2017, AJ, 153, 68
- Swain, M. R., Vasisht, G., & Tinetti, G. 2008, Nature, 452, 329
- Ter Braak, C. J. 2005, Genetic algorithms and markov chain monte carlo: Differential evolution markov chain makes bayesian computing easy (revised), Tech. rep., Wageningen UR, Biometris
- Thao, P. C., Mann, A. W., Johnson, M. C., et al. 2020, AJ, 159, 32
- Thorngren, D., Gao, P., & Fortney, J. J. 2019, ApJ, 884, L6
- Thorngren, D., Gao, P., & Fortney, J. J. 2020, ApJ, 889, L39
- Thorngren, D. P., & Fortney, J. J. 2018, AJ, 155, 214
- Thorngren, D. P., Fortney, J. J., Murray-Clay, R. A., et al. 2016, ApJ, 831, 64
- Tinetti, G., Deroo, P., Swain, M. R., et al. 2010, ApJ, 712, L139
- Tinetti, G., Vidal-Madjar, A., Liang, M.-C., et al. 2007, Nature, 448, 169
- Todorov, K., Deming, D., Harrington, J., et al. 2010, ApJ, 708, 498
- Todorov, K. O., Deming, D., Knutson, H. A., et al. 2012, ApJ, 746, 111
- Todorov, K. O., Deming, D., Knutson, H. A., et al. 2013, ApJ, 770, 102
- Toon, O. B., McKay, C. P., Ackerman, T. P., et al. 1989, J. Geophys. Res., 94, 16287
- Torres, G., Fressin, F., Batalha, N. M., et al. 2011, ApJ, 727, 24
- Tremblin, P., Chabrier, G., Mayne, N. J., et al. 2017, ApJ, 841, 30
- Triaud, A. H. M. J. 2014a, in American Astronomical Society Meeting Abstracts, Vol. 224, American Astronomical Society Meeting Abstracts #224, 416.02
- Triaud, A. H. M. J. 2014b, MNRAS, 439, L61

- Triaud, A. H. M. J., Lanotte, A. A., Smalley, B., et al. 2014, MNRAS, 444, 711
- Triaud, A. H. M. J., Gillon, M., Ehrenreich, D., et al. 2015, MNRAS, 450, 2279
- Tsai, S.-M., Kitzmann, D., Lyons, J. R., et al. 2018, ApJ, 862, 31
- Tsai, S.-M., Lyons, J. R., Grosheintz, L., et al. 2017, ApJS, 228, 20
- Tsiaras, A., Waldmann, I. P., Zingales, T., et al. 2018, AJ, 155, 156
- Venot, O., Agúndez, M., Selsis, F., et al. 2014, A&A, 562, A51
- Vidal-Madjar, A., Lecavelier des Etangs, A., Désert, J. M., et al. 2003, Nature, 422, 143
- Visscher, C. 2012, ApJ, 757, 5
- Visscher, C., Lodders, K., & Fegley, Bruce, J. 2010, ApJ, 716, 1060
- Visscher, C., & Moses, J. I. 2011, ApJ, 738, 72
- von Essen, C., Mallonn, M., Albrecht, S., et al. 2015, A&A, 584, A75
- Wakeford, H. R., & Sing, D. K. 2015, A&A, 573, A122
- Wakeford, H. R., Wilson, T. J., Stevenson, K. B., et al. 2019, Research Notes of the American Astronomical Society, 3, 7
- Wakeford, H. R., Sing, D. K., Kataria, T., et al. 2017, Science, 356, 628
- Wakeford, H. R., Sing, D. K., Deming, D., et al. 2018, AJ, 155, 29
- Wallack, N. L., Knutson, H. A., Morley, C. V., et al. 2019, AJ, 158, 217
- Welbanks, L., Madhusudhan, N., Allard, N. F., et al. 2019, ApJ, 887, L20
- Welsh, W. F., Orosz, J. A., Short, D. R., et al. 2015, ApJ, 809, 26
- Werner, M. W., Roellig, T. L., Low, F. J., et al. 2004, ApJS, 154, 1
- Wheatley, P. J., Collier Cameron, A., Harrington, J., et al. 2010, arXiv e-prints, arXiv:1004.0836
- Winn, J. N. 2010, Exoplanet Transits and Occultations, ed. S. Seager, 55
- Winn, J. N., Sanchis-Ojeda, R., & Rappaport, S. 2018, New A Rev., 83, 37
- Wolszczan, A., & Frail, D. A. 1992, Nature, 355, 145
- Wong, I., Knutson, H. A., Cowan, N. B., et al. 2014, ApJ, 794, 134
- Wong, I., Knutson, H. A., Lewis, N. K., et al. 2015, ApJ, 811, 122
- Wong, I., Knutson, H. A., Kataria, T., et al. 2016, ApJ, 823, 122
- Wright, J. T., Marcy, G. W., Howard, A. W., et al. 2012, ApJ, 753, 160
- Wright, J. T., Fakhouri, O., Marcy, G. W., et al. 2011, PASP, 123, 412
- Zahnle, K. J., & Marley, M. S. 2014, ApJ, 797, 41
- Zellem, R. T., Swain, M. R., Roudier, G., et al. 2017, ApJ, 844, 27
- Zhang, M., Chachan, Y., Kempton, E. M. R., et al. 2019, PASP, 131, 034501
- Zhang, M., Knutson, H. A., Kataria, T., et al. 2018, AJ, 155, 83
- Zhang, T. 2004, in Proceedings of the Twenty-first International Conference on Machine Learning, ICML '04 (New York, NY, USA: ACM), 116
- Zhang, X., & Showman, A. P. 2018a, ApJ, 866, 1
- Zhang, X., & Showman, A. P. 2018b, ApJ, 866, 2
- Zhao, M., O'Rourke, J. G., Wright, J. T., et al. 2014, ApJ, 796, 115
- Zilinskas, M., Miguel, Y., Mollière, P., et al. 2020, MNRAS, 494, 1490

CONTRIBUTION FROM CO-AUTHORS

The position in the author list reflects the importance of the contribution of each co-author. I have omitted Jean-Michel Désert from each chapter, as his supervision was present throughout the thesis.

Chapter 1: Introduction

The introduction was written entirely by CB.

Chapter 2: Evidence for disequilibrium chemistry from vertical mixing in hot Jupiter atmospheres: A comprehensive survey of transiting close-in gas giant exoplanets with warm-*Spitzer*/IRAC

Claire Baxter, Jean-Michel Désert, Shang-Min Tsai, Kamen O. Todorov, Jacob L. Bean, Drake Deming, Vivien Parmentier, Jonathan J. Fortney, Michael Line, Daniel Thorngren, Raymond T. Pierrehumbert, Adam Burrows, Adam P. Showman

Astronomy & Astrophysics, 648, A127 (2021)

CB developed the data reduction pipeline based on previous studies for the reduction of 3.6 and $4.5\mu\text{m}$ Spitzer/IRAC data. Data used in the paper was taken from the Spitzer heritage archive, based on proposals by Jean-Michel Désert and Drake Deming. Shang-Min Tsai created the grids of forward models and contributed text to the section describing the models. Daniel Thorngren provided a table of radius anomalies. CB performed all data analysis, comparisons between data and models and wrote the manuscript. All of the co-authors provided feedback to the complete manuscript.

Chapter 3: A transition between the hot and the ultra-hot Jupiter atmospheres

Claire Baxter, Jean-Michel Désert, Vivien Parmentier, Michael Line, Jonathan J. Fortney, Jacob Arcangeli, Jacob L. Bean, Kamen O. Todorov, Megan Mansfield

Astronomy & Astrophysics, 639, A36 (2020)

CB augmented the data reduction pipeline for reduction of Spitzer/IRAC eclipses. CB performed the search of the literature and collected all of the eclipse data. Mike Line provided the grid of forward models and contributed text to the section describing the models. Megan Mansfield provided the HST/WFC3 spectra. CB performed all data analysis on the secondary eclipses and the emission models. All of the co-authors provided feedback to the complete manuscript.

Chapter 4: Periodic variability in the brightness of an ultra-hot Jupiter atmosphere

Claire Baxter & Jean-Michel Désert

To be submitted to Astronomy & Astrophysics

CB performed the data reduction and analysis of the archival eclipses and wrote the full manuscript. All co-authors provided feedback to the manuscript.

Chapter 5: Transit timing variations of cool Kepler planets from Spitzer/IRAC analysis

Claire Baxter, Jean-Michel Désert, Daniel Fabrycky

To be submitted to Astronomy & Astrophysics

CB performed the data reduction of the Spitzer transits. Daniel Fabrycky provided the transit times of the Kepler data, fit TTV models to the Kepler data and provided propagated predictions for the transit times of the multi-planet systems. Daniel Fabrycky also performed photodynamical modelling of the Kepler-16 data from Kepler and provided the relevant text for all of his contributions. CB performed the analysis of the reduced Spitzer transits and made comparisons with TTV predictions. CB wrote the manuscript, with the exceptions of the TTV modelling sections. All co-authors provided feedback to the draft manuscript.

NEDERLANDSE SAMENVATTING

De Spitzer ruimtetelescoop werd in januari 2020 buiten gebruik gesteld, een erfenis van rijke atmosferische studies van individuele exoplaneten achterlatend. Deze dissertatie vat de enorme inspanningen van Spitzer op het gebied van exoplaneetwetenschappen van de afgelopen 15 jaar samen. Met behulp van honderden uren aan nabije-infrarood Spitzer/IRAC waarnemingen in emissie en transmissie hebben we de atmosferen van in totaal meer dan 100 exoplaneten gemeten en gekarakteriseerd. We hebben een grondig inzicht gekregen in de complexe instrumentele systematiek die komt kijken bij het analyseren van dergelijke gegevens en we hebben de belangrijke fysische processen die nodig zijn in atmosferische modellen vastgelegd.

In Hoofdstuk 2 presenteren we onze Spitzer/IRAC datareductiepijplijn. Deze pijplijn implementeert decorrelatie op pixelniveau om de sterke systematiek te corrigeren die het gevolg is van de intrapixel gevoeligheid van de IRAC detectoren. We hebben deze procedure gebruikt om 70 fotometrische lichtkrommen van 33 planeten die voor hun ster langs gaan, op uniforme wijze te analyseren. Vervolgens hebben we deze groep uitgebreid met 16 eerder gepubliceerde exoplaneten, wat resulteerde in een totaal van 49 exoplaneten met transmissiemetingen bij 3,6 en 4,5 μ m.

We vergelijken het overzicht van exoplaneet overgangsdieptes met een raster van 1-D voorspellende modellen in radiatief convectief evenwicht. Ons oorspronkelijke raster van modellen berust op twee gangbare aannames bij het modelleren van exoplaneetatmosferen. De eerste is dat de atmosfeer in chemisch evenwicht is. Dit betekent dat de abundantie van verschillende moleculaire soorten kan worden bepaald uit de temperatuur, druk, en globale chemische samenstelling van de atmosfeer. Ten tweede wordt algemeen aangenomen dat de elementaire chemische samenstelling van een typische atmosfeer gelijk is aan die van de zon (zonnesamenstelling). Onder deze aannames kunnen modellen de relatieve abundantie van elementaire en moleculaire soorten voorspellen als functie van de temperatuur en druk van de planeet, gemeten met transmissie-spectroscopie. In het bijzonder wordt een overgang van methaan naar koolmonoxide verwacht bij ongeveer 1000 K, wanneer we van de koelste reuzenexoplaneten gaan die dicht bij hun ster staan, tot aan de heetste Hete Jupiters. Wij hebben deze overgang aangetoond met ons raster van atmosfeermodellen in chemisch evenwicht en zonnesamenstelling. Bij vergelijking van onze modellen met onze waarnemingen bleek echter dat de modellen de methaanconcentraties voor de koelste planeten overschatten. Met 13

planeten van minder dan 1000K hebben we voor het eerst een sterke statistische bevestiging (7.5σ) van het ontbreken van methaan in de atmosferen van gasreuzen exoplaneten.

Hierop voortbouwend hebben we ons modelraster uitgebreid van evenwichtschemie en zonnesamenstelling met onevenwichtschemie zoals gekenmerkt door verticale menging (via een eddy-diffusiecoëfficiënt, $K_{zz} = 0 - 10^{12} \text{ cm}^2/\text{s}$) en met twee verschillende chemische samenstellingen (1x en 30x zonne-samenstelling). Door deze modellen te vergelijken met de waarnemingen konden we aantonen dat het gebrek aan methaan in de koele planeten gedeeltelijk verklaard kan worden met modellen van hogere metalliciteit (30x zonne-samenstelling) en konden we de modellen met 1x zonne-samenstelling uitsluiten met $>3\sigma$. Eerdere studies hebben gesuggereerd dat er een relatie bestaat tussen de massa en de metalliciteit in de bulksgesamenstelling van gasreuzen, waarbij de minder massieve planeten over het algemeen rijker zijn aan metaal. Onze bevindingen ondersteunen de extrapolatie van deze trend van bulkmetalliciteiten naar atmosferische metalliciteiten.

Bovendien vonden we dat deze koelste planeten (<1000K) de voorkeur geven aan de modellen met weinig verticale menging ($K_{zz} = 10^8 \text{ cm}^2/\text{s}$). Dus niet alleen hebben deze koele, minder massieve gasreuzen statistisch gezien een metaalrijkere atmosfeer dan hun hetero evenknieën, ze vertonen ook minder sterke verticale menging. Daarentegen vonden we dat de heetste planeten (>1000K) het best te verklaren zijn met 1x zonne-metalliciteit en met sterke verticale menging ($K_{zz} = 10^{12} \text{ cm}^2/\text{s}$). Hogere niveaus van verticale menging in hetero atmosferen zijn theoretisch voorspeld en waargenomen in de atmosferen van bruine dwergen. Ons resultaat ondersteunt deze beide studies.

In ons onderzoek naar planeten die voor hun ster langs gaan, vonden we geen duidelijke trends in de transmissiemetriek met toenemende temperatuur voor de ultrahete planeten, hoewel we slechts een paar ultrahete Jupiters in onze steekproef hebben. In Hoofdstuk 3 breiden we ons onderzoek uit naar de emissie van de dagzijden van exoplaneten. We hebben een onderzoek van 78 planeten met secundaire eclipsen gebruikt om te bekijken hoe de abundantie van CH₄ en CO zich manifesteert aan de dagzijde. Dit onderzoek bevatte twee keer zo veel hete planeten als ons transmissie-onderzoek, en slechts enkele daarvan vallen binnen het verwachte temperatuurbereik waarin de atmosfeer door methaan zou worden gedomineerd. Bovendien dringt emissiefotometrie dieper door in de atmosfeer (tot het 1-10 bar drukniveau) dan transmissiefotometrie (1mbar drukniveau), waardoor we hogere temperaturen en daarmee waarschijnlijk een lagere methaanabundantie zien.

We hebben deze steekproef van planeten onderzocht door de 3,6 en 4,5 μm helderheidstemperaturen van de dagzijden van de planeten te berekenen. We hebben ook een metriek gedefinieerd, die we de afwijking van een zwarte straler noemen, die de emissie of absorptie in de 4,5 μm bandfilter meet ten opzichte van de 3,6 μm filter. De 4,5 μm filter meet de CO-functie en de 3,6 μm filter meet dicht bij het continuüm door het gebrek aan methaan in de hetero planeten. Daardoor stelt deze metriek ons in staat het temperatuur-drukprofiel te bepalen door de sterkte van de relatieve CO emissie of absorptie te meten. Wij hebben een overgang gevonden in de afwijking van een zwarte straler tussen de hete en de ultrahete Jupiters rond 1700K, waar de hetero planeten een sterker teken van CO in de emissie ble-

ken te hebben. We hebben onderzocht wat de oorzaak hiervan kan zijn door het resultaat te vergelijken met een nieuw raster van zelfconsistente 1D radiatieve en convectieve modellen, variërend in metaliciteit, koolstof-zuurstofverhouding (C/O), oppervlaktezwaartekracht en effectieve stellaire temperatuur, waarbij we ervoor gezorgd hebben dat de relevante fysica voor het ontstaan van temperatuurinversies wordt meegenomen. De data zijn opmerkelijk goed in overeenstemming met deze modellen. Wij stellen voor dat de overgang tussen hete en ultrahete Jupiters een statistisch bewijs is van temperatuurinversies bij de heetste planeten, naast de verwachte verschuiving van de Planck-functie.

Hoofdstuk 3 laat zien dat een zorgvuldige berekening van de helderheidstemperaturen en de effectieve temperatuur cruciaal is. We vonden dat het niet integreren over de Spitzer bandfilter of het benaderen van de ster met een zwarte straler in plaats van een PHOENIX model bij het berekenen van de helderheidstemperaturen een vertekening in de resultaten kan veroorzaken. Deze vertekening resulteerde in een verhoging van de gemeten effectieve temperatuur van de planeet vergeleken met de voorspelling van de evenwichtstemperatuur, en de vertekening was sterker voor de planeten rond hetere sterren. Deze onevenredig hogere effectieve temperaturen bij hetere exoplaneten kunnen verkeerd worden geïnterpreteerd als een lagere efficiëntie van atmosferische herdistributie bij de heetste planeten, zoals in eerdere studies is waargenomen. Een andere bron van vertekening komt voort uit het feit dat de effectieve temperatuur gewoonlijk wordt berekend door de spectrale energieverdeling van de planeet te benaderen met een zwarte straler. Er zijn echter slechts twee fotometrische punten, waarvan er één een sterk CO-emissie-teken heeft ($4,5 \mu\text{m}$) in het geval van ultrahete Jupiters. In zo'n situatie vertekent de berekening van de effectieve temperatuur als een gewogen gemiddelde van de twee Spitzer-helderheidstemperaturen ook de metingen van de effectieve temperatuur in de richting van hogere temperaturen. Na correctie voor al deze effecten vonden we geen statistisch significante trend in de effectieve temperatuur als functie van de evenwichtstemperatuur. Deze bevinding ondersteunt eerdere beweringen van lagere herverdelingsefficiëntie in hetere planeten niet. Er bleef echter een grote spreiding in de helderheidstemperaturen van hetere planeten vergeleken met koelere planeten, wat suggereerde dat er verschillende herverdelingsefficiënties bestaan voor de heetste planeten.

In Hoofdstuk 4 hebben we 10 secundaire eclipsen van de zeer hete Jupiter WASP-18b geanalyseerd en hebben we periodieke variabiliteit gevonden in de $4,5 \mu\text{m}$ helderheid van de planeet als functie van de tijd. Met behulp van een sinusoïdaal model hebben we een variabiliteitsperiode van $23,12 \pm 1,66$ dagen en een piek-tot-dal amplitude van 456 ± 71 ppm gevonden, wat overeenkomt met een veranderlijkheid van $\sim 12\%$. We hebben mogelijke fysische processen besproken die tot zulke variabiliteit zouden kunnen leiden: koppeling van magnetische velden, variabele windsnelheden, wolken, veranderingen in chemische samenstelling, en we hebben de hypothese dat dit te wijten was aan stellaire variabiliteit uitgesloten. Tenslotte hebben wij onderzocht of dit kan worden gedetecteerd met de huidige geavanceerde instrumenten (HST, TESS) en hebben we vastgesteld dat deze niet de vereiste nauwkeurigheid hebben en dat we moeten kijken naar toekomstige missies om deze variabiliteitsmetingen op te volgen.

In Hoofdstuk 5 we hebben 48 overgangen van sommige van de koelste planeten geobserveerd door Spitzer/IRAC geanalyseerd. We hebben de overgangstijden gemeten van zes planeten uit drie multi-planeet systemen (Kepler-9, Kepler-18 en Kepler-32) en hebben deze tijden vergeleken met de voorspellingen van de Kepler waarnemingen. De onzekerheden van de Spitzer-transits bleken vrij groot te zijn, zodat de resultaten consistent waren met de voorspellingen, maar niet nauwkeurig genoeg om de modellen verder te beperken. Daarnaast hebben we twee planeetovergangen van de circumbinaire planeet Kepler-16b geanalyseerd. We gebruiken deze overgangen in combinatie met archiefgegevens van Kepler om een foto-dynamisch model te construeren en we geven updates van de baanelementen van het systeem.

Het werk dat we in deze dissertatie presenteren, heeft het potentieel om als ijkpunt te dienen voor infraroodstudies in de toekomst van exoplaneetwetenschappen, in het bijzonder met de aanstaande James Webb Space Telescope. De waargenomen trends en de effecten die we hebben beschreven in de gerapporteerde studies (verticale menging, temperatuurinversies, wolken, variabiliteit, en complexe dynamica) zullen nog duidelijker worden met de toegenomen precisie, en belangrijk zijn om mee te nemen in toekomstige inspanningen om atmosferen te modelleren. Ons onderzoek draagt bij tot een beter begrip van de atmosfeer van planeten in een brede context, en kan zo een verhelderend licht werpen op de vorming en evolutie van planeten en, uiteindelijk, op de bewoonbaarheid ervan.

SUMMARY

The *Spitzer* Space Telescope was decommissioned in January 2020, leaving behind a legacy of rich atmospheric studies of individual exoplanets. This thesis summarizes the huge efforts of *Spitzer* in the field of exoplanet science over the last 15 years. Using several hundreds of hours of near-infrared *Spitzer*/IRAC observations in emission and transmission, we measured and characterized the atmospheres of more than 100 exoplanets in total. We gained a deep understanding of the complex instrumental systematics involved in analyzing such data and we pinned down the important physical processes required in atmospheric models.

In Chapter 2 we present our *Spitzer*/IRAC data reduction pipeline. This pipeline implements pixel level decorrelation for correcting the strong systematics arising from the intrapixel sensitivity of the IRAC detectors. We used this procedure to analyze 70 photometric lightcurves of 33 transiting planets uniformly. We then augmented this sample with 16 previously published exoplanets, resulting in a total of 49 exoplanets with transmission measurements at 3.6 and $4.5\mu\text{m}$.

We compare the survey of exoplanet transit depths to a grid of 1-D radiative convective equilibrium forward models. Our initial grid of models stands on two common assumptions when modelling exoplanet atmospheres. First, is that the atmosphere is in chemical equilibrium. This means that the abundance of different molecular species can be determined from the temperature, pressure, and global chemical composition of the atmosphere. Second, it is commonly assumed that the elemental chemical composition of a typical atmosphere is equivalent to that of the Sun (solar composition). Under these assumptions, models can predict the relative abundance of elemental and molecular species as a function of planet temperature and pressure probed by transmission spectroscopy. In particular, a transition from methane to carbon monoxide is expected at around 1000K as we sample from the coolest close-in giant exoplanets to the hottest hot-Jupiters. We demonstrated this transition with our grid of equilibrium chemistry solar composition forward atmospheric models. However, when comparing our models to our observations we found that the models overestimate methane levels for the coolest planets. With 13 planets less than 1000K, we obtained a strong statistical confirmation (7.5σ) of the lack of methane in the atmospheres of gas giant exoplanets for the first time ever.

Building on this, we expanded our grid of models from equilibrium chemistry and solar composition to include disequilibrium chemistry as characterized by vertical mixing (via an

eddy diffusion coefficient, $K_{zz} = 0 - 10^{12}$ cm²/s) and with two different chemical compositions (1x and 30x solar). By comparing these models to the observations we were able to show that the lack of methane in the cool planets can be partially explained with models of higher metallicity (30x solar) and rule out the models with 1x solar composition with $>3\sigma$ confidence. Previous studies have suggested that there is a mass-metallicity relation in the bulk composition of transiting gas giant planets, whereby the less massive planets tend to be more metal rich. Our finding supports the extrapolation of this trend from bulk metallicities to atmospheric metallicities.

Additionally, we found that these coolest planets (<1000K) favor the models with low amounts of vertical mixing ($K_{zz} = 10^8$ cm²/s). So not only do these cool, less massive close-in gas giant planets have statistically more metal-rich atmospheres than their hotter counterparts, they also exhibit less vigorous vertical mixing. On the other hand, we found that the hottest planets (>1000K) are best explained by 1x solar metallicity and high vertical mixing models ($K_{zz} = 10^{12}$ cm²/s). Higher levels of vertical mixing in hotter atmospheres has been predicted theoretically and observed in the atmospheres of brown dwarfs. Our result supports both of these studies.

In our survey of transiting planets, we did not find any obvious trends in the transmission metric with increasing temperature for the ultra-hot planets, but we only have a few ultra-hot Jupiters in our sample. However, in Chapter 3, we expanded our exploration to the dayside emission of exoplanets. We used a survey of 78 planets with secondary eclipses to explore how the abundance of CH₄ and CO manifests in the dayside. This survey contained twice as many hot planets compared with the transmission survey, and only a few of which fall within the expected methane-dominated temperature range. Furthermore, emission photometry probes deeper in the atmosphere (1-10 bar pressure levels) than transmission photometry (1mbar pressure level), reaching levels of higher temperatures and likely low methane abundance.

We examined this sample of planets by calculating the 3.6 and 4.5 μ m brightness temperatures of the planetary dayside. We also defined a metric, called deviation from the blackbody, which measures the emission or absorption of the 4.5 μ m relative to the 3.6 μ m bandpass. The 4.5 μ m probes the CO feature and the 3.6 μ m probes close to the continuum due to the lack of methane in the hotter planets. Therefore, this metric allows us to probe the temperature pressure profile by measuring the strength of the relative CO emission or absorption. We found a transition in the deviation from the blackbody between the hot and the ultra-hot Jupiters at around 1700K, where the hotter planets appeared to have a stronger CO feature in emission. We explored what the origins of this might be by comparing the result to a new grid of self-consistent 1D radiative and convective models varying metallicity, carbon to oxygen ratio (C/O), surface gravity, and stellar effective temperature, making sure to incorporate the relevant physics for temperature inversions to form. The data is in remarkable agreement with these models. We propose that the transition between hot and ultra-hot Jupiters is statistical evidence of temperature inversions in the hottest planets, in addition to the expected Planck function shift.

Chapter 3 highlights the crucial importance of careful calculation of brightness temperatures and effective temperature. We found that either a failure to integrate over the *Spitzer* bandpass or approximating the star with a blackbody instead of a PHOENIX model when calculating the brightness temperatures can induce a bias in the results. This bias resulted in increasing the measured effective temperature of the planet compared to the equilibrium temperature prediction, and the bias was stronger for the planets around hotter stars. These disproportionately hotter effective temperatures in hotter exoplanets can be misinterpreted as a lower efficiency of redistribution in the hottest planets as is seen in previous studies. Another source of bias arises from the fact that the effective temperature is typically calculated by fitting a blackbody to the spectral energy distribution of the planet. However, there are just two photometric points, one of which has a strong CO emission feature ($4.5\text{ }\mu\text{m}$) for the cases of ultra-hot Jupiters. In such a situation, calculating the effective temperature as a weighted mean of the two *Spitzer* brightness temperatures also biased the effective temperature results towards hotter temperatures. After correcting for all of these effects, we did not find a statistically significant trend in the effective temperature with equilibrium temperature. This finding does not support previous claims of lower redistribution efficiency with hotter planets. However, there remained a large scatter in the brightness temperatures of hotter planets compared to cooler planets, which suggested a range of different redistribution efficiencies for the hottest planets.

In Chapter 4 we analyzed 10 archival secondary eclipses of the ultra-hot Jupiter WASP-18b and found periodic variability in the $4.5\text{ }\mu\text{m}$ brightness of the planet in time. Using a sinusoidal model, we derived a variability period of 23.12 ± 1.66 days and a peak-to-trough amplitude of 456 ± 71 ppm, corresponding to $\sim 12\%$ variability. We discussed possible physical processes that could result in such variability: magnetic field coupling, variable wind speeds, clouds, changes in chemical composition, and we ruled out the hypothesis that this was due to stellar variability. Finally, we explored whether this could be detected with the current state-of-the-art instruments (HST, TESS) and found that these do not have the required precision and that we need to look towards future missions for follow-up of these variability measurements.

In Chapter 5 we analyzed 48 transits of some of the coolest planets observed with Spitzer/IRAC. We measured the transit times of six planets from three multi-planet systems (Kepler-9, Kepler-18 and Kepler-32) and compared these transit times to predictions made from Kepler observations. We found that the uncertainties were quite large on the *Spitzer* transits and so the results were consistent with predictions but not accurate enough to further constrain the models. Additionally, we analyzed two transits of the circumbinary planet, Kepler-16b. We use these transits in combination with archival Kepler data to constrain a photodynamical model and report updates on the orbital elements of the system.

The work presented in this thesis has the potential to serve as the benchmark for infrared studies in the future of exoplanet science, particularly with the upcoming James Webb Space Telescope. The trends observed and the effects described in the studies reported (vertical mixing, temperature inversions, clouds, variability, and complex dynamics) will be even more

Summary

apparent with the increased precision, and important to include in future modelling efforts. Our research contributes to the understanding of planetary atmospheres in a broad context, thereby illuminating the issues of planet formation, evolution, and, ultimately, habitability.

ACKNOWLEDGEMENTS

Your Name,
Date

Ph.D. thesis, Anton Pannekoek Institute, Universiteit van Amsterdam
Your Name, Year

ISBN: ■ [TODO: N] ■

Cover design by .

Credits:

afterquote.

Someone

